Bioelectrochemical systems for energy and materials conversion

Habilitationsschrift

von **Dr.-Ing. Tanja Vidaković-Koch**

geb. am 02.09.1970   in Požega, Serbien

zur Verleihung des akademischen Grades

**Doktor-Ingenieurin habilitata
(Dr.-Ing. habil.)**

genehmigt von der Fakultät für Verfahrens- und Systemtechnik
der Otto-von-Guericke-Universität Magdeburg am 05.02.2019

Gutachter:

Prof. Dr.-Ing. habil. Kai Sundmacher

Prof. Dr.-Ing. habil. Thomas Turek

Prof. Dr. Gunther Wittstock

Preface

Having only had experience with "normal" electrochemical systems, where normal is defined as a noble metal (such as platinum or ruthenium) catalyst and chemicals such as strong acids, bases and simple organic molecules like methanol, the world of bioelectrochemical processes at first appeared very diverse and confusing. Chemical structures and formulas were lengthy and required me to refer to long-forgotten organic chemistry books. Additionally, enzymes turned out to be very exotic, and the idea that they can indeed function as bioelectrochemical catalysts seemed bizarre. At first, I was filled with doubt and questions. This new fascinating world was full of different preparation strategies and unfamiliar (bio)chemistry. My first approach when reading related literature in this field was to assign functionality to colorful names appearing in numerous different preparation procedures reported in the literature. In the world of catalysts, mediators, binders and supports I felt more comfortable. Since the field was dominated by exotic chemicals and enzymes, I realized fast that there were few systematic approaches to the preparation of electrodes and that the field was methodically relatively poor. Furthermore, most of the enzymatic fuel cells had a rather primitive design. In the field of bioelectrochemical synthesis, electrochemical analysis appeared highly underrepresented. The overall design of bioelectrochemical fuel cells and reactors had also been very little explored. I viewed our mission as adding an engineering touch to bioelectrochemistry. A short overview of the main research directions and results is presented in this habilitation thesis. I wish you a pleasant journey through the fascinating world of bioelectrochemical systems!

Magdeburg, March 2018   Tanja Vidaković-Koch

Inhalt

Zusammenfassung

In bioelektrochemischen Geräten werden Enzyme als katalytische Komponenten auf intelligente Weise mit elektrisch leitenden Oberflächen kombiniert. Auf diese Weise können diese elektrisch leitenden Materialien die natürlichen Enzymsubstrate in einem sogenannten direkten Elektronentransfermechanismus (DET) ersetzen. Alternativ könnte ein künstliches Enzymsubstrat, ein sogenannter Mediator, verwendet und elektrochemisch über einen vermittelten Elektronentransfermechanismus (MET) regeneriert werden. Derzeit besteht ein großes Interesse an der Verwendung von Enzymen in technischen Systemen, die hauptsächlich durch ihre hohe Selektivität und ausgezeichnete katalytische Aktivität unter milden Bedingungen (neutraler pH-Wert, niedrige Temperatur) gekennzeichnet sind. Diese Merkmale machen Anwendungen möglich, bei denen technische Systeme selektiv auf Komponenten der komplexen Mischung ansprechen, wie es von Biosensoren erwartet wird. In ähnlicher Weise ermöglicht eine hohe Selektivität bei enzymatischen Brennstoffzellen ein vereinfachtes Brennstoffzellen-Design, bei dem auf klassische Brennstoffzellen-Teile wie Separator, oder sogar Gehäuse verzichtet werden kann. Dieses Design ist vorteilhaft für das sogenannte "Energy Harvesting", bei dem der Brennstoff /das Oxidationsmittel direkt aus der Umgebung extrahiert und damit eine Miniaturisierung über das Niveau hinaus ermöglicht wird, das für andere elektrochemische Vorrichtungen (z.B. herkömmliche Batterien oder Brennstoffzellen) gilt. Aus diesen Gründen werden enzymatische Brennstoffzellen als vielversprechende implantierbare miniaturisierte Energiequellen für medizinische elektronische Geräte, wie Herzschrittmacher, medizinische Pumpen, Sensoren usw. angesehen. Neben der Nutzung als Sensoren und Energiewandler bilden elektroenzymatische Systeme eine interessante Option für die chemische Produktion. Chemikalien können sowohl in enzymatischen Brennstoffzellen als auch in elektroenzymatischen Reaktoren hergestellt werden. Im ersten Fall können partielle Oxidationsprodukte aus typischen "Brennstoffen" Glucose, Methanol, Ethanol erhalten werden. Im zweiten Fall werden selektive Reduktionsprozesse angestrebt, bei denen beispielsweise CO_2 in Methanol (oder Ameisensäure oder Formaldehyd) umgewandelt werden kann. Der Grad der Oxidation/des Reduktionsprozesses hängt von der Länge der enzymatischen Kaskade ab. Die hohe Enzymselektivität spiegelt sich theoretisch in einer höheren Produktreinheit wider als in herkömmlichen Verfahren, was die weitere Verarbeitung in der chemischen Industrie vereinfacht.

Der Fokus dieser Arbeit liegt auf enzymatischen Brennstoffzellen und deren Anwendungen in Energie- und Stoffumwandlungen. Die Leistungsfähigkeit dieser

Vorrichtungen wird hauptsächlich durch Hindernisse beim Elektronentransfer zwischen Enzymen und Elektroden begrenzt. Daher waren die meisten meiner Forschungsaktivitäten auf das Verständnis der limitierenden Prozesse auf der Ebene enzymatischer Elektroden gerichtet. In einem systematischen Ansatz untersuchten wir Hauptfaktoren, die das Verhalten enzymatischer Elektroden mit direkten und vermittelten Elektronentransfermechanismen beeinflussen. Wir haben gezeigt, wie die Elektrodenarchitektur die Elektrodenleistung beeinflusst. Zwei verschiedene Elektrodenarchitekturen wurden untersucht: geschichtet und gemischt. Zusätzlich wurde der Einfluss des Bindemittels überprüft. Wir haben gezeigt, dass das Bindemittel die Leistung der DET-Elektroden dramatisch beeinflusst, während es die Leistung der MET-Elektrode nur mäßig beeinflusst. Um das zu klären, wurde der Einfluss des Bindemittels auf die Enzymagglomeration und die Organisation auf leitfähigen Oberflächen untersucht. Schließlich wurde ein generisches Verfahren zur Herstellung von DET- und MET-Elektroden vorgeschlagen. Wir haben gezeigt, dass die Wahl des Mediators nicht immer einfach ist. Zunächst wurden zwei verschiedene Mediatoren für Glucoseoxidase (GOx) getestet. Eine künstliche Elektronentransportkette, die den Elektronentransport zwischen FAD-Redoxzentrum und Elektrodenoberfläche ermöglicht, wurde zusammengebaut. Obwohl die Ergebnisse einen Glukoseoxidationsstrom zeigten, war es nicht möglich, die elektrokatalytische Aktivität nur der GOx zuzuordnen. Stattdessen scheint die darunter liegenden Goldoberfläche hauptkatalytisch aktiv zu sein. CNT und TTF sind erwiesen sich als vielversprechende Mediatoren für weitere Anwendungen von enzymatischen Elektroden.

Unsere experimentellen Studien haben gezeigt, dass die Aktivitäten von enzymatischen Elektroden für die gleiche Enzymladung innerhalb von 2 Größenordnungen variieren. Das Herstellungsverfahren hat Auswirkungen auf die Orientierung des Enzyms auf der leitenden Oberfläche sowie auf seine Verteilung und Anordnung innerhalb der porösen Matrix. Zusätzlich beeinflusst es die Struktur der Katalysatorschicht in Bezug auf Porosität, Elektrodendicke und verfügbare Oberfläche; dies bewirkt eine weitere Enzymkinetik sowie einen Ladungs- und Massentransport innerhalb der Katalysatorschicht. Da diese Kreuzkorrelationen nicht immer intuitiv verständlich sind, haben wir neben experimentellen Ansätzen die mathematische Modellierung als ein wichtiges Werkzeug zur Beschleunigung der Evaluierung der Prozesse in Bezug auf reale Anwendungen verwendet. In Anbetracht der Tatsache, dass bei bioelektrochemischen Systemen, dass das Verständnisniveau enzymatischen Elektroden sehr niedrig ist, legen wir großen Wert auf das Verständnis und die Quantifizierung poröser enzymatischer Elektrodenreaktionen. Wir konnten zeigen, dass die elektrochemischen Methoden in Kombination mit geeigneten mathematischen Beschreibungen signifikante Einblicke in die Hintergründe liefern können, durch die das Gesamtverhalten der Elektrode begrenzt wird, was letztendlich zu einem besseren Systemdesign beigetragen hat.

Diese modellbasierte Analyse führte zu einer signifikanten Verbesserung der elektroenzymatischen Brennstoffzellenleistung. Zwischen 2011 und 2016 wurde die

Leistung für den gleichen enzymatischen Katalysatortyp um das 40-fache gesteigert. Wir haben auch gezeigt, dass enzymatische Brennstoffzellen für die Gluconsäureumwandlung verwendet werden können. In einem solchen System können sehr hohe Raum-Zeit-Ausbeuten (STY) und Selektivität erreicht werden. Eine vorläufige Nachhaltigkeitsanalyse wies jedoch auf einige Schwachpunkte aktueller elektroenzymatischer Prozesse wie niedrige Produkttiter und Zykluszeiten hin. Beide Effekte beeinflussen den E-Faktor der enzymatischen Prozesse. Weitere Verbesserungen der Enzymausnutzung und die Erhöhung der Zykluszeiten sind notwendig. Für die Entwicklung nachhaltiger Prozesse müssen Probleme im Zusammenhang mit der Trennung (Recycling) und der Toxizität ausgewählter Mediatoren sorgfältig abgewogen werden. Um neue spannende bioelektrochemische Anwendungen voranzutreiben, ist eine intensivere Interaktion zwischen verschiedenen Disziplinen (Elektrochemie, Biologie, Bioelektrochemie, Materialwissenschaften, Reaktionstechnik) dringend zu empfehlen.

Abstract

In bioelectrochemical devices, enzymes, as catalytic parts, are smartly combined with electroconductive surfaces. In this way electroconductive materials might replace one of the natural enzyme substrates in a so-called direct electron transfer mechanism (DET). Alternatively, an artificial enzyme substrate, a so-called mediator, might be used and regenerated electrochemically via a mediated electron transfer mechanism (MET). Currently, there is a high level of interest in the use of enzymes in technical systems, which is mainly triggered by their high selectivity and excellent catalytic activity under mild conditions (neutral pH, low temperature). These features favor applications where technical systems respond selectively to components of complex mixtures as expected in biosensors. Similarly, in enzymatic fuel cells high selectivity enables a simplified fuel cell design where classical fuel cell components, such as separator, fuel cell tank and even housing, can be avoided. This design is beneficial for so-called "energy harvesting" where the fuel/oxidant is directly extracted out of the environment and enables miniaturization beyond the level possible for other electrochemical devices (e.g. conventional batteries or fuel cells). For these reasons enzymatic fuel cells are considered to be promising implantable miniaturized power sources for medical electronic devices such as pacemakers, medical pumps, sensors etc. In addition to sensing and energy conversion applications, electroenzymatic systems offer good prospects for chemical production. Chemicals can be produced in both enzymatic fuel cells and electroenzymatic reactors. In the former case, partial oxidation products of typical "fuels" such as glucose, methanol and ethanol, can be obtained. In the latter case selective reduction processes are targeted where, for example, CO_2 can be converted into methanol (or formic acid or formaldehyde). The level of the oxidation/reduction process depends on the length of the enzymatic cascade. The high enzyme selectivity is theoretically reflected in greater product purity than is the case in conventional processes, which further simplifies downstream processing in the chemical industry.

This work focuses on enzymatic fuel cells and their applications in energy and material conversions. The performance of these devices is mainly limited by obstacles in electron transfer between enzymes and electrodes. Therefore, most of my research activities were directed towards understanding the limiting processes at the level of enzymatic electrodes. Taking a systematic approach, we studied the main factors influencing the performance of enzymatic electrodes with direct and mediated electron transfer mechanisms. We have shown how the electrode architecture influences the electrode performance. Two different electrode architectures were studied: layered and intermixed. Additionally, the influence of the binder was

checked. We have shown that the binder dramatically influences the performance of DET electrodes, while the performance of MET electrodes is affected only moderately. To clarify these issues, the influence of the binder on enzyme agglomeration and the organization on conductive surfaces was studied. Finally, a generic procedure for the preparation of DET and MET electrodes was suggested. We have shown that the choice of mediator is not always simple. Initially two different mediators for glucose oxidase (GOx) were tested. An artificial electron transport chain enabling electron transport between FAD redox center and electrode surface was assembled. Although the results showed a glucose oxidation current, it was not possible to ascribe the electrocatalytic activity to GOx solely but rather to the underlying gold surface. CNT and TTF are promising mediators for further applications of enzymatic electrodes.

Our experimental studies have shown that activities of enzymatic electrodes for the same enzyme loading vary within 2 orders of magnitude. The preparation procedure has an impact on the enzyme orientation on the conductive surface as well as its distribution and arrangement inside the porous matrix. Additionally, it impacts the structure of the catalyst layer in terms of porosity, electrode thickness and available surface area; this goes on to affect the enzyme kinetics as well as the charge and mass transport inside of the catalyst layer. Since these cross-correlations cannot always be understood intuitively, in addition to the experimental approaches we also used mathematical modeling as an important tool in accelerating/evaluating the processes towards real applications. In consideration of the fact that the bottleneck of bioelectrochemical systems is still at the level of understanding and improving enzymatic electrodes, we placed a great deal of emphasis on understanding and quantifying the porous enzymatic electrode responses. We were able to demonstrate that electrochemical methods combined with the proper mathematical descriptions can bring significant insights into the reasons limiting the electrode behavior as a whole. Ultimately this led to a better system design.

This model-based analysis resulted in a significant improvement in the electroenzymatic fuel cell performance. Between 2011 and 2016 the power output of the same type of enzymatic catalysts improved by a factor of 40. We have also shown that enzymatic fuel cells can be used for gluconic acid conversion. Very high space- time yields (STY) and selectivity can be achieved in such a system. Yet, a preliminary sustainability analysis highlighted some weak points in current electroenzymatic processes, such as the low product titer and cycle times. Both effects impact the E-factor of enzymatic processes. It will be necessary to achieve further improvements to the enzyme utilization and an increase in cycle times. For the development of sustainable processes, the issues relating to the separation (recycling) and toxicity of selected mediators must be carefully considered. Finally, in order to push forward new exciting bioelectrochemical applications, closer interaction between different disciplines (electrochemistry, biology, bioelectrochemistry, material science and reaction engineering) is strongly advised.

1 Introduction

Recently, the combination of biological and man-made components to create technical devices has received a lot of attention. Examples of such devices include biosensors, enzymatic fuel cells (EFC) and bioelectrochemical (electroenzymatic) reactors. In all cases enzymes are "wired" with electron conductive surfaces, where the signal of the enzymatic reaction is transduced into electrical current. This transduction can occur in a direct manner, so-called direct electron transfer mechanism (DET) or via a shuttle (a mediator), so-called mediated electron transfer mechanism (MET). This high interest in the use of enzymes in technical systems has been triggered by their high selectivity and excellent catalytic activity under mild conditions (neutral pH, low temperature). These features favor applications where technical systems respond selectively to components of complex mixtures as expected in biosensors. Similarly, in enzymatic fuel cells high selectivity enables a simplified fuel cell design where classical fuel cell components, such as separator, fuel cell tank and even housing, can be avoided. This design is beneficial for so-called "energy harvesting" where the fuel/oxidant is directly extracted from the environment and enables miniaturization beyond the level possible for any other electrochemical device (e.g. conventional batteries or fuel cells). For these reasons enzymatic fuel cells are considered to be promising implantable miniaturized power sources for medical electronic devices such as pacemakers, medical pumps, sensors etc. Due to aging populations worldwide, it is anticipated that the market for these devices will grow steadily, and one of the major obstacles to their use is a reliable energy supply. The batteries that are currently used for these applications are limited with respect to further miniaturization and life expectancy (5-10 years, after which further surgery is necessary). The future might be in harvesting the body's own energy (such as glucose contained in blood). The feasibility of this concept has been demonstrated in recent publications [1, 2]; yet not on an example of glucose contained in the blood but from other body fluids (tears or sweat).

In addition to sensing and energy conversion applications, electroenzymatic systems offer good prospects for chemical production. Chemicals can be produced in both enzymatic fuel cells and electroenzymatic reactors. In the first case, the partial oxidation products of typical "fuels", such as glucose, methanol and ethanol, can be obtained. In the second case, selective reduction processes are targeted where, for example, CO_2 can be converted into methanol (or formic acid or formaldehyde). The level of the oxidation/reduction process depends on the length of the enzymatic cascade. For example, formation of methanol from CO_2 will require 3 enzymes in the cascade, while formation of formic acid only one. In electroenzymatic reactors the main issue is the conversion of bio-based platform chemicals into higher added-value

products [3]. In a recent example, a proof of concept of a bioelectrochemical Haber–Bosch process for ammonia production was demonstrated [4]. The high enzyme selectivity is theoretically reflected in greater product purity, than is the case in conventional processes, which further simplifies down-stream processing in the chemical industry.

Among the three major fields of application (biosensors, EFCs and electroenzymatic reactors), only the biosensors can be considered sufficiently commercialized, while the other two applications are still at a level of development. The very first publications on EFCs date back to the 1960s, but much more research has commenced during the last decade [5]. The recent progress in this field regarding experimental and modeling efforts has been summarized in several review papers by us [6] as well as other groups. Despite its attractiveness and some recent progress, enzymatic fuel cells are still far from practical applications. When designing biomimetic energy conversion systems based on redox enzymes, the following points must be considered: enzyme immobilization, contact between enzyme and electrode surface, enzyme kinetics, enzyme electrode architecture and, finally, the integration of electrodes into the overall system. The first three aspects have been extensively studied in the past, mainly in the framework of the development of biosensors. This resulted in several preparation methods for biosensor enzymatic electrodes. However, not all these methods can be transferred directly to EFCs, because they will lead to electrode kinetics unfavorable for fuel cell operation. For example, for fuel cell applications, the current densities must be improved significantly. Other issues, such as long-term stability, which is relatively unimportant in the case of biosensors, have a significant effect in the case of EFCs.

This thesis summarizes my research in the field of bioelectrochemical systems. My focus was on EFCs and their applications in energy and material conversions. Since the performance of these devices is still very low, which can be traced back to complex electron transfer mechanisms between biological catalysts and electron conductive materials as well as very low enzyme utilization in these systems, the main issues were the development of technical enzymatic electrodes and their integration into enzymatic fuel cells. Finally, EFCs were evaluated with respect to gluconic acid production.

2 Development of technical enzymatic electrodes

Enzymatic electrodes that potentially can be utilized in technical systems such as EFCs or enzymatic reactors are considered to be technical electrodes. Up until now, most of the work in these fields was exploratory in nature, therefore terms such as "technical enzymatic electrodes" are not yet established. As is the case with more conventional electrochemical systems, a technical enzymatic electrode can be defined as a composite structure containing different layers e.g. catalyst layer and/or diffusion layer and current collectors. Enzymatic catalysts are integrated into the catalyst layer by immobilization into a suitable porous matrix or by entrapment behind, for example, a dialysis membrane. Although the latter approach is simpler [7], the performance of such electrodes is lower (approx. 50 μA cm^{-2} [7] compared to approx. 700 μA cm^{-2} [8] in the case of enzymatic electrodes employing hydrogenases). Bearing in mind that the electrode performance plays a significant role in the further development of technical systems, much attention has been paid to the use of immobilization procedures. Such electrodes are also termed porous enzymatic electrodes (see, for example, our paper [9]).

Porous enzymatic electrodes normally consist of a current collector (CC) and a catalyst layer (CL) (**Figure 2.1a**). In the CL, biological components (such as enzymes, or even a whole microorganism (please see for overview e.g. [10])) are combined with non-biological components that can be systematized roughly as support materials, binders and, if necessary, mediators. **Support materials** provide the support for biological components and electron conductivity throughout the porous structure. For this purpose, different carbon (nanoparticles, nanotubes, nanodots etc.) or metal (e.g. gold) nanomaterials can be used. To enhance the electron conductivity, in addition to carbon or metal nanomaterials, in some studies electron conductive polymers (such as polyaniline, polypyrrole) are added (not shown in **Figure 2.1a**). Electron conductive polymers can also serve as so-called mediators. **Mediators** shuttle electrons from enzymes to electroconductive supports (**Figure 2.1a**). They are necessary in cases where enzymes cannot exchange electrons directly with the electron conductive support, for example due to the enzyme orientation or an intrinsic structure of the enzymatic catalyst where the enzyme active center is embedded deeply in an isolating protein shell. This type of electron transfer mechanism is termed **mediated electron transfer** (MET) (**Figure 2.1a**). If direct electron transfer between an enzyme and the support is possible, then the **direct electron transfer (DET)** mechanism is invoked. **Binders** interconnect all parts of the porous electrode providing mechanical stability to the whole structure.
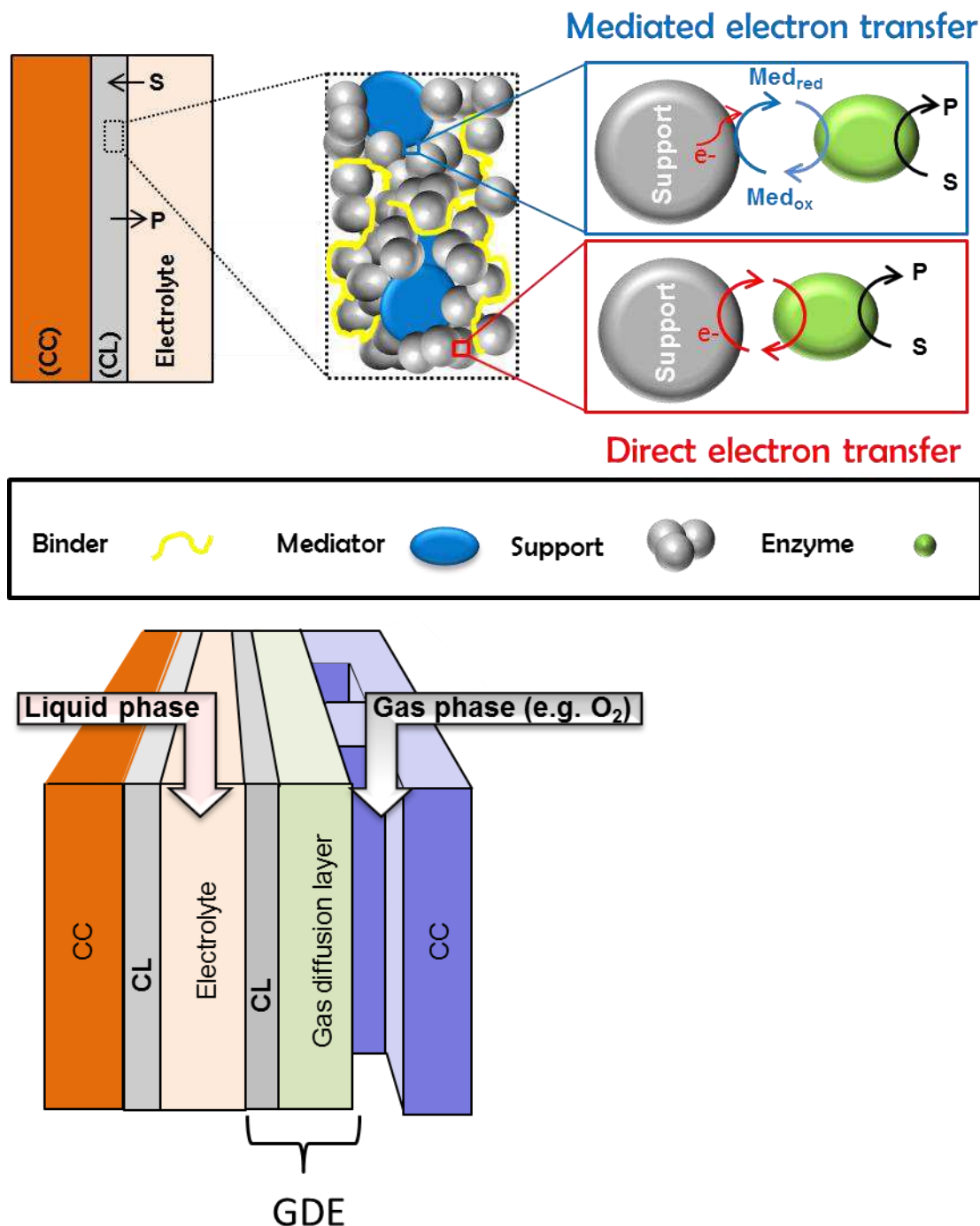
Figure 2.1: a) Schematic representation of a porous enzymatic electrode structure showing two mechanisms of enzyme/electron conductive support electron transfer (mediated electron transfer (MET) and direct electron transfer (DET)) and b) Schematic presentation of an electroenzymatic device with GDE. Abbreviations: CC (current collector), CL (catalyst layer), Medi (i=ox,red) (oxidized and reduced forms of a mediator), S (substrate), P (product). Reprinted from [9] with permission from Elsevier.

The binders are either inert to biological parts, where they are usually introduced at first to interconnect support and mediator (if necessary); enzymes are afterwards physically or chemically immobilized in the preformed porous structure. Alternatively, all components of the porous electrode are mixed together with the

biocompatible binder; afterwards mechanical stability is ensured through a cross-linking procedure. In this case the enzymes are also cross-linked. Mediators and binders are not necessarily parts of the porous electrode structures. Binder and mediator-free porous enzymatic electrodes are also reported [11]. In such cases the enzymes show the DET mechanism (**Figure 2.1a**).

In addition to a porous enzymatic electrode shown in **Figure 2.1a** where the enzymatic catalyst layer is contacted by liquid electrolyte on one side and the current collector on the other side, there is another type of porous enzymatic electrode, the so-called gas diffusion electrode (GDEs). In this case the catalyst layer is contacted by the liquid phase on one side and by the porous gas diffusion layer (GDL) on the other. The GDL distributes gas to the CL and might serve as a current collector as well. In addition, as shown in **Figure 2.1 b**, an additional current collector with a flow channel structure might be added. GDEs have a broad application in conventional fuel cells, electrolyzers and metal-air batteries. Since oxygen and other gasses (such as hydrogen) have a low solubility and diffusivity in liquid electrolytes, the electrode performance is limited due to a slow mass transfer of these gases in the liquid phase. Bearing in mind that the oxygen transport in the gas phase is much faster, the GDE should provide separate transport pathways for the gas and the liquid, thus reducing the mass transport resistance for oxygen and increasing the electrode performance. A schematic representation of a device comprising a GDE is shown in **Figure 2.1b**.

Bearing in mind the large number of preparation strategies in the literature, our main goal was to establish a generic platform for the preparation of porous enzymatic electrodes with MET or DET mechanisms. In this respect, the influence of the electrode architecture, enzyme and mediator loadings, as well as binder influence was studied systematically. Two model enzymes were selected: glucose oxidase (GOx) as a MET representative and horseradish peroxidase (HRP) as a DET representative. The DET bilirubin oxidase (BOD) electrodes were prepared based on knowledge gained with the model enzymes. Initially a mediator screening was performed.

2.1 Choice of a mediator

GOx is a classic representative of a redox enzyme requiring a mediator for an efficient electron transfer. This is due to the isolated protein shell which blocks the electron transfer between the enzyme redox center and the electrode. GOx is able to perform DET only after a partial removal of the protein shell by, for example, deglycosylation [12]. Nevertheless, DET for GOx employed in porous enzymatic electrodes with carbon nanotubes has been reported in several cases. Some possible artefacts leading to the conclusion of GOx DET are summarized in a very recent paper [13]. A successful mediator for GOx should efficiently transfer electrons from flavin adenine dinucleotide (FAD) co-factor to the electrode surface. Since the reaction between a mediator and FAD co-factor is a chemical redox reaction, an adequate thermodynamic driving force should be accompanied with fast kinetics. The potential of $FAD/FADH_2$ couple at pH 7 is -0.213 V [14], while formal redox potentials of

all listed mediators in **Table 2.1** are significantly more positive, making them thermodynamically plausible as mediator choices. However, the kinetics of the mediator itself with the electrode surface have to be fast.

Table 2.1: Mediators typically used in connection with FAD cofactors and their respective formal redox potentials

Mediator	Formal redox potential *vs.* SHE[*] / V	pH	Reference
2-methyl-1-4-naphtoquinone on PLL	-0.07	7	[15]
Os polymers	0.01 (0.09)	5	[16, 17]
	0.01 (0.04)	7	[16, 18]
pyrroloquinoline quinone	0.11(0.08)	7(7.2)	[19, 20]
p-benzoquinone	0.6	7	[21]
8-hydroxyquinoline-5-sulfonic acid	0.305	5	[22]
phenazine methosulfate	0.32	6	[23]
tetrathiafulvalene	0.419	7	[24]
poly(vinilferrocene)	0.5	7	[25]
ferrocene monocarboxylic acid	0.527	7	[26]

[*]E *vs.* Ag/AgCl=E *vs.* SHE-0.197 (V); E *vs.* SCE=E *vs.* SHE-0.24 (V)
[**]Methylene green shows two redox peaks

Os-based mediators with redox centers attached to a polymer backbone have exhibited the best performance to date [27]. Their disadvantages are their complicated synthesis procedure as well as toxicity issues associated with Os. Among other mediators, PQQ has been reported as a very efficient mediator for GOx regeneration [20]. The idea originally proposed by Willner's group is very sophisticated. It involves the electron conductive support (gold) modification by several layers: linker molecules (cystamine), mediator (pyrroloquinoline quinone (PQQ)) and enzyme co-factor (FAD). Finally, apo-enzyme (apo-GOx) is reconstituted. The artificial electron transport chain formed in this way is supposed to overcome the intrinsic DET limitation of GOx. The targeted final structure is shown schematically in **Figure 2.2**. Bearing in mind the high level of activity of this construct reported by Willner's group [20], as well as the high degree of attractiveness of using a non-diffusive mediator, we initially followed this procedure. All details on the synthesis of an amino group modified FAD (N^6-(2-amino- ethyl)-FAD) co-factor, preparation of apo-GOx as well as the electrode modification steps can be found in the Ph.D. Thesis of I. Ivanov [28] and in two publications [19, 29]. Although we were able to reproduce results from the literature, our data strongly indicated significant activity of the gold support in glucose electrocatalysis, which led us to the conclusion that indeed, in such complex constructs, many different possibilities for electrocatalysis should be taken into account, including reactions occurring on the supporting layers of the designed bioelectrodes. Our data also supported the general possibility of an efficient direct oxidation of different sugars on SAM modified high surface area gold electrodes, which could be useful for sensors and fuel cell technologies [19, 29].
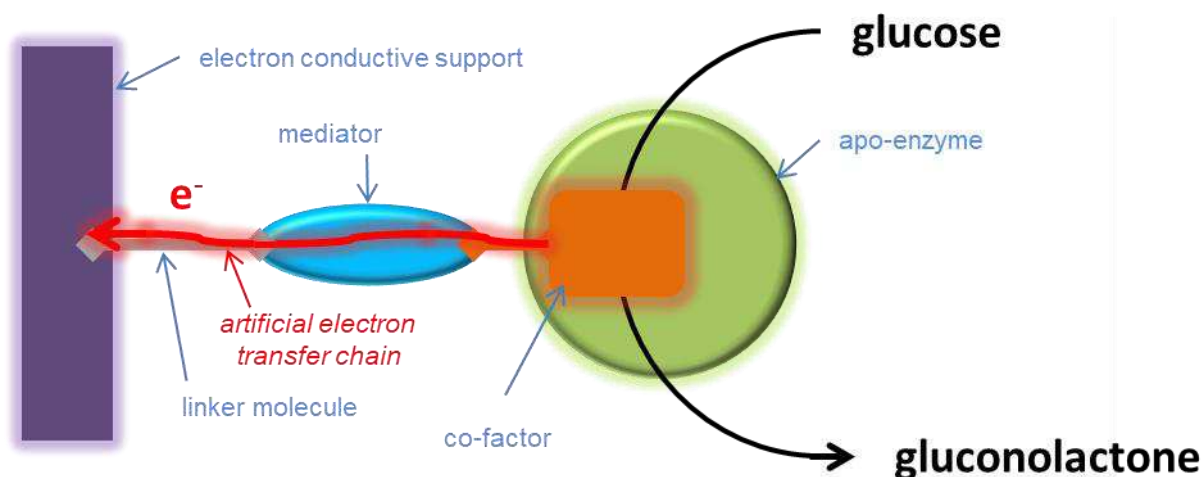
Figure 2.2: Schematic representation of enzyme-electron conductive support contacting via an artificial electron transfer chain

In the next attempt to identify a non-diffusive suitable mediator, our motivation was to use a commercially available substance that also exhibited good kinetics in respect of glucose oxidation. Our screening indicated tetrathiafulvalene (TTF) as an excellent candidate. The TTF mediator was used either alone or in combination with tetracyanoquinodimethanide (TCNQ) forming a charge transfer complex (CTC) which then acted as a mediator ([30] and references therein). While CTC is electronically conductive, the conductivity of TTF is negligible, which is why it is usually integrated in the electron conductive matrix. CTC performed excellently with regard to glucose oxidation, high oxygen tolerance and remarkable stability under continuous operation [31, 32]. Additionally, enzymatic electrodes based on TTF or CTC do not require complicated modification procedures; they can be prepared just by mixing the respective components [30]. The CTC is commercially available and has a high electronic conductivity, which is beneficial for lowering the ohmic resistance within the electrode layer. The morphology of the CTC crystals can be fine-tuned by varying the experimental conditions. They can also be prepared in the form of nanoparticles. These strategies can be applied to fine-tune the catalytic properties of the CTC and/or to increase the catalytically active surface area. Both TTF and TCNQ have low toxicity, which is attributable to their low solubility in water and physiological fluids. The focal points of our studies with respect to mediator issues were the mechanism of CTC/TTF action [30] and the incorporation of a mediator into the electrode structure [31, 33].

Different possibilities were explored in the literature in order to incorporate the CTC mediator into the electrode structure. For example Khan [32, 34] explored two methods for preparation of TTF-TCNQ electrodes. In one procedure TTF-TCNQ crystals were modified by GOx [32]. These modified crystals were mixed with a binder, covered by 20 µl cm^{-2} gelatin and cross-linked by 5 % glutaraldehyde. The performance of these electrodes was approx. 0.52 A m^{-2} at 20 mM glucose and at approx. 0.5 V_{SHE}. In the other procedure, TTF-TCNQ crystals were first grown on polypyrrole film, followed by adsorption of GOx from a buffer solution [34]. The

15

_____

electrodes were then covered by a gelatin layer (20 µl cm^{-2}) and finally cross-linked by 5 % glutaraldehyde. The performances of these electrodes were higher: 7 A m^{-2} at 20 mM glucose, approx. 0.5 V$_{SHE}$ and 1.31 mg cm^{-2} CTC loading. The procedure that was initially used in our lab was similar to the latter and the electrode performance corresponded well with results from the literature (**Figure 2.3**). This electrode preparation procedure will be referred to as "layered" below.
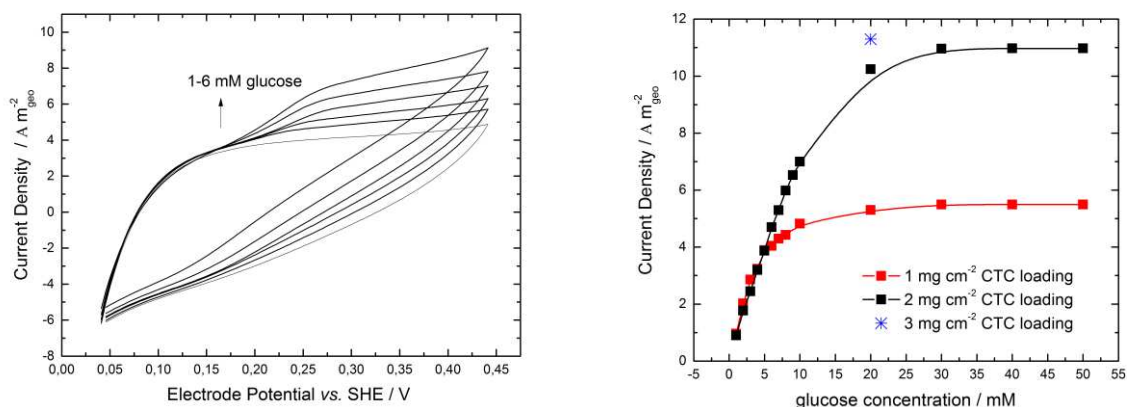

Figure 2.3: Cyclic voltammograms of (a) the layered CTC/GOx enzymatic electrode in the presence of different glucose concentrations (1–6 mM) and (b) concentration dependence of the current at 0.44 V$_{SHE}$ (corrected for the background current) for enzymatic electrodes with different CTC loadings. Conditions: 0.1 M phosphate buffer, pH 7.2, 37 °C, 400 rpm, N$_2$ atmosphere, sweep rate: 5 mV s^{-1}. Reprinted with permission from Elsevier from [31].

2.2 Influence of electrode architecture on activity

The layered CTC/GOx enzymatic electrode described previously has three distinct layers as visualized by a SEM cross-sectional image (**Figure 2.4**). The polypyrrole layer is an electron conductive support, the catalyst layer is a porous layer made of CTC crystals and enzymatic catalyst, and cross-linked gelatin forms a film on top which prevents enzymes from leaching out. We have shown that changing the mediator loading or the thickness of the gelatin layer can influence the activity towards glucose oxidation. The next question was to establish if changes to the overall electrode architecture, whilst keeping nominal loadings the same, could influence activity by, for example, changing catalyst or mediator utilizations. The new electrode architecture was checked in this regard. Unlike the first example, in the second case all components of the catalyst layer were intermixed. It was only possible to compare the two cases to a limited extent, since, in the second example, carbon nanoparticles were used instead of polypyrrole film as an electron conductive phase/support. Still, assuming that the carbon nanoparticles (Vulcan XC72)/polypyrrole behave solely as an electron conductive phase/support, the comparison can provide some insights.

The activity comparison between two architectures (both mass as well as surface area (not shown here) normalized), shows the clear advantage of intermixed layers. Interestingly, the intermixed electrodes show a decreasing trend with an

increase of GOx loading, while the trend for layered assembly appears to be the opposite. Possible reasons for this observation might be the higher porosity of layered CL as well as the absence of gelatin inside the layer.
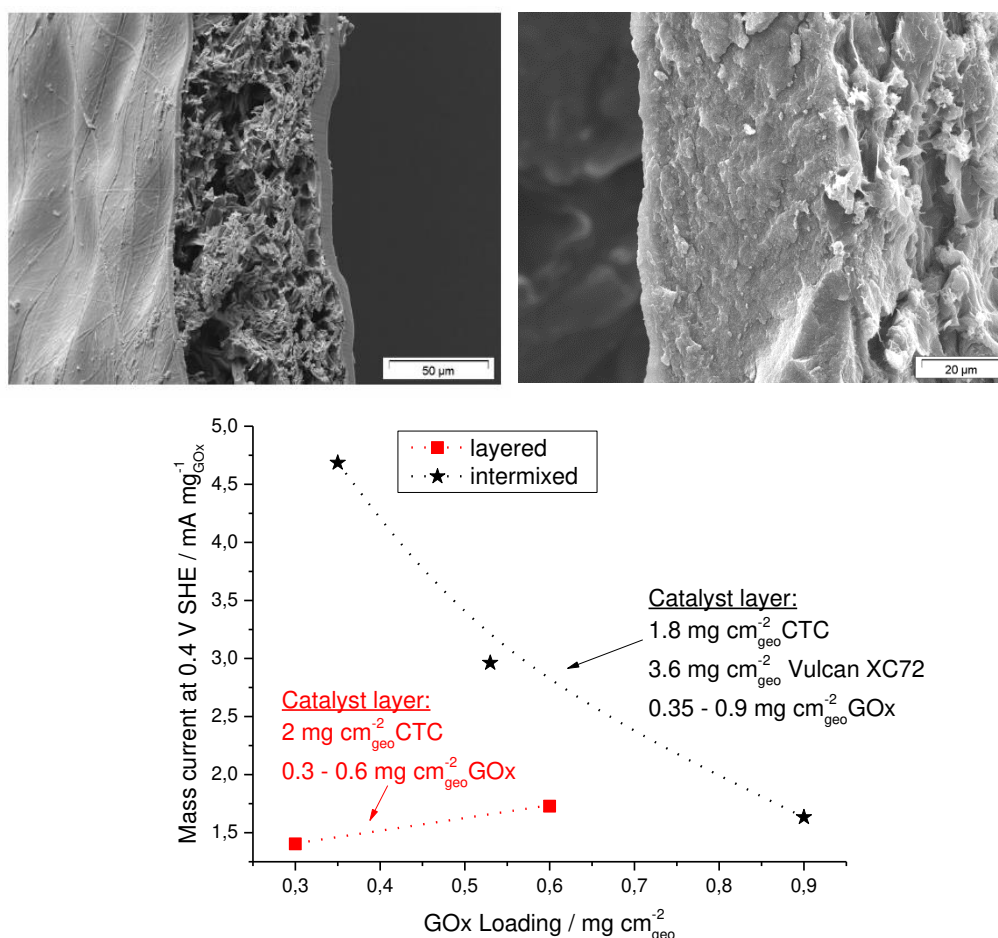

Figure 2.4: Comparison between two different archichectures. SEM image of enzymatic electrode cross-sections a) layered and b) intermixed assemblies and c) mass normalized currents at 0.4 V SHE as a function of GOx loading. Conditions: CTC loadings 2 and 1.8 mg cm^{-2} for layered and intermixed architectures respectively, 37°C, 20 mM glucose. Figures 2.4 a and b are reprinted with permission from Elsevier from [31, 33].

2.3 Generic platform for preparation of enzymatic electrodes

The previous examples of enzymatic electrodes were related to MET enzymatic electrodes. We have shown that the activity of such electrodes at similar enzyme/mediator loadings can be improved by changing the electrode architecture. The intermixed assembly proved to be suitable for the preparation of MET electrodes with other similar mediators such as TTF or TCNQ [30]. The next question was whether this could be a generic platform which might also be used for the preparation of DET-type electrodes. The first attempt in this direction was of limited success. The DET electrodes with similar BOD/Vulcan XC72/Gelatin loadings showed very low activity for the O_2 reduction (**Figure 2.5 a**). However, in the presence of soluble 2,2'-azino-bis(3-ethylbenzothiazoline-6-sulphonic acid) (ABTS) mediator the activity of the same electrode for glucose oxidation was comparable with the MET electrodes shown

previously (**Figure 2.5 b**). This indicated preserved catalytic activity of BOD inside an intermixed layer, but probably not a favorable orientation for the DET. Being aware that intermixed electrodes contain gelatin binder motivated us to check its influence in greater detail. Model electrodes were prepared in order to do so. The main concerns were enzyme organizations on different model supports and the cross-correlation with the electrochemically observable activity.
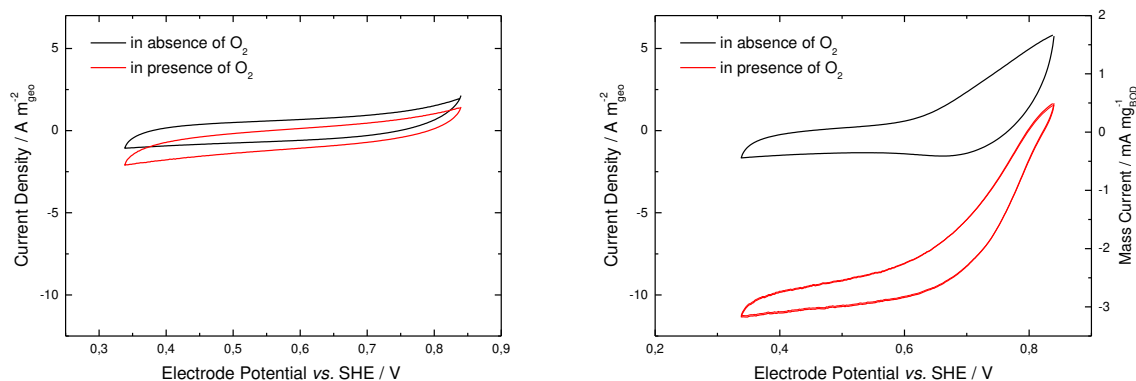

Figure 2.5: Cyclic voltammograms of a) DET and b) MET enzymatic cathodes with intermixed electrode architectures showing oxygen reduction activity. Conditions: 0.1 M phosphate buffer, pH 7.2, 37 °C, 400 rpm, scan rate 5 mV s^{-1}, BOD loading 0.36 mg cm^{-2}, Vulcan loading 3.6 mg cm^{-2}; 1 mg ml^{-1} of soluble ABTS mediator. Adopted from [28] with permission from author.

2.3.1 Model enzymatic electrodes

Fluorescence and atomic force microscopy were used to visualize enzyme organization on conductive supports. Two types of supports were checked: ideally flat surface (highly ordered pyrolytic graphite (HOPG)) and macroscopically flat surface (spectroscopically pure carbon (SPG)). At first enzymes were adsorbed on a HOPG surface. Beforehand, to facilitate their visibility in fluorescence microscopy, they were labeled with a fluorescent dye. These studies were performed only with the DET enzyme (HRP), since the direct contact of enzymes with an electrode surface and possible agglomeration effects play a larger role in DET than in MET. The uniform distribution of enzymes is possible only on ideally flat surfaces like HOPG. The fluorescence micrograph shows a uniform level of fluorescence across the whole surface (**Figure 2.6 a**). This was further confirmed by atomic force microscopy (AFM) (not shown here). The average heights of these structures were approx. 4 nm at pH 6. These values correspond well to reported values of HRP dimensions (6.2 x 4.3 x 1.2 nm [35] and references therein) indicating monolayer formation.

Enzymes adsorbed on a SPG surface were not homogenously distributed but showed a formation of agglomerates. Blue spots of different intensities, as well as very dark areas were observed (**Figure 2.6 b**). These dark areas with a very low level of fluorescence (approx. 200 A.U.) were ascribed to enzyme-free parts of the surface. The blue spots of different intensities are taken as an indication of a non-uniform distribution of enzymes on the remaining part of the surface, with spots showing a higher level of fluorescence (approx. 1500 A.U.) probably indicating enzyme

_____

agglomeration, while spots with a lower level of florescence (approx. 800 A.U.) indicate monolayer enzyme adsorption. The low intensity spots disappeared from the electrode surface upon rotation (not shown here).
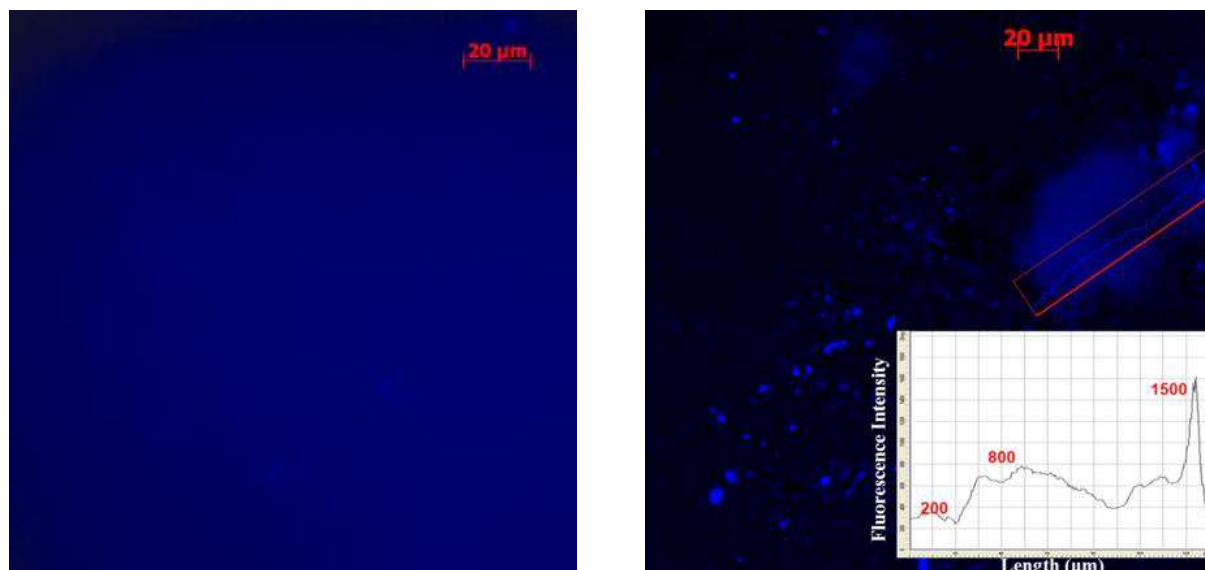

Figure 2.6: a) Fluorescence micrographs with exposure time of 200 ms of HRP adsorbed on a) HOPG and b) on SPG without electrode rotation. Reprinted from [35] with permission of the Royal Society of Chemistry.
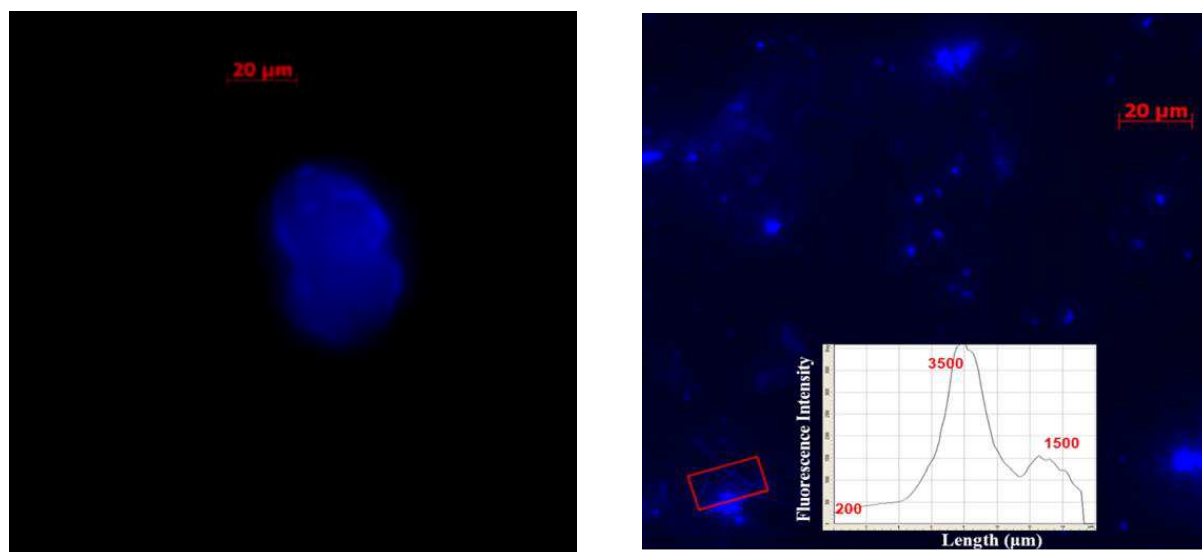

Figure 2.7: Fluorescence micrographs of HRP adsorbed on a) HOPG and b) SPG after cross-linking. Reprinted from [35] with permission of the Royal Society of Chemistry.

The level of agglomeration increased after treating the electrode with glutaraldehyde which is used as a cross-linking agent. On the HOPG surface, instead of uniformly distributed fluorescence only one spot with a high level of fluorescence is evident (**Figure 2.7 a**). Blue spots that differ in shape and size can be observed on spectroscopic graphite (**Figure 2.7 b**). The average level of fluorescence for these cross-linked agglomerates on spectroscopic graphite is approx. 3200 ± 300 A.U., while the level of fluorescence for agglomerates on SPG without cross linking has values of approx. 1500 A.U. It can be anticipated that the formation of enzyme

agglomerates decreases the number of active enzymes. This was confirmed by measuring the electrochemical activity of non- and cross-linked enzymes [35].

2.3.2. Influence of binder in intermixed architecture

Gelatin is a binder which not only offers a suitable environment for enzymes, but also results in the formation of enzymatic electrodes of a reasonable physical integrity. However, gelatin interacts with enzymes, which in the case of DET electrodes proved to be disadvantageous. Therefore, we looked for another binder that was chemically inert to enzymes. The suitable choice proved to be a poly(vinylidene fluoride) (PVDF), a stable binder with different applications in electrochemistry (batteries, fuel cells etc.). In the next step, following the idea of an intermixed architecture, a porous carbon conducting matrix was prepared, by mixing PVDF binder and Vulcan XC 72 nanoparticles. After drying at 60°C, the enzymes were introduced into the preformed matrix by means of physical adsorption. The porous matrix was supposed to offer a large surface area for enzyme adsorption, which theoretically should be able to accommodate a large number of enzymes. The new architecture was checked with respect to the hydrogen peroxide reduction by HRP DET. The data in **Figure 2.8** demonstrate the influence of binder in the intermixed assembly at the same Vulcan XC 72 loading.
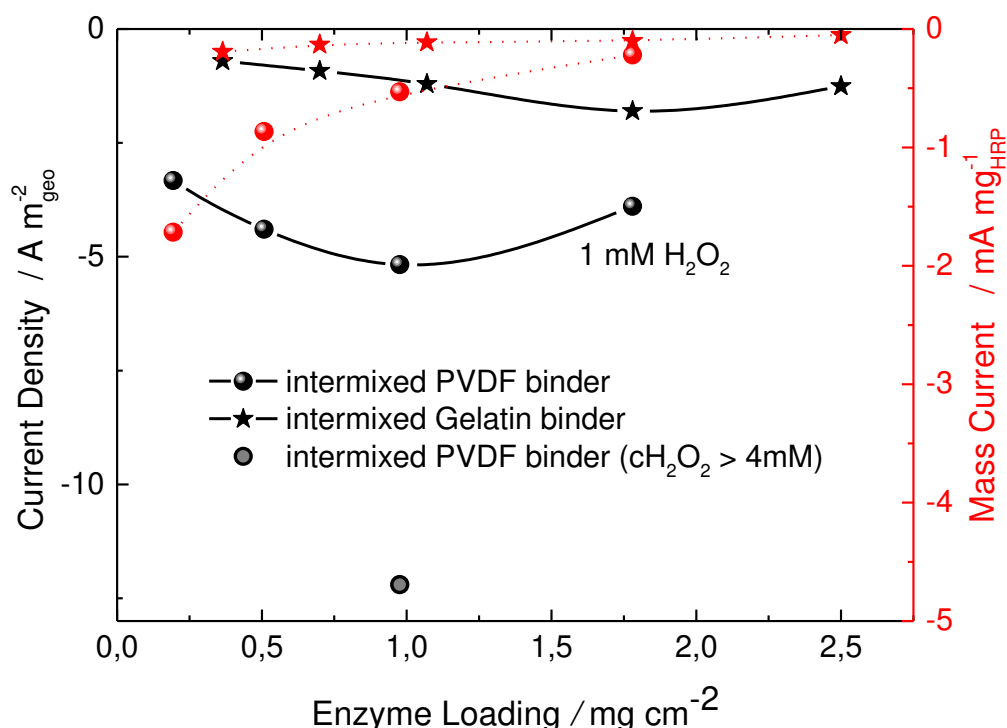

Figure 2.8: Influence of binder in intermixed architecture on hydrogen peroxide reduction by DET HRP. Conditions: potential 0.24 V SHE, 1 mM hydrogen peroxide, 400 rpm, N_2 atmosphere, pH 6.00.

The limiting currents depend on the enzyme loading. Irrespective of the chosen binder, it is possible to observe an increase in activity with an increase in enzyme loading followed by a later decrease at high enzyme loadings. The results indicate

that PVDF binder is more suitable for DET electrodes. The mass currents show a constant decrease in enzyme utilization. The current densities as well as mass currents have lower values than already shown by GOx. This is due to low peroxide concentrations. So, an increase in the concentration to 4 mM results in a significant increase in activity. It should be noted that at higher concentrations HRP is inhibited by its substrate hydrogen peroxide.

2.3.3. Can this knowledge be used for preparation of other enzymatic electrodes?

By following the idea of a generic platform for the preparation of enzymatic electrodes, BOD as well as enzymatic electrodes comprising GOx-HRP cascade were prepared using the same procedure as in the HRP case. The results in **Figure 2.9** appear promising. Both surface area (**Figure 2.9 a**) and mass normalized currents (**Figure 2.9 b**) compare well with the literature. In the case of GOx-HRP cascade 20 mM glucose was added to the solution. Hydrogen peroxide as a byproduct of enzymatic glucose oxidation was reduced further by HRP DET. Therefore, the hydrogen peroxide concentration was not readily available. The BOD electrode utilized O_2 dissolved in buffer and the concentration of hydrogen peroxide in the case of the HRP electrode was 3 mM. From all studied electrodes the BOD showed the highest surface normalized currents. The mass normalized currents show a higher activity of the HRP electrode. The comparison of BOD DET (**Figure 2.9 b**) and MET (**Figure 2.5 b**) mass normalized currents, points to higher catalyst utilization in the latter case. The reason may be an overestimation of enzyme loading in the DET case (enzymes are adsorbed from the solution and the loading depends on an adsorption time) or the fact that the BOD loading in the DET case is already on the descending part of the activity loading dependence as also observed for other enzymes (the BOD loading of the MET electrode was 0.36 mg cm^{-2}, while that of the DET was 1.8 mg cm^{-2}). Additionally, it can be expected that not all BOD enzymes will have a favorable orientation for the DET.

Finally, MET electrodes were prepared in an intermixed PVDF architecture. The results (not shown here) indicate that intermixed PVDF architecture can be considered as a generic platform and the activities of two MET electrodes are similar. Still at more negative overpotentials an intermixed gelatin electrode exhibited slightly higher activity, while at more positive overpotentials the activity of an intermixed PVDF electrode is higher. These issues will be discussed further in connection with the mathematical modeling of the electrode responses.

2.4. And how do we relate to the literature?

The majority of porous enzymatic electrodes reported in the literature have a random structure [11, 33, 36-40] (**Figure 2.10**). The typical current densities (for all electrodes limiting currents shown) of these electrodes are below 100 A m^{-2}. Our intermixed gelatin GOx electrodes display very high levels of activity, especially at low loadings. This electrode type shows a decrease even of surface area normalized activity with a

GOx loading. This was also observed for other electrodes, but trends initially showed an increase in the surface normalized activity with loading followed by a decrease at higher loadings.
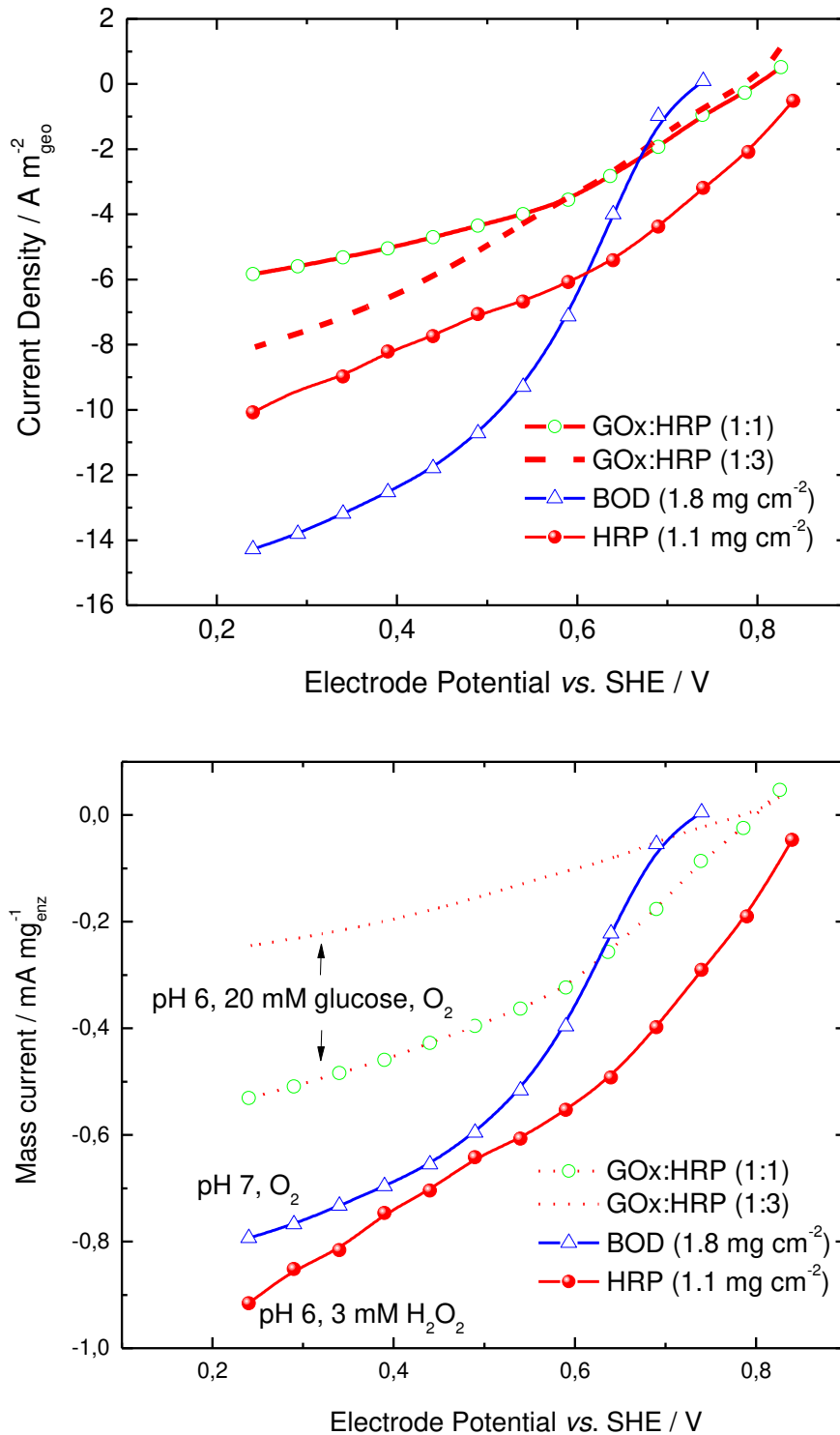

Figure 2.9: Intermixed PVDF architecture as a generic platform for preparation of DET based electrodes a) surface and b) mass normalized activities.

Our results also indicate that, in general, the intermixed PVDF procedure offers higher levels of activity than the intermixed gelatin procedure. In comparison with other examples from the literature, for all studied enzymes our electrodes show very high levels of activity (**Figure 2.10**). With respect to random structure electrodes only binder-free electrodes show superior surface normalized activity (**Figure 2.10 a**).
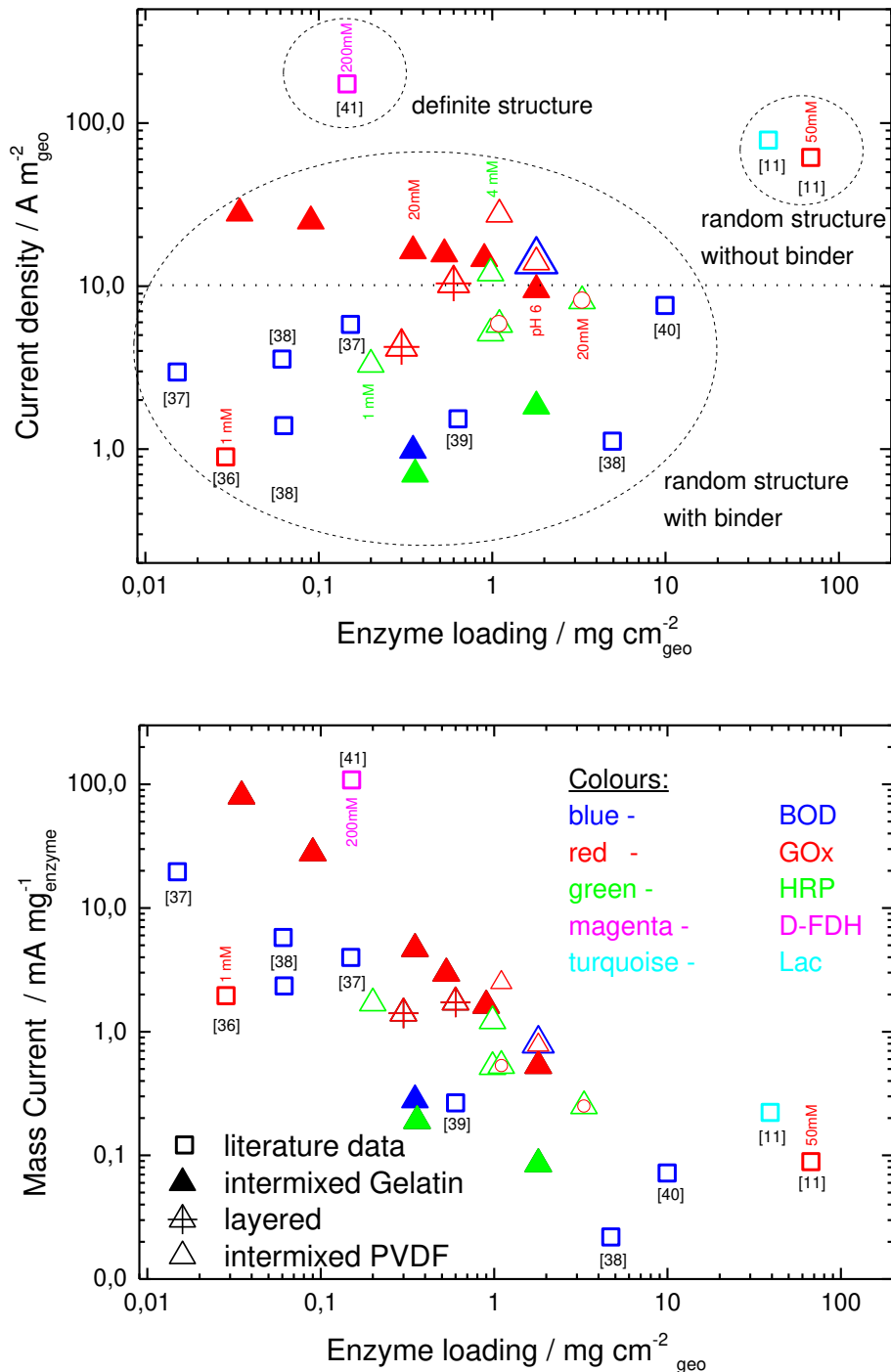

Figure 2.10: Comparison to literature a) surface normalized currents and b) mass normalized currents. The color code as well as the legend for both panels is given in the panel "b".

At this point it should be mentioned that this binder-free GOx electrode [11] was tested at a much higher glucose concentration, 50 mM, than in the present case (20 mM). Additionally, the activity was evaluated from cyclic voltammetry measurements. Bearing in mind the high carbon loadings in the system mentioned, very large capacitive current contributions can be expected (see, for example, the discussion in [35]). An exception with respect to both current density and mass current is a porous electrode with a definite structure [41]. This electrode features high current densities at low enzyme loading, which result in very high mass currents. This indicates very high enzyme utilization. It should also be mentioned that the substrate concentration in this study was 200 mM. If we consider a mass activity dependence on enzyme loadings, we see that our intermixed gelatin GOx electrodes have a very high catalyst utilization and feature mass activities close to definite structure. This figure clearly displays a decrease in enzyme utilization with an increase in loading.

3. Mathematical modeling of porous enzymatic electrodes

We have seen in the previous examples that the levels of activity of enzymatic electrodes vary significantly. The important message from the previous section is that whilst keeping the same nominal enzyme loading the enzyme utilization can be significantly influenced by the preparation procedure. The preparation procedure has an impact on enzyme orientation on the conductive surface as well as its distribution and arrangement inside the porous matrix. Additionally, it impacts the structure of the catalyst layer in terms of porosity, electrode thickness or available surface area; further, this effects enzyme kinetics as well as the charge and mass transport inside the catalyst layer. Since these cross-correlations cannot always be understood intuitively, in addition to the advanced experimental approaches, mathematical modeling might prove to be an important tool in accelerating/evaluating the processes toward real applications. Considering that the bottleneck of bioelectrochemical systems is still at the level of understanding and improving enzymatic electrodes, we place great emphasis on understanding and quantifying porous enzymatic electrode responses. Bearing in mind the importance of understanding processes in porous electrodes for the development of electrochemical systems in general, we recently provided a nice summary of porous electrode modeling [42]. We focused on macroscale models, since at present they provide a more straightforward relationship to experimentally measurable quantities. In general, macroscale modeling approaches can be classified as interface, porous and agglomerate models. The interface model can be understood as a simplification of a porous model, where all gradients (concentration, potential and current distributions) are neglected (**Table 3.1**). Therefore, the interface model has a low capability to describe the structure of the catalyst layer, but can be utilized to resolve complex reaction mechanisms, providing reaction kinetic parameters for distributed models. The physical structure of porous enzymatic electrodes appears quite random (**Figure 2.4 a & b**), for which reason, in the theoretical description we largely oriented on the porous electrode modeling framework originally proposed by John Newman and coworkers [43] and adopted it for the descriptions of porous enzymatic electrodes with DET and MET. The porous-electrode model relies on the general assumptions associated with the application of the spatial averaging theorem (for further details see, for example, [44] and sources therein). For this kind of model, the variables of interest are averaged over a representative averaging volume. The exact geometrical details of the electrode are ignored. Instead the electrode geometry is described by the volume fraction "ε" of the corresponding phase and the internal surface "a" (in m^2_{act} / m^3_{geo}). In the balance equations, all fluxes are then typically related to

superficial quantities by multiplying the interstitial flux with the corresponding volume fraction "ε".

3.1. Governing equations

The overview of governing equations for porous and interface models is shown in **Table 3.1**. For more details please see [42]. As can be seen in **Table 3.1,** in the interface model the electrode structural parameters are lumped together, the *aL* (m^2_{act} / m^2_{geo}) constant can be understood as an electrode roughness. For ideally flat electrodes the roughness factor will be equal to 1. In the porous electrode model the local current density "ι "(for example, in the charge balance equation for the interface (**eq. 3.3-p**)) is the local current production density in units A m^2_{act}. To get the current density that can be measured experimentally per geometrical surface area ($i_{electrode}$ with units A m^2_{geo}), the local current production densities are integrated over the electrode thickness and multiplied by the internal surface area (*a*). In formulating the interface charge balance equations (**eqs. 3.3-p, 3.3-i**) a convention for the cathode was followed (per convention it is assumed that $\eta_k < 0$). The mass balance equations consider concentration changes in the diffusion layer and the catalyst layer. The formation of a diffusion layer of a constant thickness was assumed, which corresponds well to the conditions established close to the surface of a rotating disc electrode. In this case the thickness of the diffusion layer can be expressed by a well-known equation (**eqs. 3.7-p or 3.7-i**) and it can be experimentally adjusted by changing electrode rotation rate. For the interface model, the concentration in the CL is constant over the electrode thickness (**eq.3.8.i**). Its change over time is obtained by integrating the concentration change (**eq.3.8.p**) over the electrode thickness with appropriate boundary conditions. In the limiting case of an electrode surface without any thickness (electrode is considered as a wall), the concentration on the electrode surface is obtained by solving the mass balance equation in the diffusion layer (**eq.3.9.i**). The interface model has fewer parameters than the porous electrode model since some parameters are lumped. If we additionally assume that the electrode can be considered to be a real interface (without any thickness) the surface morphology can be completely disregarded (except for the surface roughness). Also, some parameters, such as diffusion coefficients through porous structure, will be obsolete. This corresponds experimentally to an enzymatic layer immobilized on a flat non-permeable substrate. In this case the geometrical surface of the electrode can be easily assessed, as well as some other parameters, such as the double layer capacity. It must still be kept in mind that the measured currents will depend on the roughness of the electrode.

In addition to transport and structural parameters both porous and interface models contain kinetic parameters. They are contained in the rate expressions denoted as r_k (**Table 3.1**).

Table 3.1: An overview of main governing equations for porous and interface models

Porous		Interface	
Charge balances			
Electron conducting phase			
$0 = -\dfrac{\partial}{\partial z}\underbrace{\left(-\sigma_E^{\text{eff}}\dfrac{\partial \varphi_E}{\partial z}\right)}_{i_E} + a\iota$	3.1-p	$\dfrac{\partial \varphi_E}{\partial z} = 0 \; \forall z$	3.1-i
Ion conducting phase			
$0 = -\dfrac{\partial}{\partial z}\underbrace{\left(-\sigma_I^{\text{eff}}\dfrac{\partial \varphi_I}{\partial z}\right)}_{i_I} - a\iota$	3.2-p	$\dfrac{\partial \varphi_I}{\partial z} = 0 \; \forall z$	3.2-i
Interface charge balance			
$\eta_k(t,z) = \underbrace{(\varphi_E(t,z) - \varphi_I(t,z))}_{\Delta\varphi(t,z)} - \Delta\varphi_k^0$	3.3-p	$\dfrac{\partial \eta_k}{\partial z} = 0 \; \forall z$ $\eta_k(t) = \Delta\varphi_{\text{electrode}}(t) - \Delta\varphi_k^0$	3.3-i
$c_d \dfrac{\partial}{\partial t}(\varphi_E - \varphi_I) = -\iota + F\sum_k n_k \cdot r_k$ $i_{\text{electrode}}(t) = \displaystyle\int_{z=0}^{z=L} a \cdot \iota(t,z)\, \mathrm{d}z$	3.4-p	$c_{d\_\text{electrode}} \dfrac{\mathrm{d}\Delta\varphi_{\text{electrode}}}{\mathrm{d}t} = -i_{\text{electrode}}(t) + F\sum_k n_k \cdot r_k^*(\eta_k, c_\alpha)$ $c_{d\_\text{electrode}} = aL \cdot c_d$ $r_k^*(\eta_k, c_\alpha) = aL \cdot r_k(\eta_k, c_\alpha)$	3.4-i
Mass balances			
Diffusion layer			
$\dfrac{\partial}{\partial t}(c_\alpha^{DL}(z,t)) = D_\alpha^{DL}\dfrac{\partial}{\partial z}\left(\dfrac{\partial c_\alpha^{DL}(z,t)}{\partial z}\right)$	3.5-p	$\dfrac{\partial}{\partial t}(c_\alpha^{DL}(z,t)) = D_\alpha^{DL}\dfrac{\partial}{\partial z}\left(\dfrac{\partial c_\alpha^{DL}(z,t)}{\partial z}\right)$	3.5-i
from z=L to z=L+$\delta_{DL,\alpha}$	3.6-p	a) from z=L to z=L+$\delta_{DL,\alpha}$ b) from z=0 to z=$\delta_{DL,\alpha}$	3.6-i
$\delta_{DL,\alpha} = 1.61 D_\alpha^{1/3} v^{1/6} \omega_r^{-1/2}$	3.7-p	$\delta_{DL,\alpha} = 1.61 D_\alpha^{1/3} v^{1/6} \omega_r^{-1/2}$	3.7-i
Catalyst layer volume species			
$\dfrac{\partial}{\partial t}(\varepsilon \cdot c_\alpha^{CL}(z,t))$ $= D_\alpha^{CL}\dfrac{\partial}{\partial z}\left(\dfrac{\partial c_\alpha^{CL}(z,t)}{\partial z}\right) + a\sum_k \nu_{\alpha,k} r_k$	3.8-p	$\varepsilon\dfrac{\partial c_\alpha^{CL}(t)}{\partial t}$ $= D_\alpha^{CL}\dfrac{c_\alpha^*(L,t) - c_\alpha^{CL}(t)}{\frac{L}{2}} + aL\sum_k \nu_{\alpha,k} r_k$	3.8-i
		Catalyst layer (no thickness) $c_\alpha^{CL}(t) = c_\alpha^{DL}(0,t)$	3.9-i
Catalyst layer surface species			
$\dfrac{\partial \Gamma_\alpha^{CL}(t,z)}{\partial t} = \sum_k \nu_{\alpha,k} r_k$	3.10-p	$\dfrac{\partial \Gamma_\alpha^{CL}(t)}{\partial t} = \sum_k \nu_{\alpha,k} r_k$	3.10-i

In the porous electrode model r_k depends on the location "z" inside of the CL (only changes along the electrode thickness are considered *i.e.* 1-D model formulation) and it can be calculated with an appropriate kinetic expression:

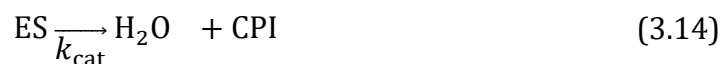$$r_k(t,z) = r_k(\eta_k(t,z), c_\alpha(t,z), T(t,z), \dots) \qquad (3.11)$$

from the concentration field $c_\alpha(t,z)$, the temperature field $T(t,z)$ and the local overpotential $\eta_k(t,z)$ of the reaction. The spatial profile of the overpotential $\eta_k(t,z)$ follows from the potential field within the electron conductor $\varphi_E(t,z)$ and the potential field within the ion conductor $\varphi_I(t,z)$ (**eqs.3.2-p and 3.3-p**), with $\Delta\varphi^0$ being the equilibrium potential difference of the reaction. For the interface model r_k is only dependent on time, since no potential and concentration distributions in the CL are assumed. It should also be noted that the r_k in the interface model is expressed in mol m^{-2}$_{geo}$ s^{-1}, while in the porous electrode model it is expressed in mol m^{-2}$_{act}$ s^{-1}. If the roughness factor is 1, geometrical and active surface areas will be the same.

The meaning of the reaction terms r_k (**Table 3.1**) is illustrated using the example of hydrogen peroxide reduction. The definition of these terms depends on the assumed reaction mechanism. The overall reaction for hydrogen peroxide reduction can be written as follows:

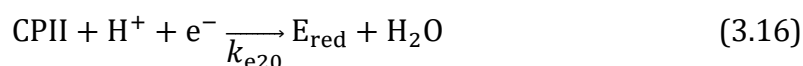$$H_2O_2 + 2H^+ + 2e^- \rightleftharpoons H_2O \tag{3.12}$$
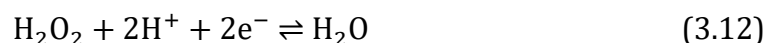
Enzymatically this reaction is catalyzed by HRP. The mechanism of this reaction involves enzymatic and electrochemical steps. It is widely accepted that the electrochemical regeneration is based on DET. According to the literature, the primary catalytic cycle of HRP hydrogen peroxide reduction involves:

- two enzymatic steps according to the Michaelis-Menten mechanism

$$H_2O_2 + E_{red} \xrightleftharpoons[k_1/k_1]{} ES \tag{3.13}$$

$$ES \xrightarrow[k_{cat}]{} H_2O + CPI \tag{3.14}$$

- and two electrochemical steps

$$CPI + H^+ + e^- \xrightarrow[k_{e10}]{} CPII \tag{3.15}$$

$$CPII + H^+ + e^- \xrightarrow[k_{e20}]{} E_{red} + H_2O \tag{3.16}$$

where E_{red} refers to the native form of the enzyme, ES to the enzyme substrate complex, CPI to the oxidized form of the enzyme (so-called compound I) and CPII to the partly reduced form of the enzyme (compound II) ([45] and references therein).

According to this scheme, HRP reacts initially with the substrate forming an enzyme substrate complex (ES). The complex decomposes further to compound I (CPI) which is then electrochemically reduced in the presence of protons H$^+$ giving compound II (CPII). The initial state of HRP is regenerated by a further electrochemical step followed by H$^+$ incorporation. Bearing in mind that the hydrogen peroxide and H$^+$ concentrations can be mass transport limited, it is possible to define different model variants based on the reaction mechanism presented (**Table 3.2**). As can be seen, in model 1, the steps **3.13-3.14** are lumped and all mass transfer effects (substrate and proton diffusion) are neglected. Model 2 is like model 1, but it includes

mass transfer effects. Model 3 is the most general considering formation and disproportion of the ES complex in accordance with steps **3.13-3.14** and all mass transfer effects. Similar assumptions were also considered in the literature, e.g. steps **3.13-3.14** were lumped in [46-48]. Moreover, two electrochemical steps are often combined in one step [46, 48]. This assumption is perfectly justified in the case of steady state model formulations (please see below), but in the case of dynamic system characterization cannot be adopted.

Now the rates of enzymatic steps were formulated based on mass law kinetics and electrochemical steps by assuming Tafel kinetics.

Table 3.2: Three model variants for hydrogen peroxide reduction and corresponding rate expressions (r_k) taking M3 as an example.

Model 1 (M1)		Model 2 (M2)	
		$H_2O_{2,bulk} \underset{diff}{\rightleftharpoons} H_2O_2$	3.20
$H_2O_2 + E_{red} \underset{K_1}{\rightleftharpoons} H_2O + CPI$	3.17	$H_2O_2 + E_{red} \underset{K_1}{\rightleftharpoons} H_2O + CPI$	3.21
$CPI + H^+ + e^- \xrightarrow{k_{e10}} CPII$	3.18	$CPI + H^+ + e^- \xrightarrow{k_{e10}} CPII$	3.22
$CPII + H^+ + e^- \xrightarrow{k_{e20}} E_{red} + H_2O$	3.19	$CPII + H^+ + e^- \xrightarrow{k_{e20}} E_{red} + H_2O$	3.23
Model 3 (M3)		**M3-rate expressions**	
$H_2O_{2,bulk} \underset{diff}{\rightleftharpoons} H_2O_2$	3.24		
$H_2O_2 + E_{red} \underset{k_1/k_1}{\rightleftharpoons} ES$	3.25	$r_1 = k_1 c_{H_2O_2}^{CL} \Gamma_{Ered} - k_{-1} \Gamma_{ES}$	3.29
$ES \xrightarrow{k_{cat}} H_2O + CPI$	3.26	$r_{cat} = k_{cat} \Gamma_{ES}$	3.30
$CPI + H^+ + e^- \xrightarrow{k_{e10}} CPII$	3.27	$r_{e1} = k_{e10} e^{-\alpha \frac{F}{RT} \eta_1} \Gamma_{CPI} c_{H^+}^{CL}$	3.31
$CPII + H^+ + e^- \xrightarrow{k_{e20}} E_{red} + H_2O$	3.28	$r_{e2} = k_{e20} e^{-\alpha \frac{F}{RT} \eta_2} \Gamma_{CPII} c_{H^+}^{CL}$	3.32

In **Table 3.2** Γ_i i=E_{red},ES,CPI and CPII are surface concentrations of reduced forms of enzyme, enzyme substrate complex, compound I and compound II respectively in mol m^{-2}$_{act}$. Over-potentials of two electrochemical steps η_1, η_2, are defined in accordance with **eqs. 3.3-p-3.3-i**. In case of HRP, the equilibrium potential differences $\Delta\varphi_i^0$ are 1.02 and 1.05 V vs. SHE for the first and second steps respectively [49].

As can be seen, the model equations contain several parameters. Some of them are available from the literature, such as equilibrium potentials, or can be measured (such as temperature). Still a large number of parameters are unknown, such as the kinetic constants of enzymatic and electrochemical reactions, and the

structural parameters of enzymatic electrodes (porosity, internal surface area, and electrode thickness). Furthermore, the total enzyme concentration is also an unknown parameter. This uncertainty has a huge impact on the determination of all kinetic constants. Since the reliability of the model depends heavily on the reliability of its parameters, a great amount of work was invested in proper parameter prediction. Bearing in mind that kinetic and transport processes are highly interrelated in the porous electrode, with the first approach we tried to determine kinetic parameters by using model systems that we assumed are largely free from the non-idealities of porous electrodes and satisfy major assumptions of the interface model.

3.2. Interface model

In the interface model, the gradients of concentration, potential and current inside the catalyst layer are neglected. In order to apply the interface model, the model electrodes must satisfy its main assumptions. Two types of electrodes that we utilized largely met these conditions. The first one was based on a macroscopically flat carbon support with immobilized enzymes (this type has already been described with respect to fluorescence microscopy measurements in section 2.3.1) and the second one was prepared by following the intermixed PVDF procedure but where the porous layer had a very low thickness. Both electrodes were studied in a rotating disc electrode assembly, which ensured defined mass transport conditions. To further reduce the number of model parameters, steady state conditions were applied.

3.2.1. Steady state solution

Steady state solution is illustrated on the basis of Model 3 (**Table 3.2**). By assuming the steady state conditions, the following overall current density expression, here shown in its reciprocal form, can be derived:

$$\frac{1}{i_{\text{electrode\_M3\_ss}}} = \frac{1}{2F\Gamma_{\text{t}}}\left[\frac{K_{\text{m}} + c_{\text{H}_2\text{O}_2}(0,\text{ss})}{k_{\text{cat}}c_{\text{H}_2\text{O}_2}(0,\text{ss})} + \frac{1}{c_{\text{H}^+}(0,\text{ss})k_{\text{e}}e^{-\alpha\frac{F}{RT}\Delta\varphi_{\text{electrode\_ss}}}}\right]$$

$$(3.33)$$

Eq. 3.33 demonstrates the series connection between enzymatic and electrochemical steps as also shown by Andreu et al [49]. In **eq. 3.33**, k_{e} stands for an effective electrochemical rate constant defined as:

$$k_{\text{e}} = \frac{k_{\text{e1}} \cdot k_{\text{e2}}}{k_{\text{e1}} + k_{\text{e2}}} \qquad (3.34)$$

where k_{e1} and k_{e2} are defined as follows:

$$k_{\text{e1}} = k_{\text{e10}}e^{\frac{\alpha_1 F}{RT}\Delta\varphi_1^0} \qquad (3.35)$$

$$k_{\text{e2}} = k_{\text{e20}}e^{\frac{\alpha_2 F}{RT}\Delta\varphi_2^0} \qquad (3.36)$$

The K_{m} is the Michaelis-Menten constant defined as usual:

$$K_m = \frac{k_{-1} + k_{cat}}{k_1}$$ (3.37)

To calculate the overall current density based on **eq.3.33**, concentrations of substrate and protons at the electrode surface are also needed. These concentrations are obtained by solving the mass balance equations (**eq.3.5-i**) with appropriate boundary conditions. Under steady state conditions, the number of original parameters is significantly reduced. Instead of two electrochemical rate constants only one lumped constant k_e appears. Similarly, from 3 enzymatic rate constants only k_{cat} and K_m can be determined independently, while k_1 and k_{-1} will be lumped together in the K_m value. An additional parameter is the total enzyme surface concentration Γ_t.

The overall rate expressions for two other model variants M1 and M2 mentioned previously (**Table 3.2**), can be derived in a similar way (not shown here). In these two models the number of model parameters is even fewer. For example, only one enzymatic rate constant K_1 and one electrochemical rate constant k_e were involved. The difference between M1 and M2 was only in the concentrations of hydrogen peroxide / protons which are considered to be the same as in bulk (M1), or their concentration on the electrode surface was considered (M2).

In the next steps the goal was to identify the most appropriate model for the description of the experimental electrode responses by comparing experimental data with the predictions of the models M1, M2 and M3. First estimations of the kinetic parameters were obtained from experimental data by using a linearized form of the overall rate expressions (e.g. **eq.3.33**) and by assuming no mass transfer resistance effects (see for example [14]), while their final values were a result of the global optimization [45]. Finally, the steady state solutions for the three different models are plotted in **Figure 3.1**.

As can be seen, all 3 models can qualitatively describe the experimental data, with M3 having the best quantitative agreement. No model discrimination was possible. We have shown previously that dynamic models have a higher capability for model discrimination [50]. Therefore, the dynamic formulation of the models was reconsidered. From different dynamic methods, electrochemical impedance spectroscopy was selected as the method of choice.
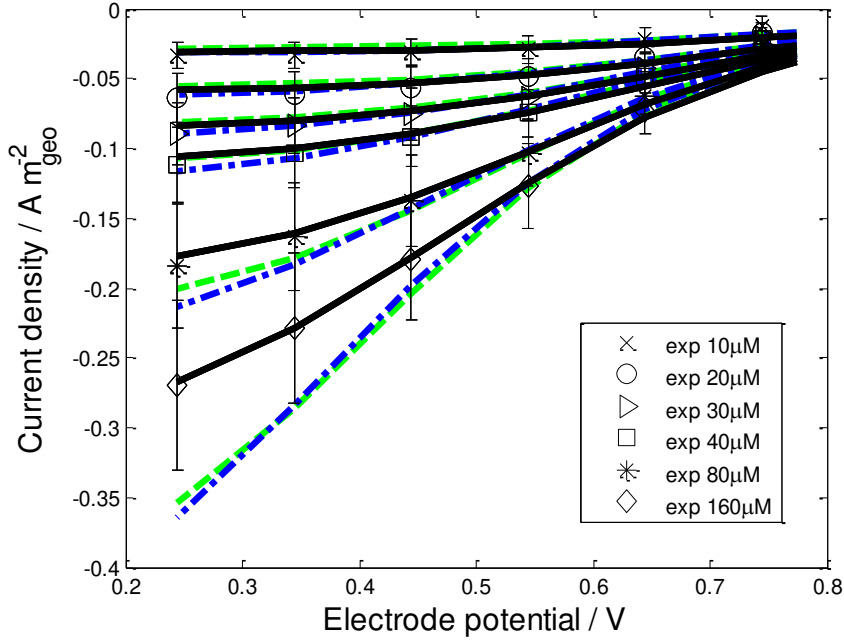
Figure 3.1: Steady state polarization curves at pH 6 for hydrogen peroxide reduction on HRP modified SPG RDE; symbols – experimental data and lines – simulated curves (M1 - blue dashed dot line, M2 – green dashed line and M3 – black solid line). Conditions: fixed delay of 1 min, hydrogen peroxide concentrations from 10 to 160 μM, pH 6, room temperature, rotation rate 400 rpm.

3.2.2. Dynamic response

At first we adopted an approach for deriving the theoretical impedance of enzyme/electrode systems based on the reaction mechanisms of enzyme catalyzed electrochemical reactions [45]. In this way mechanistic details relating to bioelectrochemical reactions including all relevant kinetic parameters were obtained. This approach overcomes the limitations of the classical equivalent circuit approach, since it does not rely on phenomenological elements, but on the particular reaction mechanism. It is based on the more general theory of nonlinear frequency response (NLFR) [51, 52], which in the present case was restricted to its linear part. This method has a generic mathematical background that allows the analysis of any weakly nonlinear system with a polynomial nonlinearity. It was initially developed for the analysis of nonlinear electrical circuits and in chemical engineering for the investigation of the adsorption equilibrium and kinetics [52, 53]. We first demonstrated the application of this method in theory and experiment using the example of simple electrochemical reaction ferrocyanide oxidation kinetics [54, 55]. For all details of the derivations related to the enzymatic electrode case, please refer to our paper [45].

For the weakly nonlinear system, its input–output behavior around the steady state $(\Delta\varphi_{electrode,SS}, i_{electrode,SS})$ can be described with a Volterra series. For a harmonic input signal:

$$\tilde{E}(t) = A cos(\omega t) = \frac{A}{2}(e^{j\omega t} + e^{-j\omega t}) \tag{3.38}$$

it follows that:

$$\tilde{\imath}(t) = \sum_{n=1}^{\infty} \left(\frac{A}{2}\right)^n \int_{-\infty}^{\infty} h_n\left(\tau_1, \dots \tau_n\right)\left(e^{j\omega(t-\tau_1)} + e^{-j\omega(t-\tau_1)}\right) \dots \left(e^{j\omega(t-\tau_n)}\right.$$
$$\left. + e^{-j\omega(t-\tau_n)}\right) d\tau_1 \dots d\tau_n \tag{3.39}$$

where $\tilde{E}(t) = \Delta\varphi_{\text{electrode}}(t) - \Delta\varphi_{\text{electrode,SS}}$ and $\tilde{\imath}(t) = i_{\text{electrode}}(t) - i_{\text{electrode,SS}}$.

After applying the n-dimensional Fourier transformation the system output can be expressed as:

$$\tilde{\imath}(t) = \left(\frac{A}{2}\right)\left[H_1(\omega)e^{j\omega t} + H_1(-\omega)e^{-j\omega t}\right]$$
$$+ \left(\frac{A}{2}\right)^2 \left[H_2(\omega, \omega)e^{2j\omega t} + 2H_2(\omega, -\omega)e^0\right.$$
$$\left. + H_2(-\omega, -\omega)e^{-2j\omega t}\right]$$
$$+ \left(\frac{A}{2}\right)^3 \left[H_3(\omega, \omega, \omega)e^{3j\omega t} + 3H_3(\omega, \omega, -\omega)e^{j\omega t}\right.$$
$$+ 3H_3(\omega, -\omega, -\omega)e^{-j\omega t}$$
$$\left. + H_3(-\omega, -\omega, -\omega)e^{-3j\omega t}\right] + \dots \tag{3.40}$$

The function $H_1(\omega)$ is the so-called first-order frequency response function of the system. It can be shown that $H_1(\omega)$, is identical to the reciprocal of the electrochemical impedance. The remaining functions $H_n(\omega, \dots \dots \omega)$ are called higher order frequency response functions. They contain the nonlinear fingerprint of the system. The higher order frequency response functions can be derived analytically from the model equations [45, 54]. Additionally, they can be determined experimentally. This can be briefly demonstrated by rearranging **eq.3.40** sorted by the power of $e^{j\omega t}$:

$$\tilde{\imath}(t) = e^0 \left[\underbrace{\frac{A^2}{2}H_2(\omega, -\omega)}_{H_{q,DC}(\omega,A)} + \dots\right]$$
$$+ \frac{1}{2}\left\{e^{j\omega t}\left[\underbrace{AH_1(\omega) + \frac{3}{4}A^3 H_3(\omega, \omega, -\omega) + \cdots}_{H_{q,I}(\omega,A)}\right]\right.$$
$$\left. + e^{-j\omega t}\left[\underbrace{AH_1(-\omega) + \frac{3}{4}H_3(-\omega, -\omega, -\omega) + \cdots}_{H_{q,I}(-\omega,A)}\right]\right\}$$
$$+ \frac{1}{2}\left\{e^{2j\omega t}\left[\underbrace{\frac{A^2}{2}H_2(\omega, \omega) + \cdots}_{H_{q,II}(\omega,A)}\right]\right. \tag{3.41}$$
$$\left. + e^{-2j\omega t}\left[\underbrace{\frac{A^2}{2}H_2(-\omega, -\omega) + \cdots}_{H_{q,II}(-\omega,A)}\right]\right\} + \dots$$

The individual higher order frequency response functions $H_n(\omega, \dots \dots \omega)$ are related to the amplitude-dependent quasi-response functions of the harmonics $H_{q,i}(\omega, A)$. The quasi-response functions of the harmonics can be obtained with an experimental setup similar to EIS. This was demonstrated taking ferrocyanide

oxidation as an example (**Figure 3.2**) [55]. The results are shown here as an illustration of a response of a simple mass transfer limited reversible electrochemical reaction.

In contrast to EIS the excitation amplitude in NLFR is considerably larger in order to exceed the quasi-linear range (EIS) and to raise higher harmonics in the output signal (to determine the linear part of the response a 10 mV amplitude is typically used, for the second order frequency response function an amplitude of 50 mV was selected as an optimal value [55]). The comparison of analytically derived and experimentally determined higher order frequency response functions can be used for model discrimination and to determine the nonlinear system parameters.
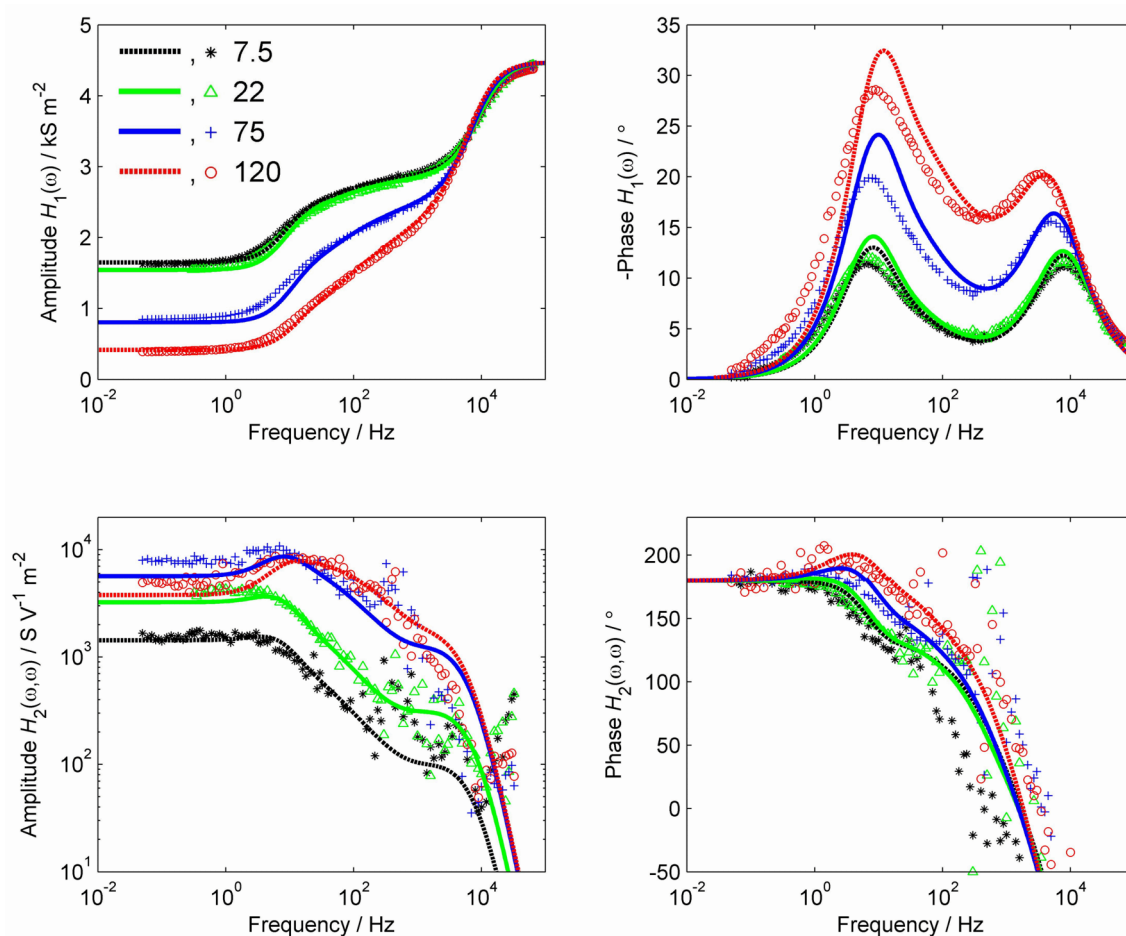

Figure 3.2: Amplitude and phase shift frequency spectra of the first ($H_1(\omega)$) and second order ($H_2(\omega,\omega)$) frequency response functions at different potentials (in mV); Symbols: experimental data; lines: theoretic curves (input amplitude: 50 mV r.m.s.; electrolyte: 20 mM $[Fe(CN)_6]^{4-/3-}$, 1.0 M KCl; rotation speed: 4500 rpm; t = 25.0 °C). Adopted from [55] with permission from the American Chemical Society.

Since the method described is generic, it was further used to derive the analytical expressions of electrochemical admittances based on the models M1, M2, M3 already introduced above[45]. The analysis was restricted to the linear part of the response. The results show that only M3 can predict the correct order of the reaction resistance change with potential, while models M1 and M2 fail in this aspect (**Figure 3.3**). Therefore, M3 was further implemented into the porous electrode model and used to simulate electrode responses. The kinetic parameters determined here were

used for simulations in the framework of the porous electrode model. The only remaining parameters were related to the electrode structure (porosity, internal surface area and the electrode thickness).
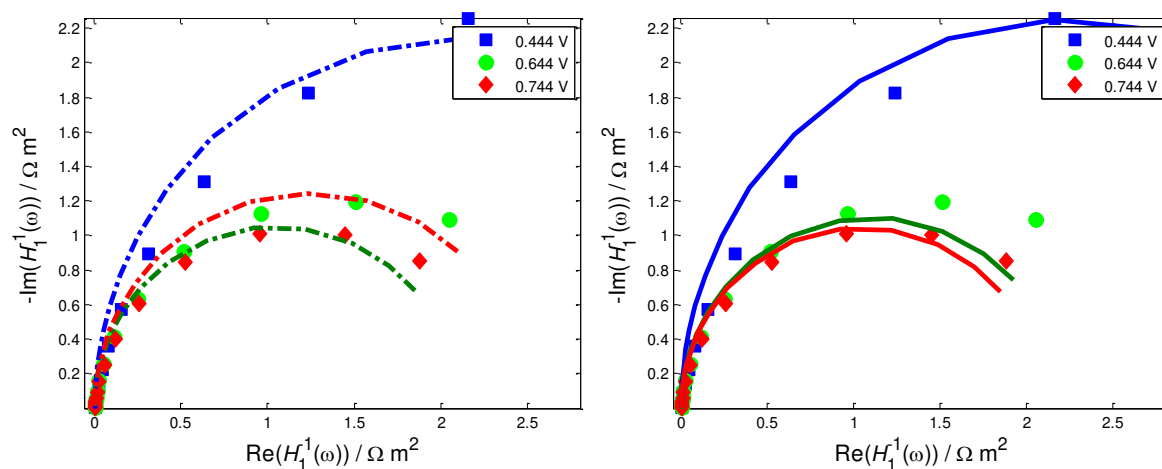

Figure 3.3: Experimental (symbols) vs. simulated (lines) EIS data with optimized parameters at three steady state potentials a) M1 (dashed line) and b) M3. Conditions: pH 5, 80 µM hydrogen peroxide concentration, room temperature and rotation rate 400 rpm. Adopted from [45] with permission from Elsevier.

3.2. Porous electrode model

As has already been shown, the porous electrode model has three structural parameters, the electrode porosity, its thickness and the internal surface area "a". The electrode thickness can be experimentally determined from SEM cross-sectional images (**Figures 2.4 a&b**). The two other parameters were considered as fitting parameters. The porosity can be estimated based on carbon and binder loadings, by calculating the theoretical compact thickness of CL and by comparing it with the experimentally determined thickness. The meaning of the internal surface area "a" is dependent on the type of electron transfer mechanism DET or MET. For the DET case, parameter "a" depends on the internal surface area of the electron conductive support in contact with an enzyme. This can be estimated based on the electron conductive material loading and the BET surface area, as well as the thickness of the porous electrode. Carbon nanomaterials, which are often employed as electroconductive supports, have BET surface areas in the range between 200 and 600 m^2 g^{-1}. For Vulcan XC 72 BET the surface area is 250 m^2 g^{-1}. The addition of binder materials, which are necessary for porous electrodes, might reduce this area significantly. From the fuel cell research, a reduction in the order of up to 10 times in the BET area was observed, depending on binder to carbon ratios [56]. Assuming a similar effect of the binder in the present case and Vulcan XC 72 loading of 3.0 mg cm^{-2} and 53 µm electrode thickness, the internal surface area can be calculated as 1.4×10^7 m^2_{act}/m^3_{geo}. Assuming further similar coverage as in the case of the flat electrode (approx. 1 % of the full monolayer), the "a" value can be estimated as being in the order of 10^5 m^2_{act}/m^3_{geo}. The values which were obtained by parameter fitting

were between 0.35 and *approx.* 8 x 10^5 m^2_{act}/m^3_{geo} depending on the electrode preparation procedure (intermixed gelatin, intermixed PVDF)[57].

The modeling results show that only the concentration distribution of the substrate plays an important role with respect to the electrode responses. Due to low current densities and high conductivities of electron and ion conducting phases, the potential field distribution in the catalyst layer can be neglected. The change of the electrode thickness does not always have a significant (positive) effect on the electrode response. The change in the intermixed PVDF electrode thickness from 19 to 53 μm results in almost no changes in the electrode responses (**Figure 3.4**). This can be rationalized based on calculated concentration profiles which show that due to the substrate depletion, a large part of the thick electrode is essentially unused. Similar results were expected for the intermixed gelatin electrode. However, in this case an almost linear increase in activity is obtained as the electrode thickness increases. The results also show a significant change in the internal surface area (fitting parameter). For the same electrode porosity, this value should theoretically remain the same. This indicates a significant reduction in the number of active enzymes for the thin intermixed gelatin electrode compared to the thick one. The physical reason for this observation may be the electrode cross-linking, which is performed by dipping the electrode into glutaraldehyde solution for a certain period.
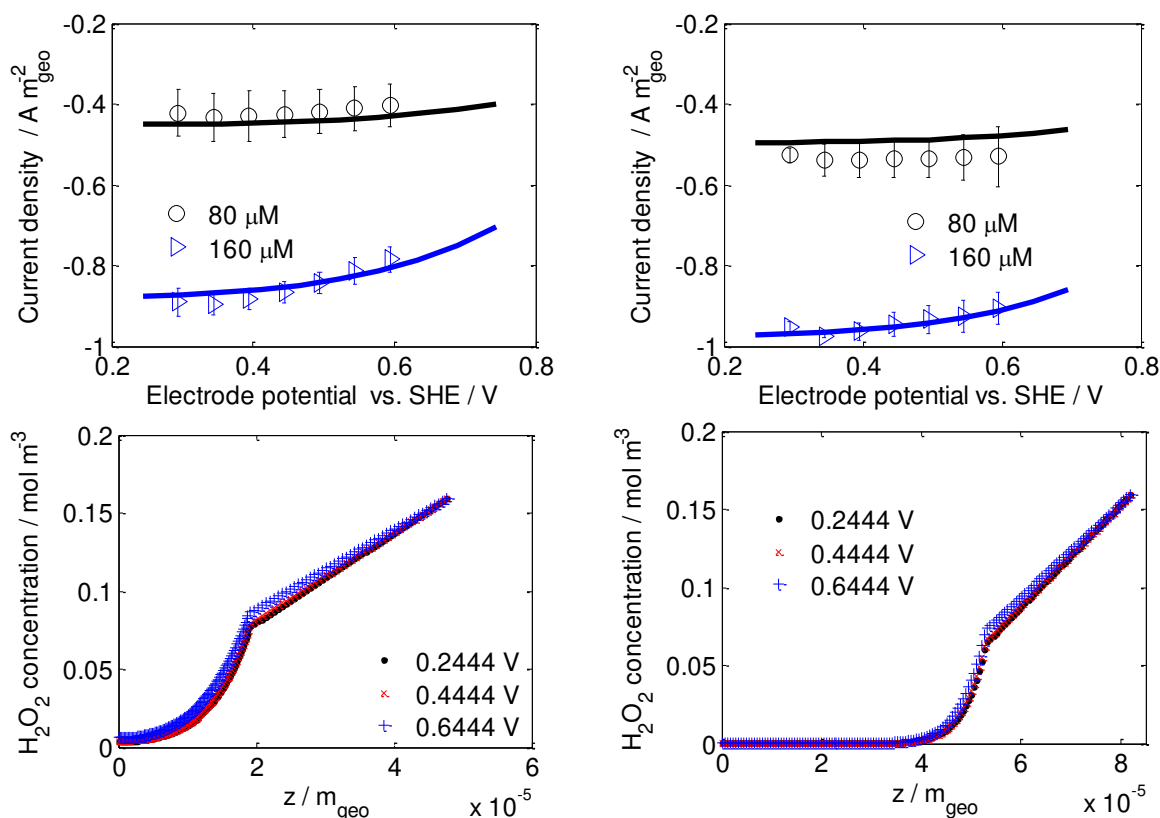

Figure 3.4: Simulated steady state profiles of a) thin and b) thick intermixed PVDF electrodes at two hydrogen peroxide concentrations and corresponding concentration change along the spatial coordinate at three steady state potential values and at 160 μm hydrogen peroxide in bulk. Conditions: fixed delay 1 min, room temperature, rotation rate 400 rpm, pH 5. Adopted with permission from Elsevier from [57].

It can be assumed that by this procedure a layer of highly cross-linked enzymes of low activity is formed close to the top of the electrode surface, while close to the bottom the enzymes are less cross-linked and more active. For DET enzymes the intermixed PVDF procedure always produced better results than the intermixed gelatin procedure. On the other hand, the intermixed gelatin procedure was highly suitable for the preparation of MET electrodes (**Figure 3.5**). It would appear that the enzyme cross-linking is of little importance in this case since the enzymes are regenerated by an assumed freely diffusive mediator. The comparison between intermixed PVDF and intermixed gelatin procedures in the case of MET is shown below (**Figure 3.5**). The intermixed gelatin thick and thin electrodes reach the same limiting current values, which is caused by glucose depletion throughout the CL in the case of a thick electrode. At more negative overpotentials the thick electrode is more active due to the higher enzyme loading. This also explains the strong decrease in the mass normalized limiting currents with enzyme loading observed experimentally (**Figure 2.10**).
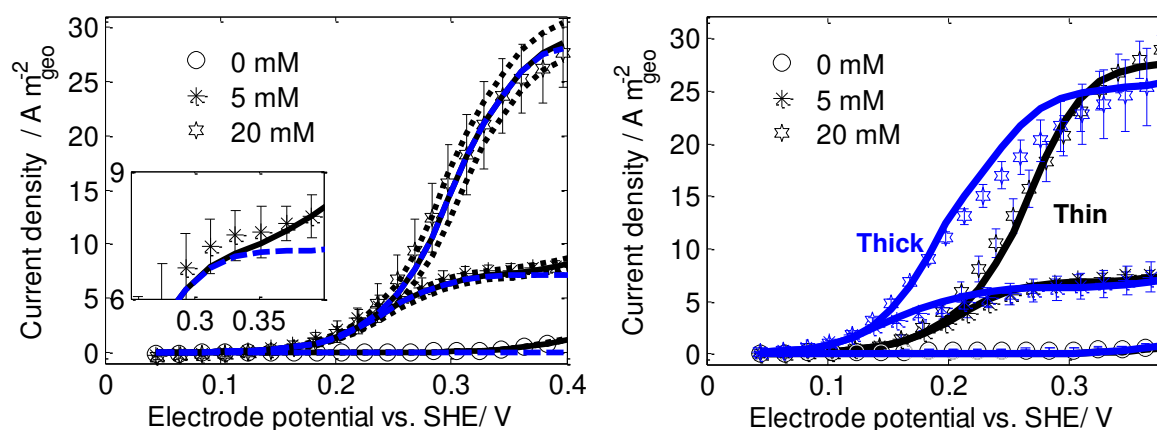

Figure 3.5: Steady state experimental (symbols) and simulated (lines) polarization curves of a) thin intermixed PVDF (black full lines - full model, dashed blue lines - simulated curves of full model with $D_{Mox} = 0$, and dashed black lines: upper and lower limits of full model with 95% individual CI and b) of thin and thick intermixed gelatin electrodes at different glucose concentrations. Conditions: fixed delay of 2 min; temperature of 37 °C; rotation rate of 400 rpm; pH 7; and enzyme loading of 1.1 mg cm^{-2} (intermixed PVDF), 0.035 mg cm^{-2} (thin intermixed gelatin) and 0.09 mg cm^{-2} (thick intermixed gelatin). Figure 3.5: a, reproduced with permission from Elsevier from [33].

4. System integration

4.1 Enzymatic fuel cells

This section shows some of the performance data on enzymatic fuel cells developed in our lab (**Figure 4.1**). In the period between 2011 and 2016 several generations of enzymatic fuel cells were developed (**Table 4.1** summarizes all the important data on these systems).
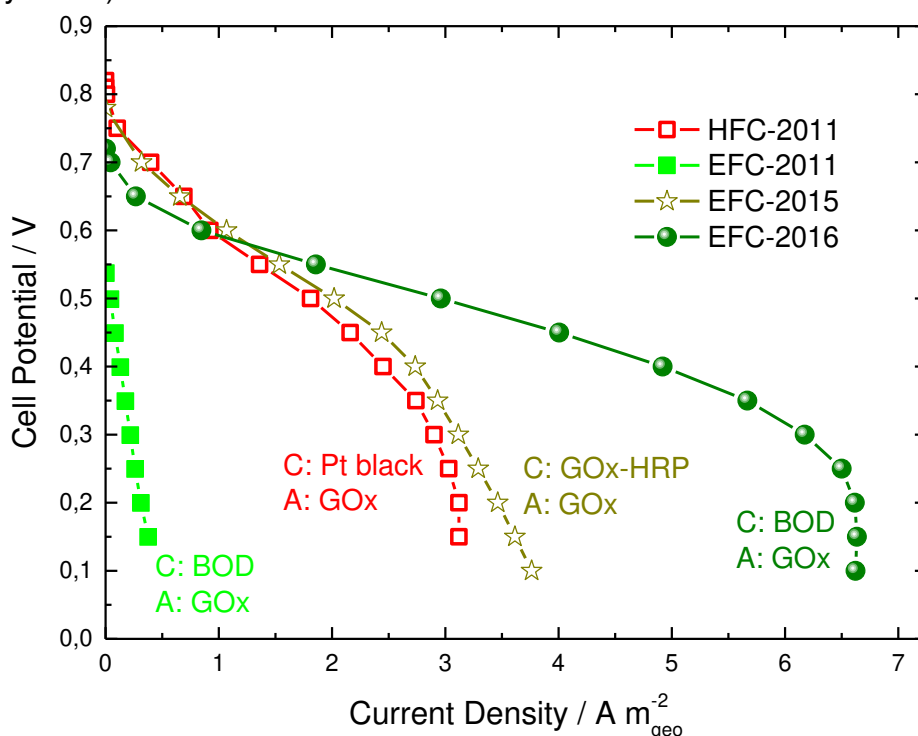

Figure 4.1: Comparison of the performance of fuel cells developed in our lab between 2011 and 2016. Other conditions of the experiments are summarized in **Table 4.1** below.

The first fuel cell in this row was a so-called hybrid fuel cell. The term "hybrid" reflects the combination of an enzymatic anode with a noble metal cathode in the same system. As can be seen in **Figure 4.1**, the HFC did not feature the best performance of all the systems studied. The low activity of HFC-2011 compared to EFC-2016 is partly due to the anode structure (layered vs. intermixed gelatin); at this point reference should be made to the different flow rates and glucose concentrations in the two systems (10 ml min^{-1} vs. 5 ml min^{-1} and 5 mM vs. 20 mM in HFC-2011 and EFC-2016 respectively). However, the main reason for the observed difference is the low activity of the Pt black cathode under studied experimental conditions (pH 7, phosphate buffer). Additionally, the stability of HFC-2011 was mainly governed by the stability of the cathode as shown below (**Figure 4.2**).

Table 4.1: Overview of performance characteristics of enzymatic fuel cells developed in our lab

Fuel Cell Type	HFC-2011	EFC-2011 MET-MET	EFC-2011 MET-DET	EFC-2015 MET-DET	EFC-2016 MET-DET
Anode:					
Mediator	CTC	CTC	CTC	TTF	TTF
Loading / mg cm^{-2}	2	2	2	1.5	1.5
Catalyst	GOx	GOx	GOx	GOx	GOx
Loading / mg cm^{-2}	0.6	0.6	0.6	1.5	1.5
Support	polypyrrole	polypyrrole	polypyrrole	Vulcan	Vulcan
Loading / mg cm^{-2}				3	3
Type	layered	layered	layered	i. gelatin	i. gelatin
Cathode					
Mediator	no	Soluble ABTS	no	no	no
Catalyst	Pt black	BOD	BOD	GOx-HRP	BOD
Loading / mg cm^{-2}	5	0.36	0.36	0.6 – 1.8	1
Support		Vulcan	Vulcan	Vulcan	Vulcan
Loading / mg cm^{-2}		3	3	3	3
Type GDE	i. Nafion	i. gelatin	i. gelatin	i. PVDF	i. PVDF
Temperature	37°C	37°C	37°C	22°C	37°C
pH	7	7	7	6	7
Glucose	5 mM	5 mM	5 mM	20 mM	20 mM
Oxygen	Gas phase	Gas phase	Gas phase	Gas phase	Gas phase
Separator	Nafion 117	no	no	no	no
Power density / μW cm^{-2}	Up to 100	25	5	100	200

Abbreviations: HFC-Hybrid Fuel Cell, EFC-Enzymatic Fuel Cell, CTC-Charge Transfer Complex, GDE-Gas Diffusion Electrode, GOx-Glucose Oxidase, ABTS- 2,2'-azino-bis(3-ethylbenzothiazoline-6-sulfonic acid), BOD-bilirubin oxidase, HRP-horseradish peroxidase, TTF- tetrathiafulvalene, i. Nafion (intermixed Nafion), i. PVDF (intermixed PVDF), i. gelatin (intermixed gelatin).

After the cathode was exchanged the performance of the HFC reverted almost to its original activity. This dramatic loss of activity was attributed to the proton exchange in the membrane by sodium ions as well as to glucose cross-over. On the other hand, the stabilities of enzymatic electrodes were quite satisfying (**Figure 4.2**). The major performance improvement between EFC-2011 and EFC-2016, which utilized the same enzymatic catalysts, can be traced back to a significant cathode

improvement. This mainly relates to an improved understanding of limiting factors in the system.

With respect to system integration, not only did the combination of noble metal and enzymatic catalysts show some incompatibilities, but compromises were also required in pure enzymatic systems. The most prominent example is the pH optimum, which might be different for different enzymatic catalysts. For example, the pH optimum of HRP is 5-6 and of GOx 7. Although GOx is functional at pH6 it shows much lower activity than at pH 7.
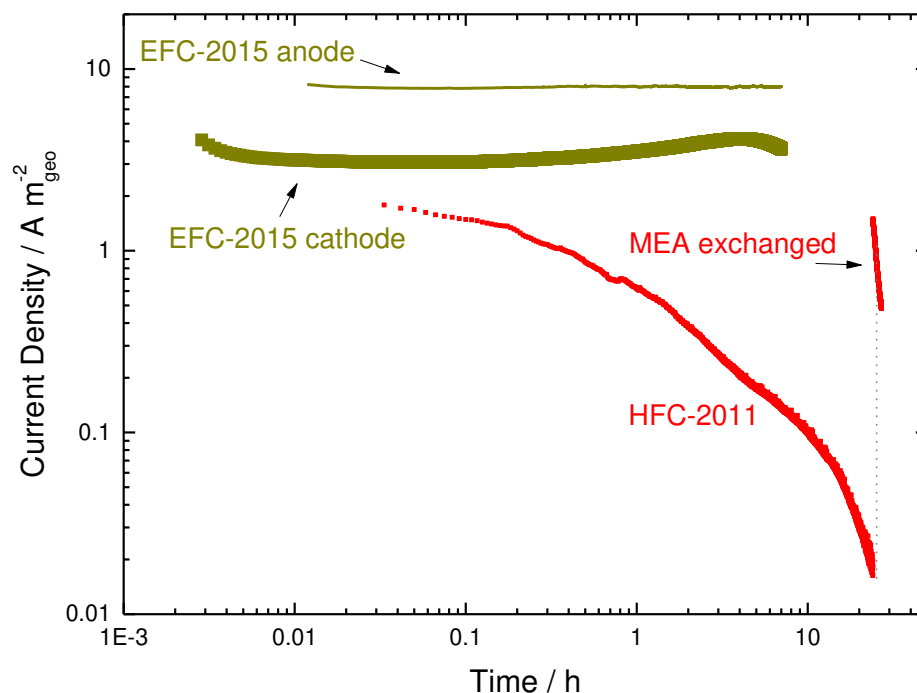

Figure 4.2: "Long" term stability of HFC-2011 and enzymatic electrodes of EFC-2015. The chart shows the absolute cathode current values.

4.2 Enzymatic fuel cells as a co-generation device

An enzymatic fuel cell can also be considered as a co-generation device (electricity + value added products). Glucose, as a fuel, is not only of interest for implantable power source applications, but in general it can also be considered as a renewable feedstock for the chemical industry. It is an abundant carbon source with good biodegradability. These aspects make it a platform chemical for different syntheses and a good candidate for replacing the use of fossil raw materials. In an enzymatic fuel cell glucose is oxidized to its partial oxidation product gluconic acid. Gluconic acid is widely used in pharmaceutical, detergent, food, textile and other industries. Glucose conversion in the electroenzymatic fuel cell was studied to evaluate the cells' performance for gluconic acid production. The product analysis was performed using nuclear magnetic resonance spectroscopy (NMR). The performance data were also compared with literature data of other electroenzymatic processes for gluconic acid production. Two types of EFC were evaluated (EFC-2015 and EFC-2016). EFC-2015 operates at pH 6 and has GOx on both anode and cathode side. This fuel cell

does not require any membrane and operates spontaneously (without additional electricity). EFC-2016 has GOx only on the anode side. It operates at pH 7 and 37°C. These conditions are more optimal for GOx which is also reflected in a significant improvement in the electrochemical performance data. On the other hand, only less than 30% glucose conversion was achieved in this reactor, while almost 60% was achieved with EFC-2015 with much lower electrochemical performance. As can be seen in **Table 4.1** EFC-2015 has higher total GOx loading (due to the presence of GOx also on the cathode side), than the EFC-2016. Additionally, it appears that a pure enzymatic conversion performs significantly better than an electroenzymatic conversion in EFC-2015. Furthermore, an interesting aspect was a gluconic acid selectivity decrease observed in EFC-2015, but not in EFC-2016. This was attributed to the enzymatic cathode, where due to development of hydrogen peroxide in an enzymatic reaction between glucose and oxygen, follow-up reactions between hydrogen peroxide by-product and gluconic acid, are possible. A possible mechanism of this reaction is demonstrated below (**Figure 4.3**). The additional product formed is arabinose. It was shown that its yield is strongly related to the process conditions. Those conditions, which favor high hydrogen peroxide concentrations (low flow rates, low overpotentials) result in higher yields of arabinose. On the other hand, the selectivity of EFC-2016 for gluconic acid production was 100%.
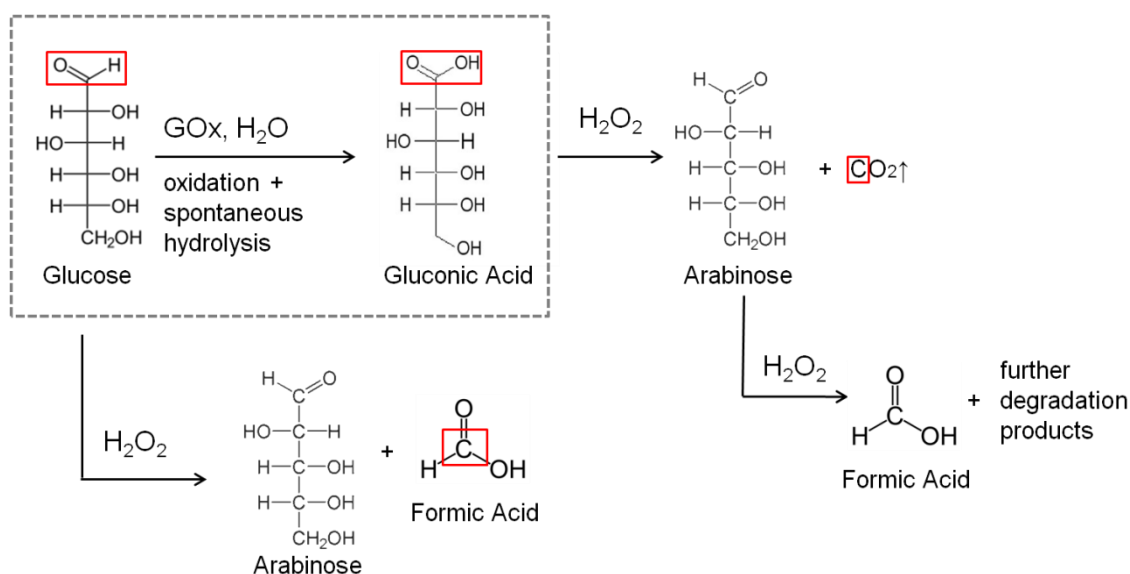

Figure 4.3: Possible reaction mechanism of by-product formation in EFC-2015 [58]

The electroenzymatic reactor with the best performance for glucose conversion was compared with the literature examples (**Table 4.2**). Several sustainability indicators were selected for comparison purposes. They were space-time yield (STY), product titer, cycle time, reaction yield, atom efficiency and E-factor. At first our process was compared with other electroenzymatic processes. As can be seen, our process has higher STY than literature examples. This is partly due to the glucose conversion on both electrodes, but also due to higher enzyme utilization in our system. Product titer is relatively low for our process. This low product titer is a common feature of many reported electroenzymatic processes. The straightforward

consequences of this high level of dilution are higher product separation costs, with a major influence on the product economy as well as on the E-factor (due to the disposal of large amounts of wastewater). The cycle times are similar to other electrochemical processes, as are the reaction yields. There is a small difference in the atom efficiency between the process developed here and literature examples. The difference comes from the different overall stochiometries of these processes. Our overall stoichiometry corresponds to the stoichiometry of fermentation. Other electrochemical processes are non-spontaneous and feature hydrogen evolution as a cathode process, which results in slightly lower atom efficiency. Due to the lack of data it was not possible to calculate the E-factor for other electroenzymatic processes. The E-factor for our electroenzymatic process is relatively high. In particular, a comparison with fermentation casts a negative light on our electroenzymatic process. The main reasons for such a high E-factor are low enzyme utilization and low cycle times. One cause for the low enzyme utilization was the substrate depletion throughout the catalyst layer. This might be circumvented by higher glucose concentrations. Providing that higher glucose concentrations can be used, not only the enzyme utilization but also the product titer could increase. Both factors should improve productivity for the same cycle time. Additionally, the cycle time should be increased from several hours to several months. In this case a significant reduction in the E-factor can be expected. The major advantages of the fermentation process are a high product titer and a low E-factor.

Table 4.2: Comparison of our process versus literature processes

Indicators	Electroenzymatic: Our process	Fermentation	Electroenzymatic: State of literature
STY / g h^{-1} dm^{-3}	33.7-36.1	0.132 – 21	0.13 – 4.9
Product titer / g dm^{-3}	3.1	100 – 350	1.66 – 14.5
t$_{cycle}$ / h	8-20	20 – 100	3 –12
Reaction yield / %	75	74 – 99.4	43 – 85*
Atom efficiency / %	100	100	99
E-factor / kg kg^{-1}	9	0.06	N/A
References	ECF-2015	[59]	[60-64]

*Calculated assuming 100 % selectivity

5. Conclusions

This thesis summarizes my research activities on bioelectrochemical systems. Most of these activities were directed towards an understanding of the limiting processes at the level of enzymatic electrodes. Taking a systematic approach, we studied main factors influencing the performances of enzymatic electrodes with direct and mediated electron transfer mechanisms. We have demonstrated that the choice of a proper mediator is not always simple. Initially, two different mediators for glucose oxidase (GOx) were tested. An artificial electron transport chain was assembled that enabled the transport of electrons between the FAD redox center and the electrode surface. Although the results showed a glucose oxidation current, it was not possible to ascribe the electrocatalytic activity solely to GOx, but rather to the underlying gold surface. CNT and TTF are promising mediators for further applications of enzymatic electrodes. Our experimental studies have shown that the levels of activity of enzymatic electrodes with the same enzyme loading vary within 2 orders of magnitude. With the help of fluorescence and AFM microscopy, a low utilization of an available surface for an enzyme adsorption as well as a formation of agglomerates (binder and surface roughness-dependent) was diagnosed. Both effects significantly decrease the enzyme utilization in DET, while the effect in the case of MET is less marked. Our results also indicated that pure physical adsorption is more favorable for the preparation of DET electrodes. The structure of a porous enzymatic electrode was further studied by SEM. We observed that the electrode preparation procedure has a significant impact on the organization and arrangement of the individual components (support, mediator, binder) of enzymatic electrodes, resulting in two major electrode architectures (interlayered and intermixed). For MET similar performance was achieved with both architectures, with intermixed electrodes performing slightly better. In the case of DET, intermixed electrodes with two different binders (gelatin and PVDF) were prepared. Here, intermixed PVDF electrodes performed better, which was attributed to a higher level of enzyme agglomeration in the intermixed gelatin electrodes. Finally, we proposed a generic procedure for the preparation of DET and MET electrodes.

The preparation procedure has an impact on the enzyme orientation on the conductive surface, as well as on its distribution and arrangement inside of the porous matrix. Additionally, it impacts the structure of the catalyst layer in terms of porosity, electrode thickness or available surface area; furthermore, these effect the enzyme kinetics as well as the charge and mass transport inside the catalyst layer. Since these cross-correlations cannot always be understood intuitively, in addition to experimental approaches, we also used mathematical modeling as an important tool

in accelerating/evaluating the processes with regard to real applications. Considering that the bottleneck of bioelectrochemical systems is still at the level of understanding and improving enzymatic electrodes, we placed a great deal of emphasis on understanding and quantifying porous enzymatic electrode responses. We adopted the frequency response method in order to discriminate DET kinetics, as well as for more valuable parameter estimation. We demonstrated that only the model including full Michaelis-Menten kinetics can describe the steady state as well as the dynamic responses of the DET enzymatic electrode. We adopted a porous electrode modeling framework in order to describe potential, current and concentration gradients inside porous catalyst layers. We showed that only the concentration/current gradient plays a significant role with respect to electrode performance. Substrate depletion is observed for both DET and MET electrodes and it was somewhat influenced by the electrode preparation procedure (binder type). In the model, this was reflected by the change of electrode porosity, active surface area and total enzyme loadings. The calculated enzyme utilization for DET electrodes was below 0.05 %.

We were able to demonstrate that the electrochemical methods, combined with proper mathematical descriptions, can bring significant insights into the reasons limiting the overall electrode behavior. Ultimately this leads to better system design. Yet, to make these models more realistic, additional porous electrode characterizations are necessary. Currently, there is little knowledge about the real structure of porous enzymatic electrodes. Only a few studies offer sufficient data on electrode thicknesses, porosity and real surface area, while there is no data at all about realistic enzyme and mediator distributions. The majority of studies are not concerned by enzyme/mediator/nanoparticle loadings or their utilization.

Furthermore, our model-based analysis resulted in a significant improvement in the performance of the electroenzymatic fuel cell. Between 2011 and 2016 the power output of EFC for the same types of enzymatic catalyst improved by a factor of 40. This was mainly due to an improvement in the enzymatic cathode. We have also shown that enzymatic fuel cells can be used for gluconic acid conversion. Very high space-time yields (STY), and selectivity can be achieved in systems of this nature. However, a preliminary sustainability analysis identified some weak points in the current electroenzymatic processes, such as low product titer and cycle times. Both latter effects impact the E-factor of the enzymatic processes. It will be necessary to achieve further improvements to the enzyme utilization and an increase in cycle times. In order to develop sustainable processes, issues relating to separation (recycling) and toxicity of selected mediators will need to be carefully considered. Bearing in mind that enzymes are catalysts that have to be produced, creating some waste in the process, this factor will need to be considered in future if enzymatic systems are ever going to be able to compete with fermentation systems. For systems where the main focus is on material production, characterizing the product distribution is of great interest. Currently, most of these studies consider much diluted systems. This is a significant drawback, since it significantly increases the separation costs and amount of waste liquids. To fully develop the potential of

bioelectrochemical systems, electroenzymatic syntheses in more concentrated solutions will need to be demonstrated.

Finally, in order to push forward new exciting bioelectrochemical applications, closer interaction between the different disciplines (electrochemistry, biology, bioelectrochemistry, material science and reaction engineering) is strongly advised.

6. References

1. Falk, M., Andoralov, V., Blum, Z., Sotres, J., Suyatin, D.B., Ruzgas, T., Arnebrant, T., Shleev, S., "Biofuel cell as a power source for electronic contact lenses". *Biosensors and Bioelectronics* 2012, 37(1), 38-45.
2. Bandodkar, A., You, J.-M., Kim, N.-H., Gu, Y., Kumar, R., A. M, V.M., Kurniawan, J.F., Imani, S., Nakagawa, T., Parish, B., Parthasarathy, M., Mercier, P., Xu, S., Wang, J., "Soft, stretchable, high power density electronic skin-based biofuel cells for scavenging energy from human sweat". *Energy & Environmental Science* 2017, 7 (10),1581-1589.
3. Varničić, M., Vidaković-Koch, T., Sundmacher, K., "Gluconic acid synthesis in an electroenzymatic reactor". *Electrochimica Acta* 2015, 174, 480-487.
4. Milton, R.D., Cai, R., Abdellaoui, S., Leech, D., De Lacey, A.L., Pita, M., Minteer, S.D., "Bioelectrochemical Haber–Bosch process: an ammonia-aroducing H_2/N_2 fuel cell". *Angewandte Chemie International Edition* 2017, 56(10), 2680-2683.
5. Cracknell, J.A., Vincent, K.A., Armstrong, F.A., "Enzymes as working or inspirational electrocatalysts for fuel cells and electrolysis". *Chemical Reviews* 2008, 108(7), 2439-2461.
6. Ivanov, I., Vidaković-Koch, T., Sundmacher, K., "Recent advances in enzymatic fuel cells: experiments and modeling". *Energies* 2010, 3(4), 803.
7. Lojou, É., Bianco, P., "Membrane electrodes for protein and enzyme electrochemistry". *Electroanalysis* 2004, 16(13-14), 1113-1121.
8. De Poulpiquet, A., Ciaccafava, A., Szot, K., Pillain, B., Infossi, P., Guiral, M., Opallo, M., Giudici-Orticoni, M.-T., Lojou, E., "Exploring properties of a hyperthermophilic membrane-bound hydrogenase at carbon nanotube modified electrodes for a powerful H_2/O_2 biofuel cell". *Electroanalysis* 2013, 25(3), 685-695.
9. Vidaković-Koch, T., Sundmacher, K., "Porous electrodes in bioelectrochemistry". In P. Vadgama, ed. *Encyclopedia of Interfacial Chemistry: Surface Science and Electrochemistry* Elsevier: 2017.
10. Santoro, C., Arbizzani, C., Erable, B., Ieropoulos, I., "Microbial fuel cells: From fundamentals to applications. A review". *Journal of Power Sources* 2017, 356, 225-244.
11. Zebda, A., Gondran, C., Le Goff, A., Holzinger, M., Cinquin, P., Cosnier, S., "Mediatorless high-power glucose biofuel cells based on compressed carbon nanotube-enzyme electrodes". *Nature Communications* 2011, 2, 370.
12. Courjean, O., Gao, F., Mano, N., "Deglycosylation of glucose oxidase for direct and efficient glucose electrooxidation on a glassy carbon electrode". *Angewandte Chemie* 2009, 121(32), 6011-6013.
13. Bartlett, P.N., Al-Lolage, F.A., "There is no evidence to support literature claims of direct electron transfer (DET) for native glucose oxidase (GOx) at carbon nanotubes or graphene". *Journal of Electroanalytical Chemistry* 2017.
14. Vidaković-Koch, T., "Electron transfer between enzymes and electrodes". In: *Advances in Biochemical Engineering/Biotechnology*. Springer, Berlin, Heidelberg, pp 1-47, 2017.
15. Togo, M., Takamura, A., Asai, T., Kaji, H., Nishizawa, M., "An enzyme-based microfluidic biofuel cell using vitamin K3-mediated glucose oxidation". *Electrochimica Acta* 2007, 52(14), 4669-4674.
16. Mano, N., Mao, F., Heller, A., "A miniature biofuel cell operating in a physiological buffer". *Journal of the American Chemical Society* 2002, 124(44), 12962-12963.

17. Chen, T., Barton, S.C., Binyamin, G., Gao, Z., Zhang, Y., Kim, H.-H., Heller, A., "A miniature biofuel cell". *Journal of the American Chemical Society* 2001, 123(35), 8630-8631.

18. Kim, H.-H., Mano, N., Zhang, Y., Heller, A., "A miniature membrane-less biofuel cell operating under physiological conditions at 0.5 V". *Journal of The Electrochemical Society* 2003, 150(2), A209-A213.

19. Vidaković-Koch, T., Ivanov, I., Falk, M., Shleev, S., Ruzgas, T., Sundmacher, K., "Impact of the gold support on the electrocatalytic oxidation of sugars at enzyme-modified electrodes". *Electroanalysis* 2011, 23(4), 927-930.

20. Willner, I., Katz, E., Patolsky, F., F. Buckmann, A., "Biofuel cell based on glucose oxidase and microperoxidase-11 monolayer-functionalized electrodes". *Journal of the Chemical Society,* Perkin Transactions 2 1998, (8), 1817-1822.

21. Kuwahara, T., Oshima, K., Shimomura, M., Miyauchi, S., "Properties of the enzyme electrode fabricated with a film of polythiophene derivative and its application to a glucose fuel cell". *Journal of Applied Polymer Science* 2007, 104(5), 2947-2953.

22. Brunel, L., Denele, J., Servat, K., Kokoh, K.B., Jolivalt, C., Innocent, C., Cretin, M., Rolland, M., Tingry, S., "Oxygen transport through laccase biocathodes for a membrane-less glucose/O_2 biofuel cell". *Electrochemistry Communications* 2007, 9(2), 331-336.

23. Bedekar, A.S., Feng, J.J., Krishnamoorthy, S., Lim, K.G., Palmore, G.T.R., Sundaram, S., "Oxygen limitation in microfluidic biofuel cells". *Chemical Engineering Communication*s 2007, 195(3), 256-266.

24. Nazaruk, E., Smoliński, S., Swatko-Ossor, M., Ginalska, G., Fiedurek, J., Rogalski, J., Bilewicz, R., "Enzymatic biofuel cell based on electrodes modified with lipid liquid-crystalline cubic phases". *Journal of Power Sources* 2008, 183(2), 533-538.

25. Tamaki, T., Yamaguchi, T., "High-surface-area three-dimensional biofuel cell electrode using redox-polymer-grafted carbon". *Industrial & Engineering Chemistry Research* 2006, 45(9), 3050-3058.

26. Matsue, T., Evans, D.H., Osa, T., Kobayashi, N., "Electron-transfer reactions associated with host-guest complexation. Oxidation of ferrocenecarboxylic acid in the presence of .beta.-cyclodextrin". *Journal of the American Chemical Society* 1985, 107(12), 3411-3417.

27. Mano, N., Mao, F., Shin, W., Chen, T., Heller, A., "A miniature biofuel cell operating at 0.78 V". *Chemical Communications* 2003, (4), 518-519.

28. Ivanov, I. "Development of a glucose-oxygen enzymatic fuel cell". Dr.-Ing. Otto von Guericke University, Magdeburg, 2012.

29. Ivanov, I., Vidaković, T.R., Sundmacher, K., "The influence of a self-assembled monolayer on the activity of rough gold for glucose oxidation". *Electrochemistry Communications* 2008, 10(9), 1307-1310.

30. Ivanov, I., Vidaković-Koch, T., Sundmacher, K., "Alternating electron transfer mechanism in the case of high-performance tetrathiafulvalene–tetracyanoquinodimethane enzymatic electrodes". *Journal of Electroanalytical Chemistry* 2013, 690, 68-73.

31. Ivanov, I., Vidaković-Koch, T., Sundmacher, K., "Direct hybrid glucose–oxygen enzymatic fuel cell based on tetrathiafulvalene–tetracyanoquinodimethane charge transfer complex as anodic mediator". *Journal of Power Sources* 2011, 196(22), 9260-9269.

32. Khan, G.F., "TTF-TCNQ complex based printed biosensor for long-term operation". *Electroanalysis* 1997, 9(4), 325-329.

33. Do, T.Q.N., Varničić, M., Flassig, R.J., Vidaković-Koch, T., Sundmacher, K., "Dynamic and steady state 1-D model of mediated electron transfer in a porous enzymatic electrode". *Bioelectrochemistry* 2015, 106, Part A, 3-13.

34. Khan, G.F., Ohwa, M., Wernet, W., "Design of a stable charge transfer complex electrode for a third-generation amperometric glucose sensor". *Analytical Chemistry* 1996, 68(17), 2939-2945.

35. Varnicic, M., Bettenbrock, K., Hermsdorf, D., Vidakovic-Koch, T., Sundmacher, K., "Combined electrochemical and microscopic study of porous enzymatic electrodes with direct electron transfer mechanism". *RSC Advances* 2014, 4(69), 36471-36479.

36. Zhao, M., Gao, Y., Sun, J., Gao, F., "Mediatorless glucose biosensor and direct electron transfer type glucose/air biofuel cell enabled with carbon nanodots". *Analytical Chemistry* 2015, 87(5), 2615-2622.
37. Ciaccafava, A., De Poulpiquet, A., Techer, V., Giudici-Orticoni, M.T., Tingry, S., Innocent, C., Lojou, E., "An innovative powerful and mediatorless H2/O2 biofuel cell based on an outstanding bioanode". *Electrochemistry Communications* 2012, 23, 25-28.
38. Ciniciato, G.P.M.K., Lau, C., Cochrane, A., Sibbett, S.S., Gonzalez, E.R., Atanassov, P., "Development of paper based electrodes: From air-breathing to paintable enzymatic cathodes". *Electrochimica Acta* 2012, 82, 208-213.
39. Gupta, G., Lau, C., Rajendran, V., Colon, F., Branch, B., Ivnitski, D., Atanassov, P., "Direct electron transfer catalyzed by bilirubin oxidase for air breathing gas-diffusion electrodes". *Electrochemistry Communications* 2011, 13(3), 247-249.
40. Babanova, S., Artyushkova, K., Ulyanova, Y., Singhal, S., Atanassov, P., "Design of experiments and principal component analysis as approaches for enhancing performance of gas-diffusional air-breathing bilirubin oxidase cathode". *Journal of Power Sources* 2014, 245, 389-397.
41. Miyake, T., Yoshino, S., Yamada, T., Hata, K., Nishizawa, M., "Self-Regulating Enzyme−Nanotube Ensemble Films and Their Application as Flexible Electrodes for Biofuel Cells". *Journal of the American Chemical Society* 2011, 133(13), 5129-5134.
42. Vidaković-Koch, T., Hanke-Rauschenbach, R., Gonzalez Martínez, I., Sundmacher, K., "Catalyst layer modeling". In Breitkopf, C., Swider-Lyons, K., eds.*Springer Handbook of Electrochemical Energy*, Springer Berlin Heidelberg: Berlin, Heidelberg, 2017; pp 259-285.
43. Newman, J.S., Tobias, C.W., "Theoretical analysis of current distribution in porous electrodes". *Journal of The Electrochemical Society* 1962, 109(12), 1183-1191.
44. Howes, F.A., Whitaker, S., The spatial averaging theorem revisited. Chemical Engineering Science 1985, 40(8), 1387-1392.
45. Vidaković-Koch, T., Mittal, V.K., Do, T.Q.N., Varničić, M., Sundmacher, K., "Application of electrochemical impedance spectroscopy for studying of enzyme kinetics". *Electrochimica Acta* 2013, 110, 94-104.
46. Ruzgas, T., Gorton, L., Emneus, J., Markovarga, G., "Kinetic-models od horseradish-peroxidase action on a graphite electrode". *Journal of Electroanalytical Chemistry* 1995, 391(1-2).
47. Lindgren, A., Tanaka, M., Ruzgas, T., Gorton, L., Gazaryan, I., Ishimori, K., Morishima, I., "Direct electron transfer catalysed by recombinant forms of horseradish peroxidase: insight into the mechanism". *Electrochemistry Communications* 1999, 1(5).
48. Tatsuma, T., Ariyama, K., Oyama, N., "Kinetic analysis of electron transfer from a graphite coating to horseradish peroxidase". *Journal of Electroanalytical Chemistry* 1998, 446(1-2).
49. Andreu, R., Ferapontova, E.E., Gorton, L., Calvente, J.J., "Direct electron transfer kinetics in horseradish peroxidase electrocatalysis". *The Journal of Physical Chemistry B* 2007, 111(2), 469-477.
50. Bensmann, B., Petkovska, M., Vidaković-Koch, T., Hanke-Rauschenbach, R., Sundmacher, K., "Nonlinear frequency response of electrochemical methanol oxidation kinetics: A theoretical analysis". *Journal of the Electrochemical Society* 2010, 157(9).
51. Petkovska, M., "Application of nonlinear frequency response to adsorption systems with complex kinetic mechanisms". *Adsorption-Journal of the International Adsorption Society* 2005, 11, 497-502.
52. Petkovska, M., "Nonlinear FR-ZLC method for investigation of adsorption equilibrium and kinetics". *Adsorption-Journal of the International Adsorption Society* 2008, 14(2-3), 223-239.
53. Weiner, D.D., Spina, J.F., "Sinusoidal analysis and modeling of weakly nonlinear circuits: with application to nonlinear interference effects". Van Nostrand Reinhold. 1980.
54. Vidaković-Koch, T.R., Panić, V.V., Andrić, M., Petkovska, M., Sundmacher, K., "Nonlinear frequency response analysis of the ferrocyanide oxidation kinetics. Part I. A theoretical analysis". *Journal of Physical Chemistry C* 2011, 115(35).

55. Panić, V.V., Vidaković-Koch, T.R., Andrić, M., Petkovska, M., Sundmacher, K., "Nonlinear frequency response analysis of the ferrocyanide oxidation kinetics. Part II. Measurement routine and experimental validation". *Journal of Physical Chemistry C* 2011, 115(35).

56. Yu, H., Roller, J.M., Mustain, W.E., Maric, R., "Influence of the ionomer/carbon ratio for low-Pt loading catalyst layer prepared by reactive spray deposition technology". *Journal of Power Sources* 2015, 283, 84-94.

57. Do, T.Q.N., Varničić, M., Hanke-Rauschenbach, R., Vidaković-Koch, T., Sundmacher, K., "Mathematical Modeling of a Porous Enzymatic Electrode with Direct Electron Transfer Mechanism". *Electrochimica Acta* 2014, 137, 616-626.

58. Varničić, M. "Novel Electroenzymatic Process for Gluconic Acid Production". Dr.-Ing. Dissertation, Otto von Guericke University Magdeburg, Magdeburg, 2017.

59. Pal, P., Kumar, R., Banerjee, S., "Manufacture of gluconic acid: A review towards process intensification for green production". *Chemical Engineering and Processing: Process Intensification* 2016, 104, 160-171.

60. Basséguy, R., Délécouls-Servat, K., Bergel, A., "Glucose oxidase catalysed oxidation of glucose in a dialysis membrane electrochemical reactor (D-MER)". *Bioprocess and Biosystems Engineering* 2004, 26(3), 165-168.

61. Obón, J.M., Casanova, P., Manjón, A., Fernández, V.M., Iborra, J.L., "Stabilization of glucose dehydrogenase with polyethyleneimine in an electrochemical reactor with NAD(P) + regeneration". *Biotechnology Progress* 1997, 13(5), 557-561.

62. Manjón, A., Obón, J.M., Casanova, P., Fernández, V.M., Ilborra, J.L., "Increased activity of glucose dehydrogenase co-immobilized with a redox mediator in a bioreactor with electrochemical NAD+ regeneration". *Biotechnology Letters* 2002, 24(15), 1227-1232.

63. Gros, P., Bergel, A., "Electrochemically enhanced biosynthesis of gluconic acid". AIChE Journal 2005, 51(3), 989-997.

64. Miyawaki, O., Yano, T., "Electrochemical bioreactor with immobilized glucose-6-phosphate dehydrogenase on the rotating graphite disc electrode modified with phenazine methosulfate". *Enzyme and Microbial Technology* 1993, 15(6), 525-529.

Appendix A: List of symbols

A	amplitude	V
a	internal active surface area	$m_{act}^2\ m_{geo}^{-3}$
c	volumetric concentration	mol m^{-3}
c_D	double layer capacitance	F m^{-2}
D	diffusion coefficient of species	$m_{geo}^2\ s^{-1}$
F	Faraday's constant=96 485	C mol^{-1}
H_1	first order frequency response function	S m^{-2}
H_n	nth order frequency response function	S V$^{-(n-1)}$ m^{-2}
i	current density	$A\ m_{geo}^{-2}$
j	imaginary number	
k	reaction rate constants	m^3 mol^{-1} s^{-1} or s^{-1}
K_M	Michaelis-Menten constant	mol m^{-3}
L	catalyst layer thickness	m_{geo}
n	number of electrons	
r	reaction rate	$mol\ s^{-1}\ m_{act}^{-2}$
R	universal gas constant=8.314	J mol^{-1} K^{-1}
T	temperature	K
z_k	space coordinate (k=1,2,3)	

Greek

α	transfer coefficient of electrochemical steps	
Γ	surface concentration	mol m^{-2}
δ	diffusion layer thickness	m_{geo}
ε	void fraction	$m^3 m_{geo}^{-3}$
η	overpotential	V
ι	local current density	$A\ m_{act}^{-2}$
ν	stoichiometric coefficient	
σ_E, σ_I	electron-and ion conductivities	$S\ m_{geo}^{-1}$
φ_E, φ_I	potentials of electron-and ion- conducting phases respectively	V

ω	angular frequency	rad s^{-1}
ω$_R$	rotation rate of rotating disc electrode	rad s^{-1}

Super- and Sub-scripts

act, geo	active and geometrical respectively
CL, DL	catalyst layer and diffusion layer respectively
e,e1,e2	electrochemical reaction steps
I, E	ion and electron conducting phase respectively
o	standard conditions
SS	steady state

List of abbreviations

Ag/AgCl	silver silver chloride reference electrode
CC	current collector
CL	catalyst layer
CPI,CPII	compound I and II
DET	direct electron transfer
D-FDH	fructose dehydrogenase
E	enzyme
ES	enzyme substrate complex
FAD	flavin adenine dinucleotide
GOx	glucose oxidase
HRP	horseradish peroxidase
Lac	lacasse
MET	mediated electron transfer
SAMs	self-assembled monolayers
SHE	standard hydrogen electrode

Selected publications from the author

[TVK1]   **T. Vidaković-Koch***, I. Ivanov, M. Falk, S. Shleev, T. Ruzgas, K. Sundmacher, "Impact of the gold support on the electrocatalytic oxidation of sugars at enzyme-modified electrodes", *Electroanalysis*, 23(4) (2011) 927 – 930

[TVK2]   I. Ivanov, **T.R. Vidaković-Koch***, K. Sundmacher, "Direct hybrid glucose-oxygen enzymatic fuel cell based on tetrathiafulvalene-tetracyanoquinodimethane charge transfer complex as anodic mediator", *J. Power Sources*, 196 (2011) 9260 - 9269

[TVK3]   **T. Vidaković-Koch***, V. Panić, M. Andrić, M. Petkovska, K. Sundmacher, "Non-Linear Frequency Response Analysis of the Ferrocyanide Oxidation Kinetics: Part I – A Theoretical Analysis", *J. Phys. Chem. C*, 115(35) (2011) 17341 – 17351

[TVK4]   V. Panić, **T. Vidaković-Koch***, M. Andrić, M. Petkovska, K. Sundmacher, "Non-Linear Frequency Response Analysis of the Ferrocyanide Oxidation Kinetics: Part II – Experimental Validation", *J. Phys. Chem. C*, 115(35) (2011) 17352 - 17358

[TVK5]   I. Ivanov, **T. Vidaković-Koch***, K. Sundmacher, "Alternating electron transfer mechanism in the case of high-performance tetrathiafulvalene-tetracyanoquinodimethane enzymatic electrodes", *J. Electroanal. Chem.*, 690 (2013) 68 - 73

[TVK6]   **T. Vidaković-Koch***, V.K. Mittal, T.Q.N. Do, M. Varničić, K. Sundmacher, "Application of electrochemical impedance spectroscopy for studying of enzyme kinetics", *Electrochim. Acta*, 110 (2013) 94-104

[TVK7]   T. Q. N. Do, M. Varničić, R. Hanke-Rauschenbach, **T. Vidakovic-Koch***, K. Sundmacher " Mathematical Modeling of a Porous Enzymatic Electrode with Direct Electron Transfer Mechanism", *Electrochim. Acta*, 137 (2014) 616-626

[TVK8]   M. Varničić, K. Bettenbrock, D. Hermsdorf, **T. Vidaković-Koch***, K. Sundmacher, "Combined Electrochemical and Microscopic Study of Porous Enzymatic Electrodes with Direct Electron Transfer Mechanism", *RSC Advances*, 4 (2014) 36471-36479

[TVK9]   M. Varničić, **T. Vidaković-Koch***, K. Sundmacher, "Gluconic acid synthesis in an electroenzymatic reactor", *Electrochim. Acta*, 174 (2015) 480-487

[TVK10] T. Q. N. Do, M. Varničić, R. Flassig, **T. T. Vidaković-Koch***, K. Sundmacher, "Dynamic and steady state 1-D model of mediated electron transfer in a porous enzymatic electrode" *Bioelectrochemistry*, 106 (2015) 3-13

[TVK1]

T. Vidaković-Koch, I. Ivanov, M. Falk, S. Shleev, T. Ruzgas,
K. Sundmacher

**Impact of the gold support on the electrocatalytic oxidation
of sugars at enzyme-modified electrodes**

Impact of the Gold Support on the Electrocatalytic Oxidation of Sugars at Enzyme-Modified Electrodes

Tanja Vidaković-Koch,*[a] *Ivan Ivanov*,[a] *Magnus Falk*,[b] *Sergey Shleev*,[b] *Tautgirdas Ruzgas*,[b]
Kai Sundmacher[a, c]

[a] Process Systems Engineering, Otto-von-Guericke University Magdeburg, Magdeburg, Germany
[b] Biomedical Laboratory Science and Technology, Faculty of Health and Society, Malmö University, Malmö, Sweden
[c] Max Planck Institute for Dynamics of Complex Technical Systems, Magdeburg, Germany
*e-mail: vidakovi@mpi-magdeburg.mpg.de

Abstract
The influence of gold support on the bioelectrocatalytic activity of glucose oxidase and cellobiose dehydrogenase immobilized on self-assembled monolayer-modified high surface area gold electrodes such as rough gold and gold nanoparticles has been studied. The two types of enzyme-modified electrodes showed very high activity towards sugar oxidation. However, it has been shown that the largest part of this electrocatalytic activity comes from the underlying gold surface. These findings are of special importance for bioelectrochemical studies of enzymatic electrodes, where the immobilization support might show electrocatalytic properties toward the substrates of investigated enzymes.

Keywords: Gold, Glucose oxidase, Cellobiose dehydrogenase, Enzymatic electrode, Sugar oxidation

One of the ways to design bioelectrocatalytically active electrodes is to physically or chemically connect redox enzymes to an electron conducting surface, acting as electron source or electron sink [1]. The surface can be made from metal, carbon or electron conducting polymers. If metals are used their electrocatalytic properties are usually neglected, which under some circumstances can lead to a misinterpretation of the electrocatalytic mechanism of the bioelectrocatalytic systems. Among metals gold is probably one of the most used materials for enzyme immobilization [2]. In order to increase both sensitivity and efficiency of bioelectrodes, high surface area gold (HSAG) systems, such as rough gold (RG) [3] or gold nanoparticle-modified (GNP) electrodes [4] are preferred. These surfaces can be modified by a self-assembled monolayer (SAM), which can ensure selective access to the underlying surface and can be used as a binding layer for further electrode modification [2,5]. In the present work the influence of gold support on the bioelectrocatalytic activity of two redox enzymes (glucose oxidase (GOx) and cellobiose dehydrogenase (CDH)) immobilized on SAM-modified HSAG electrodes has been studied.

According to literature, regeneration of reduced GOx can be efficiently accomplished via mediated electron transfer (MET) [6]. In the present study, we apply a MET approach, where apo-enzyme (enzyme lacking cofactor) is reconstituted onto SAM-modified HSAG, functionalized with a mediator molecule (pyrroloquinoline quinone (PQQ)) and a modified flavin adenine dinucleotide (FAD) co-factor [3]. This procedure should ensure a proper enzyme orientation for electrical communication between GOx and the electrode surface. It has also been successfully applied for construction of enzymatic electrodes comprising PQQ-boronic acid-FAD assembly [7], FAD-functionalized Au nanoparticles [8] and FAD-functionalized carbon nanotubes [9]. Unlike GOx, CDH exhibits dual electron transfer mechanism, direct (DET) via heme and MET via FAD [10].

The two types of enzyme-modified HSAG electrodes, RG-GOx and GNP-CDH, prepared as described in the experimental part of the paper, showed very high electrocatalytic activity towards glucose oxidation (RG-GOx and GNP-CDH), as well as lactose and cellobiose oxidation (CDH-GNP) (Fig. 1). The onset of glucose oxidation, coinciding with PQQ redox peak (see Supporting Information) and the presence of one oxidation wave in the case of RG-GOx (Figure 1a) are in very good agreement with previously reported results [3]. Contrary to GOx, CDH is able to oxidize various sugars, thus, in addition to glucose, electrooxidation of lactose and cellobiose was also observed. The GNP-CDH electrodes showed electrocatalytic activity for oxidation of different substrates. The addition of the inhibitor 3-amino-1,2,4-triazole (ATZ) suppressed the activity (Figure 1b).

As discussed above, CDH exhibits DET and MET and in the present configuration a DET mechanism should be expected. Theoretically, the oxidation onset should be de-

pendent only on the redox potential of the heme group of the enzyme and it should be substrate insensitive [11]. However, different onset potentials for different sugars were found in our studies. Moreover, instead of the limiting currents, which are usually characteristic for cyclic voltammetry experiments in the absence of mass transfer limitations, peaks were observed (Figure 1b). Well defined peaks were also observed in the case of RG-GOx electrode, even at very low sweep rates, suggesting that substrate depletion is not responsible for the electrochemical behavior of the RG-GOx electrode (Figure 1a).

It is widely accepted that gold surfaces are able to catalyze the oxidation of different sugars including glucose [12] and cellobiose [13]. The onset potential for glucose oxidation and the number of peaks are correlated with formation of AuOH species and the sharp current decrease at more positive potentials is attributed to oxide formation [12b].

In order to clarify the origin of oxidation activity, further experiments were performed on smooth gold, bare and SAM-modified HSAG electrodes (in case of RG activities of PQQ and FAD functionalized surfaces were also checked). As can be seen in Figure 2a, smooth gold appears relatively featureless with low current intensities and low activity for glucose oxidation at 37 °C. If the electrode was electrochemically (EC) activated by potential cycling extended to the region of oxide formation, the activity was enhanced resembling the behavior of alumina polished gold at room temperature [12a].

Similar to EC activated smooth gold, RG shows high activity towards glucose oxidation at room temperature, but quite low activity at 37 °C (Figure 2b). The loss of activity could be ascribed to some kind of surface restructuring, which was also evidenced by change of voltammetric features [14]. EC activation restores catalytic activity and voltammetric behavior of freshly prepared RG (Figure 2b).

Cystamine-modified RG exhibits high activity toward glucose oxidation even at 37 °C, which was ascribed to exposed Au(111) domains [14]. Similar to RG/SAM, RG surfaces functionalized by PQQ, FAD and GOx, exhibit electrocatalytic activity toward glucose oxidation (Figure 3a) but the addition of further organic layers decreases the activity, shifting the oxidation onset to more positive potentials and decreasing the peak intensity. For example, cystamine-modified RG shows an oxidation onset at about −0.3 V vs. SCE and peak current density of approximately 400 µA cm^{-2}, while the cystamine-PQQ-FAD-GOx modified RG had an oxidation onset at about −0.17 V vs. SCE and peak current density of approximately 70 µA cm^{-2}.

Analogous to RG, GNP electrodes show high activity toward lactose oxidation (Figure 3b). If the electrode is modified by mercaptopropionic acid (MPA) its activity is preserved with onset potentials shifted to more positive values. This fact indicates that the SAM on the GNP surface is not compact and some exposed regions remain catalytically active. The adsorption of CDH decreases the

activity, in all likelihood, due to blocking of the metal active sites by proteins.

Based on the results shown above, we can conclude that the largest part of the electrocatalytic activity of enzyme-modified HSAG electrodes toward different sugars comes from the underlying gold surface. This implies that in previous studies [3], in which similar procedure for enzyme immobilization was used, direct glucose oxidation on the gold surface might also occur. These findings are of specific importance for bioelectrochemical studies of enzymatic electrodes, where the immobilization support might show electrocatalytic properties toward the substrates of investigated enzymes. For instance, even suppression of activity by specific inhibitors of the enzyme is not an unambiguous proof of bioelectrocatalytic origin of the obtained current. Indeed, many different possibilities for electrocatalysis should be taken into account, including reactions occurring on the supporting layers of the designed bioelectrodes. From the point of
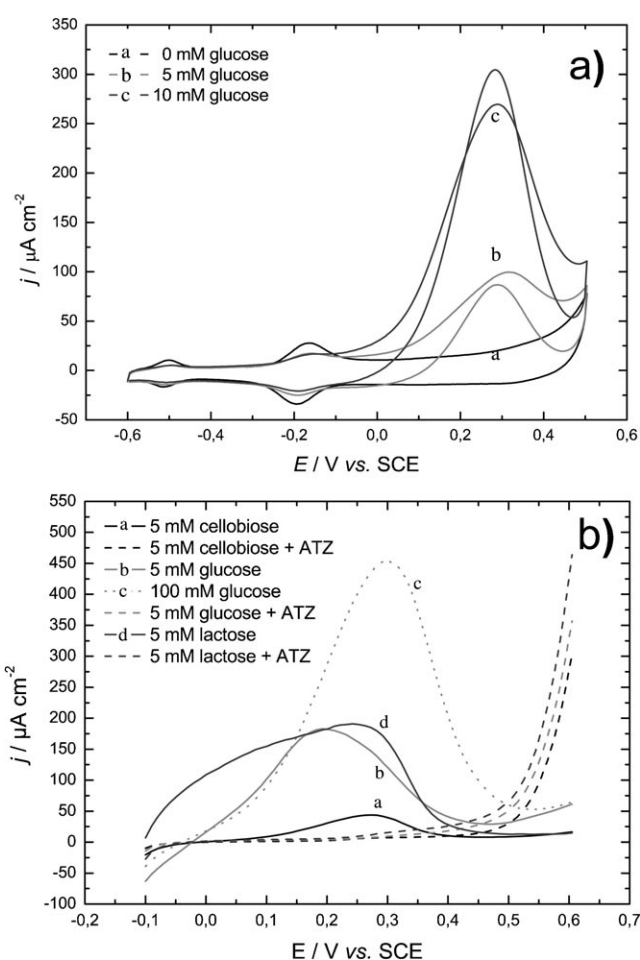

Fig. 1. a) Cyclic voltammograms of the RG-GOx electrode showing glucose oxidation activity. Conditions: 0.1 M phosphate buffer, pH 7.2, 37 °C, scan rate: 20 mV s^{-1}; b) Cyclic voltammograms (only forward scans) of the GNP-CDH electrode showing activity for oxidation of different sugars. Conditions: 0.05 M universal buffer, pH 7.4, room temperature, scan rate: 10 mV s^{-1} (50 mM of ATZ was added as CDH inhibitor).
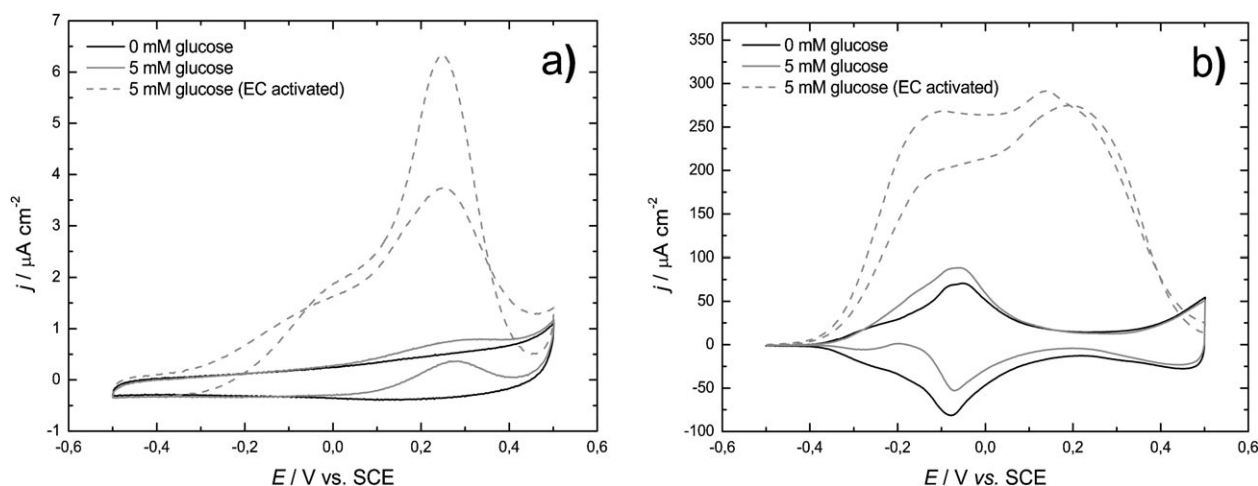
Fig. 2. Cyclic voltammograms of a) smooth gold and b) rough gold, showing activity for glucose oxidation. Conditions: 0.1 M phosphate buffer, pH 7.2, 37 °C, scan rate: 5 mV s^{-1}.
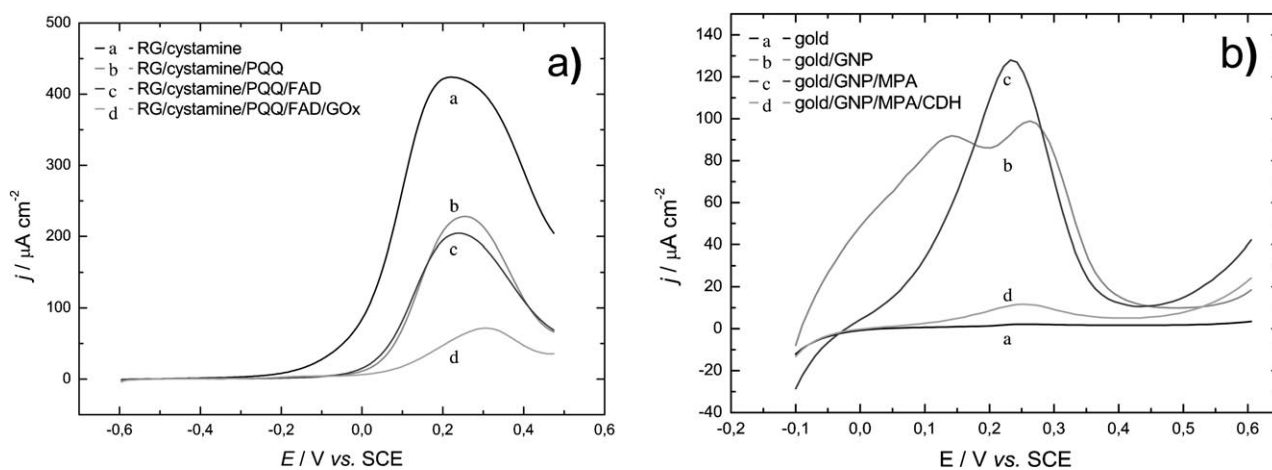

Fig. 3. Cyclic voltammograms (only forward scans) of a) RG modified with different layers in presence of 5 mM glucose. Conditions: 0.1 M phosphate buffer, pH 7.2, 37 °C, scan rate: 5 mV s^{-1}; b) GNP modified with different layers in presence of 5 mM lactose. Conditions: 0.05 M universal buffer, pH 7.4, room temperature, scan rate: 10 mV s^{-1}.

view of practical applications our results show the general possibility of efficient direct oxidation of different sugars on SAM modified high surface area gold electrodes, which could be useful for sensors and fuel cell technologies.

Experimental

Polycrystalline gold wires (0.5 mm diameter, 0.47 cm^{-2} working area) used for preparation of RG were supplied by Aldrich. RG was prepared by the reported amalgamation method [12a, 15]. The RG-GOx electrode was modified according to Willner et al. [3]. Gold nanoparticles were prepared according to the procedure described by Frens [16] and the GNP electrode was prepared according to Murata et al. [17]. More detailed information about the preparation of the enzymatic electrodes, including voltammetric characterization of the RG-GOx modi-

fication can be found in the Supporting Information. GOx from *Aspergillus niger* (198 U mg^{-1} activity as stated on the label), FAD and PQQ were supplied by Sigma. Apo-GOx was prepared according to the procedure described by Swoboda [18]. N^6-(2-aminoethyl)-FAD was synthesized in accordance to Bückmann [19]. Cellobiose dehydrogenase from *Myriococcum thermophilum* was kindly provided by Dr. Roland Ludwig (University of Natural Resources and Life Sciences, Vienna, Austria) in the frame of collaborative FP7 EU Project "3D-Nano-Biodevice". Sodium citrate-2-hydrate and lactose were supplied by Kebo AB (Stockholm, Sweden). All other chemicals were of analytical reagent grade and purchased from Sigma-Aldrich. Deionized water was used in all experiments.

Electrochemical experiments were carried out in a three-electrode electrochemical cell with saturated calomel electrode (SCE) as a reference electrode by the use of potentiostat PGSTAT302 or microAutolabIII/FRA2

(Autolab, Netherlands). The experimental solutions were thoroughly deoxygenated with nitrogen to prevent possible interferences of oxygen with the gold support and GOx. Measurements were performed at pH 7.4 in 0.05 M universal buffer (50 mM of phosphoric acid, boric acid and acetic acid adjusting pH with sodium hydroxide) in case of GNP-CDH electrode or at pH 7.2 in 0.1 M phosphate buffer in case of RG-GOx electrode.

Acknowledgements

References

[1] I. Willner, E. Katz, *Angew. Chem. Int. Ed.* **2000**, *39*, 1180.

[2] J. J. Gooding, F. Mearns, W. R. Yang, J. Q. Liu, *Electroanalysis* **2003**, *15*, 81.

[3] a) E. Katz, A. Riklin, V. Heleg-Shabtai, I. Willner, A. F. Buckmann, *Anal. Chim. Acta* **1999**, *385*, 45; b) I. Willner, V. Heleg-Shabtai, R. Blonder, E. Katz, G. L. Tao, A. F. Buckmann, A. Heller, *J. Am. Chem. Soc.* **1996**, *118*, 10321.

[4] M. Dagys, K. Haberska, S. Shleev, T. Arnebrant, J. Kulys, T. Ruzgas, *Electrochem. Commun.* **2010**, *12*, 933.

[5] N. K. Chaki, K. Vijayamohanan, *Biosens. Bioelectron.* **2002**, *17*, 1.

[6] I. Ivanov, T. Vidakovic-Koch, K. Sundmacher, *Energies* **2010**, *3*, 803.

[7] M. Zayats, E. Katz, I. Willner, *J. Am. Chem. Soc.* **2002**, *124*, 2120.

[8] Y. Xiao, F. Patolsky, E. Katz, J. F. Hainfeld, I. Willner, *Science* **2003**, *299*, 1877.

[9] F. Patolsky, Y. Weizmann, I. Willner, *Angew. Chem. Int. Ed.* **2004**, *43*, 2113.

[10] R. Ludwig, W. Harreither, F. Tasca, L. Gorton, *ChemPhysChem* **2010**, *11*, 2674.

[11] V. Coman, C. Vaz-Dominguez, R. Ludwig, W. Herreither, D. Haltrich, A. L. De Lacey, T. Ruzgas, L. Gorton, S. Shleev, *Phys. Chem. Chem. Phys.* **2008**, *10*, 6093.

[12] a) S. Cho, H. Shin, C. Kang, *Electrochim. Acta* **2006**, *51*, 3781; b) M. W. Hsiao, R. R. Adzic, E. B. Yeager, *J. Electrochem. Soc.* **1996**, *143*, 759.

[13] P. Parpot, V. P. Muiuane, V. Defontaine, A. P. Bettencourt, *Electrochim. Acta* **2010**, *55*, 3157.

[14] I. Ivanov, T. R. Vidakovic and K. Sundmacher, *Electrochem. Commun.* **2008**, *10*, 1307.

[15] E. Katz, D. D. Schlereth, H. L. Schmidt, *J. Electroanal. Chem.* **1994**, *367*, 59.

[16] G. Frens, *Nature Phys. Sci.* **1973**, *241*, 20.

[17] K. Murata, K. Kajiya, M. Nukaga, Y. Suga, T. Watanabe, N. Nakamura, H. Ohno, *Electroanalysis* **2010**, *22*, 185.

[18] B. E. P. Swoboda, *Biochim. Biophys. Acta* **1969**, *175*, 365.

[19] A. F. Bückmann, V. Wray, A. Stocker, in *Synthesis of N-6-(2-aminoethyl)-FAD, N-6-(6-carboxyhexyl)-FAD, and Related Compounds*, Vol. 280, Academic Press, San Diego, **1997**, pp. 360–374.

[TVK2]

I. Ivanov, T.R. Vidaković-Koch, K. Sundmacher

Direct hybrid glucose-oxygen enzymatic fuel cell based on tetrathiafulvalene-tetracyanoquinodimethane charge transfer complex as anodic mediator

Direct hybrid glucose–oxygen enzymatic fuel cell based on tetrathiafulvalene–tetracyanoquinodimethane charge transfer complex as anodic mediator

Ivan Ivanov [a], Tanja Vidaković-Koch [a,*], Kai Sundmacher [a,b]

[a] *Process Systems Engineering, Otto-von-Guericke University Magdeburg, Universitätsplatz 2, 39106 Magdeburg, Germany*
[b] *Max Planck Institute for Dynamics of Complex Technical Systems, Sandtorstrasse 1, 39106 Magdeburg, Germany*

ARTICLE INFO

ABSTRACT

TTF–TCNQ has been used for the first time as a mediator in a direct glucose fuel cell operating on gas-phase oxygen. It has been shown that TTF–TCNQ forms highly irregular porous structure, which emphasizes the importance of optimization of mass transport and kinetic resistance in the catalyst layer. Kinetics resistance can be optimized by variation of the mediator and/or enzyme loading, while mass transport resistance mainly by the variation of other structural parameters such as electrode thickness. The optimized anode reached limiting current densities of nearly $400\,\mu\text{A}\,\text{cm}^{-2}$ in presence of 5 mM glucose under rotation. The enzymatic fuel cell exhibited unexpectedly high OCV values (up to 0.99 V), which were tentatively ascribed to different pH conditions at the anode and the cathode. OCV was influenced by glucose crossover and was decreasing with an increase of glucose concentration or flow rate. Although the performance of the fuel cell is limited by the enzymatic anode, the long-term stability of the fuel cell is mainly influenced by the Pt cathode, while the enzymatic anode has higher stability. The fuel cell delivered power densities up to $120\,\mu\text{W}\,\text{cm}^{-2}$ in presence of 5 mM glucose, depending on the glucose flow rate.

1. Introduction

Enzymatic fuel cells belong to the group of biofuel cells. The characteristic feature of this fuel cell type is the application of enzymes (biocatalysts) instead of noble metal catalysts. Enzymatic fuel cells are a promising type of fuel cells for niche applications, which benefit from the utilization of enzymes as highly efficient natural catalysts. Advantages of enzymes include activity at mild conditions, lower price and substrate selectivity, which can theoretically enable a membraneless design [1]. The utilization of biocatalysts offers larger number of possible fuels and oxidants as natural substrates of the respective enzymes. The typical fuel in enzymatic biofuel cells is glucose [1] but other sugars, such as fructose [2] and lactose [3], as well as lower aliphatic alcohols, such as ethanol [4] and glycerol [5] have been also used. Contrary to the variety of fuel types, oxygen is almost exclusively used as an oxidant in biofuel cells [1]. Glucose–oxygen enzymatic biofuel cells are promising as power sources for implantable devices [6]. Major drawbacks of these systems are the still low power output and the limited stability.

The enzymes that are employed in this type of fuel cells are called oxidoreductases and catalyze oxidation and reduction processes involving transport of electrons. Oxidoreductases can be coupled with the electrode surface, thus forming enzymatic electrodes, and the electron transfer process can be followed by different electrochemical methods. To construct a biofuel cell system based on redox enzymes, the following points have to be considered: (1) enzyme immobilization; (2) communication between the enzyme and the electrode surface (type of electron transfer); (3) enzyme kinetics; (4) enzymatic electrode architecture; (5) coupling of the electrodes and design of the overall system. The first three points have been extensively studied in the past, mainly regarding the application of these systems as amperometric biosensors. As a result of these activities many preparation methods for enzymatic electrodes can be found in literature. However, only few of them can be employed in systems, where energy production is the main application.

Some examples of mediators in enzymatic electrodes, which have found an application in glucose biofuel cells are ferrocene [7], tetrathiafulvalene (TTF) [8], 8-hydroxyquinoline-5-sulfonic acid (HQS) [9] and Os redox hydrogels [10]. So far, the best performance exhibit Os hydrogels with redox centers attached to a polymer backbone [1]. However, the procedure of synthesizing Os redox hydrogels is usually complicated and involves several steps [11].

* Corresponding author. Tel.: +49 391 6110 319; fax: +49 391 6110 553.
  E-mail address: vidakovi@mpi-magdeburg.mpg.de (T. Vidaković-Koch).

In addition, in respect to the application of enzymatic biofuel cells as implantable power sources, some issues, associated with the toxicity of Os-containing compounds may arise [12]. Another type of mediator, which in our opinion has a great promise for biofuel cell application is the charge transfer complex (CTC) known as organic conductive salt, based on tetrathiafulvalene and tetracyanoquinodimethane (TTF–TCNQ). This complex has been so far mainly used as a mediator in enzymatic electrodes for biosensor applications as outlined in a recent review [13]. Glucose biosensors based on TTF–TCNQ exhibit high current densities, high oxygen tolerance and remarkable stability under continuous operation [14,15]. Khan et al. have shown that glucose biosensors based on TTF–TCNQ can retain up to 40% of their initial response after 100 days of continuous operation and exhibit low sensitivity to the oxygen in normal buffer solutions [14]. However, despite these promising features, TTF–TCNQ anode, to our best knowledge, has not been employed in an enzymatic fuel cell so far. In addition, CTC has several other advantages. Enzymatic electrodes based on TTF–TCNQ do not require complicated modification procedures, in fact they can be prepared as simply as carbon paste electrodes by mixing of the respective components [16]. The TTF–TCNQ salt is commercially available and has high electronic conductivity, which is beneficial for lowering the ohmic resistance within the electrode layer. The morphology of the CTC-crystals can be tuned by variation of the experimental conditions [17]. They can be also prepared in form of nanoparticles [18]. These strategies can be applied to tune the catalytic properties of the CTC and/or to increase the catalytically active surface area. Both TTF and TCNQ have low toxicity, which is attributed to their low solubility in water and physiological fluids [19]. In addition, the catalytic properties of the CTC and the overpotential for glucose oxidation can be further improved by lowering of the redox potentials of its components, e.g. of TTF [20].

To construct an enzymatic electrode for a biofuel cell application the electrode architecture has to be carefully designed and optimized. In the case of enzymes the number of active sites per volume is generally lower than in the case of noble metal electrodes, which issue is crucial in the case of energy-producing systems. This motivates the use of three-dimensional electrode structures instead of monolayer or thin layer configurations [1]. Depending on the type of electron transfer (mediated or direct), a complex network between the enzyme, the mediator and the electron conductive surface has to be established. To tackle experimentally this issue, the influence of the loadings of the respective components in the catalyst layer (composition) and the overall electrode architecture has to be studied, which has not been extensively investigated so far.

The next important aspect is the design of the whole fuel cell system. Little emphasis has been put on this issue in the past and most of the studies have been focused on single electrodes studies. In this work a hybrid biofuel cell device, based on the combination of enzymatic anode and a Pt cathode has been developed. The structure of the cathode comprises the membrane electrode assembly (MEA) design, which has been adopted from the conventional fuel cell technology. The operation with gas-phase oxygen compensates the low solubility of oxygen in aqueous solutions. The combination with a noble metal catalyst electrode allows for testing of the enzymatic electrode performance under fuel cell conditions. Similar strategy has been used both for anodes [21–23] and for cathodes [4,5,24]. Such systems have been usually referred to as biofuel cells, despite of the presence of a non-bio component. The fuel cell device in this study can be used as a platform for investigation of different enzymatic anodes and give additional information about their behavior in a whole fuel cell system when combined with a cathode with "known" catalytic properties.

To summarize, in this paper some aspects regarding the development and design of a hybrid enzymatic fuel cell, such as:
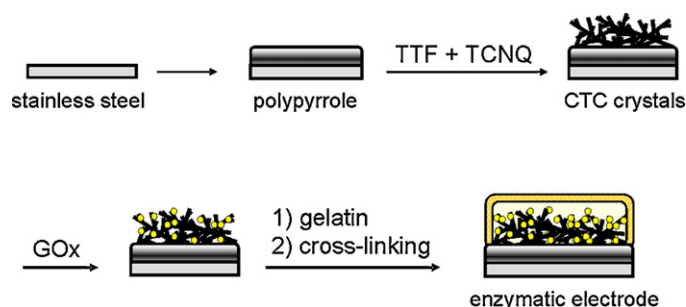

Fig. 1. Schematic presentation of the enzymatic electrode preparation procedure.

(a) the utilization of TTF–TCNQ mediator and the optimization of the three-dimensional electrode structure, (b) anode and cathode coupling and fuel cell design and (c) fuel cell system characterization have been covered.

2. Materials and methods

2.1. Chemicals and materials

Glucose oxidase (EC 1.1.3.4, GOx) from *Aspergillus niger* was supplied by Fluka. All other chemicals including glucose, TTF, TCNQ and polyvinyl sulfate potassium salt (PVS) as well as tetrahydrofuran (THF) and acetonitrile (ACN) were of analytical reagent grade and purchased from Sigma–Aldrich. Ultrapure water from Millipore was used in all experiments.

Stainless steel was used as a mechanical and electrical support for the preparation of enzymatic electrodes. Discs with a diameter of 11 mm and 1 mm thickness were used in the case of single electrode experiments (three-electrode set-up). The discs were mounted in a sample holder for rotating disc electrode (RDE) with an opening of 8 mm (0.5 cm^2 working area) for the electropolymerization and an opening of 6 mm (0.28 cm^2 working area) for the electrochemical tests. In case of the fuel cell tests (two-electrode set-up), discs with a diameter of 24 mm and 2 mm thickness were used. The surface of the disc was masked by adhesive tape in such a way that a square opening with dimensions of 10 mm × 10 mm (1 cm^{-2} working area) was left exposed.

Nafion 117 was used for the preparation of the MEA. The cathode catalyst ink was based on Platinum Black (Alfa Aesar) and aqueous Nafion solution (Pt:Nafion = 9:1).

2.2. Enzymatic electrode preparation

The enzymatic electrode preparation procedure was similar to the procedure reported by Khan et al. [14] and had several steps, which are schematically presented in Fig. 1. The stainless steel discs were polished with emery paper and degreased with acetone before further modification. In the first step, a polypyrrole film was electrochemically deposited on the stainless steel surface. The electropolymerization was done galvanostatically at a current density of 4 mA cm^{-2} until a charge of 1.2 C cm^{-2} passed. The aqueous monomer solution contained 0.02 M (per monomer molecular weight) PVS and 0.15 M pyrrole. The solution was agitated by the RDE (for 11 mm discs) or a magnetic stirrer (for 24 mm discs). No attempts to exclude oxygen from the system during the electropolymerization were made.

In the next step, CTC crystals were grown directly on the polymer surface. First, TCNQ dissolved in THF was cast several times on the electrode until the desired loading was achieved. After that, TTF dissolved in ACN was applied in several successive steps over the TCNQ layer until TTF loading of slight excess compared to the TCNQ loading was obtained. The electrode was then gently washed with
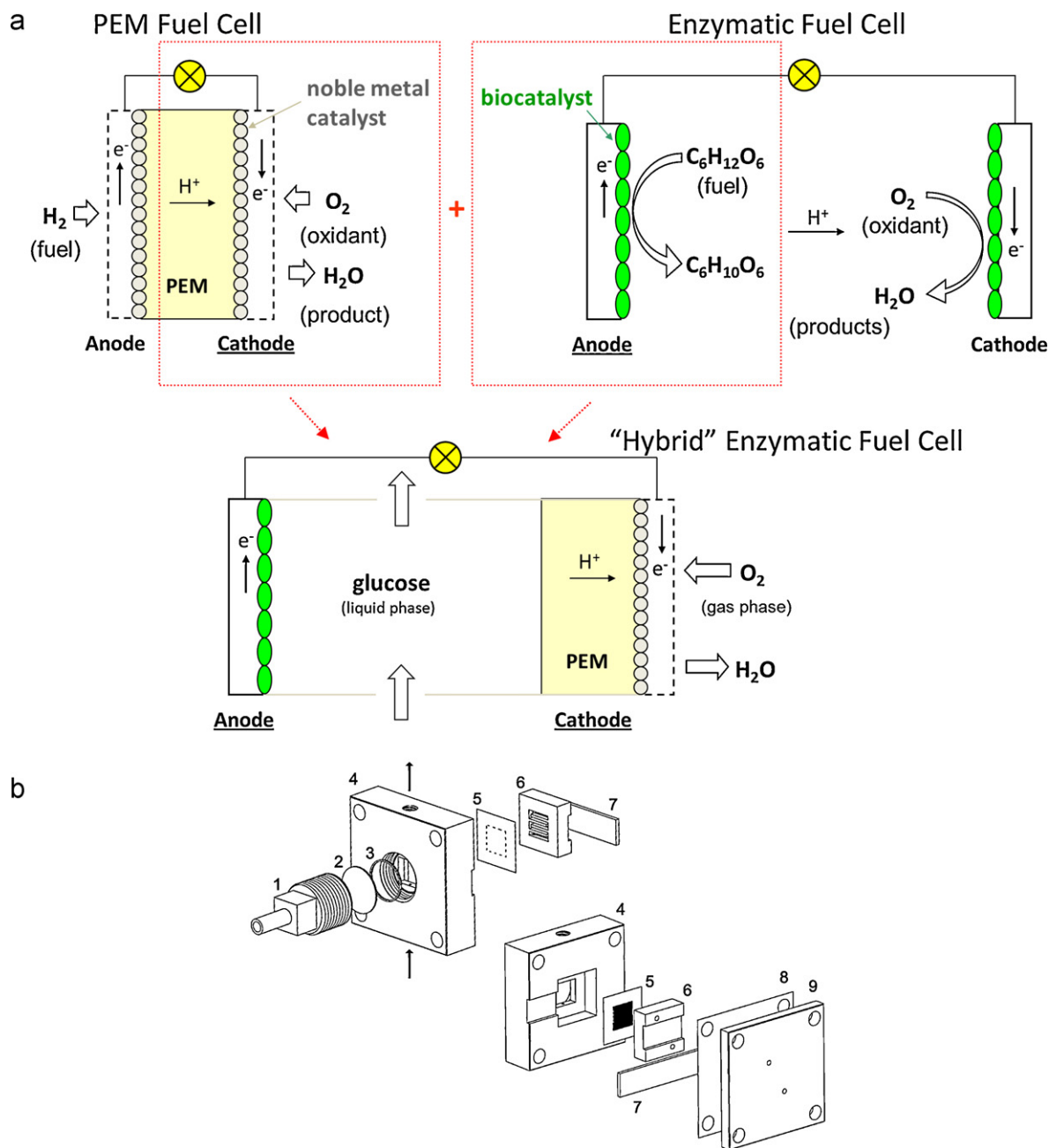
Fig. 2. (a) Schematic presentation of the concept of the hybrid enzymatic fuel cell; (b) an exploded drawing of the fuel cell device with components denoted as follows: 1 – anode current collector, 2 – stainless steel disc with enzymatic catalyst (enzymatic electrode), 3 – O-ring, 4 – cell body, 5 – MEA, 6 – graphite flow-field, 7 – cathode current collector, 8 – PTFE gasket, and 9 – end plate.

ACN in order to remove the unreacted TTF and dried under ambient conditions. After that GOx was adsorbed on the CTC crystals by applying an aliquot of 20 mg ml^{-1} GOx solution in phosphate buffer (pH 7.2) and the electrode was left to dry. Subsequently, the CTC/GOx assembly was covered by an aliquot of gelatin solution (2.5%, w/v in water, incubated for 30 min at 30 °C before use) and dried again.

Finally, the electrode assembly was cross-linked by dipping into a glutaraldehyde solution (5% in water) for 60 s, washed with plenty of water and dried at room temperature. The enzymatic electrodes were kept in plastic bags at −20 °C before use. Cross-sectional scanning electron microscopy (SEM) analysis of the enzymatic electrode assembly was performed by AQura GmbH, Germany using XL30 FEG (FEI Company).

2.3. MEA preparation and fuel cell construction

The MEA's were prepared in-house by spray-painting of the catalyst ink on one of the sides of a Nafion membrane until a loading of approximately 5 mg cm^{-2} was achieved. The projected catalyst area had a square shape with dimensions 10 mm × 10 mm (1 cm^{-2} working area, corresponding to the anode working area). After that the MEA's were sintered at 135 °C for 30 min and left to cool down.

The concept of the hybrid enzymatic fuel cell presented in this study, which is based on the coupling of a bioanode and a Pt cathode is shown schematically in Fig. 2a. It should be noted that the term "hybrid" when referred to a fuel cell, is mainly associated with the combination of two power sources with different operational principles (e.g. fuel cell and battery). However, this term can be

also used to denote the different nature of catalysts (e.g. biological catalyst at the anode and an inorganic catalyst at the cathode as in the present case) as discussed in [1]. Three-dimensional drawing of the resulting device and its components is shown in Fig. 2b. The cell body was transparent and made out of Makrolon (Bayer). The stainless steel disc covered with anodic catalyst was fixed to the cell body by the anode current collector and sealed by an O-ring. The MEA was placed on the opposite side of the cell body with the bare side of the membrane facing the anodic compartment. A graphite plate with a flow-field was used for gas distribution and a gold-coated copper plate served as a cathode current collector. The cathode components were clamped together and sealed by a poly-tetrafluoroethylene (PTFE) gasket and an end plate, which ensured leak tightness and good electrical contact in the whole assembly. In some cases cellophane P00 (Innovia Films) was used as a separator between the MEA and the anodic compartment (not shown in Fig. 2b).

The fuel cell was mounted vertically in a holder in such a way that the fuel solution was flowing upwards through the cell (see arrows indicating flow direction in Fig. 2b), whereby the perfusion flow was sustained by a peristaltic pump. The cell was connected to a fuel reservoir, equipped with a temperature control and gas supplies to allow for operation with nitrogen- or oxygen-saturated media. The fuel solution was 0.1 M phosphate buffer with different glucose concentrations. The cathode was fed with dry oxygen at a flow rate of ca. 500 ml min^{-1}.

2.4. Electrochemical experiments

Single electrode experiments were carried out in a conventional double-jacketed Pyrex electrochemical cell (Radiometer Analytical). The RDE was used as a working electrode, platinum wire as a counter electrode, and saturated calomel electrode (SCE) as a reference electrode. The experimental solutions were saturated with nitrogen or oxygen. Electrochemical single electrode and fuel cell experiments were performed by a computer controlled potentiostat PGSTAT302 (Eco Chemie/Autolab). In case of fuel cell experiments, before measurements, the cell was left to equilibrate with constant flow of reactants until a stable open circuit voltage (OCV) value was obtained. The data for polarization curves have been extracted from transient measurements after 2 min at constant voltage.

3. Results and discussion

3.1. Optimization of the electrode architecture

3.1.1. Enzymatic electrode characterization with SEM

A SEM image of the enzymatic electrode assembly cross section, peeled off from the stainless steel support, is shown in Fig. 3. Three layers can be clearly distinguished and the thickness of every layer has been estimated from the micrograph as follows: 2 μm polypyrrole layer, 60 μm catalyst layer, composed of CTC crystals with adsorbed GOx, and 5 μm gelatin layer. As can be seen in Fig. 3 the catalyst layer of the enzymatic electrode is characterized by randomly distributed CTC bundles and cavities, forming a highly irregular porous structure, which serves as a matrix for enzyme immobilization. According to previous reports, this matrix was described as a standing highly branched tree-like structure emerging from the polymer layer with a size of 40–50 μm [14,15]. This presentation seems to be unrealistic taking into account the present results for electrodes with similar CTC loading. SEM observations in the present case did not indicate CTC crystals penetrating the polypyrrole layer as reported in [15] or structures, vertically standing on the electrode surface [14]. Another important observation is
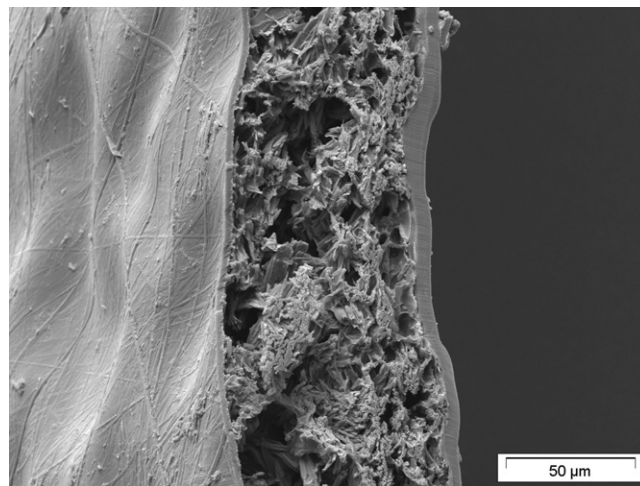

Fig. 3. A SEM image of the enzymatic electrode cross-sectional view.

that unlike the previously reported presentation of gelatin, penetrating the CTC crystals and stabilizing the respective structure, the gelatin layer in the present case penetrates little in the catalyst layer and forms a well-defined membrane on top. This will influence the transport properties of the catalyst layer, which has significance especially for further modeling of the enzymatic electrode.

3.1.2. Cyclic voltammetry characterization of the enzymatic electrodes

The electrochemical behavior of the enzymatic electrode has been studied between −0.2 and 0.2 V vs. SCE in 0.1 M phosphate buffer (pH 7.2), since this potential region is regarded as "stable", where no CTC decomposition occurs [25]. Representative cyclic voltammograms of the bioanode in presence of different glucose concentrations are shown in Fig. 4a. As can be seen, despite the low sweep rate, large capacitive currents, exceeding the reaction currents, are observed. According to experiments with electrodes lacking polypyrrole, the pronounced capacitive behavior should be ascribed to the underlying polymer surface and not to the high surface area of the CTC crystals or to the underlying stainless steel support, as shown in Fig. 4b (note the axis scales). Similar voltammetric behavior exhibiting large capacitive currents has been reported by Pauliukaite et al. in the case of a TTF–TCNQ-based biosensor for determination of glutamate [16]. The base voltammograms in absence of glucose indicate some oxidative process occurring at the stainless steel surface at more positive potentials (Fig. 4b) but the associated currents are negligible compared to the currents due to glucose oxidation. As can be seen in Fig. 4a the bioanode exhibits activity for glucose oxidation and the currents increase with substrate concentration. Maximum current in presence of 5 mM glucose reaches ca. 110 μA (corrected for the background current), which corresponds to nearly 400 μA cm^{-2} current density. The open circuit potential of the enzymatic electrodes after equilibration in the electrochemical cell under rotation in presence of glucose was typically around −0.2 V vs. SCE, while as can be seen in Fig. 4a the oxidation onset observed in the positive scans is at ca. −0.1 V vs. SCE. In general, the onset potential for the glucose oxidation reaction is mainly related to the type of mediator used in the system, which can be immobilized on the electrode or dissolved in the electrolyte. As it has been recently discussed, electrode systems with dissolved mediators are not appropriate for biofuel cell applications [1]. Some typical values for the glucose oxidation onset potentials in the case of enzymatic anodes with immobilized enzymes and mediators, which have been successfully employed in biofuel cells, are ca. 0 V vs. SCE in presence of
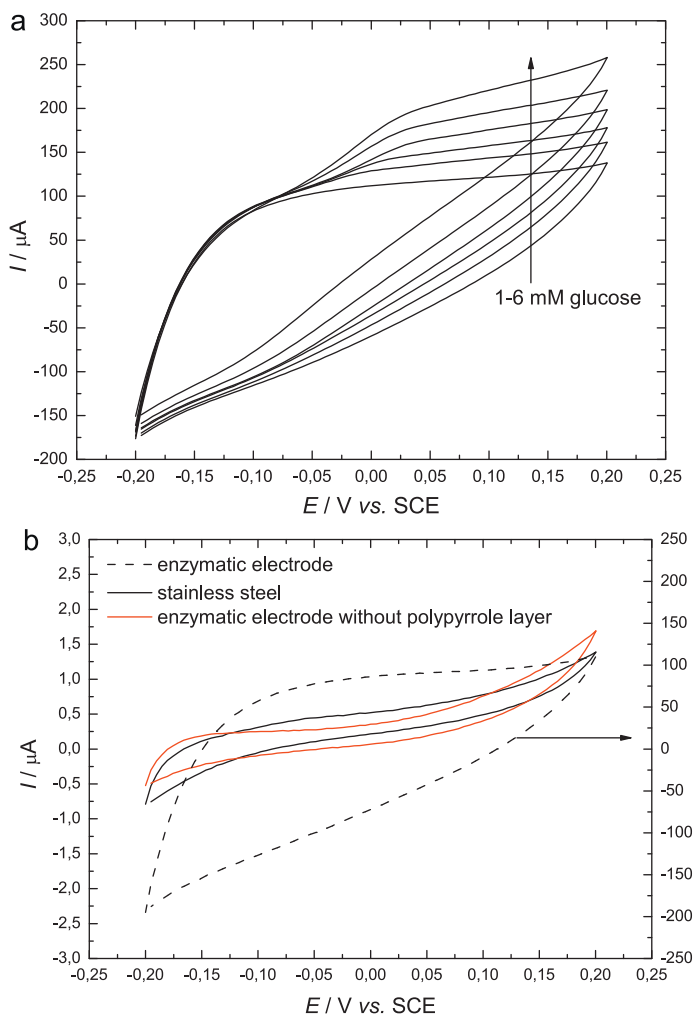
Fig. 4. Cyclic voltammograms of (a) the enzymatic electrode in presence of different glucose concentrations (1–6 mM); (b) the enzymatic electrode, stainless steel support and enzymatic electrode lacking the polypyrrole layer in absence of glucose. Conditions: 0.1 M phosphate buffer, pH 7.2, 37 °C, 400 rpm, N$_2$ atmosphere, sweep rate: 5 mV s^{-1}.

60 mM glucose for a ferrocene-based mediator [26], between ca. −0.1 and 0 V vs. SCE in presence of 20 mM glucose for electrodes based on TTF [27,28] and ca. −0.4 V vs. SCE at 15 mM glucose for an Os hydrogel [11]. The CTC-based electrode in the present work shows 100 mV more negative onset potential than the electrodes based on ferrocene and similar value to TTF, while it is clearly outreached by the Os-based mediator. However, as already discussed, the present system offers some other advantages.

3.1.3. Influence of the CTC, GOx and gelatin loadings

As already shown in Fig. 3 the catalyst layer has a highly irregular porous structure and it can be anticipated that the enzyme distribution within this layer will have significant effect on the activity of the enzymatic electrode. To optimize the performance of the electrode, the ratio between CTC and GOx has been varied in a systematic way. In addition the influence of the thickness of the gelatin layer has been also checked.

The concentration dependencies of the current at 0.2 V vs. SCE (corrected for the background current) of two enzymatic electrodes with different CTC loadings are shown in Fig. 5a. The CTC loading was found to have a minor influence at lower glucose concentrations and higher impact at higher glucose concentrations, shifting the currents at 30 mM glucose from ca. 150 μA for 1 mg cm^{-2} CTC to
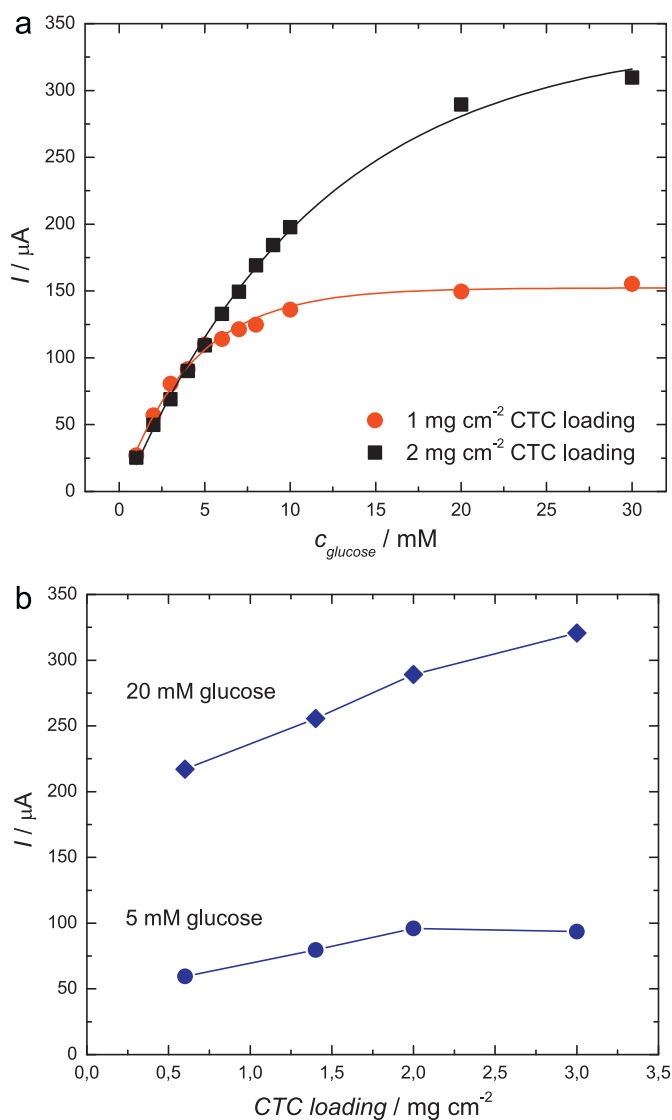

Fig. 5. (a) Concentration dependence of the current at 0.2 V vs. SCE (corrected for the background current) for two enzymatic electrodes with different CTC loadings; (b) dependence of the current at 0.2 V vs. SCE (corrected for the background current) in presence of 5 mM and 20 mM glucose on the CTC loading. Data extracted from cyclic voltammetry. Conditions for the cyclic voltammetry experiments similar as in Fig. 4.

ca. 310 μA for 2 mg cm^{-2} CTC. Also, the linear region in the concentration dependence was extended with an increase of the loading.

The influence of the CTC loading has been additionally investigated and the dependencies of the limiting currents at 5 and 20 mM glucose are presented in Fig. 5b. 5 mM glucose has been chosen as the operational concentration of interest (normal glucose concentration in the human body) and 20 mM has been chosen as a concentration, close to saturation. As can be seen, at 5 mM a CTC loading, higher than 2 mg cm^{-2} does not influence the current output anymore, while at 20 mM the current increases in the whole investigated range. Based on the current results, 2 mg cm^{-2} has been chosen as the optimum CTC loading for further tests in presence of 5 mM glucose. Similar investigation of the influence of CTC loading has been presented in a previous work, where the authors reported an optimum value of about 2 mg cm^{-2} for the CTC loading [14]. It should be noted that in the latter case the electrode modification procedure involved adsorption of the enzyme on the CTC crystals and subsequent removal of the excess enzyme solution. This implies a combined effect of both loadings, whereby the
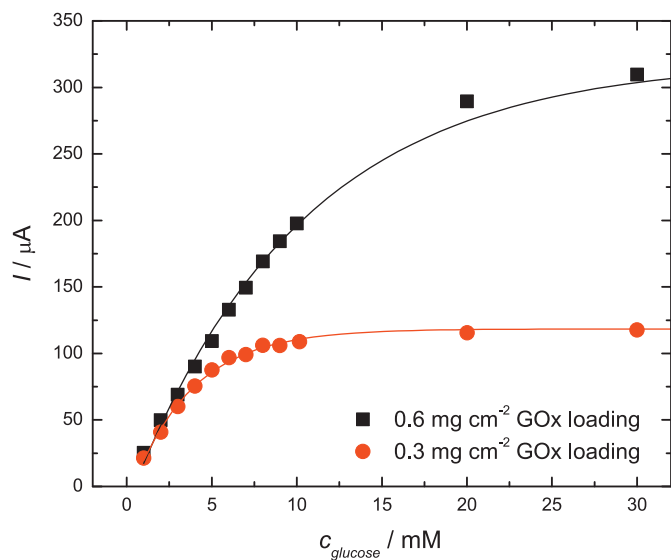
Fig. 6. Concentration dependence of the current at 0.2 V vs. SCE (corrected for the background current) for two enzymatic electrodes with different GOx loadings. Data extracted from cyclic voltammetry. Conditions for the cyclic voltammetry experiments similar as in Fig. 4.
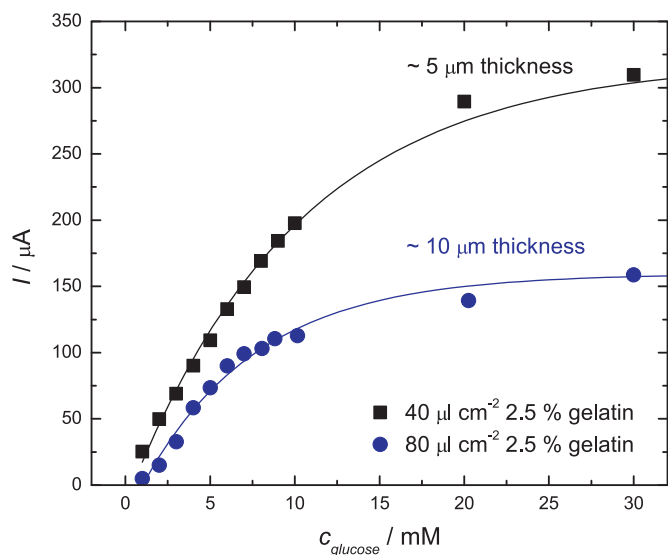

Fig. 7. Concentration dependence of the current at 0.2 V vs. SCE (corrected for the background current) for two enzymatic electrodes with different gelatin loadings. Data extracted from cyclic voltammetry. Conditions for the cyclic voltammetry experiments similar as in Fig. 4.
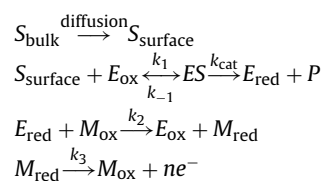
amount of adsorbed GOx increases with the CTC loading (shown by spectrophotometric measurements) and restricts the discrimination between both effects. In the latter work the authors reported also mechanical instability of the crystal structure by loadings higher than 2 mg cm^{-2}, which was not observed in the present case.

The influence of the GOx loading on the anode performance in the present study has been tested at constant CTC loading. The effect is similar to the effect observed in the case of CTC (Fig. 6). Decreasing the GOx loading twice suppresses the currents at higher glucose concentrations, decreases the linear region and shifts the saturation concentration to lower values (ca. 10 mM).

In a similar manner, the gelatin loading has been varied by keeping the other two structural parameters constant. Doubling of the gelatin loading decreases the currents as can be seen in Fig. 7. The current decrease is more pronounced at higher glucose concentrations but the relative current ratio is approximately 60%

in the whole concentration range. This effect has been ascribed to limited mass transport of glucose through the gelatin layer. Such change in the concentration dependence with an increase of the thickness was reported also in the case of polysiloxane membranes [29].

The influence of the investigated structural parameters on the bioelectrode response can be interpreted in terms of the mechanism of enzymatic glucose oxidation. Previous studies regarding electrode with a similar architecture assumed direct regeneration of the reduced enzyme at the CTC surface and discussed the influence of CTC loading in a rather phenomenological way [14]. Contrary to the latter case, the effects of the investigated structural parameters are discussed in terms of the assumed reaction mechanism. If one considers a mediated electron transfer, the overall oxidation mechanism will be governed by the following equations:

$$S_{bulk} \xrightarrow{\text{diffusion}} S_{surface}$$
$$S_{surface} + E_{ox} \underset{k_{-1}}{\overset{k_1}{\longleftrightarrow}} ES \xrightarrow{k_{cat}} E_{red} + P$$
$$E_{red} + M_{ox} \xrightarrow{k_2} E_{ox} + M_{red}$$
$$M_{red} \xrightarrow{k_3} M_{ox} + ne^-$$

where S is the substrate (glucose), E is the enzyme (GOx), ES is enzyme-substrate complex, P is the product (gluconolactone) and M is the mediator. The oxidized and reduced forms of enzyme and mediator are denoted by the respective index.

According to the literature both TTF and TCNQ can act as mediators for GOx [8,30]. The unique properties of the CTC, including high electrical conductivity and the absence of a redox peak in the catalytically relevant potential region have obstructed the unambiguous clarification of the electron transfer mechanism. Recently, the concept of alternating (involving different species) mediated electron transfer, depending on the applied potential, has been proposed ([13] and reference therein). In general it should be noted that, although important for the sake of better understanding, at this stage the exact identification of the mediator does not influence the conclusions that can be drawn from the experiments shown above.

The sensitivity of the electrode response in the limiting current region on all three investigated parameters suggests a mixed reaction-mass transfer limitation. The change of the gelatin loading effectively changes the thickness of the membrane layer, which increases the mass transfer resistance for glucose transport and decreases the glucose concentration at the electrode surface ($S_{surface}$).

The increase of enzyme loading will increase the rate of the reaction between glucose and enzyme. It can be easily anticipated, even in terms of simple Michelis–Menten kinetics that the increase of the enzyme loading will increase the slope of the concentration dependence in the linear region ($K_M \gg [S]$) and it will change the value of the current response in the limited region ($K_M \ll [S]$), which has been qualitatively observed in the present study (see Fig. 6). The increase of the CTC loading will effectively increase the concentration of the mediator in the catalyst layer, which will lead to increase in the electrode response. At lower substrate concentrations the change of CTC loading has less influence, which means that under these conditions the total reaction rate is not dominated by the enzyme–mediator reaction. At higher substrate concentrations (e.g. 20 mM) the increase of the CTC loading produces the continuous increase of the electrode response.

For further studies in the hybrid fuel cell, the following values for the investigated structural parameters have been used: 2 mg cm^{-2} CTC loading, 0.6 mg cm^{-2} GOx loading and 40 µl cm^{-2} 2.5% gelatin solution, which corresponds to ca. 5 µm thickness.
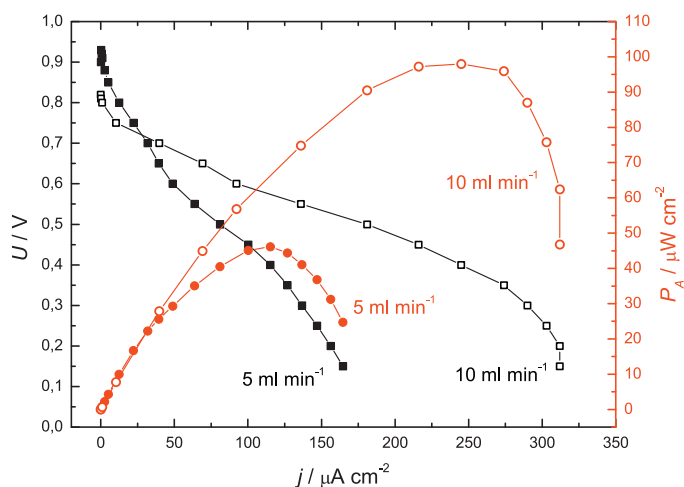
Fig. 8. Polarization (black squares) and power curves (red circles) of the hybrid fuel cell at glucose flow rates of 5 ml min^{-1} (full symbols) and 10 ml min^{-1} (empty symbols). Conditions: anode 5 mM glucose in 0.1 M phosphate buffer, pH 7.2, 37 °C, N$_2$ atmosphere; cathode 500 ml min^{-1} dry oxygen flow rate. Data extracted from transient measurements after 2 min. (For interpretation of the references to color in this figure legend, the reader is referred to the web version of the article.)

3.2. Performance of the hybrid enzymatic fuel cell

The enzymatic fuel cell device, presented in this study comprises a parallel plate design (see Fig. 2a, b). The bioanode operates in liquid phase and the flow-through design of the anodic chamber allows for perfusion of the fuel solution. The continuous flow diminishes substrate depletion and product accumulation and allows for mass transport investigations of the bioanode under fuel cell conditions. In case of a batch operation or when analysis of the oxidation products is required, the flow can be stopped and the anodic chamber can be isolated by closing the inlet and outlet valves.

The cathode operates in gas phase, which allows for overcoming of the limitations associated with the low oxygen solubility in aqueous solutions [31]. The use of pure oxygen instead of air and the high flow rate (500 ml min^{-1}) should eliminate oxygen concentration effects along the flow field channels. The oxygen gas was not humidified due to the fact that the one side of the membrane is in contact with aqueous solution and should be sufficiently hydrated. The high platinum loading (5 mg cm^{-2}) should ensure high cathode performance as it was shown by Reshetenko et al. [32], who studied the influence of cathode optimization on the performance of a direct methanol fuel cell (DMFC).

Polarization and power curves of the enzymatic fuel cell at two different glucose flow rates are shown in Fig. 8. The polarization curve at 5 ml min^{-1} flow rate exhibits a small activation region and an OCV of 0.94 V. Different OCV values for glucose–oxygen biofuel cells have been presented in the literature. For example, 0.55 V was reported for a similar flow-through fuel cell with enzymatic anode mediated by dissolved benzoquinone and a Pt cathode [33] or 0.8 V for a non-enzymatic direct glucose fuel cell based on Pt catalysts, which employed also a MEA design [34]. High OCV values (around 1 V) have been demonstrated in the case of glucose–oxygen enzymatic biofuel cells based on Os redox hydrogels [35,36]. The theoretical cell voltage for glucose oxidation to gluconolactone in presence of gas-phase oxygen under standard conditions, calculated according to [37] and assuming ionic strength of 0.25 M is 1.18 V, which corresponds to the value calculated in [35]. If conditions deviate from standard conditions as in the present case (5 mM glucose concentration and not defined concentration of gluconolactone, which is consumed in a following hydrolysis reaction) even higher theoretical cell voltage can be expected according to the Nernst equation. Although reasonable from a thermodynamic point of view, the value of 0.94 V is unexpectedly high, compared to the typical performance of similar biofuel cells.

The OCV in a fuel cell is influenced by the open circuit potentials of the anode and the cathode. As it was already mentioned, the open circuit potential of the anode in the present case is around −0.2 vs. SCE. On the other side, control experiments with Pt black-modified electrodes (not shown here) revealed current onset of the oxygen reduction at about 0.3 V vs. SCE in phosphate buffer, which was in accordance with the literature values for Pt nanoparticles on multi-walled carbon nanotubes (MWCNT's) (ca. 0.26 V vs. SCE) [38]. According to these half-cell experiments one can expect much lower OCV. The high values obtained in the present study can be tentatively explained by the specific architecture of the fuel cell, namely the enzymatic electrode is in contact with buffer, while the Pt cathode is in contact with Nafion. This implies pH difference between the electrodes. In control experiments the Pt black cathodes in 0.1 M sulfuric acid (not shown) revealed reduction onset at approximately 0.7 V vs. SCE, which was similar to the value for Pt nanoparticles on MWCNT's in 0.1 M perchloric acid [39]. Furthermore, the oxygen reduction kinetics is significantly enhanced at the Pt/Nafion interface since Nafion is a superacid (due to the highly acidic protons attached to the sulfonate sites in the polymer structure) and exhibits negligible anion adsorption effects, in addition to high oxygen solubility [40], which implies even more positive onset potential for the Pt cathode than the one observed in the case of sulfuric acid. In light of the discussion above, the measured OCV values can be expected in the present setup. Regarding the value of 0.55 V, reported for a similar hybrid setup [33], the difference can be possibly attributed to the different fuel cell architecture, the higher glucose concentration and the different mediator. Higher glucose concentration is expected to increase the glucose crossover and consequently to decrease OCV, which will be discussed below.

In addition to the activation region, observed in Fig. 8, the mass transport and resistance limitation regions in the polarization curve can be also distinguished. The current values obtained in the present setup suggest that the fuel cell is limited by the enzymatic anode since the Pt cathode can easily reach the mA range under similar conditions, e.g. in a DMFC [41]. The fuel cell exhibits maximum power density of about 45 μW cm^{-2} at 5 ml min^{-1} glucose flow rate. Increasing the flow rate to 10 ml min^{-1} decreases the OCV to 0.82 V and changes the shape of the polarization curve. The region of ohmic polarization is significantly extended and the mass transport limitation can be clearly identified at current densities around 300 μA cm^{-2} (see Fig. 8). The decrease in OCV at higher flow rate can be attributed to crossover of glucose, which can be oxidized at the cathode, creating a mixed potential. Increase in flow rate is expected to enhance the mass transport of glucose at the anode but also to increase the rate of crossover. Such phenomenon has been also demonstrated in a recent study, where the influence of operational parameters such as fuel concentration and flow rate on the performance of a DMFC has been investigated [41]. The higher flow rate in the present case resulted in an improved overall performance of the fuel cell, raising the maximum power output to nearly 100 μW cm^{-2} at 0.4 V.

The performance of the fuel cell presented in this study is somewhat superior compared to other hybrid biofuel cells employing Pt cathodes, although a straightforward comparison is difficult due to the difference in experimental conditions as outlined in [1]. For instance, a fuel cell with similar MEA architecture, which delivered around 45 μW cm^{-2} at 100 mM glucose, was reported by Tamaki et al. [42]. The anode was based on GOx and a ferrocene-modified polymer, which redox potential resulted in lower OCV and moderate output despite the high fuel concentration. Another compartmentalized fuel cell, which utilized GOx and dissolved
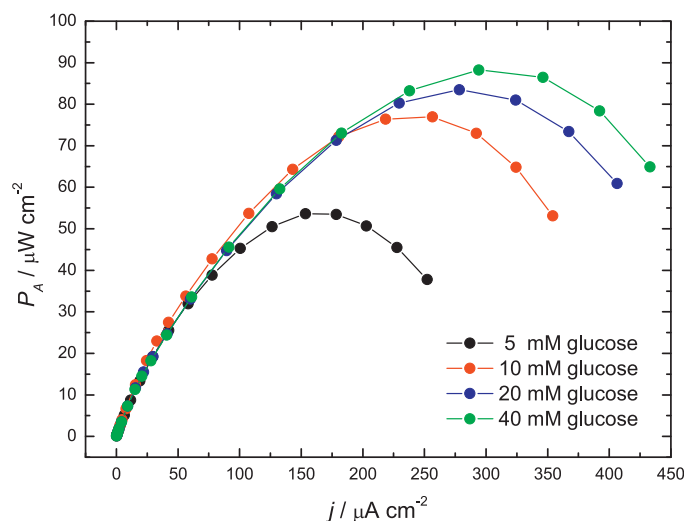
Fig. 9. Power curves of the hybrid fuel cell with separator in presence of different glucose concentrations. Conditions: anode 5 ml min^{-1} glucose flow rate, 0.1 M phosphate buffer, pH 7.2, 37 °C, N$_2$ atmosphere; cathode 500 ml min^{-1} dry oxygen flow rate. Data extracted from transient measurements after 2 min.

Fig. 10. Polarization (black squares) and power curves (red circles) of the hybrid fuel cell in presence of nitrogen- (empty symbols) and oxygen-saturated (full symbols) glucose solution. Conditions: anode 20 ml min^{-1} flow rate, 5 mM glucose in 0.1 M phosphate buffer, pH 7.2, 37 °C; cathode 500 ml min^{-1} dry oxygen flow rate. Data extracted from transient measurements after 2 min. (For interpretation of the references to color in this figure legend, the reader is referred to the web version of the article.)

benzoquinone as mediator generated similar output (42 μW cm^{-2}) also at 100 mM glucose [43].

In another study, highly efficient bioelectrodes based on Os redox hydrogels, single-walled carbon nanotubes (SWCNT's) and CDH were tested in a model membraneless configuration together with a Pt black cathode and the resulting maximum power density was 157 μW cm^{-2} in presence of 100 mM glucose.

The performance of the biofuel cell presented in this study is also comparable to the performance of biofuel cells incorporating enzymatic cathodes. For instance, a very recent study reported high current density glucose oxidation anodes based on GOx and a ferrocene-modified polymer, which generated limiting current densities of about 2 mA cm^{-2} at 0.3 V vs. SCE and ca. 60 mM glucose [26]. The bioanodes were coupled with Os-mediated laccase cathodes and the resulting biofuel cell generated 56 μW cm^{-2} with a stationary cathode and 146 μW cm^{-2} under rotation. In respect to operation at low glucose concentrations (5 mM), a notable example is the configuration based on Os redox hydrogels, which generated 280 μW cm^{-2} and was reported as the highest power biofuel cell at the lowest concentration [44]. However, this high performance in the latter case was achieved by the use of GOx from another source (*Penicillium pinophilum*) and operation at pH 5. For comparison, when GOx from *Aspergillus niger* was used, the biofuel cell generated only 90 μW cm^{-2} under the same conditions. In addition, it should be noted that the respective electrodes were 2 cm long carbon fibers with a diameter of 7 μm, which size and geometry significantly enhance mass transport conditions.

3.3. Influence of operational parameters on the performance

As already shown the glucose crossover can decrease the performance of the fuel cell. To overcome this effect, a cellophane separator has been introduced in the experiments with higher glucose concentrations. The utilization of separator resulted in an improved performance of the hybrid enzymatic fuel and increased the maximum power density. Power curves of the enzymatic fuel cell with a separator in presence of different glucose concentrations are shown in Fig. 9. The maximum power density is shifted from ca. 55 μW cm^{-2} at 5 mM glucose to ca. 90 μW cm^{-2} at 40 mM glucose. The increase is not linear, which fits well to the observations in single electrode experiments. The OCV values decreased by increasing the glucose concentration from ca. 0.99 V at 5 mM
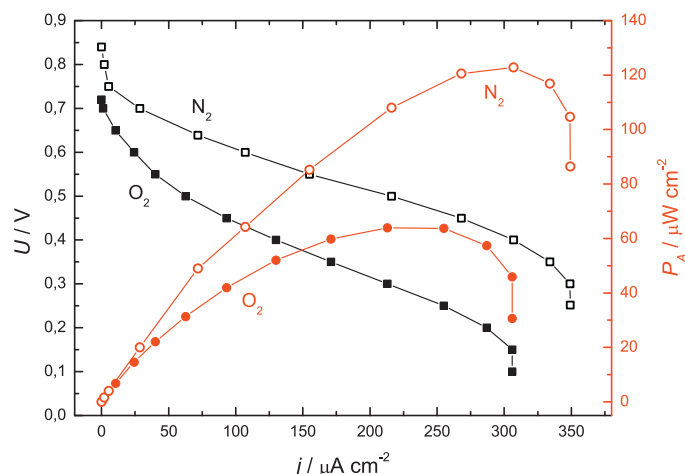
glucose to ca. 0.94 V at 40 mM glucose, which was ascribed to glucose crossover to the cathode. Similar decrease of OCV by increasing fuel concentration was demonstrated by Chen et al. in the case of a DMFC [41].

An important prerequisite for the utilization of enzymatic anodes in a membraneless fuel cell design is their oxygen tolerance. This concern is especially relevant in the case of enzymatic systems based on GOx since oxygen is believed to be the enzyme's natural electron acceptor and would compete for the electrons released by the oxidation [1]. Polarization and power curves of the hybrid enzymatic fuel cell without separator fed with nitrogen- and oxygen-saturated glucose solutions are shown in Fig. 10. As can be seen from the graph the presence of oxygen in the fuel solution decreases the overall fuel cell performance in the whole investigated range so the shape of the polarization curve remains qualitatively the same. The OCV drops by 120 mV and the maximum power density decreases from ca. 120 μW cm^{-2} to ca. 65 μW cm^{-2} in presence of oxygen. This observation is in accordance with single electrode experiments, in which a similar rate of performance reduction has been observed (not shown here). The decrease in current densities is associated with the reduced number of electrons, which instead of being transported through the mediator to the electrode surface are consumed by oxygen. The OCV drop on the other side could be the consequence of the generation of a mixed potential at the anode in presence of oxygen.

3.4. "Long-term" stability of the hybrid fuel cell

The stability of the hybrid fuel cell has been investigated by constant polarization at 0.5 V at two different glucose flow rates. For comparison, the chronoamperometric response of the enzymatic anode, polarized at 0.05 V vs. SCE under forced convection conditions has been also shown. As can be seen in Fig. 11a, the anode and the fuel cell at lower flow rate exhibit similar rather stable behavior. Increase in flow rate results in higher currents due to enhanced glucose transport to the enzymatic electrode but with the expense of reduced stability.

When the time scale at the higher flow rate was extended to 24 h, the current decayed to 1 μA cm^{-2} as shown in Fig. 11b. Such a pronounced loss of activity during long-term operation can be due to several reasons, including anode and cathode deactivation or a
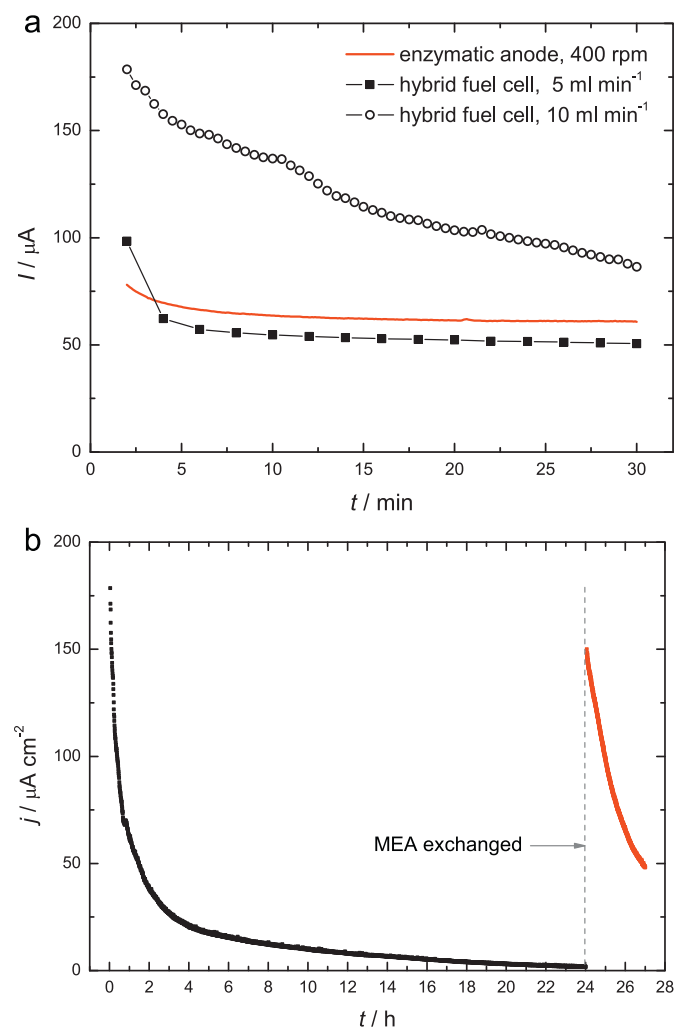
Fig. 11. Chronoamperometry of (a) the hybrid fuel cell and the enzymatic electrode at different hydrodynamic conditions for 30 min; (b) the hybrid fuel cell at 10 ml min^{-1} glucose flow rate for 24 h (exchange of the MEA denoted by a dashed line). Conditions: 5 mM glucose in 0.1 M phosphate buffer, pH 7.2, 37 °C, N$_2$ atmosphere; cathode 500 ml min^{-1} dry oxygen flow rate. Fuel cell has been polarized at 0.5 V and the enzymatic electrode at 0.05 V vs. SCE.

combination of these as well as some problems with the design of the fuel cell. According to the literature, a similar type of enzymatic anode shows very stable behavior during several days of operation [14], which corresponds to the observations in the present work. This makes anode deactivation, although possible, not likely. On the other hand, similar rate of fuel cell deactivation was reported by Fischback et al. [33], who observed pronounced current decay under constant operation. They were able to regain most of the initial performance by replacement of the MEA, which lead them to the conclusion that the loss of performance was due to poisoning of the membrane by cations from the anodic buffer solution [33]. Similar type of experiment with replacement of MEA was performed in this study and the results were in accordance to the latter work. As can be seen in Fig. 11b, the fuel cell restores activity almost to the initial level after exchange of the MEA, which is in accordance with the assumption that the enzymatic anode was not deactivated.

As discussed above, Fischback et al. assigned the fuel cell deactivation to impeded proton conductivity through the membrane caused by the competitive affinity of sodium or potassium cations to the anionic sulfonic sites of Nafion [33]. This phenomenon is expected to occur in the present case as well but according to our opinion it cannot explain such a high degree of performance

loss. Okada et al. have shown that the ionic conductivity of Nafion decreases from ca. 0.2 to approximately 0.05 S cm^{-1}, when all protons are exchanged with alkali metal cations [45]. This change is not so dramatic and the membrane resistance itself (mΩ range) is expected to increase only about four times, which will lead to a negligible voltage drop, having in mind the low current densities (μA cm^{-2}) maintained by the fuel cell.

On the other hand, the exchange of protons with metal cations in the Nafion membrane, in addition to increase of the resistance, will lead to a significant change of pH at the cathode side, which will slow down the cathode kinetics. As discussed in the previous section, the pH difference between both electrodes is tentatively considered to be accountable for the demonstrated high OCV values. It can be envisaged that during long-term operation the overpotential at the cathode side will increase with pH increase. The stability test shown in Fig. 11b has been performed as a chronoamperometric experiment at 0.5 V (voltage, which corresponds to nearly maximum power as shown in Fig. 8). However, with the gradual neutralization of the cathode interface, the OCV of the system decreases and the value of 0.5 V (maintained by the potentiostat) does not correspond to the initial conditions anymore but is rather close to the newly formed OCV and consequently generates very low current densities. In addition, the 24 h test has been performed at higher glucose flow rate, which as shown in Fig. 11a, corresponds to higher rate of Nafion neutralization and glucose crossover, respectively.

This discussion compromises partly the use of the present fuel cell as a platform for investigation of enzymatic anodes under fuel cell conditions. However, as shown in Fig. 11a, the stability of the fuel cell at lower flow rates in the time scale, which corresponds to the typical duration of polarization curve recording, is satisfactory.

4. Conclusions

In the present study an enzymatic anode based on a charge-transfer complex (TTF–TCNQ) and glucose oxidase has been applied for the first time in a hybrid glucose–oxygen fuel cell. The CTC forms highly irregular porous structure, which serves a matrix for enzyme immobilization. This points out the importance of the enzyme distribution optimization within the catalyst layer. The optimized electrode reached high current densities and the fuel cell reached high power densities in presence of low glucose concentrations. The high OCV values demonstrated in the present study have been tentatively assigned to the different pH at both electrodes. This phenomenon has been accounted also for the lower long-term stability of the fuel cell. However, additional studies (e.g. with introduction of a reference electrode) are needed for unambiguous clarification of the high OCV and the mechanism of performance loss. The constructed device can be used as a platform for testing of enzymatic anodes but at lower glucose flow rates and shorter time scales.

Acknowledgments

References

[1] I. Ivanov, T. Vidakovic-Koch, K. Sundmacher, Energies 3 (2010) 803–846.
[2] Y. Kamitaka, S. Tsujimura, N. Setoyama, T. Kajino, K. Kano, Phys. Chem. Chem. Phys. 9 (2007) 1793–1801.
[3] L. Stoica, N. Dimcheva, Y. Ackermann, K. Karnicka, D.A. Guschin, P.J. Kulesza, J. Rogalski, D. Haltrich, R. Ludwig, L. Gorton, W. Schuhmann, Fuel Cells 9 (2009) 53–62.
[4] N.L. Akers, C.M. Moore, S.D. Minteer, Electrochim. Acta 50 (2005) 2521–2525.
[5] R.L. Arechederra, S.D. Minteer, Fuel Cells 9 (2009) 63–69.
[6] A. Heller, Phys. Chem. Chem. Phys. 6 (2004) 209–216.

[7] S. Cosnier, D. Shan, S.N. Ding, Electrochem. Commun. 12 (2010) 266–269.
[8] E. Nazaruk, S. Smolinski, M. Swatko-Ossor, G. Ginalska, J. Fiedurek, J. Rogalski, R. Bilewicz, J. Power Sources 183 (2008) 533–538.
[9] G. Merle, A. Habrioux, K. Servat, M. Rolland, C. Innocent, K.B. Kokoh, S. Tingry, Electrochim. Acta 54 (2009) 2998–3003.
[10] N. Mano, F. Mao, A. Heller, J. Electroanal. Chem. 574 (2005) 347–357.
[11] F. Mao, N. Mano, A. Heller, J. Am. Chem. Soc. 125 (2003) 4951–4957.
[12] S.C. Barton, J. Gallaway, P. Atanassov, Chem. Rev. 104 (2004) 4867–4886.
[13] R. Pauliukaite, A. Malinauskas, G. Zhylyak, U.E. Spichiger-Keller, Electroanalysis 19 (2007) 2491–2498.
[14] G.F. Khan, M. Ohwa, W. Wernet, Anal. Chem. 68 (1996) 2939–2945.
[15] F. Palmisano, P.G. Zambonin, D. Centonze, M. Quinto, Anal. Chem. 74 (2002) 5913–5918.
[16] R. Pauliukaite, G. Zhylyak, D. Citterio, U.E. Spichiger-Keller, Anal. Bioanal. Chem. 386 (2006) 220–227.
[17] H.B. Liu, J.B. Li, C.S. Lao, C.S. Huang, Y.L. Li, Z.L. Wang, D.B. Zhu, Nanotechnology 18 (2007) 7.
[18] D. de Caro, K. Jacob, C. Faulmann, J.P. Legros, F. Senocq, J. Fraxedas, L. Valade, Synth. Met. 160 (2010) 1223–1227.
[19] J. Kulys, V. Simkeviciene, I.J. Higgins, Biosens. Bioelectron. 7 (1992) 495–501.
[20] H.J. Wang, J. Shi, M. Fang, Z. Li, Q.X. Guo, J. Phys. Org. Chem. 23 (2010) 75–83.
[21] N.S. Hudak, J.W. Gallaway, S.C. Barton, J. Electrochem. Soc. 156 (2009) B9–B15.
[22] A. Habrioux, K. Servat, S. Tingry, K.B. Kokoh, Electrochem. Commun. 11 (2009) 111–113.
[23] N.S. Hudak, S.C. Barton, J. Electrochem. Soc. 152 (2005) A876–A881.
[24] F. Tasca, L. Gorton, W. Harreither, D. Haltrich, R. Ludwig, G. Noll, J. Phys. Chem. C 112 (2008) 13668–13673.
[25] C.D. Jaeger, A.J. Bard, J. Am. Chem. Soc. 101 (1979) 1690–1699.
[26] M.T. Meredith, D.Y. Kao, D. Hickey, D.W. Schmidtke, D.T. Glat zhofer, J. Electrochem. Soc. 158 (2011) B166–B174.
[27] B. Kowalewska, P.J. Kulesza, Electroanalysis 21 (2009) 351–359.
[28] E. Nazaruk, K. Sadowska, J.F. Biernat, J. Rogalski, G. Ginalska, R. Bilewicz, Anal. Bioanal. Chem. 398 (2010) 1651–1660.
[29] S. Myler, S.D. Collyer, K.A. Bridge, S.P.J. Higson, Biosens. Bioelectron. 17 (2002) 35–43.
[30] P. Atanasov, A. Kaisheva, I. Iliev, V. Razumas, J. Kulys, Biosens. Bioelectron. 7 (1992) 361–365.
[31] H. Sakai, T. Nakagawa, Y. Tokita, T. Hatazawa, T. Ikeda, S. Tsujimura, K. Kano, Energy Environ. Sci. 2 (2009) 133–138.
[32] T. Reshetenko, H. Kim, H. Lee, M. Jang, H. Kweon, J. Power Sources 160 (2006) 925–932.
[33] M.B. Fischback, J.K. Youn, X.Y. Zhao, P. Wang, H.G. Park, H.N. Chang, J. Kim, S. Ha, Electroanalysis 18 (2006) 2016–2022.
[34] C.A. Apblett, D. Ingersoll, S. Sarangapani, M. Kelly, P. Atanassov, J. Electrochem. Soc. 157 (2010) B86–B89.
[35] V. Soukharev, N. Mano, A. Heller, J. Am. Chem. Soc. 126 (2004) 8368–8369.
[36] N. Mano, F. Mao, W. Shin, T. Chen, A. Heller, Chem. Commun. (2003) 518–519.
[37] R.A. Alberty, Biochem. Educ. 28 (2000) 12–17.
[38] H.F. Cui, J.S. Ye, W.D. Zhang, J. Wang, F.S. Sheu, J. Electroanal. Chem. 577 (2005) 295–302.
[39] A. Kongkanand, S. Kuwabata, G. Girishkumar, P. Kamat, Langmuir 22 (2006) 2392–2396.
[40] A. Parthasarthy, S. Srinivasan, A.J. Appleby, C.R. Martin, J. Electroanal. Chem. 339 (1992) 101–121.
[41] S.Z. Chen, F. Ye, W.M. Lin, Int. J. Hydrogen Energy 35 (2010) 8225–8233.
[42] T. Tamaki, T. Yamaguchi, Ind. Eng. Chem. Res. 45 (2006) 3050–3058.
[43] T. Kuwahara, K. Oshima, M. Shimomura, S. Miyauchi, J. Appl. Polym. Sci. 104 (2007) 2947–2953.
[44] N. Mano, Chem. Commun. (2008) 2221–2223.
[45] T. Okada, H. Satou, M. Okuno, M. Yuasa, J. Phys. Chem. B 106 (2002) 1267–1273.

[TVK3]

T. Vidaković-Koch, V. Panić, M. Andrić, M. Petkovska,
K. Sundmacher

## Non-Linear Frequency Response Analysis of the Ferrocyanide Oxidation Kinetics: Part I – A Theoretical Analysis

Nonlinear Frequency Response Analysis of the Ferrocyanide Oxidation Kinetics. Part I. A Theoretical Analysis

Tanja R. Vidaković-Koch,*,|| Vladimir V. Panić,§,† Milan Andrić,‡ Menka Petkovska,‡ and Kai Sundmacher||,§

||Process Systems Engineering, Otto-von-Guericke University Magdeburg, Universitätsplatz 2, 39106 Magdeburg, Germany
§Max Planck Institute for Dynamics of Complex Technical Systems, Sandtorstrasse 1, 39106 Magdeburg, Germany
†Institute of Chemistry, Technology and Metallurgy, University of Belgrade, Njegoševa 12, 11000 Belgrade, Serbia
‡Faculty of Technology and Metallurgy, University of Belgrade, Karnegijeva 4, 11000 Belgrade, Serbia

ABSTRACT: In this work, a nonlinear frequency response (NLFR) analysis was used for a first time in a theoretical study of nonlinear behavior of electrochemical (EC) ferrocyanide oxidation as a simple model reaction. Analytical expressions of the first- and second-order frequency response functions (FRFs) are derived. The first-order FRF is equivalent to the EC admittance and contains information about the linear behavior of the system, whereas the second-order FRF contains additional nonlinear information. The influence of different parameters, such as the heterogeneous rate constant, solution resistance, double-layer capacitance, diffusion coefficients of the reacting species, and electrode rotation rate on the characteristics of the first- and second-order FRFs was checked and discussed. It was found that the second-order FRF is more sensitive to the changes of the studied parameters than the first-order FRF. Experimental verification of the NLFR analysis of EC ferrocyanide oxidation is presented in Part II of this work.
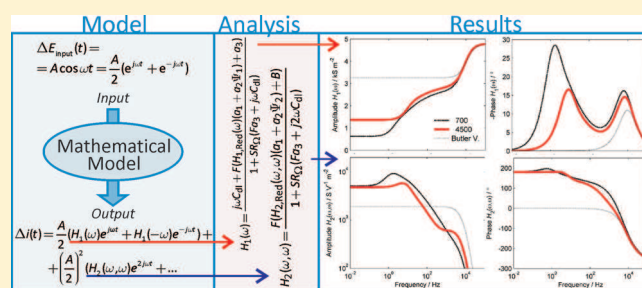
1. INTRODUCTION

It is well known that kinetics of electrochemical (EC) reactions is rather complex. In addition to charge transfer step(s), the reaction mechanisms include chemical steps in the bulk, at the electrode surface, or both as well as mass transfer of the reactants, products, or both. This complexity leads to formulation of different rivaling models for a certain EC reaction. If the model equations are solved under steady-state conditions, then good quantitative description of the same set of experimental data could be obtained by different models. This has been demonstrated recently, for example, for the case of methanol oxidation kinetics.[1−3] The lack of discriminating tools for rivaling reaction models is intrinsic not only for complex EC reactions but also generally for any complex chemical reaction. It can be stated that in modeling of chemical reactions the model discrimination is difficult, taking into account only steady-state considerations.[4]

The analysis of dynamic responses should be more sensitive to model discrimination than the steady-state analysis, because more reaction parameters can be determined independently.[5−7] However, in some cases, such as the case of methanol oxidation kinetics, qualitative model discrimination was not possible, even by electrochemical impedance spectroscopy (EIS).[2] EIS is a dynamic, frequency response method operating in a linear range, which is achieved by using small excitation amplitudes.[8] It appears that EIS can hardly treat the full complexity of electrochemical systems because it disregards the system nonlinearity.[9,10] The higher-order terms in system response, which become visible if larger input amplitudes are used, describe EC reactions in a nonlinear domain. These terms should bear new information

about the relationships between reaction parameters. To take this into consideration, different nonlinear methods have been discussed in the analysis of EC reactions and fuel cells.[5,11−14] All of these methods are based on the application of large-amplitude input signal, whereas they differ mainly with respect to the mathematical treatment of the output signal. (For short overview of nonlinear methods for the investigation of EC systems, see ref 12 and the references therein.) We have shown recently that one of these methods, the so-called nonlinear frequency response analysis (NLFRA), can be used for qualitative discrimination of different models of methanol oxidation kinetics[12] and for fuel cell diagnosis.[13,15] In NLFRA, the input−output behavior of a system is described with the help of Volterra series expansion and generalized Fourier transform through higher order frequency response functions (FRFs).[12] The linear part of the EC system frequency response is represented by the first-order FRF that corresponds to the EC admittance. In a theoretical paper,[12] we applied the nonlinear frequency response (NLFR) method for analyzing four different varieties of the model for EC methanol oxidation by deriving the FRFs up to the second order. Whereas the first-order FRF was found not to contain enough information for differentiation between model varieties, the basic features of the shapes of the second-order FRFs corresponding to the four model varieties remained unique for a whole set of tested reaction parameters. This suggested that the second-order

FRF contains sufficient information for unequivocal model discrimination.

The experimentally obtained second-order FRF has been also found sensitive for discrimination between competitive processes, which can cause the failure of polymer electrolyte membrane fuel cells (PEMFCs).[13,15] The measurements showed that the level of membrane hydration, fuel cell flooding, and anode catalyst poisoning by carbon monoxide in PEMFC can be ambiguously distinguished from the characteristic features of the second-order FRF frequency spectra. Furthermore, it has been shown that NLFR characteristics of differential H_2/H_2 PEMFC during CO poisoning can be simulated by simple and widely accepted model with original parameters.[15]

However, the above-mentioned pioneering applications of the NLFRA to rather complex EC systems bear some ad hoc approximations, whereas the correlations between the NLFR spectra and basic system parameters are not straightforward because of system complexity. Furthermore, only charge transfer and adsorption process were analyzed,[12] leaving out of scope physical steps usually involved in EC reaction mechanisms, for example, mass transport limitations. These steps can also affect the nonlinear behavior of the system. To establish the fundaments of the NLFR for analysis of EC systems, we study here ferrocyanide oxidation as an example of a rather simple EC reaction. This reaction is under pronounced diffusion control, which allows us to study theoretically and experimentally for the first time the NLFR of mass transport coupled to simple one-electron charge transfer and their influence on nonlinear characteristics of the system. The theoretical analysis of this system with detailed parameter variation is presented in this Article, whereas an experimental validation of the model is given in Part II of this work.

## 2. FREQUENCY RESPONSE FUNCTIONS FOR ELECTROCHEMICAL FERROCYANIDE OXIDATION

The procedure for derivation of the higher order FRFs in EC kinetics has already been previously established.[12] For the case of ferrocyanide oxidation, this procedure consists of the following steps:

(1) Definition of basic kinetic and mass transport equations and dynamic material and charge balances
(2) Definition of input and output variables
(3) Taylor approximation of the reaction rate expression around the steady state
(4) Substitution of the Taylor polynomials into the mass balance equations
(5) Substitution of the input and outputs into the equations gained in step 4
(6) Application of harmonic probing
(7) Solution of the equations derived in step 6

In the following sections, each step is presented in more details.

2.1. Model Definition. For derivation of the FRFs, it is necessary to postulate a nonlinear mathematical model of the investigated system.

Ferrocyanide oxidation

$$\underset{\text{Red}}{\underline{[\text{Fe(CN)}_6]^{4-}}} \leftrightarrow \underset{\text{Ox}}{\underline{[\text{Fe(CN)}_6]^{3-}}} + e^- \qquad (1)$$
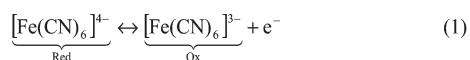
is a simple EC reaction that obeys the Butler–Volmer kinetics[16]

$$r(t) = k^e \left\{ \frac{c_{\text{red}}(0,t)}{c_{\text{red},\infty}} \exp(\beta f(E(t) - E_r)) \right.$$
$$\left. - \frac{c_{\text{ox}}(0,t)}{c_{\text{ox},\infty}} \exp(-(1-\beta)f(E(t) - E_r)) \right\} \qquad (2)$$

where r is the reaction rate, k^e is the EC rate constant, $c_{\text{red}}(0,t)$, $c_{\text{ox}}(0,t)$, $c_{\text{red},\infty}$, and $c_{\text{ox},\infty}$ are the concentrations of the reacting species at the electrode surface and in the bulk of the solution, respectively, E is the electrode potential, E_r is the equilibrium electrode potential, and β is a symmetry factor, whereas $f = F/RT$, where F is the Faraday constant, R is the universal gas constant, and T is the thermodynamic temperature. The EC constant k^e is defined as follows

$$k^e = k_{\text{red}} \cdot c_{\text{Red},\infty} \cdot \exp(\beta f(E_r))$$
$$= k_{\text{ox}} \cdot c_{\text{ox},\infty} \cdot \exp(-(1-\beta)f(E_r)) \qquad (3)$$

where k_{red} and k_{ox} are heterogeneous rate constants for forward and backward reactions, respectively. For the sake of simplicity, further consideration will refer to the special case when $c_{\text{red},\infty} = c_{\text{ox},\infty} = c_\infty$ and $E_r = 0$. (Experimentally, $E_r = 0$ can be achieved by choosing the reference electrode that corresponds to eq 1.) In this case, in accordance to eq 3, new heterogeneous rate constant $k = k_{\text{red}} = k_{\text{ox}}$ can be defined.

The concentration profiles of the red and ox forms can be obtained by solving the convective diffusion equation, which can be simplified in the case of a rotating disk electrode (RDE) to the following 1D form[16]

$$\frac{\partial c_i(z,t)}{\partial t} = D_i \frac{\partial^2 c_i(z,t)}{\partial z^2} - v_z \frac{\partial c_i}{\partial z}, \quad i = \text{red or ox} \qquad (4)$$

where D_i is the diffusion coefficient and v_z is the convective velocity in the direction z perpendicular to the electrode surface. To simplify further the derivation of the FRFs, we neglect the convective contribution to the mass transfer in eq 4.[16] This approximation can be considered to be valid in the thin layer of the solution adjacent to the electrode surface, the so-called Nernstian diffusion layer, where the v_z velocity falls below 1% of its maximal value in the bulk. This means that the diffusion becomes the main way of transport within the layer. For that case, eq 4 becomes the second Fick's law

$$\frac{\partial c_i(z,t)}{\partial t} = D_i \frac{\partial^2 c_i(z,t)}{\partial z^2}, \quad i = \text{red or ox} \qquad (5)$$

The boundary conditions for solving eq 5 are

$$D_i \frac{\partial c_i(z,t)}{\partial z}\bigg|_{z=0} = \pm r(t), \quad i = \text{red or ox} \qquad (6)$$

where "+" or "−" sign stand for i = red or ox, respectively, and

$$c_i(\delta_{D,i}, t) = c_\infty, \quad i = \text{red or ox} \qquad (7)$$

where

$$\delta_{D,i} = 1.61 D_i^{1/3} \nu^{1/6} \omega_r^{-1/2}, \quad i = \text{red or ox} \qquad (8)$$

is the thickness of diffusion layer for ox or red at the rotation speed, ω_r, of the rotating disc electrode in the solution of kinematic viscosity, ν.[16]

17342

dx.doi.org/10.1021/jp201297v |J. Phys. Chem. C 2011, 115, 17341–17351

The charge balance at the electrode surface is given by

$$C_{dl} \frac{dE(t)}{dt} = i(t) - Fr(t) \tag{9}$$

where C_{dl} is the double-layer capacitance and $i(t)$ is the cell current density.

2.2. Definition of the Input and Output Variables. In the case of NLFR, similar to EIS, the potential or the current can be chosen as the input variable. Because the system behavior around steady state is studied, all variables are defined as deflections from their steady-state values. For potential as the cosinusoidal input signal, it follows

$$\Delta E_{input}(t) = E_{input}(t) - E_{input,ss} = A \cos \omega t = \frac{A}{2}(e^{j\omega t} + e^{-j\omega t}) \tag{10}$$

where A is the input amplitude. In the experimental system, the input potential in addition to "real" electrode potential always contains the contribution of ohmic drop in the solution. To compare the experimental data with model predictions, we have to express the theoretical input potential in the same way

$$\Delta E_{input}(t) = \Delta E(t) + SR_\Omega \Delta i(t) \tag{11}$$

where $\Delta E(t)$ and $\Delta i(t)$ are the deflections of the "real" electrode potential and the cell current density from their steady-state values, respectively, R_Ω is Ohmic drop in the solution, and S is the electrode surface.

The output signal is the cell current, which can be expressed as[12]

$$\Delta i(t) = \frac{A}{2}(H_1(\omega)e^{j\omega t} + H_1(-\omega)e^{-j\omega t})$$

$$+ \left(\frac{A}{2}\right)^2 (H_2(\omega,\omega)e^{2j\omega t} + 2H_2(\omega,-\omega)e^0$$

$$+ H_2(-\omega,-\omega)e^{-2j\omega t}) + ... \tag{12}$$

where $H_1(\omega)$ is the first-order FRF that is identical to the EIS admittance, whereas $H_n(\omega,..,\omega)$ are the so-called higher order FRFs that contain a nonlinear fingerprint of the system.

In addition to the cell current as the output, the electrode potential and the concentrations of red and ox at the electrode surface are to be defined as auxiliary outputs, in a way similar to eq 12

$$\Delta E = \frac{A}{2}(H_{1,E}(\omega)e^{j\omega t} + H_{1,E}(-\omega)e^{-j\omega t})$$

$$+ \left(\frac{A}{2}\right)^2 (H_{2,E}(\omega,\omega)e^{2j\omega t} + 2H_{2,E}(\omega,-\omega)e^0$$

$$+ H_{2,E}(-\omega,-\omega)e^{-2j\omega t}) + ... \tag{13}$$

$$\Delta c(0,t)_{red} = \frac{A}{2}(H_{1,red}(\omega)e^{j\omega t} + H_{1,red}(-\omega)e^{-j\omega t})$$

$$+ \left(\frac{A}{2}\right)^2 (H_{2,red}(\omega,\omega)e^{2j\omega t} + 2H_{2,red}(\omega,-\omega)e^0$$

$$+ H_{2,red}(-\omega,-\omega)e^{-2j\omega t}) + ... \tag{14}$$

Table 1. Expressions for the Coefficients a_k and b_{ij} in the Taylor Approximation up to the Second Order (eq 16) of the Expression for the Reaction Rate

coefficient	expression
a_1	$\dfrac{k^e}{c_{red,\infty}} \exp(\beta f(E_{ss} - E_r))$
a_2	$-\dfrac{k^e}{c_{ox,\infty}} \exp(-(1-\beta)f(E_{ss} - E_r))$
a_3	$a_1 c_{red,ss}\beta f - a_2 c_{ox,ss}(1-\beta)f$
b_{12}	0
b_{13}	$a_1\beta f$
b_{23}	$-a_2(1-\beta)f$
b_{11}	0
b_{22}	0
b_{33}	$a_1 \dfrac{c_{red,ss}}{2}(\beta f)^2 - a_2 \dfrac{c_{ox,ss}}{2}((1-\beta)f)^2$

$$\Delta c(0,t)_{ox} = \frac{A}{2}(H_{1,ox}(\omega)e^{j\omega t} + H_{1,ox}(-\omega)e^{-j\omega t})$$

$$+ \left(\frac{A}{2}\right)^2 (H_{2,ox}(\omega,\omega)e^{2j\omega t} + 2H_{2,ox}(\omega,-\omega)e^0$$

$$+ H_{2,ox}(-\omega,-\omega)e^{-2j\omega t}) + ... \tag{15}$$

where $H_{1,E}(\omega)$, $H_{1,red}(\omega)$, and $H_{1,ox}(\omega)$ are the first-order auxiliary FRFs, whereas $H_{2,E}(\omega,\omega)$, $H_{2,red}(\omega,\omega)$, and $H_{2,ox}(\omega,\omega)$ are the second-order auxiliary FRFs and so on.

2.3. Taylor Approximation of the Nonlinear Terms. For application of the NLFR method, it is necessary to represent all nonlinear terms in the model equations in a polynomial form.[17] This is achieved by the Taylor series expansion of the nonlinear terms. In this step, the nonlinear terms in the eq 2 are expressed in a polynomial form by applying Taylor expansion. In general, if the output is analyzed up to nth order FRF, then in the Taylor series the terms up to nth order need to be taken into consideration. For derivation of the first and second FRFs only, it is sufficient to write only the terms up to the second order

$$\Delta r(t) = \underbrace{\frac{\partial r}{\partial c_{Red}}\Big|_{ss}}_{a_1}\Delta c_{Red}(0,t) + \underbrace{\frac{\partial r}{\partial c_{Ox}}\Big|_{ss}}_{a_2}\Delta c_{Ox}(0,t) + \underbrace{\frac{\partial r}{\partial E}\Big|_{ss}}_{a_3}\Delta E(t) +$$

$$+ \underbrace{\frac{\partial^2 r}{\partial c_{Red}\partial c_{Ox}}\Big|_{ss}}_{b_{12}}\Delta c_{Red}(0,t)\Delta c_{Ox}(0,t) + \underbrace{\frac{\partial^2 r}{\partial c_{Red}\partial E}\Big|_{ss}}_{b_{13}}\Delta c_{Red}(0,t)\Delta E(t) +$$

$$+ \underbrace{\frac{\partial^2 r}{\partial c_{Ox}\partial E}\Big|_{ss}}_{b_{23}}\Delta c_{Ox}(0,t)\Delta E(t) + \underbrace{\frac{1}{2}\frac{\partial^2 r}{\partial c_{Red}^2}\Big|_{ss}}_{b_{11}}(\Delta c_{Red}(0,t))^2 +$$

$$+ \underbrace{\frac{1}{2}\frac{\partial^2 r}{\partial c_{Ox}^2}\Big|_{ss}}_{b_{22}}(\Delta c_{Ox}(0,t))^2 + \underbrace{\frac{1}{2}\frac{\partial^2 r}{\partial E^2}\Big|_{ss}}_{b_{33}}(\Delta E(t))^2 + \cdots \tag{16}$$

The expressions for Taylor coefficients, a_k and b_{kl} from eq 16 are given in Table 1. As can be seen in Table 1, a_3 and b_{33} depend on the steady-state concentrations of red and ox at the electrode surface. The expressions for these concentrations can be easily obtained by solving eq 5 with the boundary conditions given by

eqs 6 and 7 for the steady state

$$c_{red,ss} = c_\infty - \frac{D_{ox}\delta_{D,red}c_\infty[a_1 + a_2]}{D_{red}D_{ox} - a_2 D_{red}\delta_{D,ox} + a_1 D_{ox}\delta_{D,red}},$$

$$c_{ox,ss} = c_\infty + \frac{D_{red}\delta_{D,ox}c_\infty[a_1 + a_2]}{D_{red}D_{ox} - a_2 D_{red}\delta_{D,ox} + a_1 D_{ox}\delta_{D,red}} \tag{17}$$

2.4. Substitution of the Taylor Approximation of the Rate Expression into the Balance Equations. In this step, the Taylor-approximated rate expression (eq 16) is substituted into the balance equations. For the mass balance (eq 5), the reaction rate appears in the boundary condition (eq 6)

$$D_i \frac{\partial c_i(z,t)}{\partial z}\Big|_{z=0} = \pm (a_1\Delta c_{red}(0,t) + a_2\Delta c_{ox}(0,t) + a_3\Delta E(t)$$
$$+ b_{12}\Delta c_{red}(0,t)\Delta c_{ox}(0,t) + b_{13}\Delta c_{red}(0,t)\Delta E(t)$$
$$+ b_{23}\Delta c_{ox}(0,t)\Delta E(t) + b_{11}(\Delta c_{red}(0,t))^2$$
$$+ b_{22}(\Delta c_{ox}(0,t))^2 + b_{33}(\Delta E(t))^2 + \dots \tag{18}$$

For the charge balance (eq 9), it follows

$$C_{dl}\frac{dE(t)}{dt} = i(t) - F(a_1\Delta c_{red}(0,t) + a_2\Delta c_{ox}(0,t)$$
$$+ a_3\Delta E(t) + b_{12}\Delta c_{red}(0,t)\Delta c_{ox}(0,t)$$
$$+ b_{13}\Delta c_{red}(0,t)\Delta E(t) + b_{23}\Delta c_{ox}(0,t)\Delta E(t)$$
$$+ b_{11}(\Delta c_{red}(0,t))^2 + b_{22}(\Delta c_{ox}(0,t))^2$$
$$+ b_{33}(\Delta E(t))^2 + \dots \tag{19}$$

2.5. Substitution of the Inputs and Outputs and Application of the Method of Harmonic Probing. In the next step, the input and the outputs defined by eqs 12−15 are substituted into the model equations (eqs 5, 9, 11, 18, and 19). For example, after substitution into the mass balance (eq 5) for i = red, one obtains

$$\frac{A}{2}\frac{\partial}{\partial t}(H_{1,red}(\omega)e^{j\omega t} + H_{1,red}(-\omega)e^{-j\omega t})$$
$$+ \left(\frac{A}{2}\right)^2\frac{\partial}{\partial t}(H_{2,red}(\omega,\omega)e^{2j\omega t} + 2H_{2,red}(\omega,-\omega)e^0$$
$$+ H_{2,red}(-\omega,-\omega)e^{-2j\omega t}) + \dots$$
$$= D_{red}\left(\frac{A}{2}\frac{\partial^2}{\partial z^2}(H_{1,red}(\omega)e^{j\omega t} + H_{1,red}(-\omega)e^{-j\omega t})\right.$$
$$+ \left(\frac{A}{2}\right)^2\frac{\partial^2}{\partial z^2}(H_{2,red}(\omega,\omega)e^{2j\omega t} + 2H_{2,red}(\omega,-\omega)e^0$$
$$\left. + H_{2,red}(-\omega,-\omega)e^{-2j\omega t}) + \dots\right) \tag{20}$$

In the resulting equations, the auxiliary FRFs appear instead of the corresponding auxiliary variables of time.

The next step is the application of the method of harmonic probing.[12,17] All terms in the equations obtained after substitution of the inputs and outputs of the same power of the input amplitude and the same frequency are collected separately. For the first-order FRF, by collecting the terms containing $(A/2)e^{j\omega t}$,

the following equations are obtained

$$\frac{\partial^2(H_{1,red}(z,\omega))}{\partial z^2} - \frac{j\omega}{D_{red}}H_{1,red}(z,\omega) = 0 \tag{21}$$

with boundary conditions

$$z = 0 : D_{red}\frac{dH_{1,red}(z,\omega)}{dz}\bigg|_{z=0}$$
$$= a_1 H_{1,red}(0,\omega) + a_2 H_{1,ox}(0,\omega) + a_3 H_{1,E}(\omega)$$
$$z = \delta_{D,red} : H_{1,red}(\delta_{D,red},\omega) = 0 \tag{22}$$

and

$$\frac{d^2(H_{1,ox}(z,\omega))}{dz^2} - \frac{j\omega}{D_{ox}}H_{1,ox}(z,\omega) = 0 \tag{23}$$

with boundary conditions

$$z = 0 : D_{ox}\frac{dH_{1,ox}(z,\omega)}{dz}\bigg|_{z=0} = -(a_1 H_{1,red}(0,\omega)$$
$$+ a_2 H_{1,ox}(0,\omega) + a_3 H_{1,E}(\omega))$$
$$z = \delta_{D,ox} : H_{1,ox}(\delta_{D,ox},\omega) = 0 \tag{24}$$

In a similar way, after substituting the inputs and outputs into eqs 9 and 11 and applying the method of harmonic probing, one obtains

$$H_1(\omega) = (C_{dl}j\omega + Fa_3)H_{1,E}(\omega)$$
$$+ F(a_1 H_{1,red}(0,\omega) + a_2 H_{1,ox}(0,\omega)) \tag{25}$$

$$H_{1,E}(\omega) = 1 - R_\Omega S H_1(\omega) \tag{26}$$

By solving eqs 21−26, the expression for the first-order FRF $H_1(\omega)$ is derived

$$H_1(\omega) = \frac{j\omega C_{dl} + F(H_{1,red}(\omega)(a_1 + a_2\Psi_1) + a_3)}{1 + SR_\Omega(Fa_3 + j\omega C_{dl})} \tag{27}$$

where

$$H_{1,red}(\omega)$$
$$= \frac{a_3}{(a_3 SR_\Omega F + 1 + SR_\Omega C_{dl}j\omega)(G_{12} + G_{13} - G_{11} - G_{14} - a_1)} \tag{28}$$

The expressions for the groups Ψ_1 and G_{1m} for $m = 1-4$ are given in Table 2.

When the terms containing $(A/2)^2 e^{2j\omega t}$ are collected, the equations defining the second-order FRFs are obtained

$$\frac{d^2(H_{2,red}(z,\omega,\omega))}{dz^2} - \frac{2j\omega}{D_{red}}H_{2,red}(z,\omega,\omega) = 0 \tag{29}$$

with boundary conditions

$$z = 0 : D_{red}\frac{dH_{2,red}(z,\omega,\omega)}{dz}\bigg|_{z=0} = a_1 H_{2,red}(0,\omega,\omega)$$
$$+ a_2 H_{2,ox}(0,\omega,\omega) + a_3 H_{2,E}(\omega,\omega)$$
$$+ b_{13}H_{1,red}(0,\omega)H_{1,E}(\omega) + b_{23}H_{1,ox}(0,\omega)H_{1,E}(\omega)$$
$$+ b_{33}(H_{1,E}(\omega))^2$$
$$z = \delta_{D,red} : H_{2,red}(\delta_{D,red},\omega,\omega) = 0 \tag{30}$$

Table 2. Expressions for the Constants Ψ_m and T_{mn} for $m = 1$ to 2 and $n = 1-4$, which Appear in Equations 27, 28, 35, and 37

parameter	expression
Ψ_1	$-\dfrac{D_{red}\sqrt{j\omega/D_{red}}\,\tanh(\delta_{D,ox}\sqrt{j\omega/D_{ox}})}{D_{ox}\sqrt{j\omega/D_{ox}}\,\tanh(\delta_{D,red}\sqrt{j\omega/D_{red}})}$
Ψ_2	$-\dfrac{D_{red}\sqrt{2j\omega/D_{red}}\,\tanh(\delta_{D,ox}\sqrt{2j\omega/D_{ox}})}{D_{ox}\sqrt{2j\omega/D_{ox}}\,\tanh(\delta_{D,red}\sqrt{2j\omega/D_{red}})}$
G_{11}	$\dfrac{D_{red}\sqrt{j\omega/D_{red}}}{\tanh(\delta_{D,red}\sqrt{j\omega/D_{red}})}$
G_{12}	$-a_2\Psi_1$
G_{13}	$\dfrac{a_1 a_3 SR_\Omega F}{SR_\Omega F a_3 + 1 + SR_\Omega C_{dl}j\omega}$
G_{14}	$\dfrac{G_{12}G_{13}}{a_1}$
G_{21}	$\dfrac{D_{red}\sqrt{2j\omega/D_{red}}}{\tanh(\delta_{D,red}\sqrt{2j\omega/D_{red}})}$
G_{22}	$-a_2\Psi_2$
G_{23}	$\dfrac{a_1 a_3 SR_\Omega F}{SR_\Omega F a_3 + 1 + 2SR_\Omega C_{dl}j\omega}$
G_{24}	$\dfrac{G_{22}G_{23}}{a_1}$

and

$$\frac{d^2(H_{2,ox}(z,\omega,\omega))}{dz^2} - \frac{2j\omega}{D_{ox}}H_{2,ox}(z,\omega,\omega) = 0 \qquad (31)$$

with boundary conditions

$$z = 0 : D_{ox}\frac{dH_{2,ox}(z,\omega,\omega)}{dz}\bigg|_{z=0} = -(a_1 H_{2,red}(0,\omega,\omega)$$
$$+ a_2 H_{2,ox}(0,\omega,\omega) + a_3 H_{2,E}(\omega,\omega))$$
$$-(b_{13}H_{1,red}(0,\omega)H_{1,E}(\omega) + b_{23}H_{1,ox}(0,\omega)H_{1,E}(\omega)$$
$$+ b_{33}(H_{1,E}(\omega))^2$$
$$z = \delta_{D,ox} : H_{2,ox}(\delta_{D,ox},\omega,\omega) = 0 \qquad (32)$$

$$H_2(\omega,\omega) = (2C_{dl}j\omega + Fa_3)H_{2,E}(\omega,\omega)$$
$$+ F(a_1 H_{2,red}(0,\omega,\omega) + a_2 H_{2,ox}(0,\omega,\omega))$$
$$+ F(b_{13}H_{1,red}(0,\omega)H_{1,E}(\omega)$$
$$+ b_{23}H_{1,ox}(0,\omega)H_{1,E}(\omega) + b_{33}(H_{1,E}(\omega))^2) \qquad (33)$$

$$H_{2,E}(\omega,\omega) = -R_\Omega S H_2(\omega,\omega) \qquad (34)$$

Solution of the system of eqs 29–34 results in the expression for the second-order FRF $H_2(\omega,\omega)$

$$H_2(\omega,\omega) = \frac{F(H_{2,red}(\omega,\omega)(a_1 + a_2\Psi_2) + B)}{1 + SR_\Omega(Fa_3 + j2\omega C_{dl})} \qquad (35)$$

Table 3. Values of the Parameters of Ferocyanide Oxidation Used for the Calculation of the Theoretic Frequency Response Functions

parameter	reference value	tested values
heterogeneous rate constant, $k/10^{-4}$ m s^{-1}	1.15	0.115 and 11.5
ohmic resistance, Ω	30	5, 15 and 80
double-layer capacitance, C_{dl}/F m^{-2}	0.20	0.10, 2.0, and 20
rotation rate, rpm	4500	700
diffusion coefficient of $[Fe(CN)_6]^{-4}$, $D([Fe(CN)_6]^{-4})/10^{-10}$ m^2 s^{-1}	6.0	4.0, 7.0, and 9.0
diffusion coefficient of $[Fe(CN)_6]^{-3}$, $D([Fe(CN)_6]^{-3})/10^{-10}$ m^2 s^{-1}	7.0	4.0, 6.0, and 9.0
symmetry factor, β	0.50	
kinematic viscosity, ν/m^2 s^{-1}	1.0×10^{-6}	
potential, mV	30	

where B stands instead of the following expression

$$B = fH_{1,E}(\omega)\big(H_{1,red}(\omega)(\beta a_1 + (1-\beta)\Psi_1 a_2\big)$$
$$+ \frac{f}{2}H_{1,E}(\omega)(\beta^2 a_1 c_{red,ss} + (1-\beta)^2 a_2 c_{ox,ss})) \qquad (36)$$

and the auxiliary function $H_{2,red}(\omega,\omega)$ is

$$H_{2,red}(\omega,\omega)$$
$$= \frac{B(1 + 2SR_\Omega C_{dl}j\omega)}{(SR_\Omega F a_3 + 1 + 2SR_\Omega C_{dl}j\omega)(G_{22} + G_{23} - G_{21} - G_{24} - a_1)} \qquad (37)$$

The expressions for the groups Ψ_2 and G_{2m} for $m = 1-4$ are given in Table 2.

It follows from eq 27 that $H_1(\omega)$ is really identical to EC admittance. When $\omega \to \infty$, $H_1(\omega) \to 1/SR_\Omega$; that is, it equals the solution conductivity between the working and reference electrode, as it follows from EIS of EC systems. When $\omega \to 0$, both the first- and second-order FRFs become real numbers independent of frequency.

The FRFs defined by eqs 27 and 35 appear very complex. From the point of view of practical application and acceptance of this method in the EC community, it is important to discuss the physical meaning of these functions. The physical meaning of the first-order FRF seems to be straightforward because as shown, this function corresponds to EC admittance. Just to recall, in modeling of EIS spectra, usually, so-called equivalent circuit representations based on linear electrical elements like resistors or capacitor have been used. Usual physical meaning of EIS spectra is then based on the analogy between linear elements of the equivalent electrical circuits and the elements of an EC system. This is clearly a simplification because the "elements" of the typical EC system are not linear. This nonlinearity becomes obvious if the system is perturbed with high input amplitude. In this case, nonlinear system response is obtained, which in accordance with methodology presented in this Article can be represented as a sum of the linear part of response (first-order FRF, i.e., EC admittance) and higher harmonics. In summary, one has to keep in mind that the elements of the EC system in
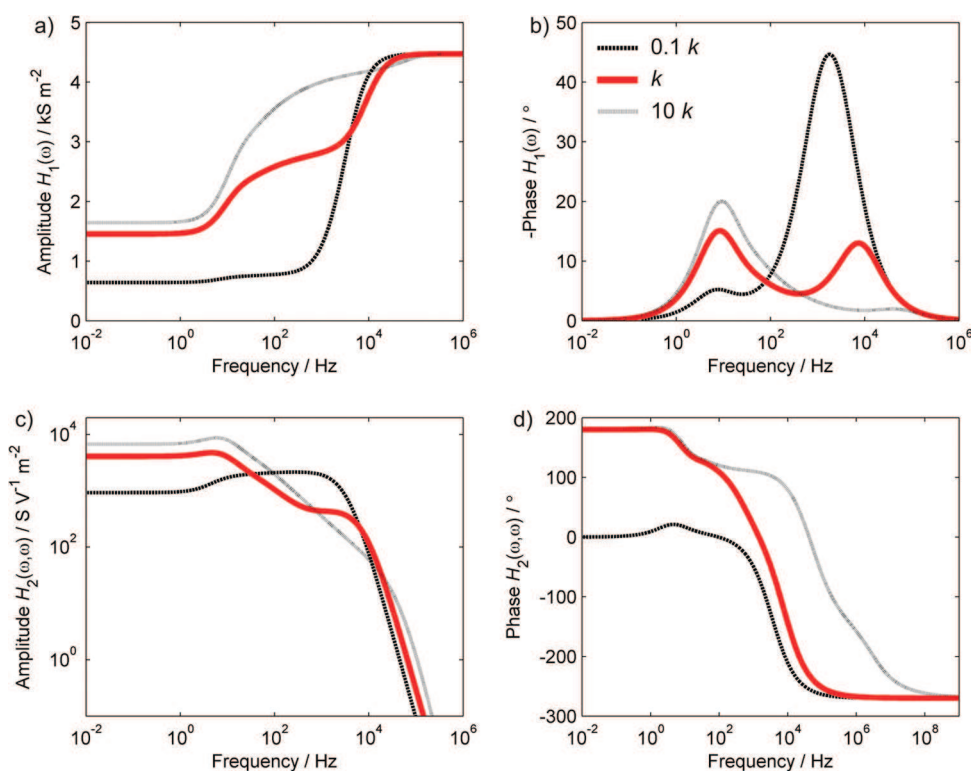
Figure 1. Influence of the reaction rate constant on (a) the amplitude and (b) the phase shift of the first-order FRF and (c) the amplitude and (d) the phase shift of second-order FRF. Other reaction parameters were fixed to their reference values (Table 3).

reality are nonlinear, and this nonlinearity will be contained in second and higher order FRFs. It can be envisaged that physically the second and higher order FRFs represent nonlinear contributions of the typical elements of the EC system (e.g., charge transfer resistance, diffusion resistance).

3. RESULTS AND DISCUSSION

In the previous sections, a step-by-step derivation of the first- and second-order FRFs for the EC ferrocyanide oxidation was presented. As can be seen from eqs 27 and 28 and 35−37, rather complex analytical solutions for $H_1(\omega)$ and $H_2(\omega,\omega)$ are obtained, without direct elucidation of the influence of different reaction parameters on the FRFs. To test this influence, we used the derived expressions for $H_1(\omega)$ and $H_2(\omega,\omega)$ for numerical simulations of the frequency spectra in MATLAB software. The reaction parameters were varied around their reference values, as defined in Table 3. (The reference values were chosen as typical for this system according to the measurements and literature data; for details, see Part II of this Article[18].) In the following sections, the influence of the tested parameters on $H_1(\omega)$ and $H_2(\omega,\omega)$ frequency spectra is discussed.

3.1. Influence of the Reaction Rate Constant on the FRFs. The calculated first- and the second-order FRFs for the reference value of the reaction rate constant and two other values differing from the reference value by an order of magnitude (Table 3) are presented in Figure 1 as the amplitude and phase shift spectra. The amplitude of the first-order FRF (Figure 1a) for reference value of the reaction rate constant shows high- and low-frequency asymptotes and a plateau in the middle-frequency range. These features correspond to different processes that dominate in different parts of the frequency spectra and can be

assigned to ohmic (high frequencies), charge transfer (mid-frequencies), and finite diffusion (low frequencies) processes. This dependence is expected for the diffusion-controlled charge transfer reaction.[8,16]

The phase shift spectra of the first-order FRF (Figure 1b) contain similar information as the amplitude spectra, represented by the appearance of two phase shift peaks. Unlike the first-order FRF, the amplitude of the second-order FRF (Figure 1c) for the reference value of the reaction rate constant shows only low-frequency asymptote and a plateau in the middle-frequency range. In the high-frequency range, the amplitude of the second-order FRF goes infinitesimally to zero when $\omega \rightarrow \infty$. This is understandable because this part of the spectra is dominated by ohmic resistance, which is essentially an element producing a linear behavior. It follows that the amplitude of the second-order FRF truly quantifies the nonlinearity.

The phase shift of the second-order FRF (Figure 1d) decreases continuously from 180° asymptote at low frequencies to −270° asymptote at high frequencies. In the middle frequency range, a shoulder (at ca. 10^2 Hz) and a small peak (at ca. 1 Hz) appear. They correspond to a shoulder and a peak, respectively, seen in the amplitude spectra in the similar frequency range (Figure 1c).

The change of the reaction rate constant does not produce any qualitative changes of the first-order FRF, which can be observed in the amplitude (Figure 1a) and the phase spectra (Figure 1b). The increase or decrease in the reaction rate constant changes only the relative dominance of the charge transfer step with respect to the diffusion. The increase in the reaction rate constant decreases the charge transfer resistance, which reflects in shifting of the charge transfer phase peak toward higher frequencies as well as in decrease in the peak intensity (ca. 3° in comparison
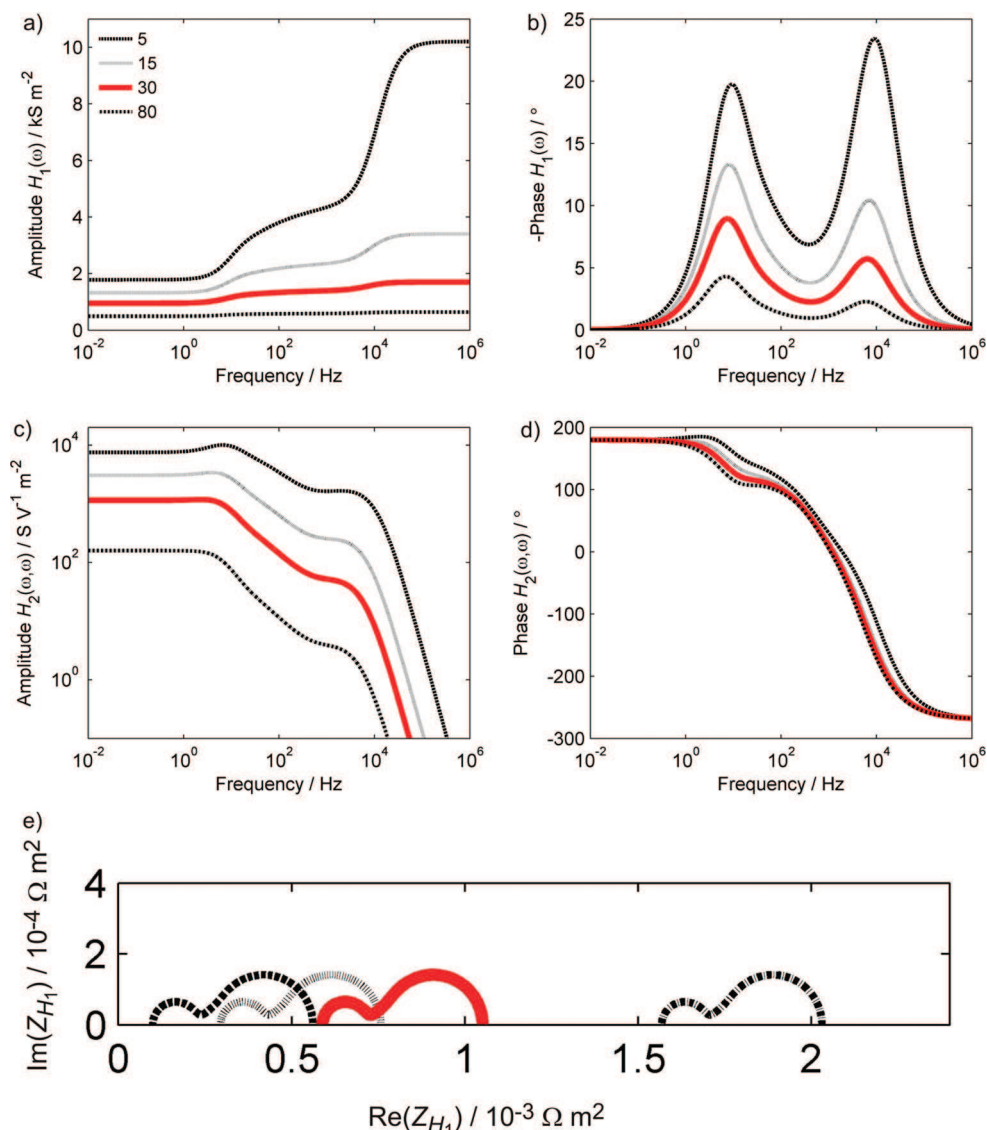
Figure 2. Influence of the ohmic resistance (R_Ω/Ω) on: (a) the amplitude and (b) phase shift of the first-order FRF and (c) the amplitude and (d) phase shift of the second-order FRF. (e) Nyquist plots for different R_Ω obtained from the first-order FRF. Other reaction parameters were fixed to their reference values (Table 3).

with ca. 12° in the reference spectra) (Figure 1b). Similar behavior can be observed by inspecting the phase shift peak assigned to diffusion, for which an increase in the peak intensity and a shift toward higher frequencies are clearly visible.

As in the case of the first order FRF, the change of the reaction rate constant produces only quantitative changes in the second-order FRF spectra, which again can be clearly seen in the phase spectra (Figure 1d). In the amplitude spectra (Figure 1c), the relative intensities of the plateau in the frequency range from ca. 10^4 to 10^3 Hz (assigned to charge transfer nonlinearity) and a peak around 10 Hz (assigned to diffusion-caused nonlinearity) are different with respect to the reference spectra. The increase in the reaction rate constant increases the relative dominance of the diffusion, which can be followed by an increase in the intensity of the peak. In a similar manner, the decrease in the reaction rate constant increases the contribution of the charge transfer step, which can again be followed by a more expressed plateau in the frequency range from ca. 10^4 to 10^2 Hz. It should also be noticed

that the phase of the second-order FRF tends to 0 for low and to π for higher values of the reaction rate constant at low frequencies. This means that the low-frequency asymptotic value of the second-order FRF is positive for low values of k (dominant charge transfer nonlinearity) and negative for higher values of k (dominant diffusion nonlinearity).

3.2. Influence of Solution Resistance and Double-Layer Capacitance. As already discussed, the potential as an input signal, in addition to the "real" electrode potential, contains a so-called ohmic drop contribution (eq 11). The influence of the ohmic drop on the first- and second-order FRFs was checked by varying the ohmic resistance, R_Ω, in the range from 5 to 80 Ω (Table 3 and Figure 2). In these simulations, the "real" electrode potential was kept constant (Table 3), whereas the input potential was changing with R_Ω according to eq 11. The variation of R_Ω influences the first-order FRF only quantitatively, whereas all characteristic features of the spectra were qualitatively not affected (two plateaus in the amplitude spectra (Figure 2a) and
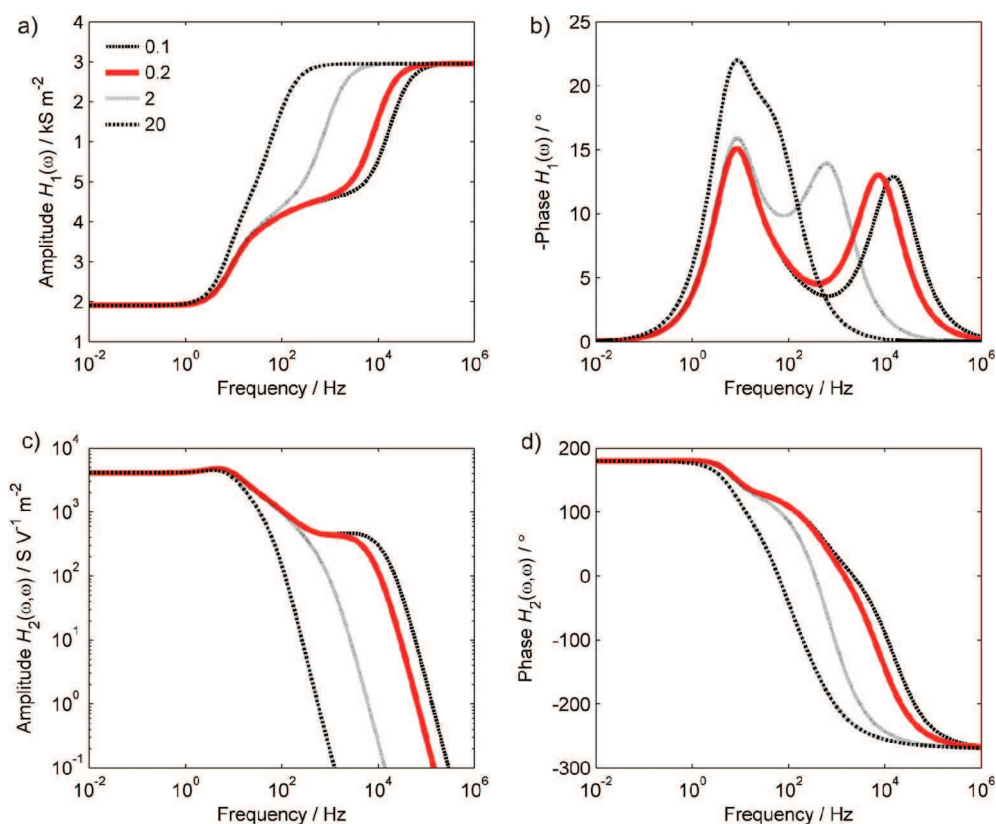
17347

dx.doi.org/10.1021/jp201297v |*J. Phys. Chem. C* 2011, 115, 17341–17351

Figure 3. Influence of double-layer capacitance (C_{dl}/F m^{-2}) on: (a) the amplitude and (b) phase shift of the first-order FRF and (c) the amplitude and (d) phase shift of the second-order FRF. Other reaction parameters were fixed to their reference values (Table 3).

two-peak appearance in the phase spectra (Figure 2b)). This can be also clearly seen in the Nyquist plot presentation of the reciprocal of the first-order FRF (which corresponds to EC impedance) (Figure 2e), where it is obvious that the EIS spectra remain unchanged and show only different offsets corresponding to different ohmic drops in the solution. In the case of $H_2(\omega,\omega)$, the variation of the ohmic drop causes not only quantitative but also qualitative changes (Figure 2c,d). As already discussed, the reference spectrum shows two characteristic features (Figure 2c,d): a plateau and a peak, which can be assigned to the charge transfer and diffusion-caused nonlinearity. Increase in the ohmic resistance influences to a greater extent the small peak at ca. 10 Hz, which shows a tendency to diminish at higher ohmic drop values in both amplitude and phase shift spectra. From these considerations, it follows that the higher values of ohmic resistance can "mask" the contribution of the diffusion process to the nonlinearity of EC reactions.

The influence of the double-layer capacitance is checked in the range from 0.1 to 20 F m^{-2}, with the reference value of 0.2 F m^{-2} as a common value for smooth metal surfaces. The low limit value of 0.1 F m^{-2} can correspond to the double-layer capacitance value of some nonactivated carbonaceous materials,[19] whereas the high limit (20 F m^{-2}) can correspond to double-layer capacitance of porous electrodes of extended real surface area. (It should be noted that the double-layer capacitance values are expressed with respect to geometrical surface area.) The obtained data are presented in Figure 3.

The increase in the double-layer capacitance influences both the first- and the second-order FRFs in a similar way. As can be seen in Figure 3, the characteristic features of the spectra (e.g., the

plateaus in the middle-frequency range in the first- and second-order FRFs' amplitude spectra), which correspond to the charge transfer process, are mostly affected. This can be clearly observed in the first-order FRF phase spectra (Figure 3b), where the charge transfer phase shift peak moves toward the lower frequency range and merges with the diffusion-related phase shift peak as the double-layer capacitance increases. The relative difference between the peak heights appears not to be affected by C_{dl}.

The processes of double-layer charging/discharging and charge transfer take place in parallel during dynamic perturbation of the EC system (eq 9). For high enough C_{dl} values, the charging/discharging current can be considerably higher than that related to charge transfer and can thus dominate the response. This is clearly seen in the spectra of the second-order FRF (Figure 3c,d), where the features related to charge transfer diminish as C_{dl} increases, with diffusion-related features (low-frequency peak) being almost unaffected. The simulations with different C_{dl} values lead to the conclusion that the contribution of the charge transfer to the NLFR will be rather negligible for the EC systems with the working electrodes of high real surface areas.

3.3. Influence of the Mass Transport Parameters. The considerations in the previous sections indicated that mass transport phenomena influence the FRFs mostly in the low-frequency domain. In this section, the influence of the rotation rate and diffusion coefficients of the reacting species on the NLFR of ferrocyanide oxidation kinetics is analyzed.

The influence of the electrode rotation rate on the first- and the second-order FRFs is shown in Figure 4 for two rotation rates. For the sake of comparison, the FRFs for pure Butler—Volmer kinetics (no diffusion limitations[16]) are also shown in
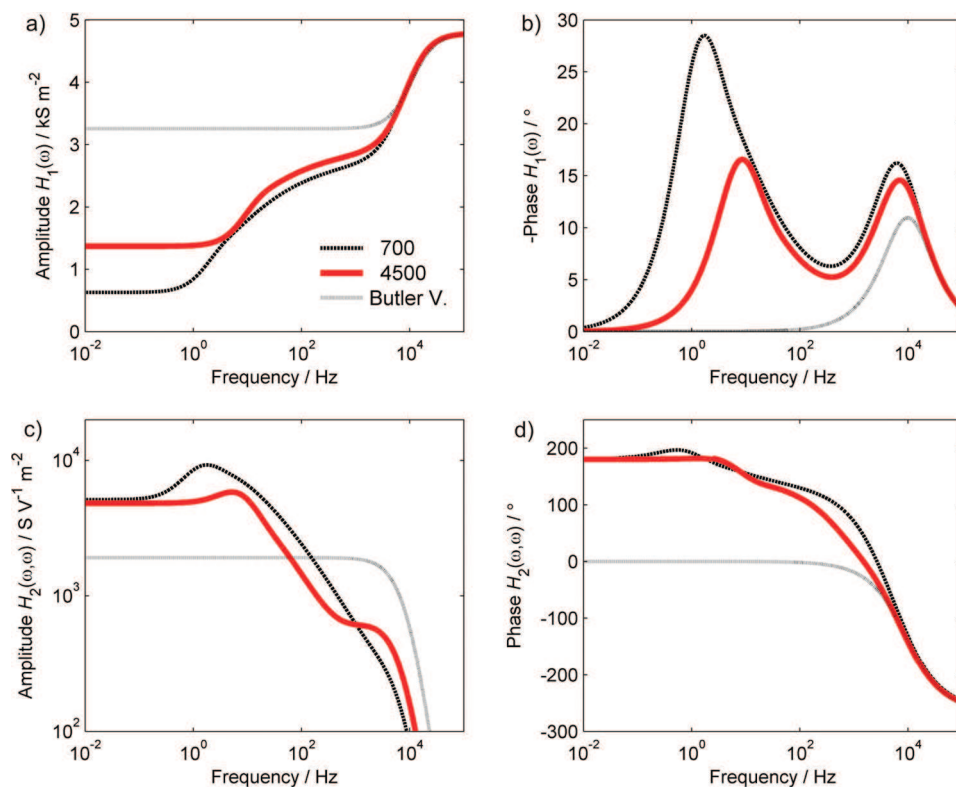
Figure 4. Influence of the rotation rate (ω_r/rpm) on: (a) the amplitude and (b) phase shift of the first-order FRF and (c) the amplitude and (d) phase shift of the second-order FRF. Other reaction parameters were fixed to their reference values (Table 3).

Figure 5. Influence of the diffusion coefficient of red ($D_{red}/10^{-10}$ m^2 s^{-1}) on: (a) the amplitude and (b) phase shift of the first-order FRF and (c) the amplitude and (d) phase shift of the second-order FRF. Other reaction parameters were fixed to their reference values (Table 3).
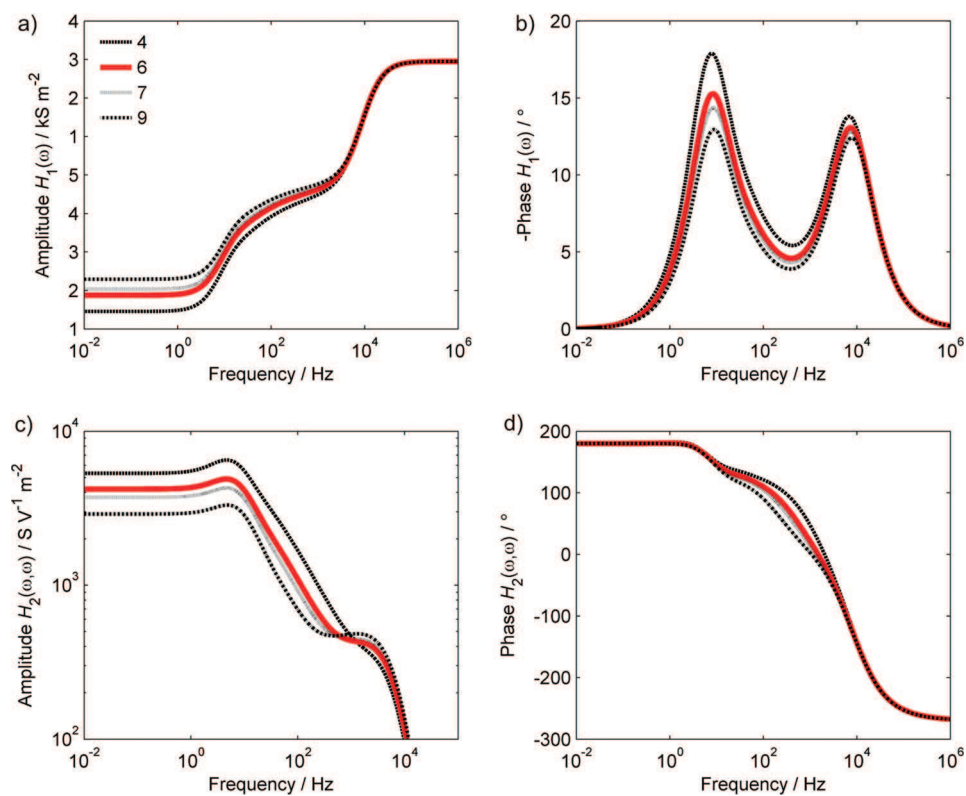
Figure 6. Influence of the diffusion coefficient of ox $(D_{ox}/10^{-10}\ m^2\ s^{-1})$ on: (a) the amplitude and (b) phase shift of the first-order FRF and (c) the amplitude and (d) phase shift of the second-order FRF. Other reaction parameters were fixed to their reference values (Table 3).
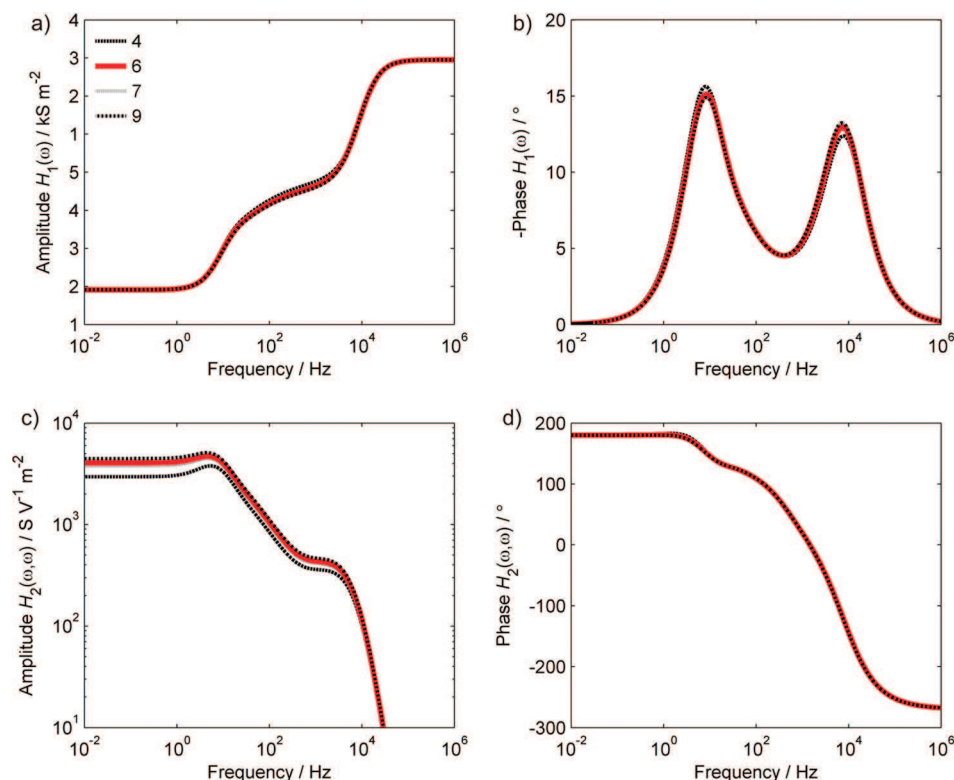
Figure 4. In the absence of mass transfer limitations (pure BV kinetics), the amplitude of the $H_1(\omega)$ reaches low-frequency asymptote, which clearly corresponds to charge transfer resistance, already in the middle-frequency range (Figure 4a), and only one phase shift peak, which corresponds to charge transfer process, can be observed (Figure 4b). Analogous to $H_1(\omega)$, in the case of the $H_2(\omega,\omega)$ in absence of mass transfer limitations, the only nonlinearity originates from the charge transfer, and it can be clearly correlated to the small plateau in the frequency range from 10^3 to 10^2 Hz (Figure 4c,d). If mass transfer limitations are involved, then in addition to charge transfer nonlinearity (a small plateau in the frequency range from 10^3 to 10^2 Hz already seen in the case of BV kinetics), a peak at ca. 1 Hz appears (Figure 4c,d). The intensity of the amplitude peak increases with the decrease in electrode rotation rate (Figure 4c), whereas the peak in the phase spectrum shifts toward lower frequencies (Figure 4d). This clearly demonstrates the less pronounced influence of the diffusion-caused nonlinearity at higher electrode rotation rates.

The variation of the diffusion coefficients of red (reactant) and ox (product) produces only quantitative changes of the first- and second-order FRFs' spectra within the investigated frequency range (Figures 5 and 6). The influence of the diffusion coefficient of red (Figure 5) is similar to the influence of increasing the electrode rotation rate, and, as it has already been discussed, this influence is more pronounced in the low-frequency range of the spectra. As can be seen in the second-order FRF amplitude spectra (Figure 5c), the increase in the diffusion coefficient of red suppresses the diffusion-caused nonlinearity (intensity of the peak at 1 Hz decreases) and brings forward charge-transfer-induced nonlinearity. (A shoulder in the frequency range 10^3-10^2 Hz at

low values of the diffusion coefficient turns into a well-defined plateau at higher values of the diffusion coefficient.)

Variation of the diffusion coefficient of ox (Figure 6) produces only small changes in the first-order FRF spectra (Figures 6a,b). More significant are the changes observed in the second-order FRF amplitude spectra (Figure 6c), where the position of the low-frequency asymptote was sensitive to the changes in diffusion coefficient of ox. Here the opposite tendency in comparison with the changes of the diffusion coefficient of red has been observed. The decrease in the asymptotic value with the decrease in the diffusion coefficient of ox clearly shows that the nonlinearity caused by the rate of product removal from the electrode surface is suppressed for higher values of the diffusion coefficient of the product.

4. CONCLUSIONS

The method of NLFRA was applied in a theoretical study of the nonlinear behavior of ferrocyanide electrooxidation as a simple model EC reaction. Analytical expressions of the first- and second-order FRFs were derived for the potential as the input periodic signal. The influence of different parameters, such as the heterogeneous rate constant, the double-layer capacitance, the diffusion coefficients of the reacting species, the rotation rate of the working electrode, and the solution ohmic resistance on the FRFs was analyzed. In general, the nonlinear information on the system is contained in the second-order FRF. In the case of ferrocyanide electrooxidation, the main sources of the nonlinearity are charge transfer and diffusion of the reacting species, and they are clearly recognized in the frequency spectra of the second-order FRF; a plateau and a peak are assignable to the

charge-transfer- and the diffusion-induced nonlinearity. These features are parameter-sensitive. It has been shown that for some combination of the reaction parameters one of these features becomes more pronounced relative to the other one. The method of NLFR thus offers a possibility for direct estimation of the parameters in EC kinetics based on analysis of the observed features of the FRFs' spectra, which is going to be a subject of further work.

■ AUTHOR INFORMATION

Corresponding Author
*Tel: +49 391 6110 319. Fax: +49 391 6110 553. E-mail: vidakovi@mpi-magdeburg.mpg.de.

■ ACKNOWLEDGMENT

■ REFERENCES

(1) Vidaković, T.; Christov, M.; Sundmacher, K. *J. Electroanal. Chem.* **2005**, *580*, 105–121.

(2) Krewer, U.; Christov, M.; Vidaković, T.; Sundmacher, K. *Electroanal. Chem.* **2006**, *589*, 148–159.

(3) Batista, E. A.; Malpass, G. R. P.; Motheo, A. J.; Iwasita, T. *Electrochem. Commun.* **2003**, *5*, 843–846.

(4) Folger, H. S. *Essentials of Chemical Reaction Engineering*; Prentice Hall: Upper Saddle River, NJ, 2010; p 340.

(5) Harrington, D. A. *Can. J. Chem.* **1997**, *75*, 1508–1517.

(6) Boillot, M.; Didierjean, S.; Lapicque, F. *J. Appl. Electrochem.* **2004**, *34*, 1191–1197.

(7) Bai, L.; Harrington, D. A.; Conway, B. E. *Electrochim. Acta* **1987**, *32*, 1713–1731.

(8) Macdonald, J. R.; Johnson, W. B. *Impedance Spectroscopy, Theory, Experiment and Applications*; Barsoukov, E., Macdonald, J. R., Eds.; John Wiley & Sons: New York, 2005; p 6.

(9) Fabregat-Santiago, F.; Garcia-Belmonte, G.; Bisquert, J.; Zaban, A.; Salvador, P. *J. Phys. Chem. B* **2002**, *106*, 334–339.

(10) Kumar, R.; Kant, R. *J. Phys. Chem. C* **2009**, *113*, 19558–19567.

(11) Huang, Q. A.; Hui, R.; Wang, B. W.; Zhang, H. J. *Electrochim. Acta* **2007**, *52*, 8144–8164.

(12) Bensmann, B.; Petkovska, M.; Vidaković-Koch, T.; Hanke-Rauschenbach, R.; Sundmacher, K. *J. Electrochem. Soc.* **2010**, *157*, B1279–B1289.

(13) Kadyk, T.; Hanke-Rauschenbach, R.; Sundmacher, K. *J. Electroanal. Chem.* **2009**, *630*, 19–27.

(14) Mao, Q.; Krewer, U.; Hanke-Rauschenbach, R. *Electrochem. Commun.* **2010**, *12*, 1517–1519.

(15) Kadyk, T.; Hanke-Rauschenbach, R.; Sundmacher, K. *J. Appl. Electrochem.* **2011**, doi: 10.1007/s10800-011-0298-8.

(16) Bard, A. J.; Faulkner, L. R. *Electrochemical Methods*; Wiley: New York, 1980; pp 280−315.

(17) Weiner, D. D.; Spina, J. F. *Sinusoidal Analysis and Modeling of Weakly Nonlinear Circuits*; Van Nostrand Reinhold: New York, 1980.

(18) Panić, V.; Vidaković-Koch, T.; Andrić, M.; Petkovska, M.; Sundmacher, K. *J. Phys. Chem. C* **2011**, doi: http://dx.doi.org/10.1021/jp201300a.

(19) Kinoshita, K. *Carbon: Electrochemical and Physicochemical Properties*; Wiley: New York, 1988.

17351

dx.doi.org/10.1021/jp201297v |*J. Phys. Chem. C* 2011, 115, 17341–17351

[TVK4]

V. Panić, T. Vidaković-Koch, M. Andrić, M. Petkovska, K. Sundmacher

Non-Linear Frequency Response Analysis of the Ferrocyanide Oxidation Kinetics: Part II – Experimental Validation

ARTICLE

Nonlinear Frequency Response Analysis of the Ferrocyanide Oxidation Kinetics. Part II. Measurement Routine and Experimental Validation

Vladimir V. Panić,[§,†] Tanja R. Vidaković-Koch,[*,∥] Milan Andrić,[‡] Menka Petkovska,[‡] and Kai Sundmacher[§,∥]

[§]Max Planck Institute for Dynamics of Complex Technical Systems, Sandtorstrasse 1, 39106 Magdeburg, Germany

[†]Institute of Chemistry, Technology and Metallurgy, University of Belgrade, Njegoševa 12, 11000 Belgrade, Serbia

[∥]Process Systems Engineering, Otto-von-Guericke University Magdeburg, Universitätsplatz 2, 39106 Magdeburg, Germany

[‡]Faculty of Technology and Metallurgy, University of Belgrade, Karnegijeva 4, 11000 Belgrade, Serbia

ABSTRACT: Kinetics of ferrocyanide electrooxidation was investigated by nonlinear frequency response analysis (NLFRA) of current output to the sinusoidal large-amplitude potential perturbation input. The aim was to establish a measurement routine and to validate experimentally the NLFRA method on an example of a simple electrochemical reaction comprising charge and mass transfer. The first-order frequency response function (FRF) contains quasi-linear information on the reaction kinetics and corresponds to electrochemical admittance. The nonlinear fingerprint of the system is contained in the second-order FRF. The first- and second-order FRFs are

determined from experimental first and second harmonics. Their intensities depend on the input signal amplitude, which has to be chosen carefully to avoid the contributions of higher order harmonics. The influence of the potential and electrode rotation speed on the first- and second-order FRFs has been studied. The experimentally obtained FRFs are compared with the theoretical FRFs determined in Part I of this work. The theoretical FRFs can predict all essential experimental observations. These findings indicate that additional information on reaction kinetics can be gained from the analysis of the second-order FRF.
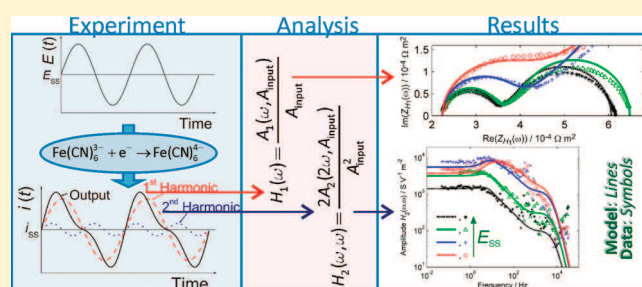
1. INTRODUCTION

Nonlinear frequency response (NLFR) can be regarded as a generalization of the traditional electrochemical impedance spectroscopy (EIS), extended to a nonlinear range by application of large input amplitudes. It is to be expected that the NLFR analysis (NLFRA) of electrochemical (EC) systems, especially those with complex mechanisms and several possible reaction paths, can give additional information and enable discrimination between reaction models. In our recent theoretical study,[1] the NLFR approach has been applied for investigation of electrochemical methanol oxidation kinetics. It was shown that the second-order frequency response function (FRF) can be used for model discrimination. The NLFR method is still a novelty in the EC community, and the measurement routine as well as the interpretation of the measured data have not yet been established. For experimental and theoretical validation of the NLFR approach, ferrocyanide oxidation kinetics, involving a diffusion-controlled 1e⁻ transfer step, has been chosen in this Article as a simple case study. A theoretical treatment of NLFR of ferrocyanide oxidation kinetics has been presented in Part I of this Article.[2] Theoretical FRFs up to the second order were derived. It was shown that the FRFs should be sensitive to all kinetic and mass transport parameters. In the present Article, the measurement routine for experimental determination of the FRFs up to the second order is developed. The influence of the potential and rotation speed of the working electrode on the FRFs features is

analyzed. Finally, the experimental FRFs are compared with the theoretical FRFs derived in Part I of this Article.[2]

1.1. Relationship Between Frequency Response Functions and Output Harmonics. According to the NLFRA of EC systems,[1,2] the quasi-stationary response of a weakly nonlinear system to a periodic (sinusoidal or cosinusoidal) perturbation of the cosinusoidal form with the amplitude A around the steady-state, for a current as an output, is given by the following equation[2]

$$
\begin{aligned}
i(t) = i_{ss} &+ \frac{A}{2}(H_1(\omega)e^{j\omega t} + H_1(-\omega)e^{-j\omega t}) \\
&+ \left(\frac{A}{2}\right)^2 (H_2(\omega,\omega)e^{2j\omega t} + 2H_2(\omega,-\omega)e^0 \\
&+ H_2(-\omega,-\omega)e^{-2j\omega t}) \\
&+ \left(\frac{A}{2}\right)^3 (H_3(\omega,\omega,\omega)e^{3j\omega t} \\
&+ 3H_3(\omega,\omega,-\omega) + 3H_3(\omega,-\omega,-\omega) \\
&+ H_3(-\omega,-\omega,-\omega)e^{-3j\omega t}) + \dots
\end{aligned}
\tag{1}
$$

where ω is the angular frequency in rad s^{-1}, $j = (-1)^{1/2}$, and $H_1(\omega)$ is the first-order FRF of an EC system. The remaining functions $H_n(\omega, ..., \omega)$ for $n \geq 2$ represent higher-order FRFs that contain the information about nonlinearity of the investigated electrochemical system. If eq 1 is rearranged as the sum of terms of the same angular frequencies, then[2]

$$
\begin{aligned}
i(t) = i_{ss} &+ \left(\frac{A^2}{2}H_2(\omega, -\omega)e^0 + ...\right) \\
&+ e^{j\omega t}\left(\frac{A}{2}H_1(\omega) + \frac{3A^3}{8}H_3(\omega, \omega, -\omega) + ...\right) \\
&+ e^{-j\omega t}\left(\frac{A}{2}H_1(\omega) + +\frac{3A^3}{8}H_3(\omega, \omega, -\omega) + ...\right) \\
&+ e^{2j\omega t}\left(\frac{A^2}{4}(H_2(\omega, \omega) + ...)\right) \\
&+ e^{-2j\omega t}\left(\frac{A^2}{4}(H_2(-\omega, -\omega) + ...)\right) \\
&+ +e^{3j\omega t}\left(\frac{A^3}{8}(H_3(\omega, \omega, \omega) + ...)\right) \\
&+ e^{-3j\omega t}\left(\frac{A^3}{8}(H_3(-\omega, -\omega, -\omega) + ...) + ...\right)
\end{aligned}
$$

$$ (2) $$

Amplitude-dependent terms in eq 2, defined as

$$
\begin{aligned}
H_{q,\,I}(\omega, A) &= \frac{A}{2}H_1(\omega) + \frac{3A^3}{8}H_3(\omega, \omega, -\omega) + ... \\
H_{q,\,II}(2\omega, A) &= \frac{A^2}{4}(H_2(\omega, \omega) + ...) \\
H_{q,\,III}(3\omega, A) &= \frac{A^3}{8}(H_3(\omega, \omega, \omega) + ...)
\end{aligned}
$$

$$ (3) $$

are the so-called quasi-response functions (QRFs).[2] They are actually the Fourier transforms of the harmonics of the output. These QRFs can be determined experimentally using an experimental setup similar to that for EIS but capable of registering individual harmonics.[3] As can be seen in eq 3, the dominant term of an individual harmonic is proportional to the corresponding FRF ($H_1(\omega)$ in $H_{q,I}(\omega,A)$; $H_2(\omega,\omega)$ in $H_{q,II}(2\omega,A)$,...). However, depending on the degree of the system nonlinearity and the input amplitude, lower order QRFs can be affected by higher order FRFs (odd-order QRFs by higher odd-order FRFs, and even-order by higher even-order FRFs). If the input amplitude is carefully chosen so that FRFs higher than the second order are negligible in the response, then the first two QRFs will contain the contributions of their basic FRFs only (the first of $H_1(\omega)$ and the second of $H_2(\omega,\omega)$). It follows from eq 3 that the amplitudes of the first- and second-order FRFs can be calculated from the measured first- and second-order QRFs ($H_{q,I}(\omega,A)$ and $H_{q,II}(2\omega,A)$)

$$
H_1(\omega) = \frac{H_{q,\,I}(\omega, A)}{A}, \quad H_2(\omega, \omega) = \frac{2H_{q,\,II}(2\omega, A)}{A^2} \quad (4)
$$

2. EXPERIMENTAL SECTION

The experiments were performed in a standard three-electrode electrochemical cell equipped with a glassy carbon RDE as the working electrode (0.20 cm^2), Pt wire as the quasi-reference, and Pt mesh as the counter electrode. The electrolyte (N$_2$-purged) was equimolar solution of K$_4$[Fe(CN)$_6$] and K$_3$[Fe(CN)$_6$] of the concentration of 20 mol m^{-3} each, which contained 1.0 mol dm^{-3} KCl as supporting electrolyte. All potentials are expressed with respect to the Pt quasi-reference electrode (as overpotentials). The open-circuit potential readings were always in the range $\pm 10 \ \mu$V.

Prior to each immersion into the solution, the GC disk was polished with alumina (0.05 μm) and cleaned in an ultrasonic bath for a few seconds. The measurements were done at 25.0 °C using a Solartron 1287 potentiostat/galvanostat coupled to Solartron 1250 frequency response analyzer. The working electrode was preconditioned by cycling the potential between -0.4 and 0.75 V at a scan rate of 100 mV s^{-1} in 20 cycles, followed by five-fold repetition of a -0.4 V (5 s)/0.4 V (5 s) potentiostatic sequence. The conditioning was done potentiostatically for 10 s at a desired steady-state value. Periodic perturbations of the potential with the amplitudes of 10, 30, and 50 mV rms around different steady-state values (7.5, 22, 75, and 120 mV), were used as input, whereas separate harmonics, up to the third order, of the periodic output current signal were recorded (technical details related to the recording of the harmonics can be found in Help files of ZPlot software, Scribner Associates, Southern Pines, NC, 2007 (http://www.scribner.com/general-electrochemistry-software.html)). All measurements have been performed in the frequency range from 65 kHz to 1 mHz.

To check the influence of mass transport limitations on the NLFR of ferrocyanide oxidation, experiments at two different rotation speeds of the working electrode (700 and 4500 rpm) were performed at a fixed value of the potential (55 mV).

Keeping in mind that the water solutions of K$_4$[Fe(CN)$_6$] and K$_3$[Fe(CN)$_6$] are unstable to some extent,[4] every experiment was performed with a freshly prepared solution.

3. RESULTS AND DISCUSSION

3.1. Steady-State Behavior of the Experimental System. Because steady-state experiments are giving a good orientation of the system behavior in broader potential range and most experimenters are familiar with this technique, we show first the steady-state behavior of ferrocyanide oxidation before starting to discuss linear and nonlinear system response in more detail. As can be seen in Figure 1, the ferrocyanide oxidation follows the typical behavior of a mass transfer limited reaction, with a relatively narrow mixed activation—diffusion control region and a well-expressed limited current region at low rotation rate. The increase in the rotation speed reduces the mass transfer resistance, giving rise to the diffusion-limited current at higher rotation rates. The experimental data are well described with the model (line presentations in the Figure 1) presented in the Part I[2] (eqs 2 and 17) of this manuscript and with the parameter values given in Table 1. To check the influence of two main "resistances", charge transfer and diffusion resistance on the overall kinetics, we have performed the dynamic experiments in the mixed activation—diffusion control region (potential range from 7.5 to 120 mV) and at rotation speeds of 1500 or 4500 rpm because the system at low rotation rate is more dominated by

Table 1. Values of the Parameters of the Ferrocyanide Oxidation System Used for the Calculation of Theoretic Frequency Response Functions

double-layer capacitance, $C_{dl}/F\ m^{-2}$	0.20
symmetry factor, β	0.50
rate constant, $k/m\ s^{-1}$	1.15×10^{-4}
dynamic viscosity, $\nu/m^2\ s^{-1}$	1.0×10^{-6}
ohmic resistance, Ω	11.4
diffusion coefficient of $[Fe(CN)_6]^{-4}$, $D([Fe(CN)_6]^{-4})/m^2\ s^{-1}$	6.2×10^{-10}
diffusion coefficient of $[Fe(CN)_6]^{-3}$, $D(Fe(CN)_6]^{-3})/m^2\ s^{-1}$	7.2×10^{-10}

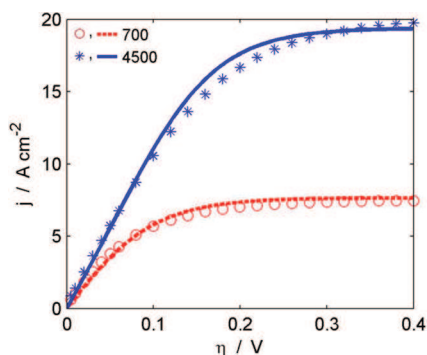**Figure 1.** Steady-state polarization curves of the ferrocyanide oxidation at GC electrode (electrolyte: 20 mol m^{-3} [Fe(CN)$_6$]$^{4-/3-}$, 1.0 M KCl; t = 25.0 °C) at rotation speeds of 700 and 4500 rpm; symbols: measurements, lines: simulations according to eqs 2 and 17 from the Part I of the paper[2] and parameter values given in Table 1.

Figure 2. Influence of the input signal amplitude on the amplitude of the first- and third-order (a) and second-order (b) quasi-response functions (steady-state potential: 10 mV; electrolyte: 20 mol m^{-3} [Fe(CN)$_6$]$^{4-/3-}$, 1.0 M KCl; rotation speed: 1500 rpm; t = 25.0 °C).

diffusion resistance (Figure 1). To check the influence of the mass transfer, we have performed the dynamic experiments at steady-state potential value of 55 mV because under this condition at both rotation rates mixed activation–diffusion control conditions are satisfied.

3.2. Input Amplitude and Quasi-Response Functions. The influence of the input signal amplitude on the intensities of the first three QRFs for ferrocyanide oxidation at the potential of 7.5 mV is presented in Figure 2. The shape and all characteristic features of the first-order QRF recorded at different input amplitudes are similar and differ only in the QRF intensity. In general, the higher the input amplitude, the higher the intensity of the QRF amplitude. The second-order QRF responds to the increase in input amplitude in a similar way. The intensities of the second- and third-order QRFs are one to three orders of magnitude lower than the intensity of the first-order QRF for the same input amplitude. These can be followed by a higher level of noise, which is clearly seen in the case of the third harmonic at all input amplitudes and of the second one at the input amplitude of 10 mV. This indicates that the reliable second-order QRF can be obtained at the input amplitudes above 30 mV.

3.3. Relations Between Quasi-Response and Frequency Response Functions. The experimentally determined first- and second-order QRFs are further "normalized" with respect to the input amplitude in accordance with eq 4, and the calculated first- and second-order FRFs are shown in Figure 3.

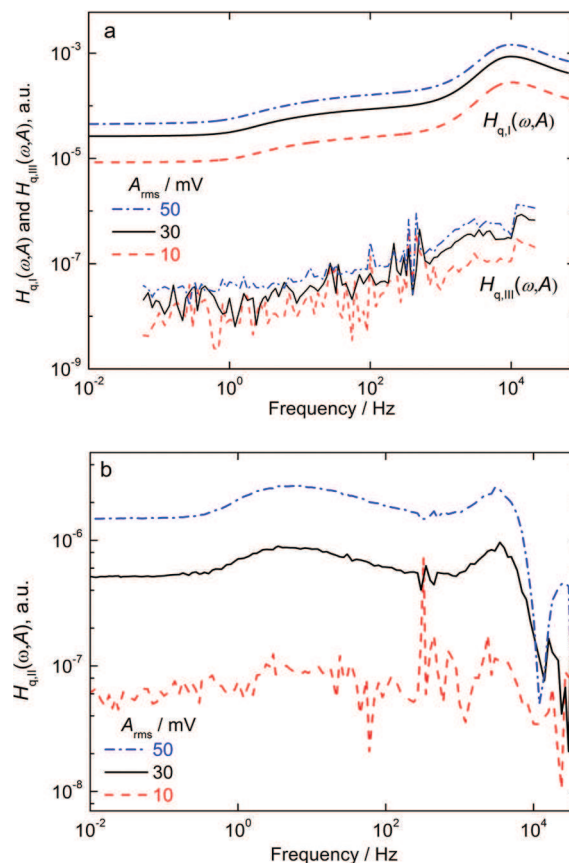The amplitude and the phase shift of the first-order FRF show some weak dependence on the input amplitude. This can be explained by the increasing contribution of the higher order FRFs in the experimentally determined first-order QRF at higher input amplitudes (eq 3). The observed differences can be additionally attributed to the sensitivity of ferrocyanide oxidation kinetics to the state of the electrode surface. This sensitivity was reported for different carbonaceous electrode materials[5−7] as well as for platinum.[8] Hence, the observed differences could be additionally caused by the changes of the state of the GC surface between and during the frequency sweep runs.

Unlike the first-order FRF, the second-order FRF does not show any dependence on the input amplitude in the range from 30 to 50 mV. Even at the amplitude of 10 mV, the intensity is similar to that recorded at 30 and 50 mV, despite the appreciable noise level. These results indicate that the input amplitude of 10 mV is sufficient for reliable determination of the first-order FRF, whereas for the determination of the second-order FRF higher amplitudes (30−50 mV) have to be used. In the present Article, input amplitude of 50 mV has been chosen for the determination of the second-order FRF because the level of noise was lower than that at the amplitude of 30 mV.

3.4. First-Order Frequency Response Function as Electrochemical Impedance. The amplitude of the first-order FRF shows two characteristic inflections that correspond to the two phase shift peaks observed in the phase shift plot (Figure 3). As already discussed, the $H_1(\omega)$ function relates to the linear part of the response and therefore is identical to the electrochemical admittance.[1,2] In Figure 4, the reciprocal
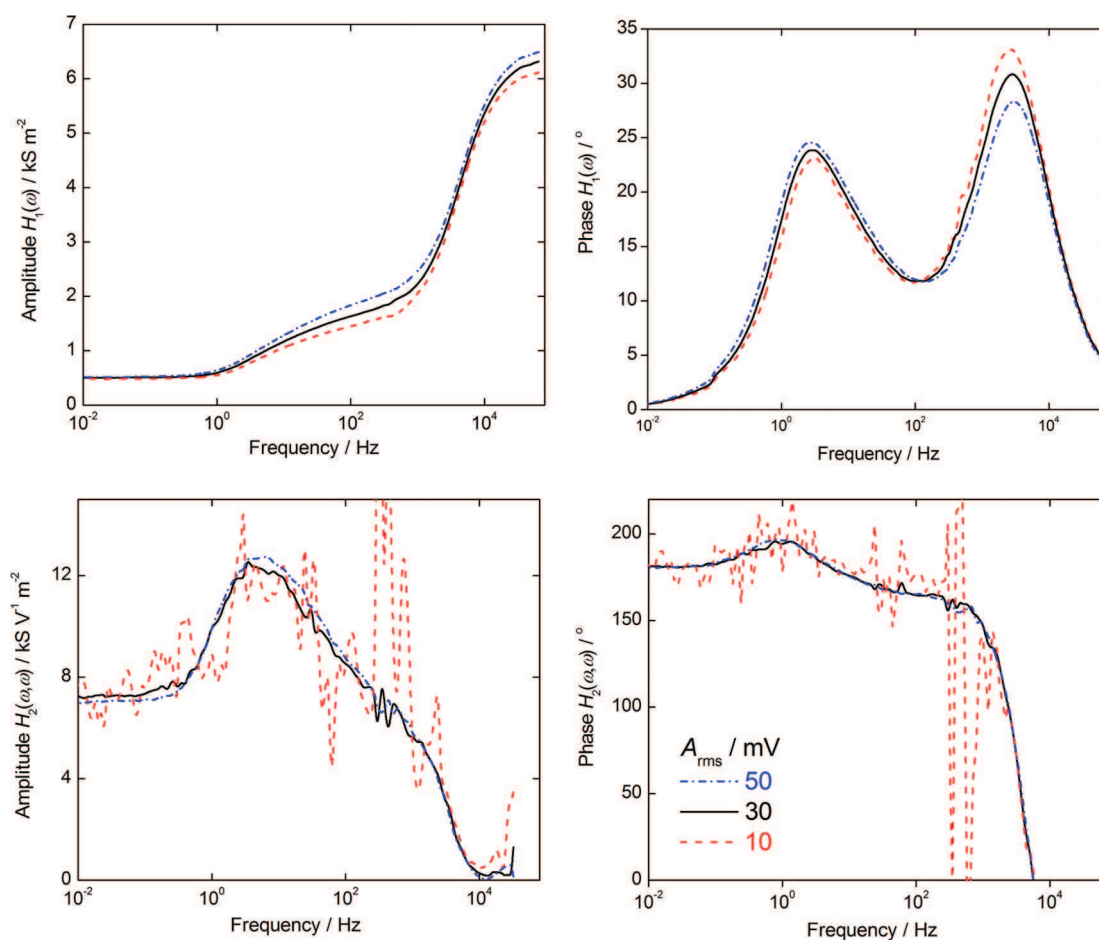
Figure 3. Amplitude and phase shift frequency spectra of the first- $(H_1(\omega))$ and second- $(H_2(\omega,\omega))$ order frequency response functions for different input signal amplitudes (steady-state potential: 10 mV; electrolyte: 20 mol m^{-3} $[Fe(CN)_6]^{4-/3-}$, 1.0 M KCl; rotation speed: 1500 rpm; $t = 25.0$ °C).
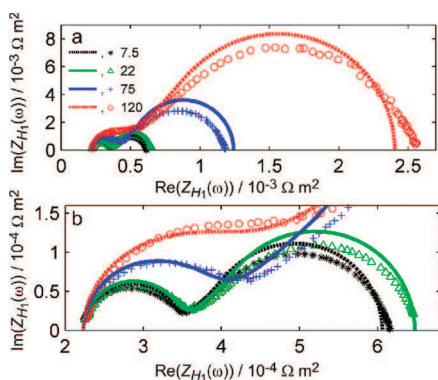

Figure 4. Complex plane plots of the first order function $(H_1(\omega))$ for different potentials (in millivolts); Symbols: experimental data; lines: theoretic curves: (a) whole spectra and (b) their high-frequency parts.

values of the experimental and calculated first-order FRFs $(H_1(\omega))$, in the form of Nyquist plots, are shown. The plots feature two well-developed semicircle loops (Figure 4a). The high-frequency loop, magnified in Figure 4b, is usually assigned to charge-transfer resistance and the low-frequency loop to mass transfer limitations.[9] The presence of the high-frequency loop is not always reported in literature; for example, Boillot et al.[10] observed only a part of the high-frequency semicircle,

probably because of relatively low higher frequency limit (10 kHz in comparison with 65 kHz in the present study). A well-developed high-frequency loop was also observed by Campbell and Peter,[11] who applied large-amplitude input current around open circuit potential for the same reaction on Au. The loop diameter in that Article,[11] observed at low overpotentials, agrees well with those in Figure 4.

The diameters of both the charge and the mass transfer semicircles increase with the increase in potential, which is in agreement with literature results.[5,12,13] If the high-frequency semicircle would be governed only by Butler–Volmer kinetics, then a decrease in the high-frequency semicircle diameter and the corresponding charge transfer resistance could be expected.[9] This is, however, not the case, which indicates that the high-frequency data are also affected by diffusion. Boillot et al.[10] obtained similar results from their theoretical approach to impedance behavior of the ferro/ferri couple. However, the experimental verification was hard on Pt RDE. The diameter of the low-frequency semicircle also increases with potential, suggesting an increase in the mass transfer resistance at more positive potentials. This behavior can be satisfactorily explained by a nonlinear mathematical model based on Butler–Volmer kinetics and including mass transfer by diffusion for reacting species, which was described in the first part of this Article.[2] As can be seen in Figure 4, the model can predict the
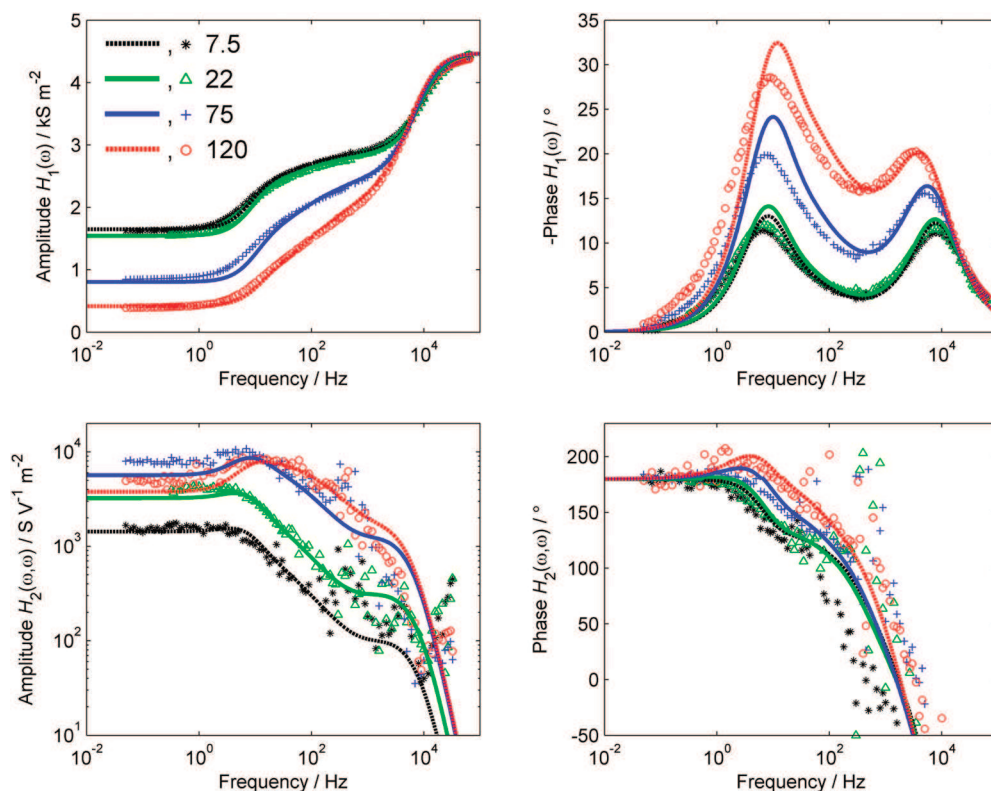
Figure 5. Amplitude and phase shift frequency spectra of the first- ($H_1(\omega)$) and second-order ($H_2(\omega,\omega)$) frequency response functions at different potentials (in millivolts); Symbols: experimental data; lines: theoretic curves (input amplitude: 50 mV rms; electrolyte: 20 mol m^{-3} $\left[\text{Fe(CN)}_6\right]^{4-/3-}$, 1.0 M KCl; rotation speed: 4500 rpm; t = 25.0 °C).

main experimental observations, and the calculated curves show very good agreement with the experimental data.

The parameter values used for calculation of the theoretical EIS spectra are presented in Table 1; similar values can be also found in the literature.[5,12−16] The same values were also used for calculation of the theoretical first- and second-order FRFs. As can be seen in Figure 4, the fitting in the high-frequency region is better than that in the low-frequency region. Experimental data in the low-frequency region show depressed semicircle in comparison with the model curves. Depressions of the EIS semicircles are usually explained in the literature by nonideality of the surface.[9] If equivalent electrical circuit representations were used for interpretation of the EIS data, then these surface nonidealities would be addressed by the introduction of the so-called constant-phase element.[17] The observed deviation in the present work can also be ascribed to the nonideality of the electrode surface, but, as discussed before, this can also be due to the instability of the ferrocyanide system[4] and to the difficulties in regaining the same electrode conditions between single-frequency runs.

3.5. Influence of the Electrode Potential on the first- and second-Order FRF. The first- and second-order FRFs, experimentally determined at different steady-state potentials are presented in Figure 5 along with the corresponding theoretical functions[2] calculated with the parameter values given in Table 1. The first-order FRF, as already discussed, is analogous to the electrochemical admittance, and, as can be seen in Figure 5, typical admittance Bode plot features with two phase shift peaks corresponding to the charge transfer and the mass transport-limited processes are obtained.[10] These characteristics of the

$H_1(\omega)$ spectra are also obtained from theoretic examinations (Figure 5).[2]

Similar to the first-order FRF, the amplitude and the phase of both experimental and calculated second-order FRFs show asymptotes in the low-frequency region at all potentials (Figure 5). The phase reaches an asymptote at 180° and shows no dependence on potential in this region (for comparison, phase shift of the first-order FRF in this region is 0° and also independent of the potential). The amplitude of the calculated second-order FRF in the frequency range from 10^4 to ca. 10^0 Hz shows two characteristic features, a relatively broad plateau in the frequency range from 10^4 to ca. 10^2 Hz, and a peak in the frequency range from 10^1 to ca. 10^0 Hz. Both features are sensitive to the change in potential. The intensity of the peak increases with the increase in the potential up to 75 mV, whereas opposite tendency has been observed in the case of the plateau. Similar features are also observed in the theoretical phase spectra of the second-order FRF. The theoretical predictions of the amplitude and the phase shift of the second-order FRF are in good agreement with the experimental data, and both character-istic features, the peak and the plateau, are fully observable in the experimental spectra, although the data are somewhat scattered, especially in the high-frequency region. The model qualitatively predicts the increase in the peak intensity up to 75 mV, followed by the decrease at 120 mV.

The change in the peak broadness for two potentials (relatively sharp peak at 75 mV transfers to a broad peak at 120 mV) is also predicted by the model. The meaning of these two characteristic features of the spectra is not straightforward. The theoretical analysis shown in the first part of this Article with
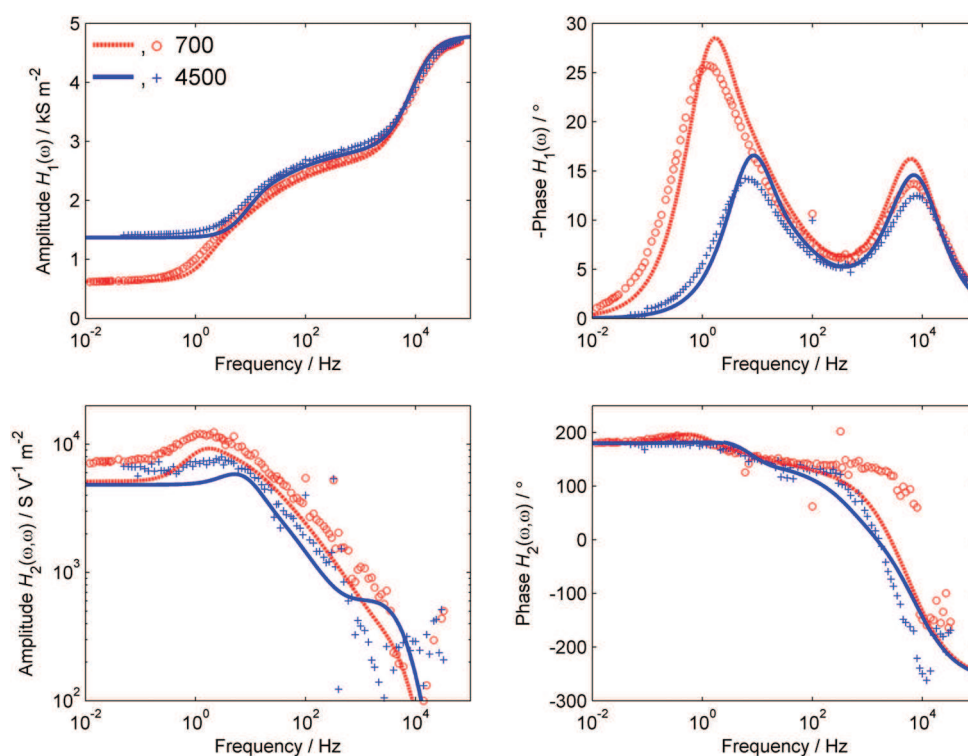
Figure 6. Amplitude and phase shift frequency spectra of the first- ($H_1(\omega)$) and second-order ($H_2(\omega,\omega)$) frequency response functions at different rotation speeds (in rpm); symbols: experimental data; lines: theoretic curves (input amplitude: 50 mV rms; electrolyte: 20 mol m^{-3} $[Fe(CN)_6]^{4-/3-}$, 1.0 M KCl; steady-state potential: 55 mV; t = 25.0 °C).

parameter variation has shown that both the peak intensity and the plateau position are influenced by the change in charge transport parameter (i.e., rate constant) and mass transport variables (e.g., electrode rotation rate). However, the influence of the rate constant and rotation rate is opposite: the peak intensity and the plateau position increases with the former and decreases with the later.[2] Additionally, the peak position is almost insensitive to the value of the rate constant, whereas it shifts toward the higher frequencies with the increase in rotation rate.[2]

Keeping in mind these theoretical considerations, it is to be concluded that the changes in the second-order FRF amplitude with the increase in potential up to 75 mV are mainly due to the increase in the charge transfer rate (peak intensity and plateau position increase with negligible change in peak position only at 75 mV). With further increase in potential to 120 mV, the reaction is about to reach mass transport limiting condition, and the change in amplitude spectra resembles that influenced by rotation speed:[2] the peak intensity and the plateau position are decreased, whereas the peak position is shifted toward higher frequencies (Figure 5).

3.6. Influence of the Mass Transport Conditions. The influence of the mass transport conditions on the first- and second-order FRF was studied further, both experimentally and theoretically by varying the electrode rotation rate at constant potential value of 55 mV. As has been already discussed, this value has been chosen because at this potential the overall kinetics at both rotation rates is in the mixed activation–diffusion control region, and the influence of the mass transfer resistance to the overall kinetics can be easily followed. The results are shown in Figure 6. The lower electrode rotation rate corresponds to higher mass transfer resistance and the higher

electrode rotation rate to lower mass transfer resistance. In the first-order FRF spectra, the influence of the mass transport limitations is evident in the low-frequency range (e.g., different values of the amplitude at low-frequency asymptotes are obtained at two different electrode rotation rates). Some differences can also be observed in the high-frequency region (phase spectra of the first-order FRF), attributable to the mass transport influence on the charge transfer kinetics.

The amplitude of the theoretical second-order FRF at the higher rotation rate shows two characteristic features, a peak and a plateau and the low-frequency asymptote, as already discussed in the case of the influence of the potential. At the lower electrode rotation rate (700 rpm), the plateau is hardly observable in the amplitude spectra, although it can be clearly observed in the phase spectra. The phase shift spectra, similar to what was already discussed in relation to Figure 5, show a low-frequency asymptote at 180°, which follows a peak and a plateau at higher frequencies. The model predicts the independence of the low-frequency asymptote in the amplitude spectra on the electrode rotation rate and the change of the peak intensity and position with the change of the electrode rotation rate. (The peak moves toward higher frequencies with the decrease in rotation rate.) Similar tendency was observed in the experiments. and the model gives a very good qualitative agreement with the experiment. However, the model predicts somewhat lower values of the amplitude of the second-order FRF than the experimentally observed. This can be due to some of the model assumptions, like the independence of the diffusion coefficients on the concentration of the reacting species, neglecting of the convection in the diffusion layer, or both.[18] In addition, the measurements lasted >10 h, during which period changes in the solution

17357

dx.doi.org/10.1021/jp201300a |*J. Phys. Chem. C* 2011, 115, 17352–17358

could be expected. Heras et al.[4] proved by in situ spectro-photometric measurements that besides some insoluble decomposition products, soluble Prussian blue is formed during extensive electrode reaction in ferro/ferri system, which can take part in some side reactions. This can influence the kinetics at low frequencies and thus cause the changes in behavior of the real system from the expected one.

4. CONCLUSIONS

The method of NLFRA was applied for investigation of the nonlinear behavior of ferrocyanide electrooxidation kinetics as a simple model electrochemical reaction. According to the NLFR approach, the linear part of the system response is contained in the first-order FRF, which has the same meaning as an electrochemical admittance, whereas the nonlinear part of the response is contained in second and higher order FRFs. It was shown that the experimental second-order FRF can be determined by applying a large-amplitude periodic input signal of the potential. For determination of the higher order FRFs, input amplitude higher than 30 mV is required because at lower amplitudes the recorded signal has too high of a level of noise.

The experimental first- and second-order FRFs were determined at different steady-state potentials and different electrode rotation rates. It was shown that a nonlinear model of ferrocyanide oxidation kinetics including a charge transfer reaction and mass transport of the reactant and the product can describe the main experimental observations in the first- and second-order FRFs spectra. The values of the parameters used to calculate the theoretic FRFs, such as the rate constant and the diffusion coefficients, are in the range of values already reported in literature.

This work shows the applicability of the NLFRA for investigation of kinetics of electrochemical reactions as it treats exactly their dynamic response in the linear and in the nonlinear domain. Further work concerning application of NLFRA for investigation of kinetics of more complex electrochemical reactions, including charge transfer and adsorption steps, is in progress.

■ AUTHOR INFORMATION

Corresponding Author
*Tel: +49 391 6110 319. Fax: +49 391 6110 553. E-mail: vidakovi@mpi-magdeburg.mpg.de.

■ REFERENCES

(1) Bensmann, B.; Petkovska, M.; Vidaković-Koch, T.; Hanke-Rauschenbach, R.; Sundmacher, K. *J. Electrochem. Soc.* **2010**, *157*, B1279–B1289.

(2) Vidaković-Koch, T.; Panić, V.; Andrić, M.; Petkovska, M.; Sundmacher, K. *J. Phys. Chem. C* **2011**, http://dx.doi.org/10.1021/jp201_97v.

(3) Kadyk, T.; Hanke-Rauschenbach, R.; Sundmacher, K. *J. Electroanal. Chem.* **2009**, *630*, 19–27.

(4) Heras, A.; Colina, A.; Ruiz, V.; Lopez-Palacios, J. *Electroanal.* **2003**, *15*, 702–708.

(5) Beley, M.; Brenet, J.; Chartier, P. *Electrochim. Acta* **1979**, *24*, 1–9.

(6) Granger, M. C.; Swain, G. M. *J. Electrochem. Soc.* **1999**, *146*, 4551–4558.

(7) Urbaniczky, C.; Lundstrom, K. *J. Electroanal. Chem.* **1984**, *176*, 169–182.

(8) Daum, P. H.; Enke, C. G. *Anal. Chem.* **1969**, *41*, 653–656.

(9) Orazem, M. E.; Tribollet, B. *Electrochemical Impedance Spectroscopy*; Wiley: Hoboken, NJ, 2008.

(10) Boillot, M.; Didierjean, S.; Lapicque, F. *J. Appl. Electrochem.* **2004**, *34*, 1191–1197.

(11) Campbell, S. A.; Peter, L. M. *J. Electroanal. Chem.* **1994**, *364*, 257–260.

(12) Sundfors, F.; Bobacka, J. *J. Electroanal. Chem.* **2004**, *572*, 309–316.

(13) Peter, L. M.; Durr, W.; Bindra, P.; Gerischer, H. *J. Electroanal. Chem.* **1976**, *71*, 31–51.

(14) Noel, M.; Anantharaman, P. N. *Analyst* **1985**, *110*, 1095–1103.

(15) Remita, E.; Boughrara, D.; Tribollet, B.; Vivier, V.; Sutter, E.; Ropital, F.; Kittel, J. *J. Phys. Chem. C* **2008**, *112*, 4626–4634.

(16) Gabrielli, C.; Keddam, M.; Portail, N.; Rousseau, P.; Takenouti, H.; Vivier, V. *J. Phys. Chem. B* **2006**, *110*, 20478–20485.

(17) Mulder, W. H.; Sluytes, J. H.; Pajkossy, T.; Nyikos, I. *J. Electroanal. Chem.* **1990**, *285*, 103–115.

(18) Stevens, N. P. C.; Fulian, Q.; Gooch, K. A.; Fisher, A. C. *J. Phys. Chem. B* **2000**, *104*, 7110–7114.

[TVK5]

I. Ivanov, T. Vidaković-Koch, K. Sundmacher

Alternating electron transfer mechanism in the case of high-performance tetrathiafulvalene-tetracyanoquinodimethane enzymatic electrodes

Alternating electron transfer mechanism in the case of high-performance tetrathiafulvalene–tetracyanoquinodimethane enzymatic electrodes

Ivan Ivanov [a], Tanja Vidaković-Koch [a,*], Kai Sundmacher [a,b]

[a] Max Planck Institute for Dynamics of Complex Technical Systems, Sandtorstraße 1, 39106 Magdeburg, Germany
[b] Otto-von-Guericke University Magdeburg, Universitätsplatz 2, 39106 Magdeburg, Germany

ABSTRACT

The electron transfer mechanism in enzymatic electrodes employing tetrathiafulvalene–tetracyanoquinodimethane (TTF–TCNQ) complex is despite of numerous publications, still a matter of controversy. To clarify this issue, enzymatic electrodes based on TTF, TCNQ and TTF–TCNQ have been prepared in an identical manner and their electrochemical behavior and activity have been tested. The enzymatic electrodes containing the respective mediator, glucose oxidase and Vulcan nanoparticles dispersed in a gelatin matrix show high activity for glucose oxidation in terms of both currents and oxidation onset potential. The observed electrochemical features, supported by infrared spectroscopy measurements, indicate that the activity of the TTF–TCNQ electrodes can be ascribed to TTF and TCNQ species released from the organic salt. The two mediators are active in different potential regions, implying an alternating electron transfer mechanism. TTF is active at more negative potentials and generates higher current densities, while TCNQ exhibits activity only at potentials more positive than 0 V vs. SCE. This work analyzes and summarizes different aspects of the most recent electron transfer hypotheses by providing the respective experimental evidences in an effort for better understanding of this puzzling bioelectrochemical system.

1. Introduction

Charge transfer complexes (CTCs) are characterized by partial transfer of electrons from a donor to an acceptor molecule. CTCs belong to the group of organic conductors together with organic conductive polymers [1]. The history of conductive organic molecules could be dated back to 1954, when the first molecular crystal (perylene–bromine complex) with high conductivity was reported [2]. However, the field of organic conductors was practically initiated by the discoveries of the tetracyanoquinodimethane (TCNQ) and the tetrathiafulvalene (TTF) molecules [3] and benchmarked by the first report of near-metal conductivity of the TTF–TCNQ complex [4]. TTF–TCNQ is a CTC (also known as organic salt or organic metal) with room temperature conductivity in the range of $400 \pm 100 \, S \, cm^{-1}$ due to efficient overlapping of the π-orbitals of the respective molecules [5]. The conductive salt is composed of segregated parallel stacks of TTF and TCNQ and the π-orbitals interact mainly along the stacking direction, which results in a quasi-one-dimensional conductor [3].

The unique electrical properties of TTF–TCNQ have naturally prompted studies on its utilization as electrode material. Jaeger and Bard first studied the behavior of TTF–TCNQ electrodes in different aqueous solutions and found a stable potential range of about 0.7 V [6]. Since this groundwork study, the TTF–TCNQ complex evolved as a highly efficient electrode material for more specific, namely bioelectrocatalytic applications. Pioneering works in this direction were done by Kulys and co-workers with other organic salts – complexes between N-methylphenazinium (NMP⁺) or N-methylacridinium (NMA⁺) and TCNQ [7,8]. Later on, Albery and co-workers investigated different CTCs as electrode materials for the oxidation of glucose oxidase (GOx). They found that the TTF–TCNQ salt had the best performance [9] and exploited it further as an electrode material for the regeneration of other flavoenzymes [10].

Since then, the enzymatic electrocatalysis on TTF–TCNQ electrodes has been the subject of extensive research, almost exclusively for biosensor applications. TTF–TCNQ has been mostly used in combination with GOx for the determination of glucose concentration, but studies involving other substrates and enzymes have been also reported. The efforts in the development of amperometric biosensors based on TTF–TCNQ have been summarized in a recent review [11].

Despite of numerous publications, the electron transfer (ET) mechanism in enzymatic electrodes employing TTF–TCNQ remains

* Corresponding author. Tel.: +49 391 6110 319; fax: +49 391 6110 553.
   E-mail addresses: ivanov@mpi-magdeburg.mpg.de (I. Ivanov), vidakovi@mpi-magdeburg.mpg.de (T. Vidaković-Koch), sundmacher@mpi-magdeburg.mpg.de (K. Sundmacher).

still controversial. Enzymes may exhibit *direct electron transfer* (DET) if they are able to exchange electrons directly with the electrode surface. However, in most of the cases additional redox active species called *mediators* have to be introduced in order to ensure efficient ET. In that case the process is termed *mediated electron transfer* (MET) [12]. GOx immobilized on TTF–TCNQ is a challenging case due to the unique properties of the CTC. GOx in general is believed to lack DET due to the thick carbohydrate shell, which isolates its redox center (flavin adenine dinucleotide, FAD), although there are some studies reporting the occurrence of DET in the case of GOx as discussed recently [13]. Deglycosylation of the enzyme partially exposes FAD, which facilitates DET, as demonstrated by Mano and co-workers [14]. TTF–TCNQ exhibits high electrical conductivity and no visible redox processes (e.g. due to salt decomposition) in the catalytically relevant potential region, so it can be regarded as an inert electrode material like, e.g. glassy carbon. On the other side both TTF [15] and TCNQ [16] are known to act as mediators for GOx.

Early studies on CTCs suggested homogeneous MET [7,8]. Further works, specifically addressing TTF–TCNQ, claimed direct regeneration of the reduced enzyme by means of DET [9]. Later on, the same group assumed heterogeneous redox catalysis (opposed to the homogeneous case) with TCNQ as a mediator adsorbed on the CTC surface [17]. This hypothesis was further supported by electrochemical and quartz crystal microbalance (QCM) measurements and soluble TTF species were completely ruled out of the possible ET pathway [18]. More recent experimental observations indicated that TTF should be also involved in the mechanism and two independent modes of MET were suggested: homogeneous with TTF$^+$ and heterogeneous with TCNQ^0 [19]. Another study excluded the possibility of homogeneous MET or heterogeneous redox catalysis and propounded the hypothesis of an electroactive enzyme, modified by incorporation of a hydrophobic mediator (TTF and possibly TCNQ), released from the CTC [20]. This suggestion was based on the successful modification of GOx with TTF by hydrophobic interactions [21]. Later on, Albery and co-workers developed a theory for a homogeneous MET with mediators being supplied from the bulk or generated *in situ* and considered the theoretical possibility to apply this mechanism in the case of organic salts [22].

After all, despite of the long debate, more recent works reported third generation (mediatorless) glucose biosensors based on TTF–TCNQ, whereby the assumption of DET corresponded well to the obtained experimental data [23,24]. Contrary to the latter publications, a very recent study suggested the concept of an alternating MET mechanism with different mediator species, depending on the applied potential, but without experimental evidences [11].

As can be seen, the mechanism of ET in the case of enzymatic electrocatalysis on CTC and especially the GOx/TTF–TCNQ system is still a matter of controversy in the scientific community. In order to provide a better understanding of this challenging issue, a simple, yet unexplored, approach has been used in the present work. The possible mediators TTF, TCNQ and TTF–TCNQ have been incorporated into a three-dimensional electrode architecture including a gelatin matrix and carbon black, which allows for a detailed characterization and direct comparison of their electrochemical behavior and glucose oxidation activity and results in high performance. In addition the conclusions based on the electrochemical tests have been supported by infrared spectroscopy.

2. Materials and methods

Glucose oxidase (EC 1.1.3.4, GOx) from *Aspergillus niger* was supplied by Fluka. Vulcan XC72R (Cabot) was supplied by Quin-Tech (Germany). TTF, TCNQ and TTF–TCNQ were of analytical re-

agent grade and purchased from Sigma–Aldrich. Ultrapure water from Millipore was used in all experiments.

Stainless steel discs, degreased with acetone before modification, were used as a mechanical and electrical support for the preparation of enzymatic electrodes. For the electrochemical tests the discs were mounted in a sample holder for rotating disc electrode (RDE) with an opening of 6 mm (0.28 cm^2 working area).

The ink used for modification of the enzymatic electrodes had the following composition: 20 mg Vulcan XC72R, 10 mg of the respective mediator (TTF, TCNQ or TTF–TCNQ) and 10 mg GOx (1920 U) in 1 ml of 2% w/v gelatin aqueous solution (heated to 35 °C before use). The mediators were ground in an agate mortar before use. Suspension of the ink components in the gelatin solution was assisted by mechanical stirring and ultrasonication for about 5 min. For preparation of the enzymatic electrodes 50 μl of the respective ink was applied on the stainless steel electrode and left to dry under ambient conditions. After that the electrode assembly was cross-linked by dipping into a glutaraldehyde solution (5% in water) for 60 s, washed carefully with water and dried again. The enzymatic electrodes were kept in plastic bags at −20 °C before use.

All electrochemical experiments were carried out in a conventional double-jacketed electrochemical cell (Radiometer Analytical). The RDE was used as a working electrode, platinum wire as a counter electrode, and saturated calomel electrode (SCE) as a reference electrode. The potential values in the text are referred to the SCE scale. All tests were done at a rotation rate of 400 rotations per minute (rpm) in order to ensure defined mass transport conditions in the investigated system. Electrochemical experiments were performed by a computer controlled potentiostat PGSTAT302 (Eco Chemie/Autolab).

Fourier transform infrared spectroscopy (FTIR) measurements were performed with a Nicolet 6700 that was equipped with ATR and DTGS detector (Thermo Electron GmbH, Germany).

3. Results and discussion

The preparation of enzymatic electrodes based on TTF–TCNQ and GOx usually involves the dispersion of the conductive salt in an inert polymer and a suitable solvent to form slurry or thick paste [9,25–27]. In some cases the CTC has been also grown directly over a conductive polymer [23,24]. The procedure described in the present study is conceptually similar to previous procedures but it involves a biopolymer and a carbon material, in addition. The enzymatic electrodes are based on Vulcan XC72R, GOx and the respective mediators, dispersed in a gelatin matrix, which altogether form a three-dimensional stable electrode architecture. Conductive high-surface area carbon materials such as Vulcan are well established as catalyst supports in fuel cell research. They have been recently adopted also in the preparation of enzymatic electrodes for biofuel cell applications as a mean to facilitate ET and to increase current densities. For instance, Vulcan XC72R has been recently used as a support for the immobilization of bilirubin oxidase (BOD) in Nafion [28]. Gelatin, on the other side, has a hydrophilic nature and swells in presence of water. The biocompatible hydrogel polymer network provides a suitable environment for the entrapped enzymes, in addition to good film-forming properties, non-toxicity and mechanical stability [29]. The utilization of Vulcan enhances the actual surface area and the ET rate and the resulting electrode demonstrates improved characteristics compared to previously reported TTF–TCNQ bioelectrodes, which will be discussed in detail in another publication.

In order to clarify the ET mechanism, enzymatic electrodes based on TTF, TCNQ and TTF–TCNQ as mediators have been prepared according to an identical procedure. This approach allows

for better understanding of the electrochemical behavior of TTF and TCNQ on the one side, and for direct comparison of the respective performances of the enzymatic anodes on the other side.

3.1. TCNQ species as ET mediators

TCNQ is a strong electron acceptor, which can undergo two redox transformations: to the monovalent ($TCNQ^-$) and subsequently to the divalent ($TCNQ^{2-}$) radical anions and the respective redox reactions can be clearly distinguished in a suitable solvent, e.g. acetonitrile [30].

However, the low solubility of TCNQ in aqueous solutions obstructs the straightforward analysis of its electrochemical behavior in phosphate buffer. Fig. 1a shows cyclic voltammograms (CVs) of the TCNQ-based enzymatic electrode in different potential windows. If the upper potential is kept below 0.2 V, a well-defined pair of redox peaks, denoted as C and D, is observed. These peaks can be tentatively assigned to the redox couple $TCNQ^{2-}/TCNQ^-$ [30]. Another redox process can be observed at potentials more positive than 0 V. This process is assigned to the $TCNQ^-/TCNQ^0$ redox couple. When the upper limit is extended further, another pair of redox peaks (A and B) appears. Qualitatively similar behavior has been obtained in the case of TCNQ on pyrolytic graphite [30].

The redox processes evident from Fig. 1 are presented here in a simplified manner for clarity. In reality the TCNQ reduction is associated with cation incorporation according to:

$$x\ TCNQ + y\ e^- + y\ M^+ \leftrightarrow (M^+)_y(TCNQ^-)_y(TCNQ)_{x-y} \quad (1)$$
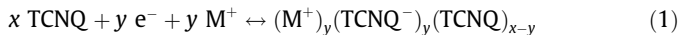
Analogically, the second reductive process involves a similar cation intercalation (more details can be found in the literature [30]). Previously the behavior of TCNQ microcrystals in aqueous solutions has been ascribed to reversible solid–solid transformations occurring via nucleation/growth mechanisms, evidenced by an "inert" zone between the redox peaks (e.g. A and B in the present case).

The behavior of the TCNQ enzymatic electrode in the present case is also similar to the behavior of a glucose biosensor based on Ketjenblack [16]. In the present case there is a negative shifting of peak B ($TCNQ^0 \rightarrow TCNQ^-$) with an increase of the positive potential limit of the CV, which impedes the differentiation between the two reductive processes in the negative scan. In addition, a decrease in peak intensities is observed with cycling, which can be ascribed to dissolution of TCNQ as reported in [30].

CVs of the TCNQ-based electrode in absence and presence of glucose are presented in Fig. 1b. In the extended potential range the enzymatic electrode exhibits oxidation activity with an onset at about 0 V and the ET process is assumed to be mediated by $TCNQ^0$. The activity for glucose oxidation has been further investigated in a limited potential range, where the $TCNQ^{2-}/TCNQ^-$ process can be clearly observed (Fig. 1c). As can be seen in the graph, steady-state (SS) experiments are in a good agreement with CV. According to the literature, $TCNQ^-$ species can theoretically act as potential mediators for GOx-catalyzed glucose oxidation, since its redox potential is more positive than the redox potential of the enzyme [11]. However, this mechanism seems not to be operative in the present case as evidenced in Fig. 1c.

3.2. TTF species as ET mediators

TTF, analogous to TCNQ, is known to undergo two redox transformations, to the TTF^+ and the TTF^{2+} radical cations, which can both act as redox mediators for the regeneration of reduced GOx [15]. Fig. 2a shows CVs of the TTF-based enzymatic electrode in different potential ranges in phosphate buffer. As can be seen, if the potential window is kept up to 0 V, the enzymatic electrode exhib-

Fig. 1. Electrochemical behavior and activity of the TCNQ-based enzymatic electrode: (a) CVs in buffer in different potential ranges; (b) CVs in absence and presence of glucose in extended potential range; (c) CVs and SS polarization curves in absence (black) and presence (red) of glucose. Conditions: 0.1 M phosphate buffer, pH 7.2, 37 °C, 400 rpm, N_2 atmosphere, scan rate 5 mV s^{-1}. (For interpretation of the references to colours in this figure legend, the reader is referred to the web version of this paper.)

its only capacitive behavior. When the positive potential limit is increased to 0.2 and 0.4 V, respectively, a redox process, assigned to the TTF^0/TTF^+ couple, occurs. The oxidation of TTF^0 to TTF^+ starts at about 0.05 V and no current peak in the positive scan is observed, regardless of the upper potential limit. However, a well-defined peak, corresponding to the reduction of TTF^+ back to TTF^0, is
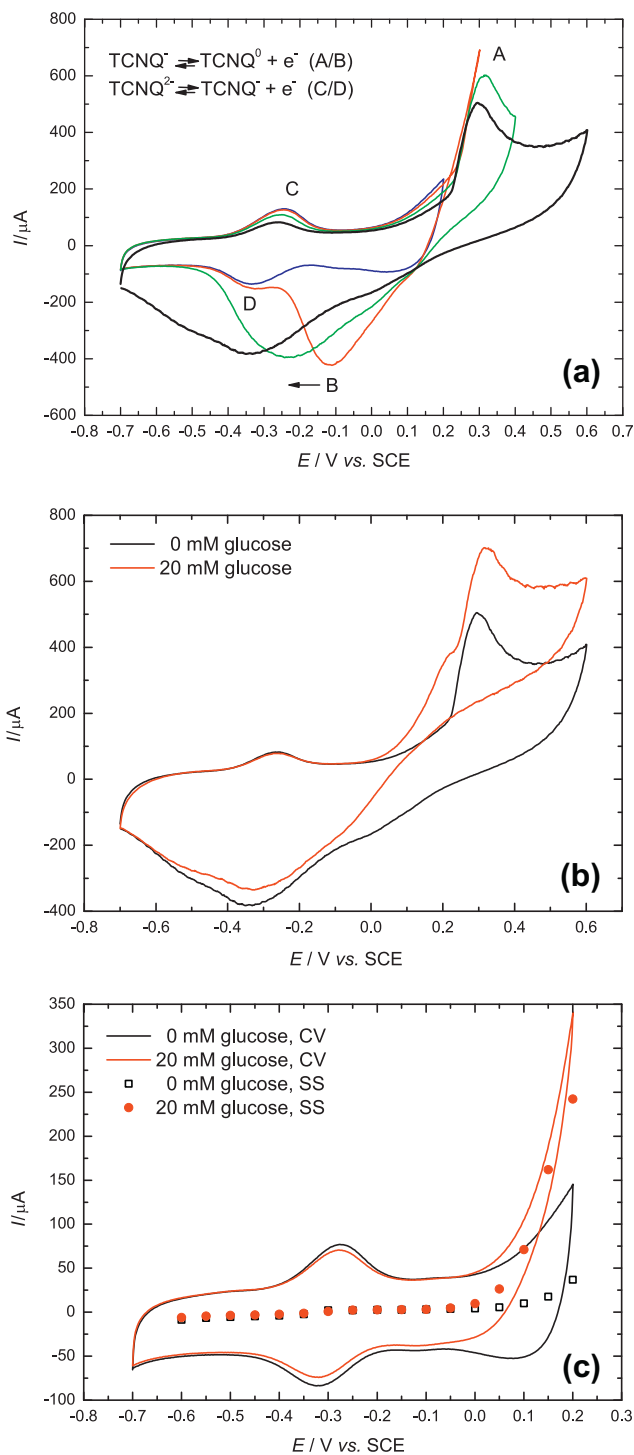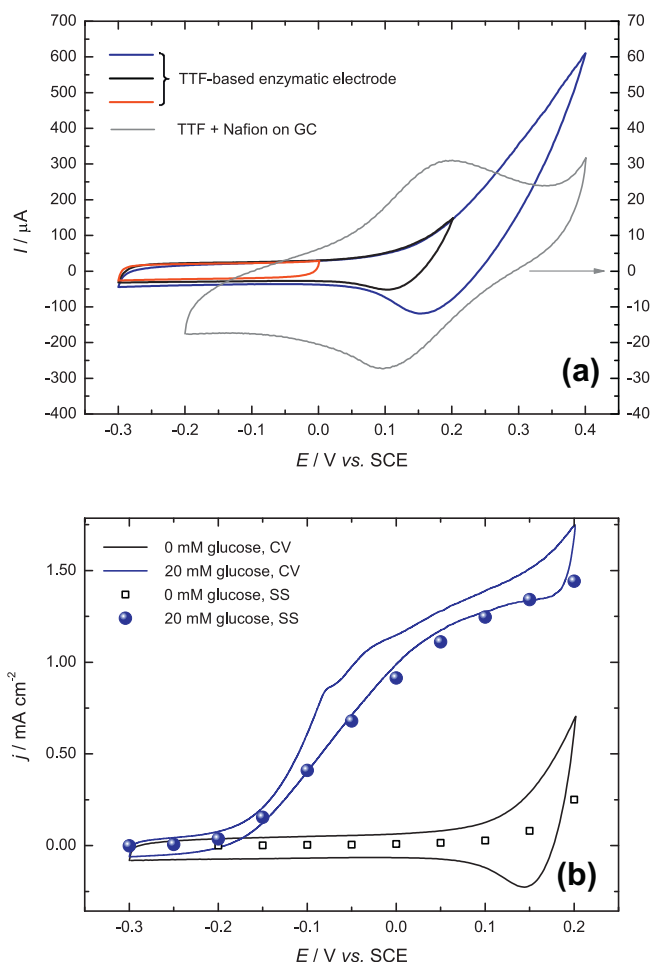
Fig. 2. Electrochemical behavior and activity of the TTF-based enzymatic electrode: (a) CVs in buffer in different potential ranges (CV of TTF on GC is presented for comparison); (b) CVs and SS polarization curves in absence (black) and presence (blue) of glucose. Conditions: 0.1 M phosphate buffer, pH 7.2, 37 °C, 400 rpm, N$_2$ atmosphere, scan rate 5 mV s^{-1}. (For interpretation of the references to colours in this figure legend, the reader is referred to the web version of this paper.)

present in the negative scan. Its position is dependent on the positive potential limit, i.e. on the amount of TTF$^+$ been generated during the oxidation. When the upper potential limit of the voltammogram is extended, the positive currents clearly surpass the reductive currents. Such behavior is typical for dissolution of metal electrodes, e.g. for copper, where dissolution (oxidation) in the positive scan and copper redeposition in the negative scan take place, respectively [31]. The absence of a defined anodic peak in the case of the TTF-based enzymatic electrode obstructs the determination of the redox potential of the TTF^0/TTF$^+$ couple.

In order to have an experimental reference for the redox potential in the aqueous phosphate buffer employed in this study TTF has been dispersed in a Nafion solution and applied as a thin layer on a glassy carbon (GC) surface. The resulting CV (see Fig. 2a) shows the reversible oxidation of TTF and the peak position corresponds to the behavior of the TTF-based enzymatic electrode. The presence of a well-defined peak can be tentatively attributed to the low amount of TTF in the Nafion film and the negative charge of the polymer, which will prevent TTF$^+$ cations to escape from the surface, opposed to the case of the neutral gelatin. The reversible redox potential of TTF on GC is around 0.15 V, which is in accordance with the values, reported in the literature [32].

The CVs and SS curves of the TTF electrode in absence and presence of glucose are shown in Fig. 2b. The enzymatic electrode exhibits high activity towards glucose oxidation and the oxidation

onset is at about −0.2 V and SS curves follow the behavior observed in CV. Similar oxidation onset and electrochemical behavior has been shown in the case of TTF-modified CNTs [32]. It should be noted that according to the literature TTF^{2+} species can also act as mediators at more positive potentials but they are less stable and easily decomposed [15].

3.3. TTF and TCNQ species as ET mediators in the CTC

After the information about the electrochemistry and the glucose oxidation activity of the single components TTF and TCNQ has been obtained, the electrochemical behavior the CTC has been investigated and directly compared with the behavior of the TTF and TCNQ electrodes. Fig. 3a shows the CVs of the CTC electrode in buffer in different potential regions. For comparison, a CV of the enzymatic electrode lacking TTF–TCNQ has been also shown. The CVs of the TTF and TCNQ electrodes are presented on the same potential scale in Fig. 3b.

According to the literature, TTF–TCNQ should exhibit a stable potential range in aqueous media, where no current peaks attributed to salt decomposition could be observed [6]. However, in the present case, the shape of the CV of CTC in the potential range between −0.2 and 0.2 V indicates some redox processes occurring at potentials close to both limits of the voltammetric experiment (Fig. 3a). This kind of response has been obtained in a reproducible manner with fresh CTC electrodes, which have not been subjected to any pretreatment or conditioning and the respective behavior was stable even after prolonged cycling. The control CV of the enzymatic electrode lacking TTF–TCNQ shows completely featureless CV with only capacitive behavior, which indicates that the observed voltammetric behavior can be assigned solely to TTF–TCNQ. The observation of redox processes between −0.2 and 0.2 V indicates that although stable, this potential region is not completely inert.

The respective CV shows that a reduction process takes place at potentials negative to −0.1 V, and a small oxidation peak can be observed immediately upon scan reversal. The reduction currents can be tentatively assigned to cathodic salt decomposition, according to Eq. (2) as proposed by Jaeger and Bard [6] and the subsequent anodic peak has been previously ascribed to the reversibility of the process at its initial stage [27].

$$TTF–TCNQ + 2e^- \rightarrow TTF^0 + TCNQ^{2-} \tag{2}$$

The CTC decomposition is accelerated when the electrode is subjected to cycling at low sweep rates in a more negative potential range and the reduction is enhanced with extension of the neg-
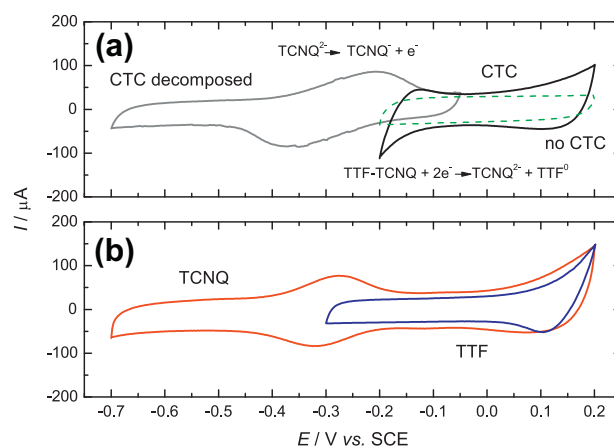

Fig. 3. CVs of (a) CTC-based enzymatic electrode in buffer in two different potential ranges (CV of electrode without CTC is presented for comparison); (b) TTF- and TCNQ-based enzymatic electrodes. Conditions: 0.1 M phosphate buffer, pH 7.2, 37 °C, 400 rpm, N$_2$ atmosphere, scan rate 5 mV s^{-1}.

ative potential limit (Fig. S1). However, the associated cathodic currents decrease with the number of cycles until a reproducible CV is obtained, which indicates decomposition of all electrochemically susceptible TTF–TCNQ (Fig. S2). The resulting CV of decomposed CTC is characterized by a clearly developed pair of redox peaks (Fig. 3a) and based on its position and shape, it can be assigned to the $TCNQ^{2-}/TCNQ^{-}$ couple (see Fig. 3b). Based on this observation, it is assumed that the small anodic peak upon scan reversal in the CV between −0.2 and 0.2 V is rather due to $TCNQ^{2-}$ oxidation to $TCNQ^{-}$, than to reversible salt decomposition. This also implies that the redox behavior observed at positive potentials above 0 V can be attributed both to the TTF^0/TTF^+ and the $TCNQ^-/TCNQ^0$ couples. However, it is difficult to discriminate between both processes since they are superimposed in the potential range of interest (Fig. 3b).

Fig. 4 shows the SS curves in absence and presence of 20 mM glucose of the CTC, TTF and TCNQ electrodes in different potential ranges. The respective polarization curves have been compared on the same potential and current scales for the sake of clarity. As can be seen, the glucose oxidation activity of the CTC electrode (Fig. 4b) significantly resembles the behavior of the TTF electrode (Fig. 4a), both in terms of oxidation onset and measured currents. The reduction currents at potentials negative to −0.2 V can be explained by the salt decomposition, which has been discussed above. Therefore, the positive shift in the currents below −0.2 V in presence of glucose should be probably ascribed to gradual decomposition of the CTC and not to glucose oxidation activity.

The polarization curves of the decomposed CTC in absence and presence of glucose are shown in Fig. 4c. As can be seen, after pretreatment no reduction currents are observed and the glucose oxidation onset potential is at about −0.2 V, which corresponds to the behavior of CTC in Fig. 4b and the behavior of TTF in Fig. 4a.
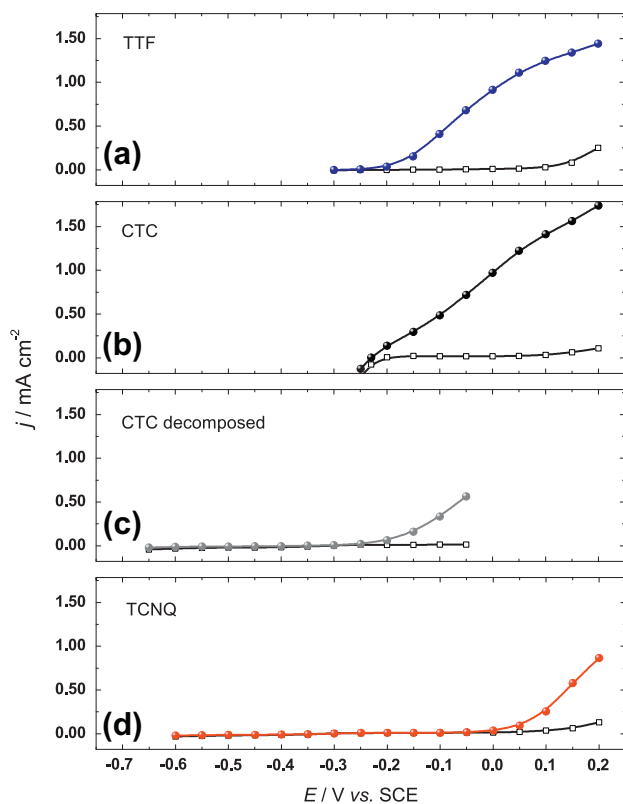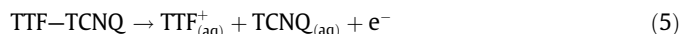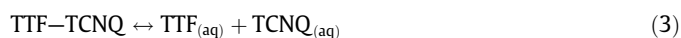
On the other side, the glucose oxidation activity of the TCNQ electrode does not start earlier than 0 V (see Fig. 4d), which indicates that TCNQ cannot be accountable for mediation at the more negative potentials observed in Fig. 4b and c. However, it is likely that at potentials more positive than 0 V, TTF and TCNQ act as mediators simultaneously but the two processes cannot be distinguished. These findings correspond to the suggested alternating ET mechanism, involving different mediator species [11] but restricted to more positive potentials.

As can be seen in Fig. 4, the CTC is active for glucose oxidation and the activity resembles significantly the activity of TTF. Activity due to TCNQ species might be superimposed at higher potentials. The presence of TTF and TCNQ species can be ascribed to in situ generation in the course of the electrochemical experiment (induced by potential). In order to prove whether the mediators are being generated by the imposed potential, control experiments in a limited region (−0.05 V to 0.05 V) have been performed. The respective CV in buffer shows pure capacitive behavior and no visible redox processes, which observation corresponds to the "stable" potential range, proposed in the literature. However, the activity in presence of glucose is similar to the activity in the extended potential range between −0.2 V to 0.2 V (Fig. 5).

The release of electroactive species within the "stable" potential window has been discussed in [33] and demonstrated also by scanning tunneling microscopy experiments (STM) [34]. The authors in the latter study observed dissolution at potentials within the stable potential region and even at equilibrium potential. They assumed the presence of neutral TTF and TCNQ species dissolved in the aqueous solution, either reversibly at equilibrium, or irreversibly at non-equilibrium potentials (Eqs. (3–5)) and distinguished the nature of these species ($TTF_{(aq)}$, $TCNQ_{(aq)}$) from the nature of the surface-confined species (TTF^0, $TCNQ^0$). The assumption of TTF–TCNQ dissolution corresponds to the behavior observed in the present study and can explain the fact that the CTC electrode exhibits activity even if it was not subjected to any special potential pretreatment.

$$TTF-TCNQ \leftrightarrow TTF_{(aq)} + TCNQ_{(aq)} \tag{3}$$

$$TTF-TCNQ + e^- \rightarrow TTF_{(aq)} + TCNQ^-_{(aq)} \tag{4}$$

$$TTF-TCNQ \rightarrow TTF^+_{(aq)} + TCNQ_{(aq)} + e^- \tag{5}$$

In order to have additional experimental evidence that dissociated TTF and TCNQ species are present on the CTC surface, the electrodes have been analyzed by FTIR spectroscopy after different

Fig. 4. Steady-state polarization curves of different enzymatic electrodes in absence (open symbols) and presence (full symbols) of 20 mM glucose: (a) TTF; (b) CTC; (c) electrochemically decomposed CTC; (d) TCNQ. Conditions: 0.1 M phosphate buffer, pH 7.2, 37 °C, 400 rpm, N_2 atmosphere.
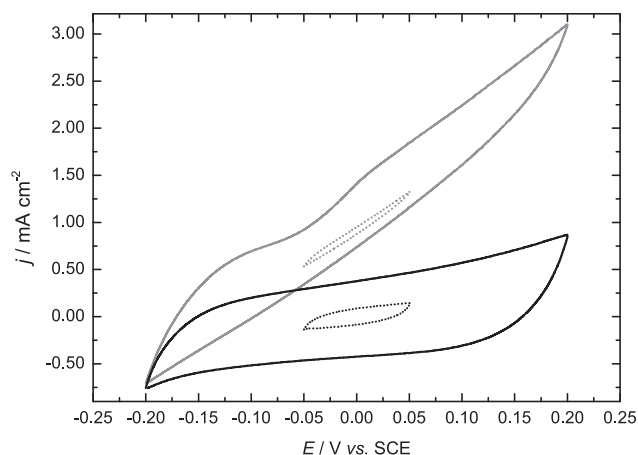

Fig. 5. CVs of the CTC-based enzymatic electrode in two different potential ranges in absence (black) and presence (grey) of 20 mM glucose. Conditions: 0.1 M phosphate buffer, pH 7.2, 37 °C, 400 rpm, N_2 atmosphere, scan rate 5 mV s^{-1}.
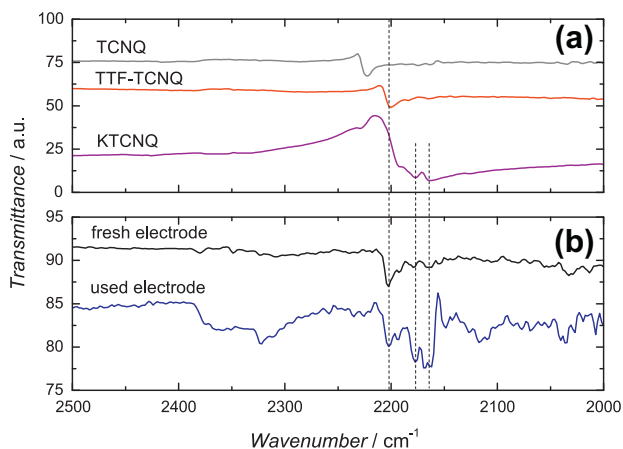
Fig. 6. FTIR spectra of (a) reference compounds and (b) enzymatic electrodes.

treatments. This is the first time, to our best knowledge, when this technique has been used for clarification of the electron transfer mechanism. The state of the TTF–TCNQ (intact or decomposed) can be determined by the shift in the nitrile stretching band of TCNQ according to the empirical dependence demonstrated in [35,36] due to the relation between the vibrational frequency and the degree of charge transfer, manifested in compounds with π-delocalized systems. According to the latter works the shift in the nitrile frequency of $TCNQ^0$ in the case of $TTF^{\delta+}TCNQ^{\delta-}$ and K^+TCNQ^- corresponds to degrees of charge transfer of 0.59 and 1.00, respectively. Thus, it makes possible to identify in a simple way the nature of TCNQ species present at the electrode surface. Fig. 6a shows referent FTIR spectra of TCNQ, TTF–TCNQ and KTCNQ recorded between 2500 cm^{-1} and 2000 cm^{-1}.

In the present case the calculated values for the charge transfer degree are 0.43 and 0.88 for the TTF–TCNQ and KTCNQ, respectively. These values are close to the literature reported values and the apparent shifts demonstrate that the respective peaks can be used for characterization of the nature of TCNQ species at the electrode surface. Fig. 6b shows spectra of the freshly prepared enzymatic electrode and the electrode after electrochemical characterization in presence of glucose. The value of the frequency (2200 cm^{-1}) of the fresh electrode indicates the presence of TTF–TCNQ in its original state. The peaks in the FTIR spectrum of the electrode, which has been subjected to several cycles between −0.2 and 0.2 V in absence and in presence of glucose, indicate the presence of intact TTF–TCNQ as well as TCNQ anions. The peak at 2177 cm^{-1} is characteristic for $TCNQ^-$ species, while the peak at 2163 cm^{-1} can be attributed to both $TCNQ^-$ and $TCNQ^{2-}$ species [37]. The presence of divalent anions can be also assumed due to the broad peak at about 2110 cm^{-1} (characteristic for $TCNQ^{2-}$) but this is a rather speculative interpretation since the peak is poorly defined. The FTIR spectrum of the used electrode confirms the presence of TCNQ anions at the electrode surface, which is in accordance to the voltammetric data and further assists the hypothesis of TTF–TCNQ dissolution in the investigated potential range. The significant similarity in the glucose oxidation activity of CTC and TTF electrodes supports the hypothesis of MET with *in situ* generated TTF species as the main mediators.

4. Conclusions

The major part of the activity of TTF–TCNQ based enzymatic electrodes for glucose oxidation is due to TTF species, which are re-

leased from the CTC. TCNQ species also act as mediators but only at potentials above 0 V. The TTF and TCNQ species can be generated from the CTC surface either by simple dissolution or by potential induced salt decomposition during the electrochemical tests. The presence of dissociated TCNQ species has been additionally confirmed by FTIR. Although the electrode architecture in the present study might show some differences to literature results, we believe that these conclusions can be extended to other studies employing CTC.

Appendix A. Supplementary material

Supplementary data associated with this article can be found, in the online version, at http://dx.doi.org/10.1016/j.jelechem.2012.11.009.

References

[1] M.R. Bryce, L.C. Murphy, Nature 309 (1984) 119–126.
[2] H. Akamatu, H. Inokuchi, Y. Matsunaga, Nature 173 (1954) 168–169.
[3] D. Jerome, H.J. Schulz, Adv. Phys. 31 (1982) 299–490.
[4] J. Ferraris, V. Walatka, J.H. Perlstei, D.O. Cowan, J. Am. Chem. Soc. 95 (1973) 948–949.
[5] D. Jerome, Chem. Rev. 104 (2004) 5565–5591.
[6] C.D. Jaeger, A.J. Bard, J. Am. Chem. Soc. 101 (1979) 1690–1699.
[7] N.K. Cenas, J.J. Kulys, Bioelectrochem. Bioenerg. 8 (1981) 103–113.
[8] J.J. Kulys, A.S. Samalius, G.J.S. Svirmickas, FEBS Lett. 114 (1980) 7–10.
[9] W.J. Albery, P.N. Bartlett, D.H. Craston, J. Electroanal. Chem. 194 (1985) 223–235.
[10] W.J. Albery, P.N. Bartlett, M. Bycroft, D.H. Craston, B.J. Driscoll, J. Electroanal. Chem. 218 (1987) 119–126.
[11] R. Pauliukaite, A. Malinauskas, G. Zhylyak, U.E. Spichiger-Keller, Electroanalysis 19 (2007) 2491–2498.
[12] L. Habermuller, M. Mosbach, W. Schuhmann, Fresenius J. Anal. Chem. 366 (2000) 560–568.
[13] I. Ivanov, T. Vidaković-Koch, K. Sundmacher, Energies 3 (2010) 803–846.
[14] O. Courjean, F. Gao, N. Mano, Angew. Chem.-Int. Ed. 48 (2009) 5897–5899.
[15] H.Y. Liu, J.Q. Deng, Biosens. Bioelectron. 11 (1996) 103–110.
[16] P. Atanasov, A. Kaisheva, I. Iliev, V. Razumas, J. Kulys, Biosens. Bioelectron. 7 (1992) 361–365.
[17] W.J. Albery, P.N. Bartlett, A.E.G. Cass, R. Eisenthal, I.J. Higgins, Philos. Trans. R. Soc. Lond. Ser. B – Biol. Sci. 316 (1987) 107–119.
[18] M.S. Freund, A. Brajtertoth, M.D. Ward, J. Electroanal. Chem. 289 (1990) 127–141.
[19] B.S. Hill, C.A. Scolari, G.S. Wilson, Philos. Trans. R. Soc. Lond. Ser. A – Math. Phys. Eng. Sci. 333 (1990) 63–69.
[20] P.N. Bartlett, J. Electroanal. Chem. 300 (1991) 175–189.
[21] P.N. Bartlett, V.Q. Bradford, J. Chem. Soc. Chem. Commun. (1990) 1135–1136.
[22] W.J. Albery, P.N. Bartlett, B.J. Driscoll, R.B. Lennox, J. Electroanal. Chem. 323 (1992) 77–102.
[23] F. Palmisano, P.G. Zambonin, D. Centonze, M. Quinto, Anal. Chem. 74 (2002) 5913–5918.
[24] G.F. Khan, M. Ohwa, W. Wernet, Anal. Chem. 68 (1996) 2939–2945.
[25] M. Cano, J.L. Avila, M. Mayen, M.L. Mena, J. Pingarron, R. Rodriguez-Amaro, J. Electroanal. Chem. 615 (2008) 69–74.
[26] G.F. Khan, Biosens. Bioelectron. 11 (1996) 1221–1227.
[27] C.P. Wilde, A. Hu, C.M. Rondeau, M. Wood, J. Electroanal. Chem. 353 (1993) 19–31.
[28] A. Habrioux, T. Napporn, K. Servat, S. Tingry, K.B. Kokoh, Electrochim. Acta 55 (2010) 7701–7705.
[29] K. De Wael, S. De Belder, S. Van Vlierberghe, G. Van Steenberge, P. Dubruel, A. Adriaens, Talanta 82 (2010) 1980–1985.
[30] A.M. Bond, S. Fletcher, P.G. Symons, Analyst 123 (1998) 1891–1904.
[31] M.R. Vogt, A. Lachenwitzer, O.M. Magnussen, R.J. Behm, Surf. Sci. 399 (1998) 49–69.
[32] B. Kowalewska, P.J. Kulesza, Electroanalysis 21 (2009) 351–359.
[33] S. Zhao, U. Korell, L. Cuccia, R.B. Lennox, J. Phys. Chem. 96 (1992) 5641–5652.
[34] P.N. Bartlett, X.Q. Tong, J. Phys. Chem. B 101 (1997) 8540–8549.
[35] J.G. Roblesmartinez, A. Salmeronvalverde, A. Zehe, R.A. Toscano, Cryst. Res. Technol. 30 (1995) K21–K25.
[36] J.S. Chappell, A.N. Bloch, W.A. Bryden, M. Maxfield, T.O. Poehler, D.O. Cowan, J. Am. Chem. Soc. 103 (1981) 2442–2443.
[37] V. Bellec, M.G. De Backer, E. Levillain, F.X. Sauvage, B. Sombret, C. Wartelle, Electrochem. Commun. 3 (2001) 483–488.

[TVK6]

T. Vidaković-Koch, V.K. Mittal, T.Q.N. Do, M. Varničić,
K. Sundmacher

Application of electrochemical impedance spectroscopy for studying of enzyme kinetics

CrossMark
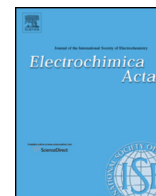
Application of electrochemical impedance spectroscopy for studying of enzyme kinetics

T. Vidaković-Koch [a,*,1], V.K. Mittal [b], T.Q.N. Do [b,1], M. Varničić [b], K. Sundmacher [a,b,1]

[a] *Otto-von-Guericke University Magdeburg, Universitätsplatz 2, 39106 Magdeburg, Germany*
[b] *Max Planck Institute for Dynamics of Complex Technical Systems, Sandtorstraße 1, 39106 Magdeburg, Germany*

ARTICLE INFO

ABSTRACT

The application of electrochemical impedance spectroscopy (EIS) in theory and experiment for investigation of redox enzyme kinetics has been described. As a model system an enzyme horseradish peroxidase adsorbed on graphite electrode has been chosen. Three different mathematical models based on generalized mechanism of horseradish peroxidase catalyzed hydrogen peroxide reduction have been formulated and used for derivation of theoretical electrochemical impedances. In this way, mechanistic details related to bioelectrochemical reaction including all relevant kinetic parameters are obtained. The presented approach overcomes limitations of classical equivalent circuit approach, since it does not rely on phenomenological elements, but on particular reaction mechanism. We have shown that the EIS is more sensitive for parameter estimation and model discrimination than a steady state response.

© 2013 Elsevier Ltd. All rights reserved.

1. Introduction

Redox enzymes can be efficiently coupled with an electrode surface giving prospect of highly efficient and selective bio(electrochemical) transformations for energy conversion and/or production of commodities or fine chemicals. One example is glucose oxidase which coupled with an electrode in presence of glucose and providing for oxygen reduction cathode generates electricity and D-glucono-1,5-lactone with applications in different industries [1]. Other examples might comprise whole enzymatic cascades performing complex sequences of biochemical reactions, turning for example such inert and environmentally polluting substances (like CO_2) into useful commodities (e.g. methanol) [2,3]. These processes have a significant potential for development of new enzyme based production systems, with electrochemistry playing an important role, especially regarding electrochemical regeneration of redox enzymes (redox co-factors). Although the electrochemical regeneration is feasible, its efficiency is still too low to be considered competitive for industrial applications [4]. Part of the reason is complexity of such electrochemical systems, commonly involving enzymes, mediators, and electron conductive materials such as carbon nanomaterials as well as some additives. All these components are interacting with an enzyme in a certain way, influencing its catalytic activity. To design, optimize and

improve an efficient bio(electrochemical) system detailed knowledge and understanding of the involved steps (enzyme kinetics, electron transfer kinetics, mass transfer) and their interactions are required. In this respect, advanced experimental methods which can enable distinction of involved processes at the different time scales and which can provide quantitative system characterization can be helpful.

An example of such a method is electrochemical impedance spectroscopy (EIS), with broad range of applications in different fields of electrochemical science and engineering. EIS has also been used for studying of bioelectrochemical systems. Major application here was monitoring of the immobilization of biomaterials such as enzymes, or antigens/antibodies on electrodes by recording the changes in the Faradaic impedance of a redox probe (e.g. ferri/ferrocyanide) [5–9]. The data evaluation was mainly phenomenological; for example by using an equivalent circuit approach [5], where kinetic data related to the Faradaic impedance of a redox probe on protein modified surfaces were obtained.

Unlike these previous reports, the focus of the present work is the Faradaic impedance of bioelectrochemical event itself. The analysis in the present paper includes the derivation of theoretical impedance of enzyme/electrode system based on reaction mechanism of enzyme catalyzed electrochemical reaction and the experimental validation. In this way mechanistic details related to bioelectrochemical reaction including all relevant kinetic parameters can be obtained. The presented approach overcomes limitations of classical equivalent circuit approach, since it does not rely on phenomenological elements, but on particular reaction mechanism.

* Corresponding author. Tel.: +49 391 6110 319; fax: +49 391 6110 553.
E-mail address: vidakovi@mpi-magdeburg.mpg.de (T. Vidaković-Koch).
[1] ISE member.

In following, three mathematical model variants based on primary catalytic cycle of HRP catalyzed hydrogen peroxide reduction have been formulated. The models have been implemented in MATLAB software and used to simulate theoretical steady state and electrochemical impedance responses. The parameter values are obtained by fitting of the experimental data. While all three models were able to describe experimental steady state data, only the model taking into account enzyme kinetics in accordance to Michaelis–Menten treatment was able to describe impedance response under all investigated conditions. It was shown that EIS is more sensitive for parameter determination and model discrimination than a steady state analysis.

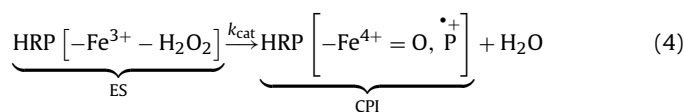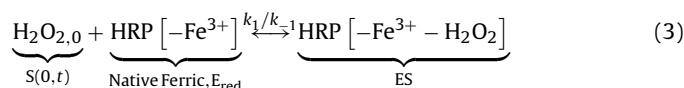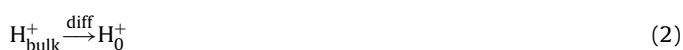## 2. Derivation of theoretical electrochemical admittance

Analytical expressions of electrochemical admittance are developed, based on nonlinear frequency response (NLFR) approach [10,11], restricted in the present case to its linear part. This method was initially developed for analysis of nonlinear electrical circuits and in chemical engineering for investigation of adsorption equilibrium and kinetics [11,12]. Its application in the case of electrochemical systems has been demonstrated in our recent papers on an example of methanol and ferrocyanide oxidation kinetics [13–15]. In general, this method provides a set of frequency response functions (FRFs), where the first order FRF contains the linear part of the response, while the higher order FRFs contain nonlinear fingerprint of the system. We have shown that the first order FRF is identical to the electrochemical admittance (reciprocal of the electrochemical impedance). The procedure for derivation of the FRFs consists of the following steps (for further details please refer to [13–15]):

(a) Definition of nonlinear mathematical model including basic kinetic, mass transport equations as well as dynamic material and charge balances.
(b) Definition of input and output variables.
(c) Taylor approximation of the reaction rate expressions around the steady state.
(d) Substitution of the Taylor polynomials into the mass balance equations.
(e) Substitution of the input and outputs into the equations gained in step "d" and application of harmonic probing.
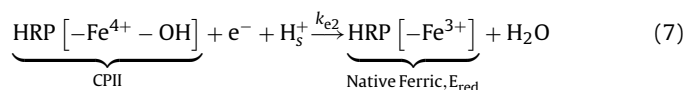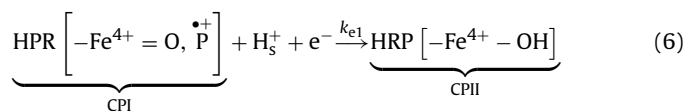(f) Solution of the equations derived in step "e".

In following some details related to model definition as well as final expressions for steady state current and theoretical electrochemical admittance (reciprocal of impedance) are provided. For additional information please see Appendix B.

2.1. Model definition

As a model system horseradish peroxidase (HRP) adsorbed on graphite electrode has been chosen. First report of direct electron transfer (DET) of this enzyme on carbon surface in presence of hydrogen peroxide dates back to 1979 [16]. Since then extensive research on this enzyme, with evidences of DET on different materials has been conducted [17]. The mechanism of HRP catalyzed hydrogen peroxide reduction has been also studied extensively [18–20]. According to literature primary catalytic cycle, can be represented as follows [17,20]:

$$\underbrace{H_2O_{2bulk}}_{S_{bulk}} \xrightarrow{\text{diff}} \underbrace{H_2O_{2,0}}_{S(0,t)} \tag{1}$$

$$H^+_{bulk} \xrightarrow{\text{diff}} H^+_0 \tag{2}$$

$$\underbrace{H_2O_{2,0}}_{S(0,t)} + \underbrace{HRP\left[-Fe^{3+}\right]}_{\text{Native Ferric, }E_{red}} \underset{k_{-1}}{\overset{k_1/k_{-1}}{\rightleftharpoons}} \underbrace{HRP\left[-Fe^{3+}-H_2O_2\right]}_{ES} \tag{3}$$

$$\underbrace{HRP\left[-Fe^{3+}-H_2O_2\right]}_{ES} \xrightarrow{k_{cat}} \underbrace{HRP\left[-Fe^{4+}=O, \overset{\bullet+}{P}\right]}_{CPI} + H_2O \tag{4}$$

or

$$\underbrace{H_2O_{2,0}}_{S(0,t)} + \underbrace{HRP\left[-Fe^{3+}\right]}_{\text{Native Ferric, }E_{red}} \xrightarrow{K_1} \underbrace{HRP\left[-Fe^{4+}=O, \overset{\bullet+}{P}\right]}_{CPI} + H_2O \tag{5}$$

$$\underbrace{HPR\left[-Fe^{4+}=O, \overset{\bullet+}{P}\right]}_{CPI} + H^+_s + e^- \xrightarrow{k_{e1}} \underbrace{HRP\left[-Fe^{4+}-OH\right]}_{CPII} \tag{6}$$

$$\underbrace{HRP\left[-Fe^{4+}-OH\right]}_{CPII} + e^- + H^+_s \xrightarrow{k_{e2}} \underbrace{HRP\left[-Fe^{3+}\right]}_{\text{Native Ferric, }E_{red}} + H_2O \tag{7}$$

where S refers to substrate (in this case hydrogen peroxide H_2O_2), E_{red} to the native form of enzyme, ES, to the enzyme substrate complex and CPI, and CPII, to the oxidized forms of the enzyme, the so-called compound I (CPI), and compound II (CPII). The subscript "bulk" refers to the bulk of the solution and the subscript "0" to the electrode surface.

According to this scheme, HRP reacts initially with the substrate forming an enzyme substrate complex (ES). The complex decomposes further to compound I (CPI) which is then electrochemically reduced in presence of proton H^+ giving compound II (CPII). The initial state of HRP is regenerated by a further electrochemical step followed by H^+ incorporation.

In addition to above presented steps, which correspond to primary catalytic cycle of HRP, more generalized catalytic cycles include also effects of HRP inhibition [17,21]. According to literature the effect of inhibition becomes significant at higher substrate concentrations and longer time of experiment (e.g. in [21] inhibition was reported for concentrations higher than $500\,\mu M$). To avoid this, analysis in the present paper is restricted to lower concentration range and shorter time of experiments where it can be assumed that the inhibition is significantly small and therefore can be neglected.

Based on reaction mechanism presented above and by introduction of different assumptions three model variants have been formulated in the present work.

In the model 1, steps 3 and 4 are lumped (step 5) and all mass transfer effects (substrate and proton diffusion, steps 1 and 2) are neglected. The model 2 is alike model 1, but it includes mass transfer effects. The model 3 is the most general one considering formation and disproportion of ES complex in accordance to steps 3 and 4 and all mass transfer effects. Similar assumptions have been also considered in literature, e.g. steps 3 and 4 were lumped in [18,19,22]. Besides, two electrochemical steps are often lumped in one step [18,22]. This assumption is perfectly justified in the case of steady state model formulations, but in the case of dynamic system characterization cannot be adopted.

The rate expressions for enzymatic steps Eqs. (3)–(5) are formulated as follows:

$$r_1(t) = k_1 \times \Gamma_{E_{red}}(t) \times c_S(0,t) - k_{-1} \times \Gamma_{ES}(t) \tag{8}$$

$$r_2(t) = k_{cat} \times \Gamma_{ES}(t) \tag{9}$$

in model 3 or

$$r_1(t) = K_1 \times \Gamma_{E_{red}}(t) \times c_S(0,t) \tag{10}$$

in models 1 and 2.

The kinetics of electrochemical steps can be described either by Butler–Volmer (Tafel) formalism or more theoretically sounded Markus–Hush approach. One of major differences between these two approaches is the dependence of the electrochemical rate constant on potential, which in the case of Butler–Volmer increases exponentially without any bound, while the Markus–Hush predicts leveling off of the electrochemical reaction rate at sufficiently high values of overpotential [23]. This important difference cannot be so easily experimentally proven, since in real systems number of other "sources" (mass transfer limitations or chemical steps) causes the saturation of the reaction rate. In the present case the kinetics of enzymatic reaction as well as mass transport resistances are possible rate limiting steps at higher overpotentials. The Butler–Volmer (Tafel) approach as mathematically simpler (especially taking into account necessity of reaction rate linearization in the here presented approach for derivation of theoretical impedance) has been adopted in the present paper. The downside of this particular choice is an introduction of phenomenological transfer coefficient α, instead of reorganization energy in the Markus–Hush approach. We additionally neglected the reverse reaction rate in Butler–Volmer equation, using effectively Tafel equation (Eqs. (11) and (12)). This assumption can be considered valid since the horseradish peroxidase behaves experimentally as a "one way enzyme" and the recordable catalytic currents appear at overpotentials of ca. −200 mV. Dispersion of the enzyme orientation at the electrode surface and hence the dispersion of the heterogeneous rate constants determining the electron transfer rate between an enzyme and an electrode has been also neglected, assuming effective heterogeneous rate constants.

Proton involvement in the formulations of rates of electrochemical steps was so far omitted in mathematical models in literature. However, the dependence of apparent electrochemical rate constant on proton concentration, was proven experimentally and it was taken as an indication of the proton involvement in the charge transfer step [24]. We followed this assumption in the present work, taking into account proton participation in the electrochemical steps in accordance with power law kinetics. As a consequence electrochemical rate constants k_{e10} and k_{e20} are defined as second order heterogeneous rate constants.

$$r_{e1}(t) = -k_{e10} \times \exp\left(-\frac{\alpha_1 F}{RT}(E(t) - E_{r1})\right) \times \Gamma_{CPI}(t) \times c_{H^+}(0, t) \quad (11)$$

$$r_{e2}(t) = -k_{e20} \times \exp\left(-\frac{\alpha_2 F}{RT}(E(t) - E_{r2})\right) \times \Gamma_{CPII}(t) \times c_{H^+}(0, t) \quad (12)$$

where α_1 and α_2 are transfer coefficients, which in the present case are assumed to have the same value (only one effective α value), $E(t)$ is the electrode potential, $E_{r,i}$ is the formal potential of step i ($i = 1,2$) and F, R and T have meanings of Faradays and universal gas constants and temperature respectively.

The concentration profiles of substrate is obtained by solving the convective diffusion equation, which in the case of a rotating disc electrode and by neglecting the convective mass transfer contributions in the Nernstian diffusion layer [14], simplifies to the second Fick's law:

$$\frac{\partial c_S(z, t)}{\partial t} = D_S \frac{\partial^2 c_S(z, t)}{\partial z^2} \quad (13)$$

In the case of proton, in addition to diffusion, the influence of chemical source/sink in the solution on the proton concentration profile has been considered. It can be assumed that due to the proton consumption at the electrode surface, local pH value close to the electrode surface changes, which might influence the equilibrium of the proton donor dissociation. This effect was observed experimentally by Ferapontova and Gorton [24] who studied the influence of different proton donors on direct electron transfer of HRP on gold and showed that at higher pH the apparent electrochemical rate constant increases in presence of additional proton donors (e.g. NH_4^+). In the present case only first acid dissociation step was taken into account, since the dissociation constants of the second and third dissociation steps of H_3PO_4 dissociation are several orders of magnitude smaller than the first one:

$$HA \overset{k_{a1}, k_{-a1}}{\longrightarrow} H^+ + A^- \quad (14)$$

where HA stands for H_3PO_4 and A^- for $[H_2PO_4]^-$.

The mass balance equation in this case reads

$$\frac{\partial c_{H^+}(z, t)}{\partial t} = D_{H^+} \frac{\partial^2 c_{H^+}(z, t)}{\partial z^2} + k_{a1} \times c_{HA}(z, t)$$
$$- k_{-a1} \times c_{A^-}(z, t) \times c_{H^+}(z, t) \quad (15)$$

Boundary conditions for solving of Eqs. (13) and (15) are
For $z = 0$ in the case of substrate

$$D_S \frac{\partial c_S(z, t)}{\partial z}\Big|_{z=0} = r_1(t) \quad (16)$$

while in the case of proton

$$D_{H^+} = \frac{\partial c_{H^+}(z, t)}{\partial z}\Big|_{z=0} = -(r_{e1}(t) + r_{e2}(t)) \quad (17)$$

and for $z = \delta_{D,i}$

$$c_i(\delta_{D,i}, t) = c_{i,\infty} \quad (18)$$

where $\delta_{D,i} = 1.61 D_i^{1/3} \nu^{1/6} \omega_r^{-1/2}$ is the thicknesses of diffusion layer at rotation speed ω_r of rotating disc electrode in the solution of kinematic viscosity ν and "i" refers to S or H^+.

To account for concentration changes of adsorbed species mass balance equations for adsorbed species have been formulated

$$\frac{d\Gamma_{ES}(t)}{dt} = r_1(t) - r_2(t) \quad (19)$$

$$\frac{d\Gamma_{CPI}(t)}{dt} = r_2(t) - |r_{1e}(t)| \quad (20)$$

$$\frac{d\Gamma_{CPII}(t)}{dt} = |r_{1e}(t)| - |r_{2e}(t)| \quad (21)$$

To complete the model, the charge balance at the electrode surface has to be formulated

$$C_{dl} \frac{dE(t)}{dt} = i(t) - F \times (r_{1e}(t) + r_{2e}(t)) \quad (22)$$

where C_{dl} is double layer capacitance and $i(t)$ is the cell current density. In a case of steady state conditions all time derivate become zero.

2.2. Rate expression under steady state conditions

For steady state conditions and Model 3 following overall electrochemical rate expression can be derived

$$-r_{e,ss} = \frac{k_{cat} \times \Gamma_t \times c_{H^+,ss}(0, E_{ss}) \times c_{S,ss}(0, E_{ss}) \times k_e \times \exp\left(-\frac{\alpha F}{RT}E_{ss}\right)}{k_{cat} \times c_{S,ss}(0, E_{ss}) + k_e \times \exp\left(-\frac{\alpha F}{RT}E_{ss}\right) \times c_{S,ss}(0, E_{ss}) \times c_{H^+,ss}(0, E_{ss}) + K_m \times k_e \times \exp\left(-\frac{\alpha F}{RT}E_{ss}\right) \times c_{H^+,ss}(0, E_{ss})} \quad (23)$$

which represented in its reciprocal form

$$\frac{1}{-r_{e,ss}} = \frac{1}{\Gamma_t}\left[\frac{K_m + c_{S,ss}(0, E_{ss})}{k_{cat} \times c_{S,ss}(0, E_{ss})} \right.$$

$$\left. + \frac{1}{c_{H^+,ss}(0, E_{ss}) \times k_e \times \exp\left(-\frac{\alpha F}{RT} E_{ss}\right)} \right] \quad (24)$$

shows the series connection between an enzymatic and electrochemical steps as also shown by Andreu et al. [20]. The expression in the present paper is somewhat different compared to [20], accounting explicitly for proton concentration and having a different definition of the electrochemical rate constant.

In Eqs. (23) and (24), k_e stands for an effective electrochemical rate constant defined as:

$$k_e = \frac{k_{e1} \times k_{e2}}{k_{e1} + k_{e2}} \quad (25)$$

where k_{e1} and k_{e2} are defined as follows:

$$k_{e1} = k_{e10} \times \exp\left(\frac{\alpha_1 F}{RT} E_{r1}\right)$$

$$k_{e2} = k_{e20} \times \exp\left(\frac{\alpha_2 F}{RT} E_{r2}\right)$$

The K_m is the Michaelis–Menten constant defined as usual:

$$K_m = \frac{k_{-1} + k_{cat}}{k_1} \quad (26)$$

To obtain the reaction rate values (Eq. (23)), concentrations of substrate and proton at the electrode surface are also needed. These concentrations are obtained by solving convective diffusion equations (Eqs. (13) and (15)) with given boundary conditions. As can be anticipated from Eq. (23), under steady state conditions, separate values of rate constants of two electrochemical steps cannot be determined, but only an effective rate constant, which value is more influenced by the rate of the slower step. Similarly, from 3 enzymatic kinetic constants only k_{cat} and K_m can be determined independently, while k_1 and k_{-1} will be lumped together in K_m value. Unlike steady state conditions, all these constants can be determined from frequency response analysis as it will be shown below.

2.3. Analytical expression for electrochemical admittance

The final expression for the electrochemical admittance $H_1(\omega)$ which is identical to the reciprocal of the electrochemical impedance reads

$$H_1(\omega) = \frac{2FR_4R_1 - R_3C_{dl}j\omega}{2F(R_4R_2 - R_3R_5)} \quad (27)$$

where the groups R_i ($i = 1,5$) and further coefficients contained in groups R_i are defined in Table 1.

In Eq. (27), the enzymatic kinetic constants are contained only in the group R_4 (please see Table 1) The group R_4 in addition to k_{cat} and K_m, depends also on k_1 constant. The remaining k_{-1} constant can be easily calculated based on the other three constants and the definition of Michaelis–Menten constant. It can be also easily seen that at very low frequencies ($\omega \to 0$) the $H_1(\omega)$ will become insensitive to k_1 constant, which will correspond to the steady state case. The rate constants of two electrochemical steps (k_{e1} and k_{e2}) are contained in all R groups, except for the R_5 and they do not merge into one effective rate constant (k_e) as is the case of steady state conditions. This makes possible to determine them separately by using frequency response analysis.

Following the same procedure other two frequency response functions (not shown here), based on models 1 and 2 can be derived.

Table 1

Expressions for the groups R_i ($i = 1,5$) which appear in equation 27 as well as of further coefficients contained in groups R_i (P_i ($i = 1$ to 6), T_i ($i = 1,3$) and a_i ($i = 1,2$)).

Groups	Expression
R_1	$\frac{C_{dl}j\omega - FP_3}{P_2F}[1 - T_3P_2] - T_3P_3$
R_2	$\frac{(1 + (C_{dl}j\omega - FP_3)SR_\Omega)}{P_2F}(1 - T_3P_2) - T_3P_3SR_\Omega$
R_3	$-\frac{(P_1j\omega + 2P_4P_1)}{P_2(j\omega + P_4)}$
R_4	$\frac{j\omega(j\omega + P_4 + (P_1/2))}{(j\omega + P_4)} + \frac{k_{cat}(j\omega + P_4 + P_1)(C_{S,SS} + \Gamma_{E_{red},ss}T_1)}{\left(\frac{j\omega}{k_1} + K_m - \Gamma_{E_{red},ss}(T_2 - T_1) + C_{S,SS}\right)(j\omega + P_4)}$
R_5	$\frac{1 + SR_\Omega C_{dl}j\omega}{2F}$
P_1	$-k_{e10} \times C_{H^+,SS} \times e^{(-(\alpha_1 F/RT)(E_{ss} - E_{r1}))}$
P_2	$-k_{e10} \times \Gamma_{CPI,SS} \times e^{(-(\alpha_1 F/RT)(E_{ss} - E_{r1}))}$
P_3	$k_{e10} \times \Gamma_{CPI,SS} \times C_{H^+,SS} \times \frac{\alpha_1 F}{RT} \times e^{(-(\alpha_1 F/RT)(E_{ss} - E_{r1}))}$
P_4	$-k_{e20} \times C_{H^+,SS} \times e^{(-(\alpha_2 F/RT)(E_{ss} - E_{r2}))}$
P_5	$-k_{e20} \times \Gamma_{CPII,SS} \times e^{(-(\alpha_2 F/RT)(E_{ss} - E_{r2}))}$
P_6	$k_{e20} \times \Gamma_{CPII,SS} \times C_{H^+,SS} \times \frac{\alpha_2 F}{RT} \times e^{(-(\alpha_2 F/RT)(E_{ss} - E_{r2}))}$
T_1	$\frac{-\tanh(a_1\delta_{D,Red}\sqrt{\omega})k_1C_{S,SS}}{D_S a_1\sqrt{\omega} + \tanh(a_1\delta_{D,Red}\sqrt{\omega})k_1\Gamma_{E_{red},ss}}$
T_2	$\frac{\tanh(a_1\delta_{D,Red}\sqrt{\omega})k_{-1}}{D_S a_1\sqrt{\omega} + \tanh(a_1\delta_{D,Red}\sqrt{\omega})k_1\Gamma_{E_{red},ss}}$
T_3	$\frac{-\tanh(a_2\delta_{D,H^+})}{D_{H^+}a_2}$
a_1	$\sqrt{\frac{j}{D_S}}$
a_2	$\sqrt{\frac{k_{-a1}C_{A^-} + j\omega}{D_{H^+}}}$

3. Experiment

Horseradish peroxidase (E.C. 1.11.1.7, HRP) from *Amorica rusticana* was supplied by Serva Electrophoresis GmbH. All other chemicals were of analytical reagent grade and purchased from Merck or Sigma–Aldrich. Ultrapure water from Millipore was used in all experiments.

Spectroscopically pure carbon (graphite) planchets (Ted Pella, INC, USA) with impurities equal to or less than 2 ppm were used as a mechanical and electrical supports for the preparation of enzymatic electrodes. For the electrochemical tests the discs were mounted in a sample holder for rotating disc electrode (RDE) with an opening of 6 mm (0.28 cm² working area). Graphite electrodes were polished by fine emery paper (P1000), rinsed with deionized water and then further polished with ordinary white paper to smoothen the rough electrode surface.

For preparation of HRP modified electrodes, 50 μl of 6 mg ml^{-1} HRP solution in phosphate buffer was placed on the top of the graphite electrode and left to dry under ambient conditions. After that, the electrodes were fitted into a rotating disk holder, rinsed with phosphate buffer solution and placed in cell for 2 h under rotation in order to desorb all weakly adsorbed enzymes.

All electrochemical experiments were carried out in a conventional double-jacketed electrochemical cell (Radiometer Analytical). The RDE was used as a working electrode, platinum wire as a counter electrode, and saturated calomel electrode (SCE) as a reference electrode, but the potential values in the paper are recalculated with respect to the standard hydrogen electrode (SHE) scale. All experiments were carried out at $21 \pm 1\,°C$ at a rotation rate of 400 rotations per minute (rpm) in order to ensure defined mass transport conditions in the investigated system. Before the experiments, the solution was purged with nitrogen and nitrogen atmosphere was kept during all experiments. Electrochemical experiments were performed by a computer controlled potentiostat PGSTAT302 (Eco Chemie/Autolab).

Steady state experiments were performed potentiostatically with a fixed delay of 45 s at every potential, in the potential range from 0.5 to 0.0 V vs. SCE. The potential step was 100 mV.

The electrolyte was 0.1 M phosphate buffer solution, containing potassium dihydrogen phosphate (Merck) and disodium hydrogen phosphate (Sigma–Aldrich). The buffer was prepared at two diffident pH, pH 5 and pH 6.

Impedance measurements were performed in a frequency range from 10 Hz to 50 kHz at different steady state potentials. The amplitude of the sinusoidal signal was 10 mV (from base to peak).

4. Results and discussion

The mathematical models derived in previous section have been implemented in MATLAB software and used for simulation of steady state and electrochemical impedance responses.

4.1. Steady state behavior

Steady state experiments are performed at two different pH values (5 and 6) and at different hydrogen peroxide concentrations. The experimental data in Fig. 1a and b correspond to average of at least three independent experiments. Since the enzymes were only physically adsorbed at the electrode surface, some level of desorption during the experimental runs can be expected, which was also reflected in a better reproducibility of experiments at lower concentrations (experiments were always performed in sequences from lower to higher concentrations). The dynamics of enzyme desorption was beforehand checked in a separate experiment, where it was seen that after a pronounced desorption in the beginning, the activity remained stable for a certain time window (ca. 30 min), after which it continued to decrease (not shown here). To control the impact of the enzyme desorption, all experiments have been performed in this stable time window. The simulated curves (lines, for color code please see the figure caption) corresponding to the three different models introduced before and with parameter values given in Table 2 are shown along with experimental data (symbols) in Fig. 1.

The parameter values in Table 2, have been determined by global optimization using weighted least square method. The objective function (Eq. (28)) was minimized using fminsearch command in MATLAB.

$$\min \sum_{j=1}^{6} \sum_{k=1}^{6} (i_{\text{sim}}(c_{s,j}, E_k, p) - i_{\text{exp}}(c_{s,j}, E_k))^2 \times w_{jk} \qquad (28)$$

where p corresponds to parameters appearing in Eq. (23), w is the weighting factor and subscripts "sim" and "exp" correspond to simulated and experimental data, respectively. For fitting more significance (higher weight) was given to points at lower concentrations, since these data are less affected by possible inhibition effects and they also had lower variance. The sums of residuals for different models at different pH conditions are given in Table 2.

All three models describe qualitatively well the experimental data. However, the Model 3, which takes into account ES formation
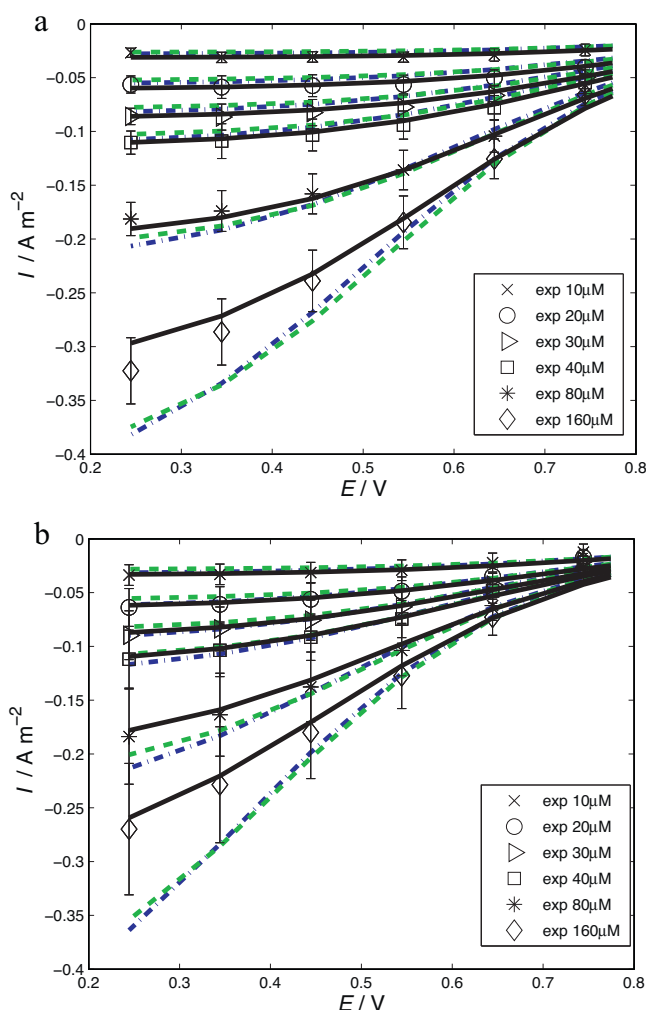

Fig. 1. Steady state polarization curves at (a) pH 5 and (b) pH6 for hydrogen peroxide reduction on horseradish peroxidase modified graphite electrode; symbols – experimental data and lines – simulated curves (model 1 – blue dash dot line, model 2 – green dash line and model 3 – black solid line). Conditions: fixed delay of 1 min, hydrogen peroxide concentrations from 10 to 160 μM, room temperature; rotation rate 400 rpm; parameter for simulations are given in Table 2. (For interpretation of the references to color in this figure legend, the reader is referred to the web version of the article.)

step, shows better quantitative agreement (please see the sums of residuals, Table 2) compared to other two models, especially at higher substrate concentrations. The predictions of models 1 and 2 almost coincide, which can be taken as an indication of a small influence of mass transfer resistances in the present case. Still, the enzymatic kinetic constants obtained by fitting the experimental

Table 2
Globally optimized parameter values based on steady state data for all three models under different conditions of pH and hydrogen peroxide concentrations.

Parameters	pH 5			pH 6		
	M1	M2	M3	M1	M2	M 3
α	0.17	0.17	0.17	0.17	0.17	0.17
$K_1/10^3$ m^3 mol^{-1} s^{-1}	5.58	7.00	–	5.57	6.78	–
k_{cat}/s^{-1}	–	–	1898	–	–	1202
K_{m}/mol m^{-3}	–	–	0.21	–	–	0.20
$\mathbf{k_{e0}}/10^3$ m^3 mol^{-1} s^{-1}	2.77	2.77	3.78	17.17	17.17	18.9
$k_{e0} \times c_{\text{H}^+,\infty}$/s^{-1} *	27.74*	27.74*	37.80*	17.17*	17.17*	18.9*
$\Gamma_t/10^{-13}$ mol cm^{-2}	2.61	2.61	2.20	3.0	3.0	3.1
Sum of residuals	0.0089	0.0089	0.0014	0.014	0.013	0.0015

* Calculated (not fitted) values.

Table 3
Globally optimized parameter values based on EIS data for model 3 under different conditions of pH and hydrogen peroxide concentrations.

Parameters	pH 5	pH 6
α	0.17[a]	0.17[a]
$k_1/10^3\,\mathrm{m}^3\,\mathrm{mol}^{-1}\,\mathrm{s}^{-1}$	12.18	15.9
k_{-1}/s^{-1}	614[b]	1962[b]
$k_{\mathrm{cat}}/\mathrm{s}^{-1}$	1898[a]	1202[a]
$K_{\mathrm{m}}/\mathrm{mol}\,\mathrm{m}^{-3}$	0.21[a]	0.20[a]
$k_{e10}/10^5\,\mathrm{m}^3\,\mathrm{mol}^{-1}\,\mathrm{s}^{-1}$	5.62	2.63
$k_{e20}/10^3\,\mathrm{m}^3\,\mathrm{mol}^{-1}\,\mathrm{s}^{-1}$	6.19	36.7
$k_{e0}/10^3\,\mathrm{m}^3\,\mathrm{mol}^{-1}\,\mathrm{s}^{-1}$	6.12[b]	32.2
$k_{e0} \times c_{\mathrm{H}^+,\infty}/\mathrm{s}^{-1}$	61.20[b]	32.2[b]
$\Gamma_t/10^{-13}\,\mathrm{mol}\,\mathrm{cm}^{-2}$	3.0	2.2
Sum of residuals	1.54	3.36

[a] Adopted (not fitted) values.
[b] Calculated (not fitted) values.

data using models 1 and 2 although similar, are not identical. The value in the case of model 2 is a bit higher and can be probably considered more correct, since the substrate concentration at the electrode surface shows small dependence on mass transport conditions (not shown here). The electrochemical constants (α and k_{e0}) are the same for both models, but k_{e0} is somewhat pH dependent.

Before discussing further the values of kinetic parameters from different models (Table 2), their dependence on total enzyme concentration will be shortly addressed. This issue was already discussed in literature in different publications [17,18,20]. If the total enzyme concentration at the electrode surface was not known, as in the present case, two approaches regarding kinetic parameter determination were followed. In the first approach an assumption on total enzyme concentration was made, while in the second one kinetic parameter values were assumed. The first approach was adopted by Ruzgas et al. [18], who approximated the total enzyme concentration, based on literature results with proteins with similar molecular weight as HRP and an assumption of the electrode surface roughness [18]. Similarly, Ferapontova nd Gorton [24] assumed total enzyme coverage of 23 pmol cm^{-2} on Au electrode based on quartz crystal microbalance data. Other approach was followed by Limoges [21] et al. and Andreu et al. [20], who assumed that the enzyme activity at the electrode surface was the same as for the enzyme in the solution. The later authors also argued that the upper limit for a fully packed enzyme monolayer of ca. 10 pmol cm^{-2} based on enzyme crystallographic data is rather unrealistic, due to the absence of nonturnover catalytic current and they suggested that the more realistic upper limit of enzyme monolayer coverage is ten times lower (ca. 1 pmol cm^{-2}). Also taking into account that not all adsorbed enzyme will contribute to DET (according to Ruzgas et al. [18] below 50%), the low enzyme surface coverage adopted by Andreu et al. [20] appears realistic. These different approaches resulted in different surface coverage, with values ranging from ca. 40 pmol cm^{-2} [18] to ca. 0.1 pmol cm^{-2} [20]. Since the kinetic constants are directly related to the surface coverage, the assumption of higher enzyme coverage led to significantly lower values of kinetic parameters than in the case of the enzyme in the solution.

As already mentioned, the explicit value of the enzyme surface coverage in the present work was not known. Since, the enzyme adsorption conditions as well as the current values in the present work were in a similar range as in [20], low enzyme coverage values similar to [20] were assumed as starting values for parameter fitting. The average enzyme coverage value that was obtained based on described mathematical models and previously discussed assumptions was 0.27 ± 0.04 pmol cm^{-2}. As can be seen in Tables 2 and 3, a small difference was observed between surface coverage values at two different pH. This difference can be due to differences in enzyme orientation at different pH values,

or different level of electrostatic interaction with the electrode surface, but more probably is a random effect, as discussed by Andreau et al. [20].

The models 1 and 2 are based on similar reaction mechanisms as in [18,19,22,24] therefore, the kinetic constants in models 1 and 2 in this paper will have similar meanings as in already mentioned literature sources. For example, the k_1 constant in mentioned publications has the similar meaning as the K_1 constant in the present work. The reported values of K_1 constants for HRP adsorbed on different kind of electrodes in literature were: $0.039 \pm 0.014 \times 10^6\,\mathrm{M}^{-1}\,\mathrm{s}^{-1}$ (enzyme coverage 40 pmol cm^{-2}) [18] and $0.13 \pm 0.02 \times 10^6\,\mathrm{M}^{-1}\,\mathrm{s}^{-1}$ (enzyme coverage 40 pmol cm^{-2}) [19] on graphite electrodes, $0.031 \pm 0.014 \times 10^6\,\mathrm{M}^{-1}\,\mathrm{s}^{-1}$ (enzyme coverage 14 pmol cm^{-2}) on graphite coating [25], and $0.13 \pm 0.02 \times 10^6\,\mathrm{M}^{-1}\,\mathrm{s}^{-1}$ (enzyme coverage 23 pmol cm^{-2}) on gold[24]. The values reported in the present paper are more than 100 times bigger ($5.58 \times 10^6\,\mathrm{M}^{-1}\,\mathrm{s}^{-1}$ based on Model 1 and ca. $7.0 \times 10^6\,\mathrm{M}^{-1}\,\mathrm{s}^{-1}$ based on model 2) and closer to value reported for the enzyme in the solution $15 \times 10^6\,\mathrm{M}^{-1}\,\mathrm{s}^{-1}$ [18]. As we already discussed this is mainly a consequence of an adoption of low surface coverage (ca. 0.3 pmol cm^{-2}) of the enzyme in the present work. Same reasons were discussed by Ruzgas et al. [18] who concluded that the low bimolecular constant value in their case was a consequence of either very low activity of immobilized enzyme at the electrode surface or overestimation of an enzyme surface coverage. These reasoning are also valid in the present case, with the results indicating somewhat lower activity of immobilized enzymes, compared with enzyme in the solution. The activity of enzyme in turn of K_1 constant at two different pH values based on models 1 and 2 are almost the same, which is in accordance with literature observations [24].

The rate constants of electrochemical reactions, in the present study are defined as second order constants. In the case of steady state only one effective electrochemical rate constant in accordance to (Eq. (23)) can be determined, which we denoted as k_{e0}. For comparison with literature results this value has to be multiplied with proton concentration, giving an apparent electrochemical rate constant with values in the range from 27.74 s^{-1} at pH 5 to 17.17 s^{-1} at pH 6 (Table 2). Similar pH dependence of the apparent electrochemical reaction rate constant was also obtained by Ferapontova and Gorton [24]. Unlike this apparent rate constant, the "intrinsic" rate constant increases with pH, this might indicate more favorable enzyme orientation to the electrode surface at higher pH values.

Similar to enzymatic constants, the values of the electrochemical rate constants depend on the total enzyme concentration. This can be easily anticipated by analyzing rate expressions under steady state conditions. As a consequence an assumption of low total enzyme concentration leads to higher value of the electrochemical rate constant, than reported by Ruzgas et al. [18] (0.66 ± 0.28 s^{-1}). In addition electrochemical rate constants in literature e.g. in [18] were determined using data at high overpotentials, where the total reaction rate is mainly controlled by enzymatic kinetics and/or mass transfer, which might influence the reliability of such determination.

The model 3 takes into account the formation of ES complex in accordance to Michaelis–Menten mechanism, therefore provides an additional enzymatic kinetic constant compared to models 1 and 2. The assumption of the ES complex formation was first introduced by Andreu et al. [20]. As we already commented these authors assumed a constant ratio of the values of the enzymatic constants ($k_{\mathrm{cat}}/K_{\mathrm{m}}$) as for the enzyme in the solution. In addition they assumed that this ratio is pH independent. Based on these assumptions the enzyme surface coverage of ca. 0.11 ± 0.03 pmol cm^{-2} in the pH range from 4.1 to 8.0 was calculated. As we already discussed we adopted similar low enzyme coverage values and determined kinetic parameters by fitting of

the experimental data (Table 2). This procedure resulted in following kinetic constants: k_{cat} value was 1898 s^{-1} and K_m 0.21 mM at pH 5, while at pH 6 k_{cat} was 1202 s^{-1} and K_m 0.20 mM. As can be seen, these values at two different pH were similar, but a bit lower than assumed by Andreu et al. [20].

The values of electrochemical rate constants (pH 5 and 6) obtained by using model 3 were similar to values determined using models 1 and 2. These values (37.8 and 18.9 s^{-1} at pH 5 and 6 respectively) are significantly higher than similar kinetic constant (1.4 and 3.5 s^{-1} at pH 5 and 6, respectively) reported by Anreu et al. [20]. This difference can be partly attributed to different ways of describing the rate of electrochemical steps (Tafel formalism in the present case vs. Markus-DOS theory in the [20]). On the other hand this constant sets the onset potential of the reaction and higher values obtained in the present work can reflect the experimentally observed shift in the catalytic current to more positive potentials in the present case, compared to [20]. In this case the differences in these electrochemical rate constants might reflect the differences in the catalytic properties of electrode materials in these two studies.

In addition to already discussed kinetic parameters, the value of transfer coefficient α has been also determined. The obtained α value was 0.17 (Table 2) independent on the model used for the data fitting. As we already discussed α value in the present case is an effective phenomenological coefficient. It reflects partly the downside of the choice of Tafel formalism in the present case. Tafel formalism can be understood as a limiting case of Markus–Hush theory, valid if the reorganization energy is much higher than the applied overpotential. This condition is not perfectly satisfied in the case of bioenzymatic reactions, since the values of the reorganization energies are small and in the range of imposed overpotential [20]. This will be basically equivalent to potential dependence of transfer coefficient α, with 0.5 value only at zero overpotential and values close to zero at high overpotential values (e.g. 0.08 value can be obtained at -1 V overpotential and by assuming the reorganization energy of 0.6 eV). In the present case this dependence was neglected, which resulted in an effective α value of 0.17.

4.2. Electrochemical impedance spectroscopy

The theoretical electrochemical impedances for model 3 (reciprocal of Eq. (27)) along with experimental data (symbols) in the form of Nyquist plots and as a function of an applied electrode potential at two different pH conditions and different substrate concentrations have been shown in Fig. 2. The corresponding parameter values used for simulation of theoretical electrochemical impedances are shown in Table 3. These values, similar to parameters determined for steady state models, have been obtained by global optimization using weighted least square method with following objective function:

$$\min \sum_{i=1}^{3} \sum_{k=1}^{30} \left\{ \left[\left(Re(Z)_{sim}(E_i, \omega_k, p) - Re(Z)_{exp}(E_i, \omega_k) \right]^2 w_{ik} \right. $$

$$\left. + \left[\left(Im(Z)_{sim}(E_i, \omega_k, p) - Re(Z)_{exp}(E_{i,\omega_k}) \right]^2 w_{ik} \right\} \quad (29)$$

The sums of residuals for different pH conditions are provided in Table 3. In fitting procedure some parameters, already known from steady state case, were fixed (coefficient α and two enzymatic constants k_{cat} and K_m). The constants which were fitted (presented as bold in Table 3) are enzymatic and electrochemical constants k_1, k_{e10} and k_{e20} respectively, as well as the total enzyme surface coverage. The remaining enzymatic rate constant k_{-1} was calculated using the definition for K_m. For pH 6 only data at 80 μM were used for parameter determination. The data at 160 μM were simulated using the same parameter values. For fitting, data at lower
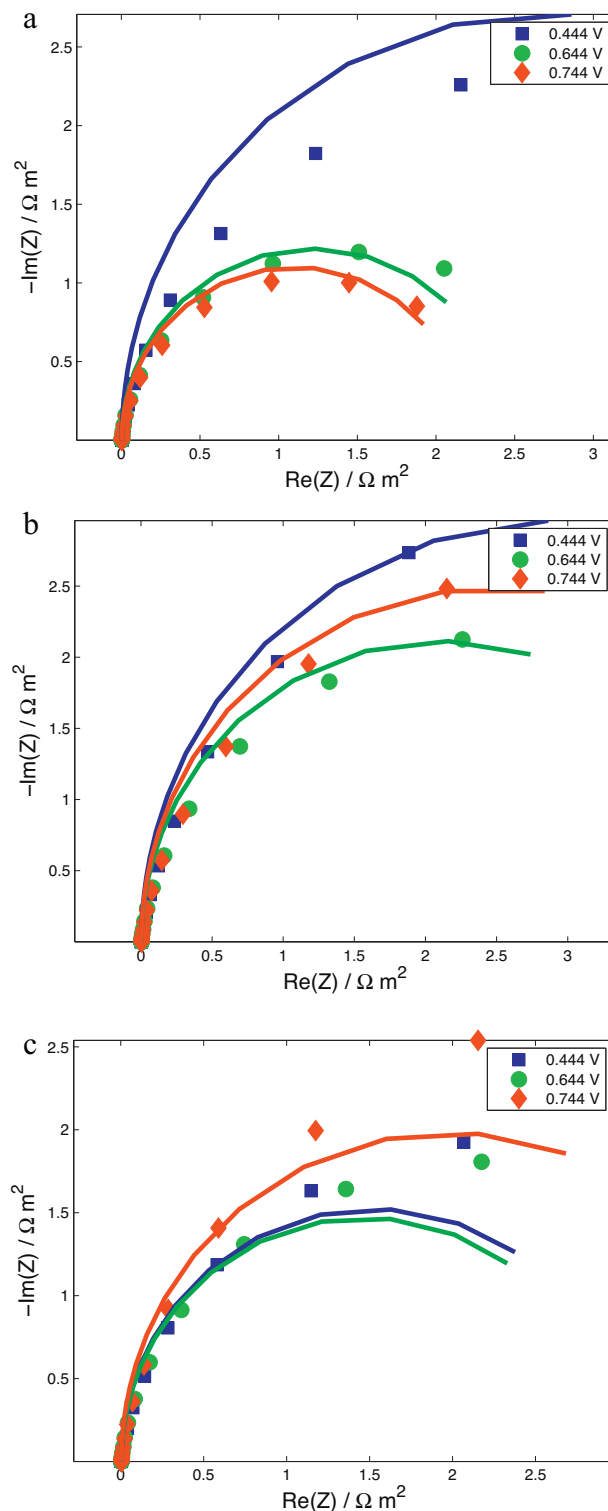

Fig. 2. Experimental EIS (symbols) vs. simulated (lines-model 3) with optimized parameters (see Table 3) at three potentials; (a) pH5 at 80 μM hydrogen peroxide concentration, (b) pH 6 at 80 μM hydrogen peroxide concentration and (c) pH 6 at 160 μM hydrogen peroxide concentration. Other conditions: room temperature and rotation rate 400 rpm

frequencies were given more significance (higher weight), since they have higher sensitivity to kinetic model parameters. However, these data were measured with higher uncertainty, which might impact the values of the constants. Still, the variance of the experimental data was more expressed for experimental runs using different electrodes (prepared under same conditions), than for repeated experiments on a single electrode. This indicates that the major variability comes from variations in enzyme concentration on different electrodes and not from time stability or possible inhibition effects (for more information, please see Figs. S3 and S4, Supporting information).

Only model 3 was able to describe qualitatively and quantitatively the enzyme/electrode kinetics under studied conditions (both pH values and different hydrogen peroxide concentrations). Other two models, although able to describe experimental data at single potential values, failed to provide correct order of change of observed impedance responses, with the change of potential (not shown here).

The electrochemical impedance spectroscopy is more sensitive for parameter determination than a steady state response which is reflected in higher number of parameters in the former case (Table 3) [14]. Model 3, in addition to two electrochemical constants, provide further enzymatic kinetic constants in accordance with Michaelis–Menten mechanism. It gives also further support that the rate of the first electrochemical step is faster than the second one (at least 10 times). However, the sensitivity of theoretical impedance on this constant is lower compared to other constants which allows the determination of only lower limit value of this constant (close to here reported value). Further increase of k_{e10} produces only minor changes in the theoretical impedance response (please see Fig. S2, Supporting information). The effective electrochemical rate constant is again influenced mainly by the rate of the slower step, with values which resemble reasonably well the steady state conditions. From enzymatic kinetic constants, the k_{cat} values and K_m as already mentioned were not fitted but adopted based on their steady state values. In addition, two other kinetic constants become available (k_1 from fitting and k_{-1} from calculation). Their values are somewhat pH dependent, which might indicate, some influence of pH on enzyme activity as shown in [26]. However, for more sounded analysis experiments at additional pH values would be necessary. The values of the total enzyme coverage are similar to those obtained from steady state experiments. The somewhat lower value at pH 6 might indicate lower level of enzyme stability at higher pH, which was also seen in lower reproducibility of the experimental steady state data at pH 6 (Fig. 1b).

The total reaction resistance, which can be roughly approximated with the diameter of semicircles (Fig. 2), is not changing uniformly with the change of potential. One can expect that an increase of the imposed overpotential, increases the driving force for the reaction, which should be reflected further in an increase of the catalytic current (e.g. in steady state response) or a decrease of the total reaction resistance in the electrochemical impedance response. This reasoning holds as long as the electrochemical reaction rate is the slowest step in the reaction mechanism. This was observed experimentally in certain potential range; for example at pH 6 (both concentrations) the total resistance in the potential range from 0.744 V to 0.644 V (complies with the direction of an increase of the overpotential) decreases. However, further increase of the overpotential leads to an increase of the reaction resistance, implying that some other step than electrochemical becomes limiting. If one analyses the reaction mechanism presented in the beginning, two steps can contribute to this limitation, namely enzymatic reaction step and mass transfer resistances. Although the reaction rate is somewhat influenced by mass transfer conditions, this effect is not so significant (please see e.g. the results of models 1 and 2 in Fig. 1), it is more likely that the enzymatic reaction
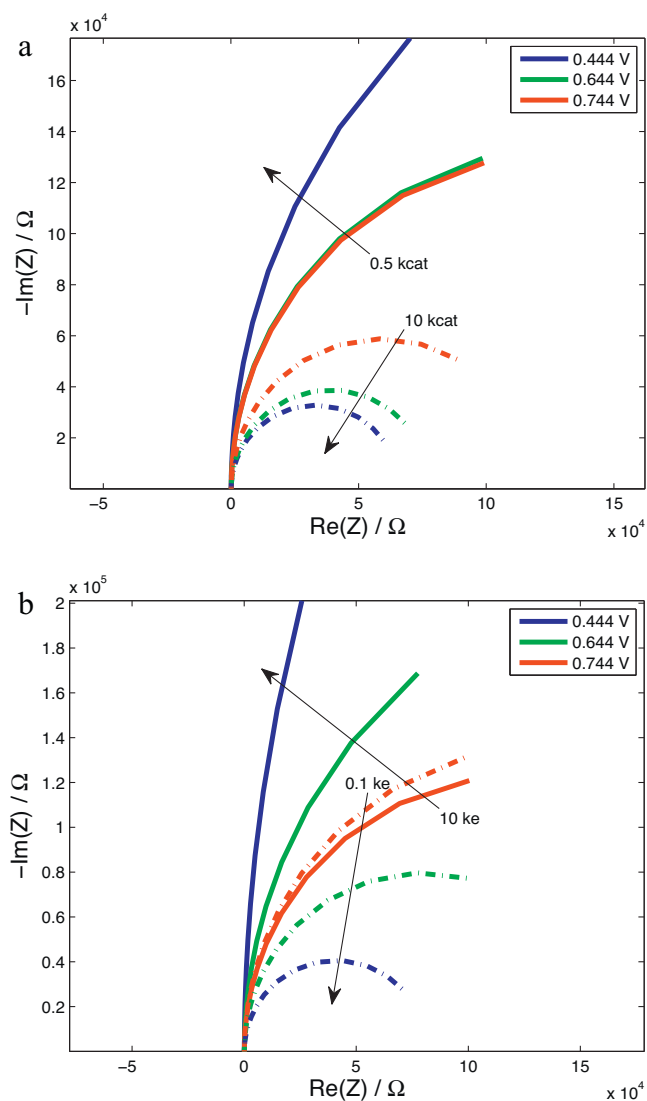

Fig. 3. Simulated EIS of model 3 showing the influence of the variation of the reaction rate constants with respect to their optimized values (Table 3) (a) variation of k_{cat} at pH 6 and (b) variation of k_e at pH 5. Other conditions: 80 μM hydrogen peroxide concentration, room temperature, rotation rate 400 rpm and with other parameters given in Table 3.

becomes rate limiting in this potential range. This effect is obvious in simulations shown below (Fig. 3a), where the influence of the change of the enzymatic reaction rate (here k_{cat}) on impedance response at pH 6 considering two limiting cases, small k_{cat} (0.5 times smaller than the nominal k_{cat} value) and large k_{cat} (10 times bigger than the nominal value) was studied. Similarly the simulated data at pH 5 and 80 μM substrate concentration shows the influence of the change of the effective electrochemical rate constant on the overall impedance response (Fig. 3b). As can be seen in Fig. 3a, the low k_{cat} value induces prevailing enzymatic reaction rate control in the whole range of studied potentials, while in case of the high k_{cat} value, the electrochemical steps become rate limiting. The real case at pH 6 is clearly between these two limiting cases with the change of the rate limiting step in the investigated potential range from electrochemical to enzymatic. At pH 5 the situation is somewhat different, with results indicating prevailing enzymatic reaction control in the whole range of investigated potentials. This is also reflected in the steady state response at pH 5 and 80 μM (Fig. 1a) where, the curve reaches very fast saturation current, controlled in this case mainly by enzymatic process.

At higher concentrations (e.g. 160 μM of substrate) electrochemical impedance response behaves similarly, as at pH 6 showing shift of the overall kinetic control from electrochemical to enzymatic step (not shown here).

5. Conclusions

We have demonstrated for the first time the application of electrochemical impedance spectroscopy in theory and experiment for studying of the mechanism of a bio-enzymatic process. As a model system HRP adsorbed on graphite electrode was chosen. Three different mathematical models, based on primary catalytic cycle of HRP including all relevant kinetic steps have been formulated. The models denoted as 1 and 2 in the paper neglect formation and consumption of ES complex. In addition model 1 does not account for mass transfer resistances in the system. Model 3 was the most complex one, accounting for ES formation and all mass transfer resistances. The influence of proton concentration was also taken into account, with protons participating in the electrochemical steps. The models were first solved for steady state conditions and steady state results were presented and compared with literature. The model 3 showed the best quantitative description of the experimental data and was selected further for the analysis of electrochemical impedances. The analysis in the present work could not circumvent the problem of unknown enzyme surface concentration, which influences all kinetic constants (enzymatic and electrochemical), as already discussed in other publications. We adopted here an assumption of low enzyme surface concentration in accordance with [20], which resulted in enzymatic kinetic constant values in the range of those reported for the enzyme in solution. We also showed that the impact of mass transfer resistances in the present case was small compared to other two resistances (electrochemical and enzymatic). In electrochemical impedance response only model 3 was able to describe qualitatively experimental data at different conditions (pH, concentration and potential), proving the potential of EIS for model discrimination. EIS is also more sensitive to parameter estimation giving additional parameters compared to steady state and demonstrating high potential of EIS for studying and understanding of bioelectrochemical processes.

Appendix A. Nomenclature

c_s, c_{H+} concentrations of substrate (here H_2O_2) and proton, mol m^{-3}
i surface concentrations of different forms of enzyme ($i = t$, E_{red}, ES, CPI, CPII)
K_1 enzymatic kinetic constant in models 1 and 2, m^3 mol^{-1} s^{-1}
k_1, k_{-1}, k_{cat}, K_m enzymatic kinetic constants in model 3 with units m^3 mol^{-1} s^{-1}, s^{-1}, s^{-1}, mol m^{-3}, respectively
k_{e1}, k_{e2}, k_e kinetic constants of first and second electrochemical steps as well as the effective electrochemical rate constant, m^3 mol^{-1} s^{-1}
k_{a1}, k_{-a1} forward and backward kinetic constants of the H_3PO_4 dissociation (arbitrary) = 5.4×10^5 s^{-1} and 7.5×10^7 m^3 mol^{-1} s^{-1}
r_1, r_2, r_{e1}, r_{e2} reaction rates of enzymatic and electrochemical steps, mol m^{-2} s^{-1}
E_{r1}, E_{r2} formal potential value of CPI and CPII, here 1.05 and 1.02 V at pH 5 and 0.989 and 0.963 V at pH 6 [27,28]
E electrode potential, V
α_1, α_2 transfer coefficient of the first and second electrochemical steps

F Faraday constant = 96,485 C mol^{-1}
R universal gas constant = 8.314 J mol^{-1} K^{-1}
T temperature (here 294.15 K), K
D_s, D_{H+} diffusion coefficients of H_2O_2 and proton = 1.6×10^{-9} and 5.5×10^{-9} m^2 s^{-1}, respectively
$\delta_{D,i}$ thickness of the Nernstian diffusion layer, m
ν kinematic viscosity, m^2 s^{-1}
ω_r rotation rate of rotating disc electrode = 41.87 rad s^{-1}
C_{dl} double layer capacitance = 2.78 F m^{-2}
S_a electrode surface area = 2.8×10^{-5} m^2
i cell current density, A m^{-2}
R_Ω Ohmic resistance = 108 (pH 5) and 113(pH 6), Ω
$H_1(\omega)$ 1st order frequency response function i.e. electrochemical admittance, S m^{-2}
$H_{1,i}(\omega)$ 1st order auxiliary frequency response functions
P_i coefficients in the Taylor approximation of the nonlinear terms (Table 1)

Appendix B.

In this section some details related to the derivation of analytical expression of electrochemical admittance for Model 3 are given. For further details please see [13–15].

B.1. Definition of input and output variables

In the present case the potential has been chosen as an input variable. Because the system behavior around steady state is studied all variables are defined as deflections from their steady state values. For potential as the cosinusoidal input signal it reads

$$\Delta E_{input}(t) = E_{input}(t) - E_{input,ss} = A \cos \omega t = \frac{A}{2}(e^{j\omega t} + e^{-j\omega t}) \quad (A-1)$$

where A is the input amplitude. In electrochemical systems, the input potential in addition to "real" electrode potential contains always the contribution of Ohmic drop in the solution. Since, the rate of the electrochemical reaction is influenced only by the Ohmic drop free fraction of the imposed electrode potential, the theoretical input potential has to account for Ohmic drop in the solution [14]:

$$\Delta E_{input}(t) = \Delta E(t) + S_a R_\Omega \Delta i(t) \quad (A-2)$$

where $\Delta E(t)$, $\Delta i(t)$ are the deflections of the 'real' electrode potential and the cell current density from their steady state values respectively, S_a is the electrode surface area and R_Ω is Ohmic drop in the solution.

The output signal is the cell current, which in the case of linear frequency response reads

$$\Delta i(t) = i(t) - i_{ss} = \frac{A}{2}(H_1(\omega)e^{j\omega t} + H_1(-\omega)e^{-j\omega t}) + \cdots \quad (A-3)$$

where $H_1(\omega)$ is the 1st order FRF, which is, as already mentioned, identical to the EIS admittance.

In addition to the to the cell current density as the "main" output signal, the electrode potential and the concentrations of all species are defined as auxiliary outputs:

$$\Delta E = \frac{A}{2}(H_{1,E}(\omega)e^{j\omega t} + H_{1,E}(-\omega)e^{-j\omega t}) + \cdots \quad (A-4)$$

$$\Delta \Gamma_i(t) = \frac{A}{2}(H_{1,i}(\omega)e^{j\omega t} + H_{1,i}(-\omega)e^{-j\omega t}) + \cdots \quad (A-5)$$

$$\Delta C_k(0, t) = \frac{A}{2}(H_{1,k}(\omega)e^{j\omega t} + H_{1,k}(-\omega)e^{-j\omega t}) + \cdots \quad (A-6)$$

where $H_{1,E}(\omega)$, $H_{1,i}(\omega)$ and $H_{1,k}(\omega)$ are the 1st order auxiliary FRF where subscript "i" refers to E_{red}, ES, CPI or CPII and subscript "k" to S or H$^+$ respectively.

B.2. Taylor approximation of the nonlinear terms

In this step, all terms in the reaction rate expressions must be expressed in a polynomial form, which is achieved by applying the Taylor series expansion of the nonlinear terms. In this study is sufficient to write the terms only up to the 1st order, since the 1st order FRF has been derived. It follows:

$$
\Delta r_{e1}(t) = \underbrace{\frac{\partial r_{e1}}{\partial \Gamma_{CPI}}\bigg|_{ss}\Delta\Gamma_{CPI}(0,t)}_{P_1} + \underbrace{\frac{\partial r_{e1}}{\partial C_{H^+}}\bigg|_{ss}\Delta C_{H^+}(0,t)}_{P_2}
$$
$$
+ \underbrace{\frac{\partial r_{e1}}{\partial E}\bigg|_{ss}\Delta E(t)}_{P_3} + \cdots \tag{A-7}
$$

$$
\Delta r_{e2}(t) = \underbrace{\frac{\partial r_{e2}}{\partial \Gamma_{CPII}}\bigg|_{ss}\Delta\Gamma_{CPII}(0,t)}_{P_4} + \underbrace{\frac{\partial r_{e2}}{\partial C_{H^+}}\bigg|_{ss}\Delta C_{H^+}(0,t)}_{P_5}
$$
$$
+ \underbrace{\frac{\partial r_{e2}}{\partial E}\bigg|_{ss}\Delta E(t)}_{P_6} + \cdots \tag{A-8}
$$

The expressions for Taylor coefficients, P_i, $i = 1$–6 are given in the Table 1. Similar expressions are formulated for the rate of enzymatic steps (not shown here). As can be seen in Table 1 the values of the Taylor coefficients depend on the steady state concentrations of surface species as well as on the steady state concentrations of substrate and protons. The expressions for these concentrations can be obtained by solving simultaneously system of mass balance equations for surface (Eqs. (19)–(21)) and volume species (Eqs. (13) and (15) with boundary conditions Eqs. (16)–(18)) under steady state conditions.

B.3. Substitution of the Taylor approximation of the rate expressions into the balance equations

In this step the Taylor approximated rate expressions (e.g. Eqs. (A-7) and (A-8)) are substituted into the balance equations (all mass balance equations (Eqs. (13)–(21)) and charge balance equation (Eq. (22)). In case of mass balance equations for substrate and protons the reaction rates appear in the boundary conditions. For example for proton mass transfer it reads

$$
D_{H^+}\frac{\partial C_{H^+}(z,t)}{\partial z}\bigg|_{z=0} = -(P_1\Delta\Gamma_{CPI}(0,t) + P_2\Delta C_{H^+}(0,t)
$$
$$
+ P_3\Delta E(t) + P_4\Delta\Gamma_{CPII}(0,t) + \cdots) \tag{A-9}
$$

For the charge balance, it follows:

$$
C_{dl}\frac{dE(t)}{dt} = i(t) - F(P_1\Delta\Gamma_{CPI}(0,t) + P_2\Delta C_{H^+}(0,t) + P_3\Delta E(t)
$$
$$
+ P_4\Delta\Gamma_{CPII}(0,t) + \cdots) \tag{A-10}
$$

B.4. Substitution of the inputs and outputs and application of the method of harmonic probing

In the next step the input and outputs defined by Eqs. (A-1)–(A-6) are substituted into the model equations (Eqs. (13)–(22)). For example, after the substitution into the charge balance equation (Eq. (22)), and application of the method of harmonic probing i.e.

collection of all terms containing the same power of the input amplitude and the same frequency, one obtains:

$$
C_{dl}\frac{d\left(\frac{A}{2}H_{1,E}(\omega)e^{j\omega t}\right)}{dt} = \frac{A}{2}H_1(\omega)e^{j\omega t} -
$$
$$
F \times \begin{pmatrix} P_1\frac{A}{2}H_{1,CPI}(\omega)e^{j\omega t} + P_2\frac{A}{2}H_{1,H^+}(0,\omega)e^{j\omega t} \\ +P_3\frac{A}{2}H_{1,E}(\omega)e^{j\omega t} + P_4\frac{A}{2}H_{1,CPII}(\omega)e^{j\omega t} + \\ P_5\frac{A}{2}H_{1,H^+}(0,\omega)e^{j\omega t} + P_6\frac{A}{2}H_{1,E}(\omega)e^{j\omega t} \end{pmatrix} \tag{A-11}
$$

which after some rearrangement gives

$$
H_1(\omega) = (j\omega C_{dl} + F(P_3 + P_6))H_{1,E}(\omega) + F(P_1 H_{1,CPI}(\omega)
$$
$$
+ (P_2 + P_5)H_{1,H^+}(0,\omega) + P_4 H_{1,CPII}(\omega)) \tag{A-12}
$$

As can be seen from Eq. (A-12) the $H_1(\omega)$, depends on other auxiliary FRFs where the $H_{1,E}(\omega)$ FRF is defined as follows:

$$
H_{1,E}(\omega) = 1 - S_a R_\Omega H_1(\omega) \tag{A-13}
$$

The expressions for other auxiliary FRFs can be obtained in a similar way as Eq. (A-12) by substituting input and outputs into mass balance equations and by application of method of harmonic probing. This will result in five further expressions defining auxiliary FRFs for proton, compounds I and II, enzyme substrate complex as well as substrate. The last auxiliary FRF defining the change of concentration of native form of the enzyme can be obtained from condition for conservation of total enzyme surface concentration.

$$
H_{1,H^+}(0,\omega)
$$
$$
= \frac{(-\tanh(a_2\delta_{D,H^+}))(P_1 H_{1,CPI}(\omega) + P_3 H_{1,E}(\omega) + P_4 H_{1,CPII}(\omega))}{(D_{H^+}a_2 + \tanh(a_2\delta_{D,H^+})P_2)} \tag{A-14}
$$

$$
H_{1,CPI}(\omega) = \frac{k_{cat}H_{1,ES}(\omega) - (P_2/2)H_{1,H^+}(0,\omega) - (P_3/2)H_{1,E}(\omega)}{(j\omega + P_1)} \tag{A-15}
$$

$$
H_{1,CPII}(\omega) = \frac{P_1}{j\omega + P_4}H_{1,CPI}(\omega) \tag{A-16}
$$

$$
H_{1,ES}(\omega) = \frac{(k_1 C_{S,SS}H_{1,E_{red}}(\omega) + k_1\Gamma_{E_{red},ss}H_{1,S}(0,\omega))}{(j\omega + k_{-1} + k_{cat})} \tag{A-17}
$$

$$
H_{1,S}(0,\omega) = \frac{-\tanh(a_1\delta_{D,S}\sqrt{\omega})k_1 C_{S,SS}H_{1,E_{red}}(\omega) + \tanh(a_1\delta_{D,S}\sqrt{\omega})k_{-1}H_{1,ES}(\omega)}{D_S a_1\sqrt{\omega} + \tanh(a_1\delta_{D,S}\sqrt{\omega})k_1\Gamma_{E_{red},ss}} \tag{A-18}
$$

$$
H_{1,E_{red}}(\omega) + H_{1,ES}(\omega) + H_{1,CPI}(\omega) + H_{1,CPII}(\omega) = 0 \tag{A-19}
$$

The expressions for groups a_i ($i = 1,2$) and P_i ($i = 1,6$) are given in Table 1. By solving (Eqs. (A-12)–(A-19)) the final expression for the $H_1(\omega)$ frequency response function, which is identical to the reciprocal of the electrochemical impedance is derived (Eq. (27)). In a similar way, analytical expressions of theoretical impedances for models 1 and 2 can be derived.

Appendix C. Supplementary data

Supplementary data associated with this article can be found, in the online version, at http://dx.doi.org/10.1016/j.electacta.2013.03.026.

References

[1] N.M. Xavier, A.P. Rauter, Y. Queneau, Carbohydrate-based lactones: synthesis and applications, Topics in current chemistry 295 (2010) 19.

[2] R. Obert, B.C. Dave, Enzymatic conversion of carbon dioxide to methanol: enhanced methanol production in silica sol–gel matrices, Journal of the American Chemical Society 121 (1999).

[3] P.K. Addo, R.L. Arechederra, A. Waheed, J.D. Shoemaker, W.S. Sly, S.D. Minteer, Methanol production via bioelectrocatalytic reduction of carbon dioxide: role of carbonic anhydrase in improving electrode performance, Electrochemical and Solid State Letters 14 (2011).

[4] F. Hollmann, A. Schmid, Electrochemical regeneration of oxidoreductases for cell-free biocatalytic redox reactions, Biocatalysis and Biotransformation 22 (2004).

[5] F. Patolsky, M. Zayats, E. Katz, I. Willner, Precipitation of an insoluble product on enzyme monolayer electrodes for biosensor applications: characterization by faradaic impedance spectroscopy, cyclic voltammetry, and microgravimetric quartz crystal microbalance analyses, Analytical Chemistry 71 (1999).

[6] H.Y. Gu, A.M. Yu, H.Y. Chen, Direct electron transfer and characterization of hemoglobin immobilized on a Au colloid-cysteamine-modified gold electrode, Journal of Electroanalytical Chemistry 516 (2001).

[7] E. Katz, I. Willner, Probing biomolecular interactions at conductive and semiconductive surfaces by impedance spectroscopy: routes to impedimetric immunosensors, DNA-sensors, and enzyme biosensors, Electroanalysis 15 (2003).

[8] J.J. Feng, G. Zhao, J.J. Xu, H.Y. Chen, Direct electrochemistry and electrocatalysis of heme proteins immobilized on gold nanoparticles stabilized by chitosan, Analytical Biochemistry 342 (2005).

[9] G.C. Zhao, L. Zhang, X.W. Wei, Z.S. Yang, Myoglobin on multi-walled carbon nanotubes modified electrode: direct electrochemistry and electrocatalysis, Electrochemistry Communications 5 (2003).

[10] M. Petkovska, Application of nonlinear frequency response to adsorption systems with complex kinetic mechanisms, Adsorption: Journal of the International Adsorption Society 11 (2005) 497.

[11] M. Petkovska, Nonlinear FR-ZLC method for investigation of adsorption equilibrium and kinetics, Adsorption: Journal of the International Adsorption Society 14 (2008) 223.

[12] D.D. Weiner, J.F. Spina, Sinusoidal Analysis and Modeling of Weakly Nonlinear Circuits: with Application to Nonlinear Interference Effects, Van Nostrand Reinhold, New York, 1980.

[13] B. Bensmann, M. Petkovska, T. Vidakovic-Koch, R. Hanke-Rauschenbach, K. Sundmacher, Nonlinear frequency response of electrochemical methanol oxidation kinetics: a theoretical analysis, Journal of the Electrochemical Society 157 (2010).

[14] T.R. Vidakovic-Koch, V.V. Panic, M. Andric, M. Petkovska, K. Sundmacher, Nonlinear frequency response analysis of the ferrocyanide oxidation kinetics. Part I. A Theoretical analysis, Journal of Physical Chemistry C 115 (2011).

[15] V.V. Panic, T.R. Vidakovic-Koch, M. Andric, M. Petkovska, K. Sundmacher, Nonlinear frequency response analysis of the ferrocyanide oxidation kinetics. Part II. Measurement routine and experimental validation, Journal of Physical Chemistry C 115 (2011).

[16] A.I. Iaropolov, V. Malovik, S.D. Varfolomeev, I.V. Berezin, Electroreduction of hydrogen peroxides on the electrode with immobilized peroxidase, Doklady Akademii Nauk SSSR 249 (1979).

[17] E.E. Ferapontova, Direct peroxidase bioelectrocatalysis on a variety of electrode materials, Electroanalysis 16 (2004).

[18] T. Ruzgas, L. Gorton, J. Emneus, G. Markovarga, Kinetic-models of horseradish-peroxidase action on a graphite electrode, Journal of Electroanalytical Chemistry 391 (1995).

[19] A. Lindgren, M. Tanaka, T. Ruzgas, L. Gorton, I. Gazaryan, K. Ishimori, I. Morishima, Direct electron transfer catalysed by recombinant forms of horseradish peroxidase: insight into the mechanism, Electrochemistry Communications 1 (1999).

[20] R. Andreu, E.E. Ferapontova, L. Gorton, J.J. Calvente, Direct electron transfer kinetics in horseradish peroxidase electrocatalysis, Journal of Physical Chemistry B 111 (2007).

[21] B. Limoges, J.-M. Savéant, D. Yazidi, Quantitative analysis of catalysis and inhibition at horseradish peroxidase monolayers immobilized on an electrode surface, Journal of the American Chemical Society 125 (2003) 9192.

[22] T. Tatsuma, K. Ariyama, N. Oyama, Kinetic analysis of electron transfer from a graphite coating to horseradish peroxidase, Journal of Electroanalytical Chemistry 446 (1998).

[23] G.P. Stevenson, R.E. Baker, G.F. Kennedy, A.M. Bond, D.J. Gavaghan, K. Gillow, Access to enhanced differences in Marcus–Hush and Butler–Volmer electron transfer theories by systematic analysis of higher order AC harmonics, Physical Chemistry Chemical Physics (2013).

[24] E.E. Ferapontova, L. Gorton, Effect of proton donors on direct electron transfer in the system gold electrode-horseradish peroxidase, Electrochemistry Communications 3 (2001).

[25] T. Tatsuma, K. Ariyama, N. Oyama, Kinetic analysis of electron transfer from a graphite coating to horseradish peroxidase, Journal of Electroanalytical Chemistry 446 (1998) 5.

[26] Z. Temocin, M. Yigitoglu, Studies on the activity and stability of immobilized horseradish peroxidase on poly(ethylene terephthalate) grafted acrylamide fiber, Bioprocess and Biosystems Engineering 32 (2009).

[27] Y. Hayashi, I. Yamazaki, Oxidation–reduction potentials of compound-I–compound-II and compound-II–ferric couples of horseradish peroxidases A2 and C, Journal of Biological Chemistry 254 (1979) 9101.

[28] B. He, R. Sinclair, B.R. Copeland, R. Makino, L.S. Powers, I. Yamazaki, The structure–function relationship and reduction potentials of high oxidation states of myoglobin and peroxidase, Biochemistry 35 (1996) 2413.

[TVK7]

T. Q. N. Do, M. Varničić, R. Hanke-Rauschenbach,
T. Vidakovic-Koch, K. Sundmacher

Mathematical Modeling of a Porous Enzymatic Electrode with Direct Electron Transfer Mechanism
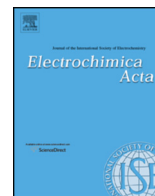
Mathematical Modeling of a Porous Enzymatic Electrode with Direct Electron Transfer Mechanism

T.Q.N. Do[a], M. Varničić[a], R. Hanke-Rauschenbach[a], T. Vidaković-Koch[a,*,1], K. Sundmacher[a,b,1]

[a] Max Planck Institute for Dynamics of Complex Technical Systems, Sandtorstraße 1, 39106 Magdeburg
[b] Otto-von-Guericke University Magdeburg, Universitätsplatz 2, 39106 Magdeburg

ABSTRACT

1-D model of a porous enzymatic electrode with direct electron transfer mechanism has been developed. As a model reaction, hydrogen peroxide reduction catalyzed by Horseradish Peroxidase has been chosen. The model description includes material and charge balances in different phases as well as detailed kinetics of bioelectrochemical hydrogen peroxide reduction. The model has been solved numerically and validated experimentally under steady state conditions. To investigate the influence of the electrode structure and the immobilization procedure, two types of enzymatic electrodes have been developed. In one procedure (Vulcan-PVDF) enzymes were entrapped into a porous conductive matrix, while in the second one (Vulcan-Gelatin) gelatin was used as a binder and enzymes were cross-linked. The performances of Vulcan-PVDF electrodes were significantly better than of Vulcan-Gelatin electrodes under all studied conditions. According to the model, the main reasons for this observation are higher number of active enzymes and higher diffusivity of hydrogen peroxide in the catalyst layer (CL) in case of Vulcan-PVDF procedure. The model pointed out that the major limitation in both studied systems is mass transfer limitation. Enzyme utilization in both systems is very low.

© 2014 Elsevier Ltd. All rights reserved.

1. Introduction

Enzymatic electrodes have found applications in different devices, like biosensors, enzymatic fuel cells and enzymatic reactors [1–5]. In all of these applications, enzymes as catalytic elements are combined with electron conducting materials and additional additives forming complex composite structures. In general, the performance of such electrodes is low, specifically in comparison to traditional metal based electrodes [2,4]. Still, due to excellent catalytic properties of enzymes under mild reaction conditions and in complex reaction environments the interest in further development of these systems sustains. In particular, use of such electrodes in enzymatic fuel cells motivates a large amount of research in last years [2,6]. The employment of these electrodes in bioorganic synthesis is also of high importance specifically with respect to partial oxidation or reduction processes where enzymatic catalysts due to their high selectivity have significant advantageous over conventional catalysts [2,5].

Up to date number of preparation methods for fabrication of enzymatic electrodes have been reported [4,6]. Major foci were on enzyme immobilization, testing of different mediators and usage of diverse nanomaterials (like gold and carbon nanoparticles or carbon nanotubes) [4,6]. Due to number of different procedures and materials employed in production of such electrodes, it is difficult to establish general design rules pointing out the correlation between preparation protocol, electrode structure and its performance.

In this respect, in addition to experimental efforts, further progress can be achieved/accelerated by bringing mathematical modeling into play. This can likely provide new insights into the interactions between components of enzymatic electrodes and their performances, reducing number of required experiments.

In general, electrode models can be formulated at different scales (macro, meso, micro) with varying degrees of complexity [7,8]. Among these model presentations macroscale models are still the most "practical" for correlating with experiments. They can be roughly classified into interface models and distributed models. While the interface models neglect the thickness and the morphology of the electrode, the distributed models take into account the electrode structure. In the field of enzymatic electrodes the interface models prevails [9]. In these studies enzymes were freely diffusive, entrapped behind a thin membrane, immobilized inside

of a non conductive matrix or adsorbed at the electrode surface [9]. In all cases the electrochemical reaction was taking place only at the conductive surface. Accordingly these models do not include spatial distributions of potential fields, but only distribution of concentrations of involved species in different layers. They can be very useful for determination of enzymatic electrode kinetics as shown for e.g. in [10]. However, they are not helpful in cases where the thickness of the electrode can not be disregarded and where electrode structural parameters and interplay between enzyme and electrode kinetics as well as mass transfer limitations inside of the porous electrode start to play a role. In such cases distributed models are better suited. Examples of such studies from literature are works of Lyons [11], Baronas et al. [12], Barton [13], and Chan et al. [14]. Lyons [11] developed a model of a carbon nanotube electrode where enzymes were assumed to be uniformly distributed within a layer of finite thickness considering two cases relevant for practical applications, namely conductive and less conductive porous matrixes. Baronas et al. [12] used a macro-homogeneous 1-D model to investigate the behavior of the amperometric biosensors based on the carbon nanotubes deposited on the perforated membrane. The simulations pointed out that only 0.5% of nominal enzyme loading was able to participate in the direct electron transfer. The model also suggested that the longer linear calibration range of biosensor can be obtained if operating at diffusion limiting conditions and not under enzymatic reaction limiting conditions. A 1-D macro porous model, including additional micro scale along cylindrical fibers where the enzymatic reaction takes place was developed by Barton [13] for an enzyme-catalyzed oxygen cathode. This model pointed out an importance of the enhanced reactant transport for high performance enzymatic electrodes and was able to predict limiting current densities. Chan et al. [14] employed transient material balances along with steady-state charge balances for the electron- and ion- conducting phases, to study the dynamic behavior of a bio fuel cell anode at high mediator concentrations. The rate limiting process in different ranges of applied potentials was determined and the controlled potential range for electrode optimal operation was recommended.

Most of literature studies consider porous electrodes with mediated electron transfer. These studies provide indications that the electrode response is significantly influenced by electrode structural parameters like porosity and thickness. However, an attempt of investigating these parameters in simulations which is validated further by experimental data can not be found in literature.

In this contribution one dimensional (1-D) porous electrode model has been formulated based on porous electrode theory [8]. The balance equations for potential fields in the electron- and ion-conducting phases as well as concentration field have been developed and solved numerically. The enzymatic kinetics has been described in agreement with Michaelis-Menten mechanism, followed by direct electron transfer to the electrode [10]. To justify the necessity of distributed model formulation, spatial model reduction has been performed, resulting in reduced 1-D model. The comparison of reduced (1-D) and reference (1-D) models provided further understanding about the importance of inner mass transfer limitations. The main goal of the present study is to get more insight into interplay between reaction and diffusion resistances inside of the porous layer. While the former one is governed by enzyme kinetics and the total number of immobilized enzymes (which in turn is influenced by structural parameters/enzyme immobilization), the latter one is impacted by the porous electrode structural parameters like porosity, internal active surface area and thickness. In the present study it is assumed that the porous electrode structure influences only the number of active enzymes, while intrinsic enzyme kinetics remains largely unchanged. The validity of this assumption is discussed later on in the text. The electrode structural parameters are assumed to be influenced by the preparation procedure. Some of these parameters can be readily measured (like thickness), while some are more insecure (internal active surface area). In the present study these parameters have been varied in experiments and their impact has been assessed in simulations.

The 1-D model has been experimentally validated in different concentration ranges, at varying electrode thicknesses and by following two different protocols for the preparation of enzymatic electrodes, giving valuable insights into electrode preparation/performance relationship.

2. Mathematical model

A schematic representation of modeling domains is shown in Fig. 1. The first modeling domain (from $z = 0$ to $z = L$) is the catalyst layer (CL). Here electron- and ion- conducting phases are modeled as distinct phases characterized by respective void fractions "ε" with electrochemical reaction taking place at the interface between two phases, defined further as internal active surface area "$a = A_{act}/(A_{geo}L)$" (in $m^2_{act} m^{-3}_{geo}$), where A_{act} is active surface area, A_{geo} geometrical surface area and L thickness of the porous electrode. Balance equations for potential distributions in the electron- ($\phi_E^{CL}(z, t)$) and ion- ($\phi_I^{CL}(z, t)$) conducting phases as well as the potential distribution $E(z,t)$ at the interface of these two phases have been formulated. To complete the model description mass balance equations for species involved in enzymatic and electrochemical reactions have been introduced.

In the balance equations, all fluxes are related to superficial quantities by multiplying the interstitial flux with the corresponding void fraction ε.
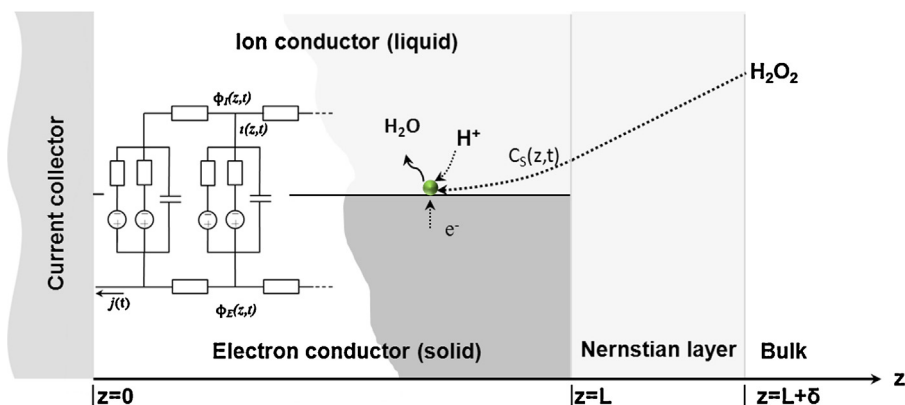

Fig. 1. Schematic representation of modeling domains.

The second modeling domain (from $z = L$ to $z = L + \delta$) is a Nernstian diffusion layer, where the charge balance equation for the potential field distribution in the ion-conducting phase as well as mass balance equations for dissolved species are developed.

In following the model equations of full macro homogeneous 1-D model are presented. To prove the necessity of distributed model formulation, spatial model reduction (reduced 1-D model) has been performed by integrating the model equations over the electrode thickness (for details please see Appendix B) and by including all boundary conditions.

2.1. Charge balance equations

For the formulation of charge balance equations a quasi-steady state approximation has been applied. This is well justified having in mind the condition of electroneutrality in the ion-conducting phase and a very small time constant (compared to time constants of other processes (diffusion, enzymatic and electrochemical reactions)) of the potential field relaxation in the electron-conducting phase [15]. The charge balance equations read:

$$0 = \frac{\partial}{\partial z}\left(\kappa_E^{CL} \frac{\partial \phi_E^{CL}(z,t)}{\partial z} \right) + a\iota(z,t) \tag{1}$$

$$0 = \frac{\partial}{\partial z}\left(\kappa_I^{CL} \frac{\partial \phi_I^{CL}(z,t)}{\partial z} \right) - a\iota(z,t) \tag{2}$$

where "κ_i" i = E, I refer to conductivities of electron- and ion- conducting phases, "ι" to local current density and "a" to the internal active surface area.

For Eqs. 1-2 following boundary conditions are defined:

$$\kappa_E^{CL} \left.\frac{\partial \phi_E^{CL}(z,t)}{\partial z}\right|_{z=L} = 0 \tag{3}$$

$$\kappa_I^{CL} \left.\frac{\partial \phi_I^{CL}(z,t)}{\partial z}\right|_{z=0} = 0 \tag{4}$$

$$\phi_E^{CL}(0,t) = \phi_E^{LB}(t) \tag{5}$$

$$\phi_I^{CL}(L^-,t) = \phi_I^{D}(L^+,t) \tag{6}$$

The potential distribution of $E(z,t) = \phi_E^{CL}(z,t) - \phi_I^{CL}(z,t)$ follows from:

$$C_{dl}\frac{\partial E(z,t)}{\partial t} = -\iota(z,t) + Fr_e(z,t) \tag{7}$$

In the second modeling domain, i.e. Nernstian diffusion layer, only one charge balance equation describing spatio-temporal evolution of the potential field in the ion-conducting phase can be formulated:

$$0 = \frac{\partial}{\partial z}\left(\kappa_I^{D} \frac{\partial \phi_I^{D}(z,t)}{\partial z} \right) \tag{8}$$

with the following boundary conditions:

$$\kappa_I^{CL} \left.\frac{\partial \phi_I^{CL}(z,t)}{\partial z}\right|_{L^-} = \kappa_I^{D} \left.\frac{\partial \phi_I^{D}(z,t)}{\partial z}\right|_{L^+} \tag{9}$$

and

$$\phi_I^{D}(L+\delta,t) = \phi_I^{RB}(t) \tag{10}$$

The conductivities of electron- and ion-conducting phases are defined as effective conductivities related to conductivities of pure phases in accordance to Bruggemann's correlation:

$$\kappa_E^{CL} = \kappa_E(1-\varepsilon)^{1.5} \tag{11}$$

$$\kappa_I^{CL} = \kappa_I(\varepsilon)^{1.5} \tag{12}$$

The conductivity of pure ion-conducting phases is calculated from:

$$\kappa_I = F^2 \sum_i \zeta_i^2 \frac{D_i}{RT}C_i \tag{13}$$

i refers to dissociated ions from buffer solution e.g: H^+, Na^+, K^+, $H_2PO_4^-$, HPO_4^{2-}

The cell current density is obtained by spatial integration of local current densities along the CL:

$$j(t) = \int_0^L \iota(z,t)a\,dz \tag{14}$$

2.2. Mass balance equations

Before introducing mass balance equations, kinetics of the system will be briefly introduced.

2.2.1. Kinetics

The reaction kinetics of the enzyme Horseradish Peroxidase (HRP) in presence of substrate hydrogen peroxide (H_2O_2) on conductive surface has been discussed in our recent publication [10]. We have shown that it is necessary to include formation of enzyme substrate complex in accordance to Michaelis-Menten kinetics and mass transfer effects in order to describe reaction kinetics under steady state and dynamic conditions. This kinetic description, with small modifications, is implemented in the present work in the distributed model framework. Unlike original model [10], effect of proton diffusion was not taken into account. This assumption is well satisfied in well-buffered systems. It was further assumed that absorbed enzymes are either fully active or fully inactive. This has major influence on estimation of number of active enzymes, compared to the nominal number of immobilized enzymes and on determination of kinetic parameters. Taking into account that all kinetic constants are related to the total amount of enzymes we followed the strategy adopted in [10], where the kinetic constants are assumed to be similar to constants of non-immobilized enzyme. The total number of active enzyme is taken as a constant. It was assumed further that enzymes are uniformly distributed along the CL. A short summary of kinetics is briefly reviewed here. For more details the reader is referred to the paper [10].

The major reaction steps are as follows: two enzymatic steps according to Michaelis-Menten mechanism

$$S + E_{red} \underset{k_{-1}}{\overset{k_1}{\rightleftharpoons}} ES \tag{15}$$

$$ES \xrightarrow{k_{cat}} CPI + H_2O \tag{16}$$

and two electrochemical steps

$$CPI + H^+ + e^- \xrightarrow{k_{e10}} CPII \tag{17}$$

$$CPII + H^+ + e^- \xrightarrow{k_{e20}} E_{red} + H_2O \tag{18}$$

where S refers to substrate (in this case hydrogen peroxide H_2O_2), E_{red} to the native form of enzyme, ES to enzyme substrate complex, CPI to oxidized form of enzyme (so called compound I) and CPII to partly reduced form of enzyme (compound II) [10].

Reaction rates of enzymatic steps are expressed as follows:

$$r_1(z,t) = k_1 C_S^{CL}(z,t)\Gamma_{Ered}(z,t) - k_{-1}\Gamma_{ES}(z,t) \tag{19}$$

$$r_{cat}(z,t) = k_{cat}\Gamma_{ES}(z,t) \tag{20}$$

Rate expressions for electrochemical steps are expressed in accordance with Tafel equation:

$$r_{e1}(z,t) = -k_{e10}e^{-\alpha\frac{F}{RT}\eta_1(z,t)}\Gamma_{CPI}(z,t)C_{H^+}(z,t) \tag{21}$$

$$r_{e2}(z,t) = -k_{e20}e^{-\alpha \frac{F}{RT}\eta_2(z,t)}\Gamma_{CPII}(z,t)C_{H^+}(z,t) \tag{22}$$

where the over-potential of two electrochemical steps η_1, η_2, are defined as:

$$\eta_1(z,t) = E(z,t) - E_{r,1} \tag{23}$$

$$\eta_2(z,t) = E(z,t) - E_{r,2} \tag{24}$$

The meaning of symbols is as follows: α is an effective transfer coefficient, $E_{r,1}$, $E_{r,2}$ are the formal potentials of electrochemical steps 1,2 respectively, and F, R and T are Faradays, universal gas constants and temperature respectively.

2.2.2. Mass balances

The mass balances of substrate S in the catalyst and in the Nernstian diffusion layers are formulated as:

$$\varepsilon \frac{\partial C_S^{CL}(z,t)}{\partial t} = D_S^{CL}\frac{\partial}{\partial z}\left(\frac{\partial C_S^{CL}(z,t)}{\partial z}\right) - ar_1(z,t) \tag{25}$$

$$\frac{\partial C_S^{D}(z,t)}{\partial t} = D_S^{D}\frac{\partial}{\partial z}\left(\frac{\partial C_S^{D}(z,t)}{\partial z}\right) \tag{26}$$

with following boundary conditions:

$$D_S^{CL}\frac{\partial C_S^{CL}(z,t)}{\partial z}\bigg|_{z=0} = 0 \tag{27}$$

and

$$C_S^{D}(z = L + \delta_S, t) = C_S^{RB}(t) \tag{28}$$

The remaining boundary conditions to solve the system of equation (25) and (26):

$$-D_S^{D}\frac{\partial C_S^{D}(z,t)}{\partial z}\bigg|_{L^+} = -D_S^{CL}\frac{\partial C_S^{CL}(z,t)}{\partial z}\bigg|_{L^-} \tag{29}$$

and

$$C_S^{D}(L^+, t) = C_S^{CL}(L^-, t) \tag{30}$$

The thickness of a diffusion layer for substrate δ_S in case of a rotating disc electrode can be calculated according to

$$\delta_S = 1.61 \; D_S^{1/3}\nu^{1/6}\omega_r^{-1/2} \tag{31}$$

where ω_r is electrode rotation rate in the solution of kinematic viscosity ν.

The diffusion coefficient of the substrate in the CL is an effective one expressed in accordance to Bruggemann's correlation:

$$D_S^{CL} = D_S\varepsilon^{1.5} \tag{32}$$

where D_s is the diffusion coefficient in the bulk phase.

Concentrations of the surface species taking part in enzymatic and electrochemical equations (Eq. 15-18) follow from the following mass balances:

$$\frac{\partial \Gamma_{ES}(z,t)}{\partial t} = r_1(z,t) - r_{cat}(z,t) \tag{33}$$

$$\frac{\partial \Gamma_{CPI}(z,t)}{\partial t} = r_{cat}(z,t) - |r_{e1}(z,t)| \tag{34}$$

$$\frac{\partial \Gamma_{CPII}(z,t)}{\partial t} = |r_{e1}(z,t)| - |r_{e2}(z,t)| \tag{35}$$

In addition, in relation with conservation of total enzyme concentration in the CL it follows:

$$\Gamma_{CPI}(z,t) + \Gamma_{Ered}(z,t) + \Gamma_{ES}(z,t) + \Gamma_{CPII}(z,t) = \Gamma \tag{36}$$

3. Experiment

3.1. Materials

Horseradish Peroxidase (EC 1.11.1.7, HRP) from *Amorica rusticana* was purchased from Serva Electrophores GmbH and used without further purifications. Vulcan XC72R was purchased from Cabot EMEA. Poly(vinylidene fluoride) (PVDF), glutaraldehyde (GA/50% w/v) and 1-methyle-2-pyrrolidone were supplied by Sigma Aldrich. Gelatin and hydrogen peroxide (30% w/v) were supplied by Merck. All chemicals were of analytical reagent grade and all solutions were prepared using ultrapure water from Millipore.

3.2. Preparation of electrodes

Porous electrodes incorporating enzymes and Vulcan nanoparticles have been prepared by following two different procedures. In the first procedure denoted as "Vulcan-PVDF", poly(vinylidenefluoride) (PVDF) was used as a binder for Vulcan nanoparticles and enzymes were physically entrapped into the porous matrix. This procedure was similar to those reported by Tsujimura et al. [18]. In short, 20 mg of Vulcan was dissolved in 1 ml of 0.25 wt% PVDF solution prepared using 1-methyle-2-pyrrolidone. Different amounts (25 µl, 70 µl) of the prepared ink were casted on spectroscopic graphite disks (Ted Pella INC, 10 mm) resulting in Vulcan loadings of 1.0 and 3.0 mg cm^{-2} respectively and left to dry at 60 °C. Additionally, ultra thin film electrodes with Vulcan loading of 0.056 mg cm^{-2} have been prepared by diluting further the original ink. After drying, Vulcan-PVDF electrodes were modified with HRP solution. Adsorption of enzymes on Vulcan-PVDF electrodes was performed for 2 h at room temperature by applying 50 µl of 6 mg ml^{-1} of HRP solution prepared in 0.1 M phosphate buffer, pH 5.00. Electrodes were then left to dry at room temperature and were ready for use.

In the second procedure gelatin has been used as a binding agent and the electrodes were cross-linked. This procedure denoted in the text as "Vulcan-Gelatin" is similar to the procedure reported by Ivanov et al. [19]. Briefly, catalyst ink was prepared by dissolving 20 mg Vulcan powder and 10 mg HRP in 1 ml of 1.96 wt% gelatin solution (at 35 °C). The ink was then cast on stainless steel disks degreased with acetone before usage. The aliquots of catalyst ink applied on the disks were varied from 20 µl to 50 µl, resulting in Vulcan loadings of 1.43 and 3.6 mg cm^{-2} respectively. The electrodes were left to dry at ambient temperature and afterwards cross linked by dipping into the 5% glutaraldehyde (GA) for 1 minute. After that, the electrodes were again dried at room temperature and stored at -20 °C before usage.

3.3. Electrochemical experiments

The enzymatic electrodes were mounted into a rotating disk electrode holder (RDE, Radiometer Analytical, model ED101) with the opening of 6 mm and were used as working electrodes in three electrode electrochemical cell. Pt wire and saturated calomel electrode (SCE) were used as a counter electrode and a reference electrode, respectively. Steady state polarization curves were obtained from current time dependences at constant potentials by extracting the values after 1 minute. Experiments were done in nitrogen atmosphere at constant rotation rate of 400 rpm (rounds per minute) in order to ensure defined mass transport conditions.

All electrochemical experiments were repeated at least 3 times using Autolabpotentiostat (PGSTAT302, Eco Chemie).

4. Results and Discussion

The 1-D mathematical model introduced in Section 2 has been implemented in MATLAB® software and used for simulations of steady state responses. The model has been validated with experimental data obtained under different experimental conditions by varying electrode structure (Vulcan-PVDF and Vulcan-Gelatin), electrode thicknesses and substrate concentration. The simulated data rely on the following main assumptions:

a) the intrinsic enzyme kinetics is not influenced by electrode structural parameters. This assumption allows us to suppose that the kinetic constants of enzymatic and electrochemical steps are unchanged upon enzyme immobilization into porous electrode matrix. The immobilization in the porous matrix influences effectively only the total number of enzymes. This assumption allows to utilize directly kinetic constants determined for HRP catalyzed hydrogen peroxide reduction on flat electrode under same operating conditions. To test the validity of this assumption ultra thin film Vulcan-PVDF electrodes have been prepared and tested for hydrogen peroxide reduction at two different concentrations. The very low Vulcan loading allows to assume that in such a system all concentration gradients can be neglected which is a major assumption of thin film models. At the same time, the properties of this surface for enzyme immobilization correspond to conditions in porous electrode matrix. As can be seen in Fig. S5 (supporting information), the activity of ultra film thin electrode is very similar to activity of flat graphite electrode. The simulated lines for ultra thin film electrode has been obtained using reduced 1-D model and by assuming infinitely large diffusion coefficient of hydrogen peroxide in the CL (which corresponds to the assumption of absent of gradients in the CL) with same kinetic parameters as determined in reference 10 and the same active enzyme coverage. These results indicate that the immobilization conditions on ultra thin film Vulcan-PVDF electrode are similar to those on graphite electrode described in [10]. They also support our assumption that in porous electrodes the intrinsic enzymatic kinetics in case of physical adsorption remains largely unchanged and that only number of active enzymes changes in dependence of electrode structural parameters. It should be mentioned that this assumption suits better Vulcan-PVDF system than Vulcan-Gelatin due to possible impact of cross-linking on enzyme kinetics in latter case.
b) The enzyme coverage per active surface area takes the same value as in the case of flat electrode for the same nominal enzyme loading. This assumption is supported by experimental results on ultra thin film electrode.
c) The porosity of the enzymatic electrodes is not changing with the electrode thickness. This assumption appears well justified for the electrodes prepared using catalyst ink of the same composition (as in the present case) and by only changing the ink loading on the electrode surface.

In the following the strategy for determination of model parameters has been presented.

4.1. Model parameters

The model parameters can be roughly classified as structural, thermodynamic, operating, and kinetic parameters as shown in Table 1. The former ones are electrode void fraction, thickness and internal active surface area. Among these parameters the

Table 1
Overview of model parameters.

Parameters			
Kinetic [10]		**Operating [measured]**	
$k_1/\text{m}^3\,\text{mol}^{-1}\,\text{s}^{-1}$	12.18×10^3	T/K	298
k_{-1}/s^{-1}	614	$\omega/\text{rad}\,\text{s}^{-1}$	41.87
$k_{\text{cat}}/\text{s}^{-1}$	1898	$C/\text{mol}\,\text{m}^{-3}$	0.08-3.0
$k_{\text{e10}}/\text{m}^3\,\text{mol}^{-1}\,\text{s}^{-1}$	5.62×10^5	E vs. SHE/V	0.244-0.644
$k_{\text{e20}}/\text{m}^3\,\text{mol}^{-1}\,\text{s}^{-1}$	6.19×10^3		
Thermodynamic [10,28,29]		**Structural [measured, fitted]**	
$E_{\text{r,1}}$ vs. SHE/V	1.05	$L/\mu\text{m}_{\text{geo}}$	47, 53
$E_{\text{r,2}}$ vs. SHE/V	1.02	$\varepsilon/\text{m}^3\,\text{m}_{\text{geo}}^{-3}$	(see Table 2)
α	0.17	$a/\text{m}^3\,\text{m}_{\text{geo}}^{-3}$	(see Table 2)

void fraction and the internal active surface area were obtained by fitting, while the electrode thickness was determined from the scanning electron microscopy (SEM) cross sections of the investigated electrodes (data not shown here) [21].

In literature on porous electrode modeling in non-enzymatic systems, the internal active surface area "a" is related to catalyst loading ($g_{\text{cat}}\,\text{m}_{\text{geo}}^2$), the thickness of the CL and the catalyst specific surface area per unit mass of the catalyst ($\text{m}_{\text{act}}^2\,\text{g}_{\text{cat}}^{-1}$), where the latter one is usually estimated based on the size of catalyst nanoparticles, or on producer data [16,17]. In case of enzymatic systems one can expect that the "a" will depend on electron conductive material loading, as well as on the thickness of the CL. Additionally "a" will be highly related to the total number of immobilized enzymes. Having in mind that it is difficult to deduce all these interrelations, "a" has been considered as a fitting parameter. The lower limit for this value corresponds to reciprocal of electrode thickness, while the upper limit can be obtained in the simplest way from geometrical considerations assuming effective radius of Vulcan nanoparticles and the effective CL porosity.

Knowing the enzyme coverage per active surface area (assumption "b") one can calculate the total number of enzymes based on the following equation:

$$n_\text{t} = \Gamma_\text{t} a A_\text{a} L \tag{37}$$

The second fitting parameter is the porosity of the CL. This value has theoretical limits between 0 and 1. It can be also estimated based on measured thickness of the CL by e.g. scanning electron microscopy (SEM) and calculated compact thickness of the layer based on loadings and densities of all components in the CL as presented in [21]. These estimated values of porosities have been used as starting values in the present work.

In addition to already discussed parameters, in Vulcan Gelatin procedure, one additional fitting parameter, namely diffusivity of substrate in the CL appears. The reason for this is the presence of gelatin in the CL which has been also visualized by SEM [21] and which we believe slows down the diffusion in the Vulcan-Gelatin case. As the upper limit of diffusivity its value in bulk solution has been assumed.

Operating parameters were based on experimental conditions; the thermodynamic (formal potentials of electrochemical steps, charge transfer coefficient) are extracted from literature [10,28,29] whereas the reaction kinetic parameters as already discussed were adopted from our previous detail investigations of HRP kinetics on flat surface electrode system [10].

The fitting parameters (2 in the case of Vulcan-PVDF and 3 in the case of Vulcan-Gelatin procedure) are obtained by global optimization using weighted least square method with the following objective function:

$$\min \chi^2(\text{p}) = \min \sum_{j=1}^{m} \sum_{k=1}^{n} \left(j_{\text{sim}}(C_{\text{s},j}, E_k, \text{p}) - j_{\text{exp}}(C_{\text{s},j}, E_k) \right)^2 w_{\text{jk}}$$

$$\tag{38}$$

Where j_{exp} are experimental outputs and j_{sim} are observables predicted by the model for a set of parameters (p). The optimized parameter values have been presented in Table 2. The upper limits of fitting parameters are well defined and they were used as starting values.

For parameter determination at first, experiments at low substrate concentrations, using thin electrode and Vulcan-PVDF procedure have been chosen. The reasons are possibility of enzyme inhibition at higher substrate concentrations and lower level of electrode utilization due to mass transport resistances along the CL, in the case of thicker electrodes at low substrate concentrations. Additionally in Vulcan-PVDF electrodes, the enzymes are only physically adsorbed (entrapped) in the porous matrix, satisfying better the previously introduced assumptions regarding kinetic parameters than Vulcan-Gelatin case. Since an inhibition effect was reported negligible at hydrogen peroxide concentrations lower than 500 μM [20], parameterization has been performed at lower range of substrate concentrations (80 μM to 160 μM).

4.2. Steady state responses at low H_2O_2 concentration

4.2.1. Vulcan-PVDF procedure

The steady state experimental and simulated data of 1-D model for thin Vulcan-PVDF electrode (25 μL ink loading) at two hydrogen peroxide concentrations are presented in Fig. 2a. As can be seen the model can describe well the experimental data. The two fitting parameter values have been given in the Table 2. The electrode void fraction is 0.35, while the internal active surface area is 5.04×10^5 m^2_{act} m^{-3}_{geo}. The obtained value of electrode porosity suggests a dense electrode structure, which follows also from SEM graphs of studied electrodes [21]. The value of the electrode void fraction based on simulations is a bit smaller than the calculated value of 0.45 for the same type of electrode in [21]. However, the calculated value in [21] did not take into account the enzyme phase in the porous electrode, which can explain lower value of porosity obtained in simulations. The value of the internal active surface area suggests that ca. 4.6% of the theoretical value of Vulcan surface is utilized for enzyme adsorption. This rather low utilization of the theoretical surface area might suggest an overestimation of theoretical value due to neglection of surface area reduction caused by addition of PVDF binder. Additionally our fluorescence microscopy characterizations of enzyme adsorption on graphite surface suggest rather low enzyme coverage on the surface [21]. As already discussed the internal active surface area is strongly correlated with enzyme coverage per active surface area and only product of these two values can be determined (Eq.37). The calculated total number of enzymes of 8×10^{-13} mol is as expected higher than the value reported for the flat electrode [10] indicating an increase of the amount of active enzymes in case of porous structure (enhancing effect of the internal active surface area "a"). As awaited, the current response is significantly improved (ca. 3 times) compared to the flat electrode case, due to an increase of the total number of immobilized enzymes (ca. 10 times compared to the flat electrode case [10]). However, the increase of the total number of enzymes is not followed by the increase of the current density in the same amount. The possible reason is the distribution of the substrate concentration along the CL due to mass transfer limitations. This can be easily seen in the simulated concentration profiles in different layers (Fig. 2b). As one can observe the studied electrode shows significant mass transfer limitations. The effect is more pronounced at lower substrate concentrations, which can be also evidenced from the steady state response at 80 μM concentration showing practically no potential dependence (Fig. 2a). Even at higher substrate concentrations, the concentration profiles show significant concentration drop yet in the Nernstian diffusion layer, followed by further drop in the CL. These profiles appear similar at all potential
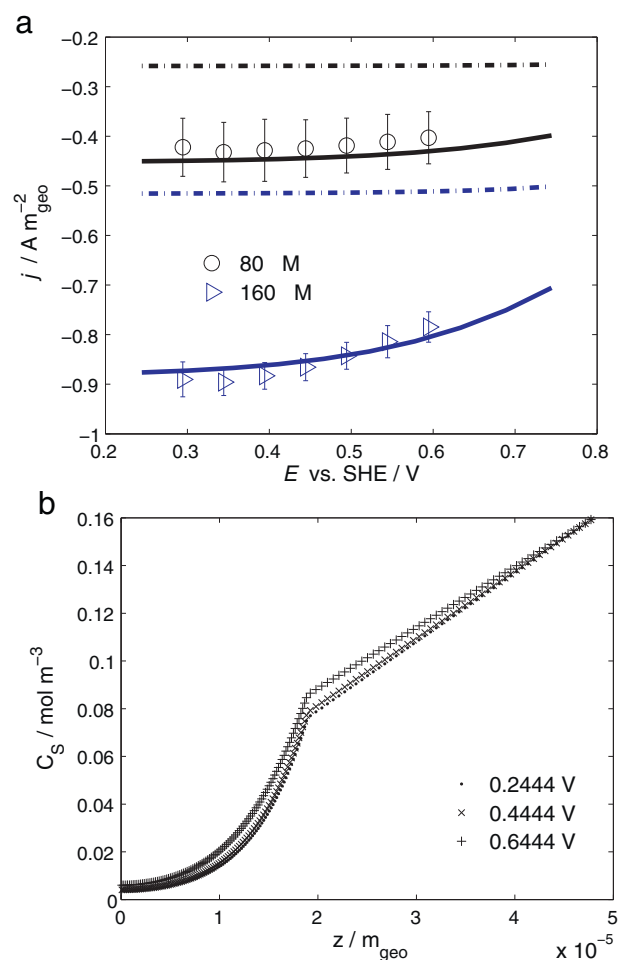

Fig. 2. a) Steady state polarization curves: symbols–experimental data, dash lines–simulated curves of reduce 1-D model; continuous lines–simulated curves of full 1-D model b) simulated local profiles of hydrogen peroxide concentration along spatial coordinate Conditions: thin Vulcan-PVDF electrode, fixed delay of 1 minute, hydrogen peroxide concentrations 80 and 160 μM, room temperature; rotation rate 400 rpm, pH 5 and with other parameters given in Table 1 and Table 2.

values, suggesting that the major resistance in the system is the mass transfer resistance.

As it was already mentioned the 1-D model can be simplified by integration of the model equations along the thickness of the CL. Typically in such a case, the information on concentration distribution in the layer is lost, but structural information of the CL, like void fraction, the thickness of the layer and the internal active surface area are preserved (please see the Appendix B). The simulated steady state responses of a reduced model have been also shown in Fig. 2a (dashed-lines). The simulations are performed with the optimized set of parameters for the full 1-D model (same void fraction, electrode thickness and the total number of enzymes). As can be seen in Fig. 2a the reduced model can not fit the data quantitatively, pointing out a necessity of the distributed model formulation. The simulated responses by the reduced model underestimate the experimental data. This is probably the consequence of lower concentration in the CL (10-15 μM), calculated by the reduced model in comparison to the average concentration level in the full model. The reduced model can fit the experimental data quantitatively but with very unreasonable parameters (please see the Supporting information Fig. S1 Table S1).

The 1-D model has been further used for simulations of electrode responses in the case of a thick electrode. For these simulations the electrode void fraction was kept the same as in the case of the thin

Table 2
Estimated parameter values for Vulcan-PVDF and Vulcan-Gelatin electrodes under different conditions of ink loading and hydrogen peroxide concentrations.

Parameter	Vulcan-PVDF				Vulcan-Gelatin			
	25 μL	70 μL	70 μL ($C_{H_2O_2}$=1000 μM)	70 μL ($C_{H_2O_2}$=3000 μM)	20 μL	50 μL	50 μL ($C_{H_2O_2}$=1000 μM)	50 μL ($C_{H_2O_2}$=3000 μM)
ε	0.35 [a]	0.35 [c]	0.35 [c]	0.35 [c]	0.3 [a]	0.3 [c]	0.3 [c]	0.3 [c]
$D_s/10^{-9} \, m_{geo}^2 \, s^{-1}$	1.6	1.6	1.6	1.6	0.5 [a]	0.5 [c]	0.5 [c]	0.5 [c]
$L/10^{-6} \, m_{geo}$	19 [b]	53	53	53	19 [b]	47	47	47
$\Gamma_t/10^{-9} \, mol \, m_{act}^{-2}$	3 [c]	3 [c]	2.1 [a]	1.5 [a]	3 [c]	3 [c]	2.1 [a]	1.2 [a]
$a/10^5 \, m_{act}^2 \, m_{geo}^{-3}$	5.04 [a]	7.97 [a]	7.97 [c]	7.97 [c]	0.35 [a]	2.35 [a]	2.35 [c]	2.35 [c]
$n_t/10^{-13} \, mol$	8 [b]	35.5 [b]	24.85 [b]	17.75 [b]	0.56 [b]	9.2 [b]	6.44 [b]	3.68 [b]

[a] fitted values
[b] calculated (not fitted) values,
[c] adopted (not fitted) values

electrode. This appears logical having in mind that the ink composition in both cases was the same and that only the ink loading at the electrode surface was varied (25 μl and 70 μl for thin and thick electrode respectively). The electrode thickness is estimated from SEM cross-section of this electrode [21] (the thin electrode thickness was obtained by linear scale down of the thick electrode thickness, following the assumption of the same porosity of both electrodes). The only fitting parameter in this case was the internal active surface area. As can be seen in Fig. 3a the simulations reproduce well

Fig. 3. a) Steady state polarization curves: symbols–experimental data, dash lines–simulated curves of reduce 1-D model; continuous lines–simulated curves of full 1-D model b) simulated local profiles of hydrogen peroxide concentration along spatial coordinate. Conditions: thick Vulcan-PVDF electrode, fixed delay of 1 minute, hydrogen peroxide concentrations 80 and 160 μM, room temperature; rotation rate 400 rpm, pH 5 and with other parameters given in Table 1 and Table 2.

the experimental values. The increase in the internal active surface area (ca. 1.6 times compared to the thin electrode) does not follow the theoretical prediction, which anticipates no change in the internal active surface area at constant porosity. This result indicates that assumptions of either constant porosity and/or the constant enzyme coverage per active surface area were not fully satisfied. At the moment it is not possible to deduce which effect is more significant.

By following the procedure described for the thin electrode the total number of immobilized enzymes has been calculated. The value of 35.5×10^{-13} mol shows ca. 4 times enhancement compared to the thin electrode case; however; the current increase is rather modest. The possible explanation follows from the simulated concentration profiles, which show again severe mass transfer limitations (Fig. 3b). As can be seen in Fig. 3b, only part of the electrode thickness is effectively utilized, while the rest is under-supplied by the substrate. The divergence between the 1-D and the reduced model is even higher compared to the thin electrode case (Fig. 3a). This confirms further the necessity of the full 1-D model for understanding of processes taking place in the porous enzymatic electrode.

Obviously, an increase of the electrode thickness is an efficient strategy to enhance the active surface area for enzyme adsorption. However, from the analysis above, thicker electrodes always lead to performance limitations associated with mass transport of reactants and might create a "dead portion" on the electrode which is not effectively working. In the present case, it was calculated that only 27 μm of nominally 53 μm of the thick electrode contribute effectively to the recorded current. The system works under mass transfer control and is effectively independent on the applied potential. All other transport processes like charge transport in electron and ion-conducting phases have almost no influence on the electrode performance (Fig. S2: Supporting information). Alike thick electrode, the thin electrode is working through the layer. Still, the mass transport resistance is important for the thin electrode. Compared to the thick electrode, the thin electrode works more effectively.

4.2.2. Vulcan-Gelatin Procedure

The Vulcan-PVDF system, as already described was prepared by physical adsorption of enzymes on high surface area electro conductive matrix. This assembly might have benefit of better diffusivity, which as it was shown has high importance due to significant mass transfer limitations in such a system. On the other hand, such an "open" structure can lead to enzyme leakage in practical applications. An approach to circumvent this problem is a cross-linking of enzymes with GA in combination with gelatin. This casts an insoluble matrix, which stabilizes additionally Vulcan nanoparticles, forming composite electrode structure, denoted in the text as Vulcan-Gelatin.
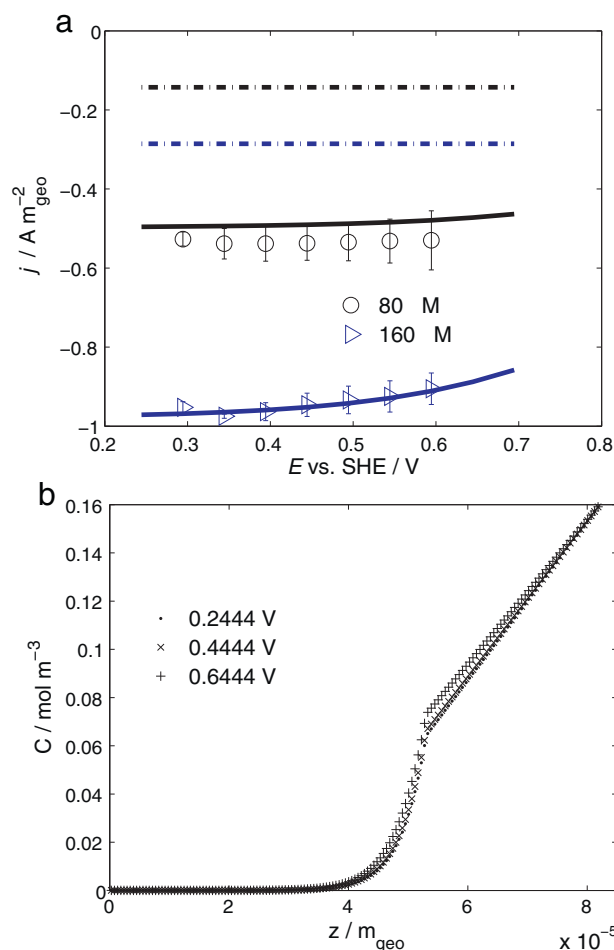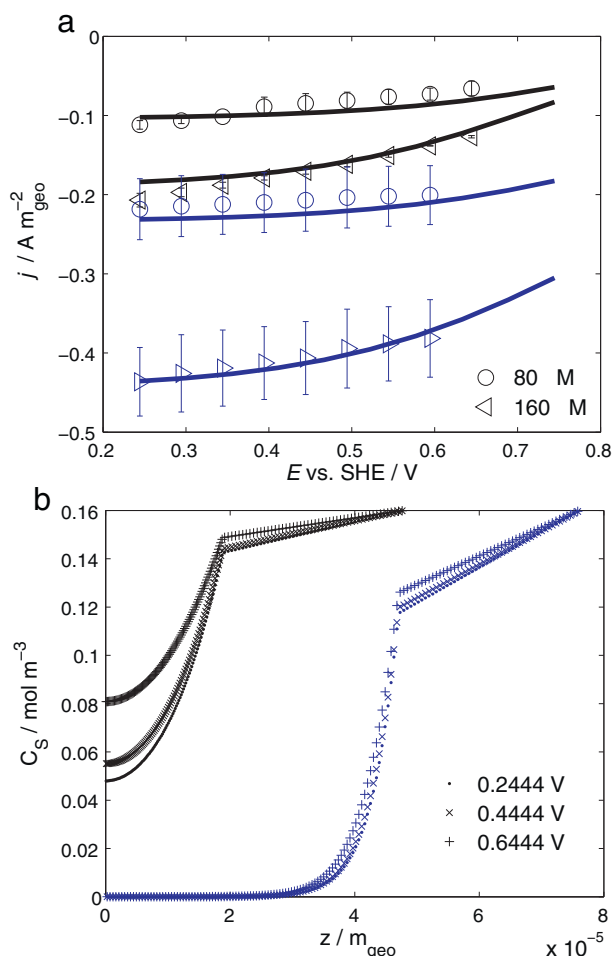
Fig. 4. a) Steady state polarization curves: symbols–experimental data, continuous lines–simulated curves of 1-D model b) simulated local profiles of hydrogen peroxide concentration for a thin (in black color) and a thick (in blue color) Vulcan-Gelatin electrode along spatial coordinate. Conditions: fixed delay of 1 minute, hydrogen peroxide concentrations 80 and 160 μM, room temperature; rotation rate 400 rpm, pH 5 and with other parameters given in Table 1 and Table 2.

In addition to the electrode void fraction (ε) and the internal active surface area, further fitting parameter in this system is diffusion coefficient of substrate D_S in the gelatin environment. The parameterization procedure for this system is similar to those applied in Vulcan-PVDF system. Namely, at first optimized set of parameters was obtained for the thin electrode at low concentrations. Secondly, electrode void fraction and the diffusion coefficient were fixed leaving only the internal active surface area as a fitting parameter for two thick electrodes. The thickness of one electrode (50 μl) was determined from its SEM cross-section [21], while the thicknesses of the thin electrode were obtained by linear scale down of this electrode thickness. Table 2 shows the optimized parameters of 1-D model for the two electrodes.

The experimental data along with simulated data of reduced and 1-D models under steady state conditions for two different electrode thicknesses are illustrated in Fig. 4a. The experimental data for the thin electrode at two different substrate concentrations show some changes of slope at more negative overpotentials (at ca. 0.4 and 0.45 V) (Fig. 4a, for more detail, please see Fig. S3a-b, supporting information). This feature cannot be seen in the case of thick electrode (Fig. 4a, Fig. S3c, supporting information) and it was also not observed in the case of Vulcan-PVDF system irrespective of the electrode thickness. The 1-D model simulated curves cannot predict this change of the slope (Figs. 4a, Fig. S3a-b). The model

can fit either the data at more positive overpotentials or at more negative overpotentials. A possible reason for the observed change of slope in experimental data can be high dispersion of enzyme orientations, causing higher level of rate constant distributions. As a consequence, the enzymes in more favored orientation react at more positive overpotentials, while those with less favored orientation require more negative overpotentials. In the model the distribution of the rate constants was not considered, which can explain the fail of the model to describe this behavior. The kinetic constants in the model are adopted from the study of HRP kinetics on the flat electrode and can be considered as effective rate constants for given enzyme orientations at the flat electrode surface [10]. The results here imply that the dispersion of enzyme orientations is higher than in the case of the flat electrode. Additionally, in the Vulcan-Gelatin case, cross-linking of enzymes and possibly formation of enzyme agglomerates can contribute to higher dispersion of the rate constants. The reason, that this effect was not observed in the case of Vulcan-PVDF system and the thick Vulcan-Gelatin electrode can be the dominance of mass transfer resistance in these systems, which masks efficiently all other effects.

Similar to the Vulcan-PVDF system, the performance of Vulcan-Gelatin electrodes is improved with an increase of the electrode thickness, but these electrodes are in general less efficient than the Vulcan-PVDF electrodes. This improvement can be again correlated with an increase of the total amount of the active enzyme (Table 2). The numbers in the Table 2 indicate very low enzyme utilization in the CL (between 10^{-3} to 10^{-2}%), or they point out that the kinetic constants for enzymes entrapped in the porous electrode structure are highly overestimated. The possible reason for low enzyme utilization in the Vulcan-Gelatin case can be cross-linking of enzymes which forms agglomerates, leaving theoretically only enzymes at the surface of the agglomerate active for direct electron transport. The formation of agglomerates and lessening of the electrode activity by cross-linking has been demonstrated in [21]. The effect of cross linking using GA on enzyme agglomeration was also discussed intensively in [22,23]. Our results also imply that the effect of the cross-linking is more severe in the case of thin-electrodes (almost 10 times lower enzyme utilization than for the thick electrode) which can be due to the cross-linking procedure, where the Vulcan-Gelatin electrode after preparation was dipped in the GA solution for a certain time, allowing in the case of the thin electrode more through cross-linking and leaving possibly in the case of thick electrode non-cross linked parts of the CL. This can explain the non-linear increase of the total number of active enzymes between the thick and the thin electrode (ca. 17 times for ca. 2.5 times increase of the electrode surface) and implies further that the kinetic constants for these two cases can not be considered the same. Obviously, the cross linking has a positive effect concerning the stability of electrodes, but a negative contribution to electrode performance.

At the same set of optimized parameters, the reduced model can qualitatively describe the experimental data in the case of thin electrode, while for the thick electrode it fails both qualitatively and quantitatively (Fig. S3, supporting information). The quantitative fit for the thin electrode can be obtained by changing the diffusion coefficient of the substrate (Fig. S4a: supporting information). For the thick electrode (50 μL ink loading), the discrepancy between the 1-D and the reduced model is significant (Fig. S3c, supporting information). The quantitative fitting in this case can be achieved, but with unreasonable parameter values (Fig. S4b, Table S2 supporting information).

More insights into the electrode behavior can be obtained by studying simulated substrate concentration profiles at the different electrode thicknesses (Fig. 4b). Similar to Vulcan-PVDF system, mass transfer limitations can be observed in all studied cases. In the case of thick electrode the large part of the CL is depleted

by the substrate (Fig. 4b) Based on the concentration profiles, the so-called effective electrode thickness and the amount of effective active working enzymes can be recalculated giving values of 24 μm and 4.5×10^{-13} mol respectively; it follows that only half of the electrode thickness contributes effectively to the electrode performance. The concentration profiles of thin electrode show more expressed dependence on potential while in the case of thick electrode is less pronounced (Fig. 4b)

The determined void fraction in the present system of 0.3 indicates even denser packing than in the Vulcan-PVDF case which corresponds well with the SEM pictures of electrode cross section and the top views reported in [21]. Based on simulation results, the diffusion coefficient of substrate in the gelatin environment is 5×10^{-10} m^2 s^{-1} which is significantly smaller than its value in the bulk, but it is close to the reported value for hydrogen peroxide diffusion in hydrogels [24].

4.3. Steady state responses at high H$_2$O$_2$ concentrations

Steady state responses at higher H$_2$O$_2$ concentrations are simulated by keeping all parameters the same as in the low concentration range. These simulations resulted in much better electrode performance than experimentally observed (data not shown here).

The possible reason for this discrepancy can be enzyme inhibition [20]. In the catalytic cycle of HRP, side-reactions can take place, forming catalytically non-active enzyme forms. This effect becomes more pronounced at higher substrate concentrations. Since the inhibition kinetics was not considered in the model, this effect has been approximated through change of the enzyme coverage per active surface area (Table 2), which influenced further the total number of active enzymes. The simulations assuming reduced enzyme coverage per active surface area have been presented in Fig. 5a for thick Vulcan-PVDF and Vulcan-Gelatin electrodes at higher concentrations (1000–3000 μM). The 1-D model can describe well the experimental data. The maximum current density can reach ca. 10 A m^{-2} for Vulcan-PVDF optimized electrode (Fig. 5a). This performance is very high compared to other reported enzymatic cathodes. For example this performance is comparable to the value reported for mediated electron transfer of laccase on the "wired" cathode at pH 5, 37 °C [25] and higher than reported values of all other HRP/nanotube based electrodes at pH6 [26,27]. The data in the Table 2 show a decrease of the calculated total number of active enzymes with an increase of peroxide concentration for both studied systems. For Vulcan-PVDF system the total number of active enzyme at 1000 μM is ca. 70% of its value at low substrate concentrations (Table 2), and it drops to ca. 50% at 3000 μM. Similar trend has been observed in the case of Vulcan-Gelatin electrode (ca. 25% reduction at 1000 μM and 40% reduction at 3000 μM).

The simulated concentration profiles of two electrodes at different applied potentials are shown in Fig. 5b. These profiles reveal that the both electrodes work through. However, the mass transport is still an obstacle for the system performance.

5. Conclusions

1-D full and reduced porous electrode models have been developed to simulate and analyze the behavior of an enzymatic porous electrode, with a direct electron transfer. As a model system HRP entrapped in a porous electron conductive matrix has been chosen. Model formulations included governing equations for calculation of potential fields in the electron and ion-conducting phases, as well as concentration field of the substrate. In kinetic expressions of HRP catalyzed hydrogen peroxide reduction, only primary catalytic cycle has been considered.

The 1-D model has been experimentally validated and structural parameters of porous enzymatic electrodes, like void fraction and the internal active surface area have been determined for two different electrode preparation procedures (Vulcan-PVDF and Vulcan-Gelatin). Vulcan-PVDF electrodes have better performance than Vulcan-Gelatin electrodes in all studied cases. According to the model, this is the consequence of higher porosity (better diffusivity) and higher number of active enzymes in the Vulcan-PVDF case. The major limitation in both studied systems is mass transfer limitation, which has been revealed from concentration profiles of the substrate along the spatial coordinate. As a consequence, the electrodes are not working through the layer. This is especially true in the case of thick electrode and Vulcan-PVDF system due to higher number of active enzymes. At higher substrate concentrations, the electrodes work more through, but the inhibition effect of the substrate might become significant.

The enzyme utilization compared to nominal enzyme loading in both systems is low. In the Vulcan-Gelatin case according to simulations only 0.001 to 0.01% of nominal enzyme loading is active. The data of Vulcan-PVDF electrode indicate the increase of number of active enzymes with an increase of the electrode thickness. In the case of Vulcan-Gelatin electrode non-linear increase of the total number of active enzyme with an electrode thickness has been also observed. The increase in the total number of enzymes in both
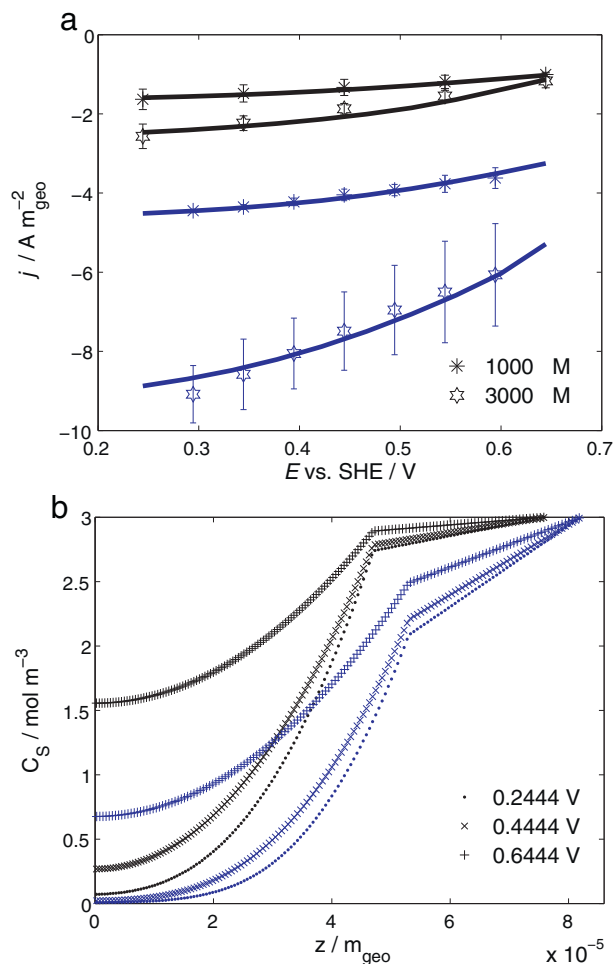
Fig. 5. a) Steady state polarization curves at high concentration for the thick electrode: symbols–experimental data, continuous lines–simulated curves of 1-D model b) simulated local profiles of hydrogen peroxide concentration for Vulcan-Gelatin (in black color) and Vulcan-PVDF (in blue color) electrode along spatial coordinate. Conditions: fixed delay of 1 minute, hydrogen peroxide concentrations 1000 μM and 3000 μM, room temperature; rotation rate 400 rpm, pH 5 and with other parameters given in Table 1 and Table 2.

systems was not followed by the projected increase in catalytic currents, which has been assigned to influence of mass transfer resistance in the CL.

The reduced model can predict behavior of some experimental systems, like thin Vulcan-Gelatin electrode, but only by adjusting the substrate diffusion coefficient. In case of thicker electrodes the reduced model fails largely to describe the experimental data. This underlines the necessity of the distributed model description for analysis of porous enzymatic electrodes.

The results of this paper show strong correlation between kinetic and some structural parameters of the studied systems. They underline necessity of determination of number of immobilized enzymes using some independent method. Although the absolute values of kinetic and structural parameters (internal active surface area) are unsure (due to interrelation between these parameters and the total number of enzymes) the main results of this study remain reliable.

Understanding the rate determining processes in enzymatic systems is very critical for system design and its optimization. According to present data, the optimized design of CL layer is needed to minimize mass transport resistance of reactants and to increase the enzyme utilization.

Appendix A. Appendix A

List of symbols

a	internal active surface area	$m^2_{act}\,m^{-3}_{geo}$
A_{geo}	geometrical surface area of electrode $= 0.28 \times 10^{-4}$	m^2_{geo}
C_{dl}	double layer capacitance $= 2.78$	$F\,m^{-2}_{act}$
C	volumetric concentration	$mol\,m^{-3}$
D	diffusion coefficient of species in bulk	$m^2_{geo}\,s^{-1}$
d	diameter	m
E	applied potential	V
F	Faraday's constant $= 96\,485$	$C\,mol^{-1}$
j	total cell current density	$A\,m^{-2}_{geo}$
k_1, k_{-1}, k_{cat}	reaction constants of enzymatic reaction	$m^3\,mol^{-1}\,s^{-1}, s^{-1}, s^{-1}$
k_{e10}, k_{e20}	kinetic constant of the 1st and 2nd step of electrochemical reactions	$m^3\,mol^{-1}\,s^{-1}$
L	catalyst layer thickness	m_{geo}
n_t	total number of active enzyme	mol
R	universal gas constant $= 8.314$	$J\,mol^{-1}\,K^{-1}$
T	temperature	K
Greek		
α	transfer coefficient of the first and second electrochemical steps $= 0.17$	
ω	rotation rate of rotating disc electrode	$rad\,s^{-1}$
ι	local current density	$A\,m^{-2}_{act}$
ϕ_E, ϕ_I	potentials of electron- and ion-conducting phases respectively	V
κ_E, κ_I	electron- and ion conductivities	$S\,m^{-1}_{geo}$
δ	diffusion layer thickness	m_{geo}
ε	void fraction	$m^3\,m^{-3}_{geo}$
Γ	surface concentration of enzyme species	$mol\,m^{-2}_{act}$
η	overpotential of electrochemical reaction i	V
ζ	charge number	
Super- and Sub-scripts		
RB, LB	right boundary and left boundary respectively	
dl	double layer	
*	interface between diffusion layer and catalyst layer	
I, E	ion and electron conducting phase respectively	
sim, exp	simulation and experiment respectively	
red, ox	reduced and oxidized respectively	
CL, D	catalyst layer and diffusion layer respectively	
S	substrate	
1/-1, cat	forward, backward enzymatic and catalytic reaction step respectively	
e10, e20	first and second electrochemical reaction step respectively	
act, geo	active and geometry respectively	

Appendix B. Appendix B: Model reduction

The model reduction has been performed by integration of Eq. (1, 2, 7, 8, 25, 26) along the spatial coordinate and by incorporation of all corresponding boundary conditions.

B.1. Charge balance

- for the electron-conducting phase

$$0 = -\kappa_E^{CL}\frac{\phi_E^{CL}(t) - \phi_E^{LB}(t)}{L/2} + j(t) \tag{B.1}$$

- for the ion-conducting phase

$$0 = \kappa_I^{CL}\frac{\phi_I^*(t) - \phi_I^{CL}(t)}{L/2} - j(t) \tag{B.2}$$

- for the ion-conducting phase in diffusion domain

$$0 = \kappa_I^D\frac{\phi_I^{RB}(t) - \phi_I^D(t)}{\delta_S/2} - \kappa_I^D\frac{\phi_I^D(t) - \phi_I^*(t)}{\delta_S/2} \tag{B.3}$$

- Boundary condition between CL and diffusion layer

$$\kappa_I^{CL}\frac{\phi_I^*(t) - \phi_I^{CL}(t)}{L/2} = \kappa_I^D\frac{\phi_I^D(t) - \phi_I^*(t)}{\delta_S/2} \tag{B.4}$$

- The potential distribution

$$C_{dl}\frac{dE(t)}{dt}aL = -j + F(r_{e1}(t) + r_{e2}(t))aL \tag{B.5}$$

B.2. Mass balance

- The mass balance of substrate S (H_2O_2) in the diffusion layer

$$\frac{dC_S^D(t)}{dt}\delta_S = D_S^D\frac{C_S^{RB}(t) - C_S^D(t)}{\delta_S/2} - D_S^D\frac{C_S^D(t) - C_S^*(t)}{\delta_S/2} \tag{B.6}$$

- The mass balance of substrate S (H_2O_2) in the CL

$$\varepsilon\frac{dC_S^{CL}(t)}{dt}L = D_S^{CL}\frac{C_S^*(t) - C_S^{CL}(t)}{L/2}$$
$$+ a(-k_1 C_S^{CL}(t)\Gamma_{Ered}(t) + k_{-1}\Gamma_{ES}(t))L \tag{B.7}$$

- The boundary condition between diffusion and catalyst layers:

$$-D_S^D\frac{C_S^D(t) - C_S^*(t)}{\delta_S/2} = -D_S^{CL}\frac{C_S^{CL}(t) - C_S^*(t)}{L/2} \tag{B.8}$$

- The surface concentration of all related enzyme species

$$\frac{d\Gamma_{ES}(t)}{dt} = k_1 C_S^{CL}(t)\Gamma_{Ered}(t) - k_{-1}\Gamma_{ES}(t) - k_{cat}\Gamma_{ES}(t) \tag{B.9}$$

$$\frac{d\Gamma_{CPI}(t)}{dt} = k_{cat}\Gamma_{ES}(t) - |r_{e1}(t)| \tag{B.10}$$

$$\frac{d\Gamma_{CPII}(t)}{dt} = |r_{e1}(t)| - |r_{e2}(t)| \tag{B.11}$$

Appendix C. Supplementary data

Supplementary data associated with this article can be found, in the online version, at http://dx.doi.org/10.1016/j.electacta.2014.06.031.

References

[1] S.C. Barton, J. Gallaway, P. Atanassov, Enzymatic biofuel cells for implantable and microscale devices, Chemical reviews 104 (2004) 4867–4886.

[2] D. Leech, P. Kavanagh, W. Schuhmann, Enzymatic fuel cells: Recent progress, Electrochimica Acta 84 (2012) 223–234.

[3] J.-K. Guterl, V. Sieber, Biosynthesis debugged: Novel bioproduction strategies, Engineering in Life Sciences 13 (2013) 4–18.

[4] I. Ivanov, T. Vidaković-Koch, K. Sundmacher, Recent Advances in Enzymatic Fuel Cells: Experiments and Modeling, Energies 3 (2010) 803–846.

[5] I. Ivanov, T. Vidaković-Koch, K. Sundmacher, Direct hybrid glucose–oxygen enzymatic fuel cell based on tetrathiafulvalene–tetracyanoquinodimethane charge transfer complex as anodic mediator, Journal of Power Sources 196 (2011) 9260–9269.

[6] Z. Zhou, M. Hartmann, Progress in enzyme immobilization in ordered meso-porous materials and related applications, Chemical Society Reviews 42 (2013) 3894–3912.

[7] T. Vidakovic-Koch, R. Hanke-Rauschenbach, I. Gonzalez Martinez, K. Sund-macher, *Catalyst layer modeling for Gas Diffusion-Electrodes*, in: C. Breitkopf, K. Swider Lyons (Eds.), Springer Handbook of Electrochemistry, Ch.9, Springer, 2014. accepted.

[8] A.Z. Weber, J. Newman, Modeling transport in polymer-electrolyte fuel cells, Chemical reviews 104 (2004) 4679–4726.

[9] P.N. Bartlett, C.S. Toh, E.J. Calvo, V. Flexer, Modelling Biosensor Responses, in: P.N. Bartlett (Ed.), Bioelectrochemistry: Fundamentals, Experimental Techniques and Applications, Ch. 8, John Wiley & Sons, Ltd, Chichester, UK, 2008, pp. 267–325.

[10] T. Vidaković-Koch, V.K. Mittal, T.Q.N. Do, M. Varničić, K. Sundmacher, Application of electrochemical impedance spectroscopy for studying of enzyme kinetics, Electrochimica Acta 110 (2013) 94–104.

[11] M.E.G. Lyons, Transport and Kinetics at Carbon Nanotube -Redox Enzyme Composite Modified Electrode Biosensors Part 2. Redox enzyme dispersed in nanotube mesh of finite thickness, *International Journal of Electrochemical Science.* 4 (2009) 1196–1236.

[12] R. Baronas, J. Kulys, K. Petrauskas, J. Razumiene, Modelling Carbon Nanotubes-Based Mediatorless Biosensor, Sensors 12 (2012) 9146–9160.

[13] S. Calabrese Barton, Oxygen transport in composite mediated biocathodes, Electrochimica Acta 50 (2005) 2145–2153.

[14] D.-S. Chan, D.-J. Dai, H.-S. Wu, Dynamic Modeling of Anode Function in Enzyme-Based Biofuel Cells Using High Mediator Concentration, Energies 5 (2012) 2524–2544.

[15] B. Bensmann, R. Hanke-Rauschenbach, E. Meißner, I. Koch, K. Sundmacher, Model Simulation and Analysis of Proton Incorporation into the Positive Active Mass of a Lead/Acid Battery, Journal of The Electrochemical Society 157 (2010) A243–A253.

[16] P.K. Das, X. Li, Z.-S. Liu, Analytical approach to polymer electrolyte membrane fuel cell performance and optimization, Journal of Electroanalytical Chemistry 604 (2007) 72–90.

[17] M. Secanell, K. Karan, A. Suleman, N. Djilali, Optimal Design of Ultralow-Platinum PEMFC Anode Electrodes, Journal of The Electrochemical Society 155 (2008) B125–B134.

[18] S. Tsujimura, Y. Kamitaka, K. Kano, Diffusion-Controlled Oxygen Reduction on Multi-Copper Oxidase-Adsorbed Carbon Aerogel Electrodes without Mediator, Fuel Cells 7 (2007) 463–469.

[19] I. Ivanov, T. Vidaković-Koch, K. Sundmacher, Alternating electron transfer mechanism in the case of high-performance tetrathiafulvalene–tetracyanoquinodimethane enzymatic electrodes, Journal of Electroanalytical Chemistry 690 (2013) 68–73.

[20] B. Limoges, J.-M. Savéant, D. Yazidi, Quantitative Analysis of Catalysis and Inhibition at Horseradish Peroxidase Monolayers Immobilized on an Electrode Surface, Journal of the American Chemical Society 125 (2003) 9192–9203.

[21] M. Varničić, K. Bettenbrock, D., Hermsdorf, T. Vidaković-Koch, and K. Sundmacher Combined Electrochemical and Microscopic Study of Porous Enzymatic Electrodes with Direct Electron Transfer Mechanism, *Physical Chemistry Chemical Physics*, (2014).submitted.

[22] D. Jung, M. Paradiso, M. Hartmann, Formation of cross-linked glucose oxidase aggregates in mesocellular foams, Journal of Materials Science 44 (2009) 6747–6753.

[23] J. Kim, H. Jia, P. Wang, Challenges in biocatalysis for enzyme-based biofuel cells, Biotechnology advances 24 (2006) 296–308.

[24] S.A.M. van Stroe-Biezen, F.M. Everaerts, L.J.J. Janssen, R.A. Tacken, Diffusion coefficients of oxygen, hydrogen peroxide and glucose in a hydrogel, Analytica Chimica Acta 273 (1993) 553–560.

[25] S.C. Barton, H.-H. Kim, G. Binyamin, Y. Zhang, A. Heller, Electroreduction of O2 to Water on the Wired Laccase Cathode†, The Journal of Physical Chemistry B 105 (2001) 11917–11921.

[26] C. Gomez, S. Shipovskov, E.E. Ferapontova, Peroxidase biocathodes for a biofuel cell development, Journal of Renewable and Sustainable Energy 2 (2010) 013103-1–013103-12.

[27] A. Pizzariello, M. Streďansky, S. Miertuš, A glucose/hydrogen peroxide biofuel cell that uses oxidase and peroxidase as catalysts by composite bulk-modified bioelectrodes based on a solid binding matrix, Bioelectrochemistry 56 (2002) 99–105.

[28] Y. Hayashi, I. Yamazaki, Oxidation-Reduction Potentials of Compound-I-Compound–II and Compound-II-Ferric Couples of Horseradish Peroxidases A2 and C, Journal of Biological Chemistry 254 (1979) 9101–9106.

[29] B. He, R. Sinclair, B.R. Copeland, R. Makino, L.S. Powers, I. Yamazaki, The structure-function relationship and reduction potentials of high oxidation states of myoglobin and peroxidase, Biochemistry 35 (1996) 2413–2420.

[TVK8]

M. Varničić, K. Bettenbrock, D. Hermsdorf, T. Vidaković-Koch, K. Sundmacher

Combined Electrochemical and Microscopic Study of Porous Enzymatic Electrodes with Direct Electron Transfer Mechanism

CrossMark
click for updates

Combined electrochemical and microscopic study of porous enzymatic electrodes with direct electron transfer mechanism†

M. Varničić,[a] K. Bettenbrock,[a] D. Hermsdorf,[a] T. Vidaković-Koch*[a] and K. Sundmacher[ab]

In the present work electrochemical and microscopic methods have been utilized to get more insight into the complex relationship between the preparation route, structure and activity of porous enzymatic electrodes. Enzymatic electrodes have been prepared following two procedures. In one procedure enzymes were physically entrapped into a porous conductive matrix stabilized by "inert" binder (Vulcan-PVDF), while in the second one (Vulcan-Gelatin) gelatin has been used as a binder and the electrodes were cross-linked. Vulcan-PVDF electrodes show exceptionally high activity (up to 1.2 mA cm^{-2}) compared to Vulcan–Gelatin electrodes (0.3 mA cm^{-2}) at nominally lower enzyme loading. The scanning electron microscopy cross-sections of these electrodes revealed similar thicknesses, but a higher level of Vulcan nanomaterial agglomeration, somewhat reduced porosity and formation of gelatin film on top in the case of Vulcan–Gelatin electrodes. Additionally, fluorescence microscopy studies provided evidence of a higher level of enzyme agglomeration in the case of cross-linking. Although the gelatin matrix and the reduced catalyst layer porosity might slow down hydrogen peroxide diffusion, Vulcan–Gelatin electrodes are less affected by mass transfer conditions than Vulcan–PVDF electrodes. A plausible cause of the Vulcan–Gelatin electrode inferior performance is a lower number of active enzymes (lower enzyme utilization) compared to the Vulcan–PVDF electrode caused by a higher level of enzyme agglomeration in former case.

1. Introduction

Broader applications of redox enzymes as catalysts in bio-based technical systems like enzymatic fuel cells, bio-batteries or bioelectrochemical reactors require significant increase of the catalytic current per geometrical surface area of the electrode. This goal can be possibly achieved by improvement of the electrode structure, for example by introduction of high surface area materials, resulting in 3-D electrodes.[1–4] 3-D structuring introduces various materials into electrode design; enzymes as catalytic elements, additives like hydrogels for enhancing the enzyme stability and various nanomaterials as conductive supports for immobilization of the biocatalyst. In addition, suitable mediators might be required if the enzyme does not allow direct electron transfer (DET). All these components are commonly self-organized in the catalyst layer and their dispersion is unknown. A similar problem has been faced in the field

of conventional gas diffusion electrodes, where the designer task is to create a large so-called 3-phase interface. In case of enzymatic electrodes and DET, for optimal design, enzymes should be contacted by both an electron- and ion-conductive phases such that the reaction can take place. It can be easily anticipated that the formation of enzyme agglomerates, which might result from some preparation procedures, will drastically reduce the enzyme utilization. Similarly, additional components in the catalyst layer, like different hydrogels might break the electron conductive network, rendering parts of the catalyst layer inactive. It clearly follows that understanding of the relationship between the preparation conditions and the electrode performance is crucial for the optimal design of enzymatic electrodes.

Experimental methods for preparation of enzymatic electrodes can be roughly classified into two groups. First group of methods is based on physical immobilization of enzymes. The simplest approach is physical adsorption where only weak interactions between a support and an enzyme are involved. As supports, electron conductive materials like gold or carbon surfaces or in the case of 3-D electrodes, different types of nanomaterials have been typically used.[5–8] It has been demonstrated that using this method high performance enzymatic electrodes can be prepared even without any surface

[a]*Max Planck Institute for Dynamics of Complex Technical Systems, Sandtorstraße 1, 39106 Magdeburg, Germany. E-mail: vidakovic@mpi-magdeburg.mpg.de*

[b]*Otto-von-Guericke University Magdeburg, Universitätsplatz 2, 39106 Magdeburg, Germany*

modification in order to promote DET.[8] Another possibility for physical immobilization is entrapment of enzymes into gel matrixes such as gelatin, collagen and polysaccharides. This approach usually stabilizes enzymes more than only physical adsorption.[9–11] Second group of methods is based on chemical immobilization of enzymes. These methods include covalent enzyme immobilization on the electrode surface which requires functionalization of supports to create surface chemical groups for enzyme binding. Various surface modifications have been described in literature providing carboxyl, epoxy, acetyl or amino groups. These surface groups can be further either directly linked to enzymes or by using additional cross linkers like glutaraldehyde.[12]

Although methods based on covalent attachment have major benefit of higher enzyme stability at the expanse of somewhat lower activity due to reduction in enzyme flexibility[13] and in some cases oriented enzyme immobilization can be achieved proving especially beneficial in case of the DET,[14] we concentrate in the present paper on physical methods for enzyme immobilization. The major goal is to check how the preparation procedure influences electrode structural parameters like porosity and the electrode thickness. A further question is how enzyme organization at the conductive surface is dependent on the preparation procedure. To answer these questions porous enzymatic electrodes following two main routes of physical enzyme immobilization *i.e.* physical adsorption into porous structure and enzyme entrapment into gelatin matrix stabilized by cross-linking have been prepared. As a model enzyme horseradish peroxidase showing DET has been chosen. These electrodes have been characterized electrochemically for hydrogen peroxide reduction. Several factors which can influence electrode activity like: electrode surface area, thickness, enzyme distribution and agglomeration have been hypothesized. To prove their influence on observed activity, the electrodes, in addition to electrochemical methods, have been characterized using different microscopic methods. Scanning electron microscopy (SEM) has been used in order to get information on overall electrode structure (porosity, and its thickness), while fluorescence microscopy has been employed to visualize enzyme distribution on different supports.

2. Experimental part

2.1 Reagents

Horseradish peroxidase (EC 1.11.1.7, HRP) from *Amorica rusticana* was supplied from Serva Electrophoresis GmbH. Hydrogen peroxide (H$_2$O$_2$, 30 wt%) and gelatin were purchased from Merck. The H$_2$O$_2$ solution (3%) was prepared daily by dilution of 30% hydrogen peroxide. Poly(vinylidene fluoride) (PVDF), glutaraldehyde (GA) and 1-methyle-2-pyrrolidone were supplied by Sigma Aldrich. For fluorescence measurements DyLight 350 NHS ester dye, supplied by Thermo scientific with an excitation wavelength of 353 nm and an emission wavelength of 432 nm was used. All chemicals were of analytical reagent grade and all solutions were prepared using ultrapure water from Millipore.

2.2 Preparation of enzyme modified surfaces

For electrochemical measurements spectroscopically pure carbon (SPG) rods with impurities equal to or less than 2 ppm supplied by Ted Pella, 330 INC, USA were cut in 11 mm diameter discs and have been used as supports for enzyme modification. Before modification, they were polished by fine emery paper (P1000), rinsed with deionized water and then further polished with ordinary white paper to smoothen the surface.[15,16] For preparation of HRP modified electrodes, 50 μl of HRP solution in phosphate buffer (6 mg ml^{-1}, pH 6.00) was placed on the top of the SPG disc and left for 2 h under ambient conditions. After that it was washed with distillated water and used for measurements. The discs have been mounted in a sample holder for rotating disc electrode experiments (RDE, Radiometer Analytical, model ED101) with an opening of 6 mm.

Cross-linked electrodes were prepared by dipping enzyme modified discs in GA solution (5% in water) for 1 min, rinsing with water and drying at room temperature.[17]

Porous enzymatic electrodes incorporating enzymes and carbon nanoparticles (Vulcan XC72R supplied by Cabot Corporation) have been prepared by following two different procedures. In the first procedure, denoted in text as "Vulcan-Gelatin", gelatin has been used as a binder and electrodes were cross-linked. This procedure was similar to procedure reported by Ivanov *et al.*[18] Briefly, 20 mg of carbon nanomaterial and 10 mg HRP were suspended in 2% gelatin at 37 °C and cast on stainless steel discs degreased with acetone before usage. Electrodes were subsequently dried at ambient temperature and afterwards cross linked as previously described.

In the second procedure denoted in the text as "Vulcan-PVDF", poly(vinylidene fluoride) (PVDF) was used as a binder material. This procedure was similar to those described by Tsujimura *et al.*[7] Shortly, carbon nanomaterial was dissolved in 0.25 wt% PVDF solution in 1-methyle-2-pyrrolidone. In the next step, the ink was cast on SPG discs and left to dry at 60 °C. After drying, electrodes were ready for modification with HRP solution. Adsorption of enzyme on Vulcan electrodes was performed for 2 h at room temperature by applying 50 μl of 6 mg ml^{-1} HRP solution in 0.1 M phosphate buffer. Electrodes were then rinsed with buffer and were ready for use.

For atomic force microscopy (AFM) experiments highly oriented pyrolytic graphite (HOPG), supplied also from Ted Pella, 330 INC, USA was cut in the size of 5 mm × 4 mm. For preparation of HRP electrodes, a droplet of diluted HRP solution in phosphate buffer (6 mg ml^{-1}, pH 6.00) was placed on the top of the HOPG and left to dry. The dilution was made in order to obtain a monolayer on the HOPG surface.

For fluorescence microscopy experiments, both SPG and HOPG supports have been used. Before surface modification, HRP was labeled in the following way: HRP solution (2 mg ml^{-1}, pH 7.00) was mixed with fluorescence dye dissolved in dimethylformamide (DMF) and left for 1 h at room temperature. Afterwards, the excess non-reacted dye was removed by dialysis for 4 h using three dialysis buffer changes. The labeled enzymes were stored at 4 °C. For modification of SPG and HOPG

surfaces, a droplet of diluted HRP solution was applied on an appropriate surface and left to dry.

2.3 Measurements

Electrochemical experiments were performed using Autolab potentiostat (PGSTAT302, Eco Chemie). Saturated calomel (SCE) and Pt electrodes were used as reference and counter electrodes, respectively. The electrolyte was a 0.1 M phosphate buffer with pH 6.0. All electrochemical experiments have been done under nitrogen atmosphere at 400 rpm (rounds per minute). Steady state polarization curves were obtained by extracting the current values after 60 s at constant potential values.

Fluorescence microscopy has been performed with Imager M1 Microscope, Carl Zeiss. The objective was EC Plan Neofluar and filter set with excitation 365, beamer splitter 395 and emission 445/50 were used. In order to obtain high-contrast images and at the same time to avoid saturation, different exposure times have been used for different images (for further information please see the respective figure captions).

AFM measurements have been performed in air using 5500 SPM (Agilent Technologies), with tapping mode (Acoustic AC Mode). A rectangular silicon cantilever (PPP-NCSTAuD, Nanosensors) with a nominal force constant of 7.4 N m^{-1} has been used for the measurements.

Cross-sectional scanning electron microscopy (SEM) analysis of the enzymatic electrodes was performed using XL30 FEG (FEI Company).

3. Results and discussion

Porous enzymatic electrodes prepared based on two immobilization strategies described in the Experimental section have been tested for their activities towards hydrogen peroxide reduction (Fig. 1). Shortly, in one procedure, enzymes are immobilized by physical entrapment into a porous structure stabilized by "inert" binder (Vulcan-PVDF) while in the other one "active" binder (gelatin) and cross-linking to form and stabilize enzyme/nanoparticle composites (Vulcan-Gelatin) has been used. The performances of the enzymatic electrodes have been evaluated by means of cyclic voltammetry and steady state measurements. Fig. 1 shows cyclic voltammograms of the Vulcan-PVDF (Fig. 1a) and Vulcan-Gelatin (Fig. 1b) electrodes in phosphate buffer in absence and in presence of hydrogen peroxide, in quiet solution (0 rpm) and at 400 rpm rotation. As can be seen after addition of hydrogen peroxide, an increase of the reduction current can be observed indicating biocatalytic reduction of H_2O_2 by HRP. According to expectations[16] the electrode activity in quiet solution is lower than at 400 rpm. This is especially true for Vulcan-PVDF electrode (current density (after background current subtraction) in the limiting current region is *ca.* 0.66 mA cm^{-2} with and 0.13 mA cm^{-2} without stirring), while Vulcan-Gelatin electrode is less affected by stirring conditions (current density in the limiting current region is *ca.* 0.22 mA cm^{-2} with and 0.13 mA cm^{-2} without stirring). These results indicate stronger mass transfer limitations in the
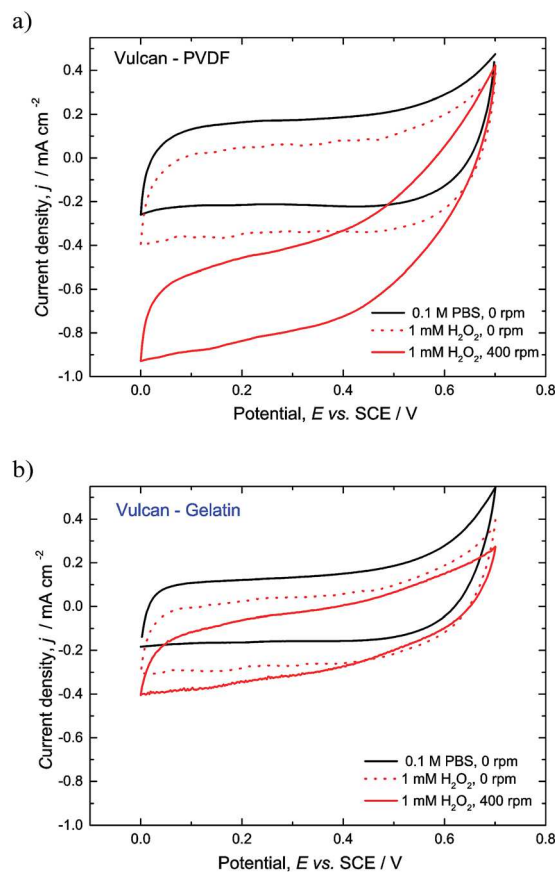

Fig. 1 Cyclic voltammograms of porous enzymatic electrodes in phosphate buffer and in 1 mM hydrogen peroxide, without rotation and at 400 rpm. (a) Vulcan-PVDF and (b) Vulcan-Gelatin. Conditions: scan rate 5 mV s^{-1}, pH 6.00, room temperature, N_2 atmosphere, enzyme loadings (1 mg cm^{-2} for Vulcan-PVDF and 1.75 mg cm^{-2} for Vulcan-Gelatin electrodes).

Vulcan-PVDF compared to Vulcan-Gelatin case. Furthermore, these results suggest higher amount of active enzymes in the Vulcan-PVDF case.

The activity of Vulcan-Gelatin electrode in terms of current densities is similar to reported values in literature, while Vulcan-PVDF electrode outperforms all literature results. Some examples are composite electrodes made of HRP immobilized on carbon nanotubes[19] with activity of *ca.* 0.1 mA cm^{-2} at 1 mM hydrogen peroxide concentration in the limiting current region, or HRP immobilized on single walls carbon nanotubes (SWCNT) with activity of *ca.* 0.03 mA cm^{-2} at 0.3 mM hydrogen peroxide concentration.[20] It should be stressed out that for fair comparison of electrode activities in different publications, some benchmarking is necessary. This benchmarking includes in addition to substrate concentration, pH and temperature, control of mass transfer resistance in the Nernstian diffusion layer and the same method for sampling of current–potential data. The control of mass transfer resistance in the diffusion layer over time can be only achieved under forced convection conditions. This control is very important for quantitative description of electrode processes since in quiet solution the

thickness of the diffusion layer is changing over time of the experiment in a quantitatively unpredictable manner. This appears especially important in processes strongly controlled by mass transfer. For example in the present case the activity of Vulcan-PVDF electrode is highly underestimated under non-stirred conditions in comparison to Vulcan-Gelatin electrode.

The influence of the sampling method has been demonstrated in Fig. 2 below. The comparison between background subtracted cyclic voltammogram at 5 mV s^{-1} with steady state measurements at two different sampling times (60 and 120 s), show that the cyclic voltammetry overestimates significantly the catalytic current. Regarding the sampling time, one can see that the results after 60 s and 120 s are almost identical for which reason 60 s sampling time has been chosen in further measurements. The chronoaperometric data which have been used for construction of steady state current density–potential relationship are presented in Fig. S1 (ESI†).

Having in mind previous discussion, forced convection conditions at constant rotation rate of 400 rpm and steady state method with sampling time of 60 s have been fixed in further measurements.

As can be seen in Fig. 2 both electrodes show high onset potential values (*ca.* 0.62 and 0.57 V *vs.* SCE for Vulcan-PVDF

and Vulcan-Gelatin electrodes respectively), comparable with literature values on high surface area electrodes *e.g.* 0.57 V *vs.* SCE at pH 6,[20] 0.55 V *vs.* SCE at pH 7,[19] and 0.63 V *vs.* SCE at pH 7.00.[21] The onset potential value of the Vulcan-PVDF electrode, is *ca.* 50 mV more positive than the measured value for Vulcan-Gelatin electrode. In general, for the same type of peroxidase, onset potential values depend on pH of the solution,[22] on peroxide concentration, (with more negative onset potential values at lower concentrations) and on immobilization procedure. The later effect might impact enzyme orientation at the surface as well as the number of active enzymes. It can be anticipated that both issues might contribute to observed differences between onset potentials of Vulcan-PVDF and Vulcan-Gelatin electrodes. In the case of Vulcan-PVDF electrodes enzymes were only physically adsorbed, while in the case of Vulcan-Gelatin procedure they were also cross-linked. One can hypothesize that enzyme cross-linking causes less favored enzyme orientations than the physical adsorption of enzymes (Vulcan-PVDF case) resulting in more negative onset potential. As it was discussed the results in Fig. 1 and 2 indicate higher number of active enzymes in the case of Vulcan-PVDF electrode. Alternatively at the same number of active enzymes, lowering of the kinetic constants of cross-linked enzymes could also explain the experimental observations. These two effects can not be separated, without being able to quantify the number of active enzymes (ref. 16 and references therein).

Next, the influence of enzyme loading at constant peroxide concentration has been checked for both immobilization procedures (Fig. 3). As can be seen in Fig. 2 Vulcan-PVDF electrodes are more active than Vulcan-Gelatin electrodes in the whole range of studied loadings. The dependences of current densities at constant potential (0.0 V *vs.* SCE) on enzyme loading show a bell-shaped form with optimal loading at *ca.* 1 mg cm^{-2} and 1.75 mg cm^{-2} for Vulcan-PVDF and Vulcan-Gelatin electrodes respectively. While an initial increase of the activity with enzyme loading can be correlated with an increase of the number of active enzymes, decrease of activity at higher enzyme loadings might be a consequence of a mass transfer resistance increase, in the catalyst layer at higher enzyme loadings.
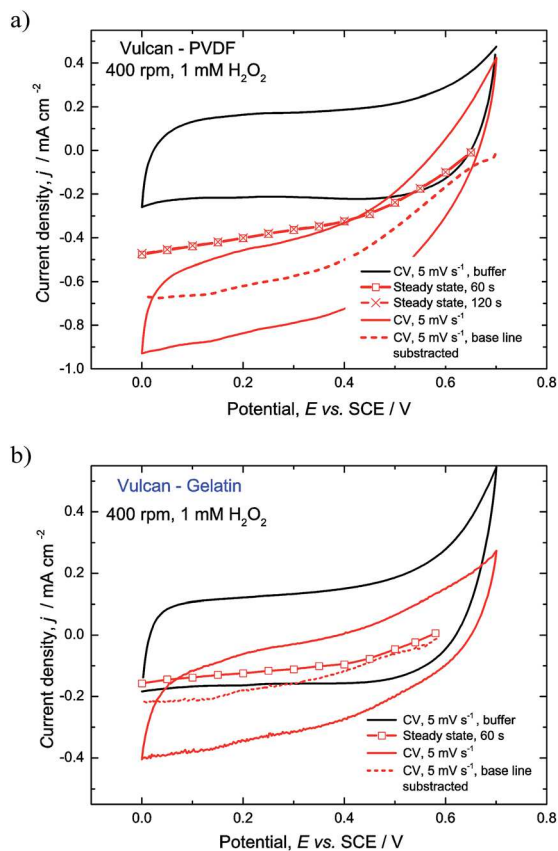

Fig. 2 Comparison of the electrode performance obtained using cyclic voltammetry and steady state methods. (a) Vulcan–PVDF and (b) Vulcan–Gelatin electrodes. Conditions: scan rate 5 mV s^{-1} pH 6.00, N$_2$ atmosphere, enzyme loadings: Vulcan-PVDF – 1 mg cm^{-2} and Vulcan-Gelatin – 1.75 mg cm^{-2}.
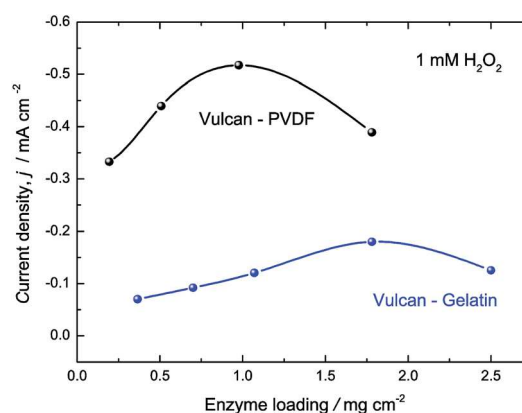

Fig. 3 Influence of enzyme loading on the activity of Vulcan HRP – electrodes. Conditions: 1 mM hydrogen peroxide, electrode potential 0.0 V *vs.* SCE, 400 rpm, N$_2$ atmosphere, pH 6.00.

As a consequence dead portions of the catalyst layer can be created, which are under supplied with substrate.[23] In addition to this reason unfavoured enzyme orientation is often commented in literature as a possible cause of activity decrease at higher loadings.[21] Regarding different optimal loadings for two different procedures there are several reasons which can contribute to this observation. In accordance to our recent modeling study[23] utilization of the catalyst layer depends on the thickness of the layer, its porosity, number of active enzymes and the concentration of reactant. In addition at higher hydrogen peroxide concentrations the effect of enzyme inhibition can become evident.[24] The results indicate a lower number of active enzymes in Vulcan-Gelatin case. The reduced number of active enzymes, at the same concentration of reactant can cause better utilization of the catalyst layer in case of Vulcan-Gelatin electrode shifting position of the maximum to higher enzyme loadings.

The effect of hydrogen peroxide concentration was further studied for two optimal loadings of Vulcan-PVDF and Vulcan-Gelatin electrodes (Fig. 4). The increase of reduction current with an increase of hydrogen peroxide concentration indicates that the immobilized HRP retains its catalytic activity for the reduction of hydrogen peroxide. The results show that saturation conditions are reached at *ca.* 5 mM and *ca.* 4 mM hydrogen peroxide concentration for Vulcan-PVDF and Vulcan-Gelatin electrodes respectively. The Vulcan-PVDF electrode has excellent performance comparable with performance of bilirubin oxidase (BOD) based biocathode prepared on Ketjen Black (KB) suggesting that also these HRP-enzymatic electrodes are suitable for biofuel cell application.[25]

To understand the origin of the high activity of Vulcan-PVDF and lower activity of Vulcan-Gelatin electrodes, these two electrodes have been further characterized electrochemically in the absence of hydrogen peroxide as well as physically with SEM. The electrochemical characterization in the absence of active component (hydrogen peroxide) gives a rough orientation on active surface area available f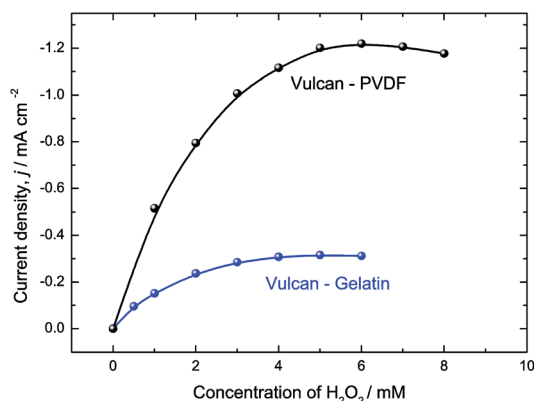or enzyme adsorption. As can be seen in Fig. 5, the CVs of both electrodes in absence of hydrogen peroxide appear almost identical, showing only characteristic features of carbon material.[26] Although Vulcan-Gelatin electrode had a bit higher Vulcan loading (3.6 mg cm^{-2}) than Vulcan-PVDF electrode (3.0 mg cm^{-2}), the results indicate similar active surface area for enzyme adsorption.

Furthermore cross-sections of two types of electrodes have been studied by SEM (Fig. 6). It can be seen that the thicknesses of two electrodes are 47 μm and 53 μm for Vulcan-Gelatin and Vulcan-PVDF electrodes respectively. Magnification of the electrode cross sections (Fig. 6c and d) provides better insights into electrode morphology. Vulcan nanomaterial in Vulcan-Gelatin electrode forms knot-shaped agglomerates with the size around 250 nm which are significantly bigger than unit-structures in the Vulcan-PVDF electrode. This can be due to hydrophilic nature of gelatin, resulting in a higher degree of agglomeration of hydrophobic Vulcan nanoparticles. If PVDF was used, distribution of Vulcan nanoparticles is more uniform and *ca.* 100 nm spherical units can be observed (Fig. 6d). This indicate lessening of available surface area in the case of Vulcan-Gelatin electrode compared to Vulcan-PVDF electrode, which is also in accordance to electrochemical characterization (Fig. 5) where the CVs of both electrodes appear very similar despite a bit higher Vulcan loading of Vulcan-Gelatin electrode.

The top views of the Vulcan-Gelatin and Vulcan-PVDF electrode surfaces are also affected by preparation conditions as shown in Fig. 6e and f. Vulcan-Gelatin electrode has a layer of gelatin on the top which additionally stabilizes the electrode structure, might prevent/decrease leaching of enzymes, but introduces additional mass transfer resistance for hydrogen peroxide transfer in the catalyst layer. The surface of Vulcan-PVDF electrode has similar morphology to the electrode cross section. Additionally, porosities of both electrodes have been estimated based on the electrode thickness measured by SEM and theoretical compact electrode thickness based on loadings of all electrode components and their densities, according to the equation provided by Gode *et al.*[27] Taking into account density of dry gelatin, the estimated value of electrode porosity for Vulcan-Gelatin procedure is 0.27. Calculated porosity for the
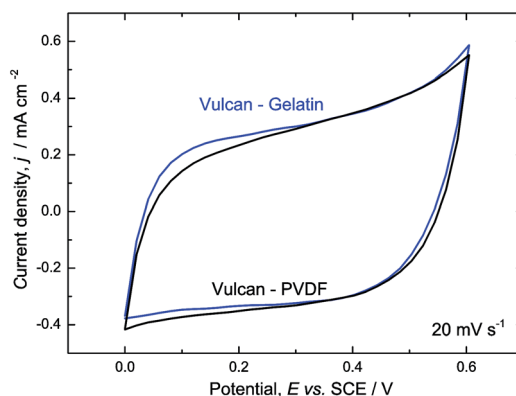

Fig. 4 Influence of the hydrogen peroxide concentration on the activity of Vulcan HRP – electrodes at optimized enzyme loadings. Conditions: enzyme loadings 1.75 mg cm^{-2} for Vulcan-Gelatin and 1.1 mg cm^{-2} for Vulcan-PVDF, electrode potential 0.0 V *vs.* SCE, 400 rpm, N$_2$ atmosphere, pH 6.00.

Fig. 5 Cyclic voltammograms of Vulcan HRP – electrodes in 0.1 M phosphate buffer. Conditions: scan rate 20 mV s^{-1}, 400 rpm, N$_2$ atmosphere, pH 6.00.
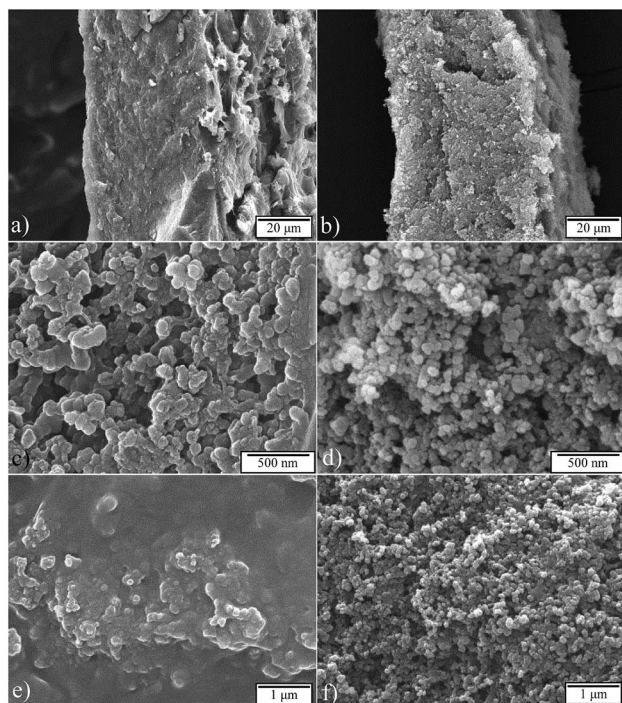
Fig. 6 SEM images of Vulcan HRP electrodes: cross sections of Vulcan-Gelatin (a) and Vulcan-PVDF (b); magnified view of the cross-sections of Vulcan-Gelatin (c) and Vulcan-PVDF (d) and top views of Vulcan-Gelatin (e) and Vulcan-PVDF (f).

Vulcan-PVDF electrode of 0.45 indicates lower mass transport limitations through the electrode layer in comparison to Vulcan-Gelatin electrodes.

The missing part of information is the influence of cross-linking on enzyme distribution and organization in the catalyst layer. Enzymes are protein structures having a size of several nm.[28] They have been visualized by different microscopic methods like atomic force microscopy (AFM)[29–33] scanning electrochemical microscopy (SECM), electrochemical scanning tunnelling microscopy (ESTM)[34] and fluorescence microscopy (FM).[35] In the present work FM has been applied for studying the enzyme organization on conductive supports. This method provides optical images of enzymes on surfaces, utilizing either their native fluorescence (*e.g.* flavin enzymes (FAD)[36] are fluorescent) or more common foreign fluorescence obtained by labelling of enzymes with fluorescent markers. It has been so far successfully applied to investigate interactions of proteins entrapped in different polymers[35,37–39] and for verification of enzyme self-assembly layer formation on the microarray electrodes.[40,41]

Since, HRP lacks its natural fluorescence it was first modified with amine-reactive dye containing *N*-hydroxysuccinimide (NHS) ester which is one of the most commonly used reactive groups for protein labeling. Modification occurs through formation of covalent bonds between the NHS ester and surface-oriented primary amines of the protein.[42] In order to verify that the labeling procedure was successful, the electrophoresis of modified and unmodified enzymes has been done.

Prepared gel contained two lanes, one with labeled HRP and one with unlabeled HRP. After separation and before applying standard staining procedure (in order to color all separated proteins), gel was observed under UV lamp (Fig. S2a ESI†). In this way, only fluorescent proteins are visualized. In the second step, after staining procedure, all proteins have been visualized. As can be seen in Fig. S2b ESI,† in both lanes HRP with molecular weight of 44 kDa was observed at the expected position and only the labeled protein showed fluorescence properties (Fig. S2a ESI†). It has been already shown that the presence of label does not perturb significantly the behavior of the enzymes.[35] However, in order to verify that the labeling procedure does not affect the enzyme properties in the present case, the electrochemical activities of enzymatic electrodes modified with labeled and non-labeled enzymes were compared. The performances of these electrodes were found to be almost identical, indicating that the labeling did not affect the activity of the enzyme on the electrode surface (data not shown).

The following fluorescence microscopy measurements have been performed on model surfaces, but we believe that they provide good indications on enzyme distribution inside of porous structures. The effects of surface roughness and the cross-linking on enzyme distribution have been checked. To test the influence of the surface roughness, labeled HRP has been physically adsorbed on HOPG (ideally flat surface) and SPG (roughness factor 5 (ref. 43)). In both cases the quantity of an adsorbed enzyme corresponded to the calculated monolayer coverage. In case of the HRP–HOPG surface, the fluorescent image (Fig. 7a) shows a uniform level of fluorescence across the whole surface, which can be probably associated with a uniform distribution of enzymes on the flat HOPG surface. To check the flatness of the surface and the assumption of monolayer enzyme coverage, the HOPG surface before and after the modification was screened by AFM. The roughness of
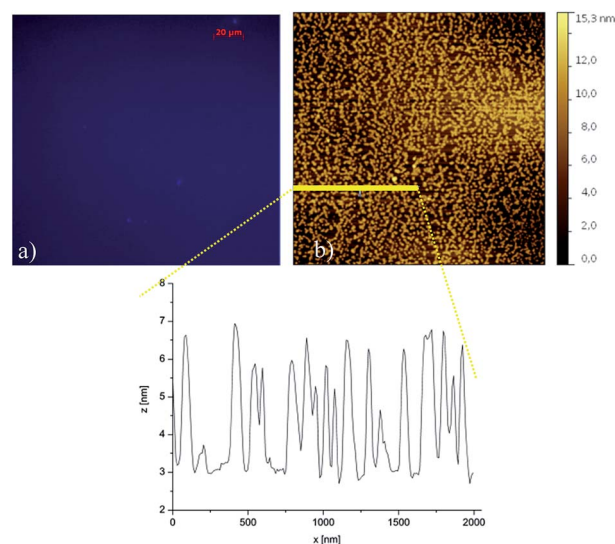

Fig. 7 Labeled-HRP on HOPG support visualized by fluorescence microscopy with exposure time of 200 ms (a) and AFM image of HRP adsorbed on HOPG in a monolayer at pH 6 (b).

unmodified HOPG was found to be low with a maximum height of the profile below 0.4 nm (Fig. S3 ESI†). The AFM images with physically distributed enzyme patterns at relatively large areas (Fig. 7b). This pattern formation was strongly pH sensitive, showing for example more expressed branchy-like structures at pH 7.2 (Fig. S4 ESI†). The average heights of these structures are *ca.* 4 nm and *ca.* 5 nm at pH 6 and pH 7.2, respectively. These values correspond well to reported values of HRP dimensions (6.2 × 4.3 × 1.2 nm (ref. 3 and 34)) indicating monolayer formation. Interestingly, although the height of enzyme aggregates is not pH dependent, the width of these aggregates is pH sensitive (*ca.* 100 nm and *ca.* 300 nm at pH 6 and pH 7.2, respectively; Fig. 7b and S4 ESI†). This can possibly have an impact on the resulting enzyme catalytic activity.

Unlike the HRP–HOPG surface, the fluorescence image of HRP–graphite surface (Fig. 8a) shows a non-uniform distribution of fluorescence with blue spots of different intensities as well as very dark areas. These dark areas have a very low level of fluorescence (*ca.* 200 A.U.) and can be probably ascribed to enzyme-free parts of the surface. The blue spots with different intensities indicate a non-uniform distribution of enzymes on the remaining part of the surface, with spots showing a higher level of fluorescence (*ca.* 1500 A.U.) probably indicating enzyme agglomeration, while spots with a lower level of fluorescence (*ca.* 800 A.U.) (similar to those observed on HOPG surface) indicating monolayer enzyme adsorption.

The non-uniform distribution of enzymes on the graphite surface corresponds well to the higher level of its surface inhomogeneity compared to HOPG. This result suggests that a monolayer of enzymes can be formed only on ideally flat surfaces like HOPG. If the roughness of the surface is of higher order than the size of the enzyme one can always expect the formation of agglomerates and consequently a non-uniform enzyme distribution. It can be further anticipated that the adsorption strength between the enzyme and the surface will vary for different adsorption sites like flat areas or depressions on the surface. This is confirmed by the image in Fig. 8b where the graphite surface after pronounced electrode rotation is shown. One can easily see that the blue spots of lower intensity, which were assigned to monolayer adsorption, disappeared. The enzyme distribution on the surface has a significant influence on the enzyme activity, especially in the case of DET, where

the enzyme's active centers should be in close proximity of the electrode to allow for electron transfer. Our results indicate that in addition to orientation, enzyme agglomeration decreases the number of enzymes being in direct contact with the electrode surface.

The effect of cross-linking has been studied on HOPG and graphite surfaces (Fig. 9). According to literature cross-linking increases enzyme stability without influencing its activity (except in case of extremely high ratios between cross-linker and enzymes).[44]

In addition, cross-linking is responsible for formation of enzyme agglomerates which can be clearly seen on both HOPG and spectroscopic graphite surfaces (Fig. 9a and b). While on HOPG one large agglomerate forms, on spectroscopic graphite "agglomeration centers" which differ in shape and size can be observed. The average level of fluorescence for these cross linked agglomerates on spectroscopic graphite is *ca.* 3200 ± 300 A.U. (profile shown only for one agglomerate), while the level of fluorescence for agglomerates on graphite without CL has values of *ca.* 1500 A.U. It can be anticipated that formation of enzyme-agglomerates decreases the number of active enzymes
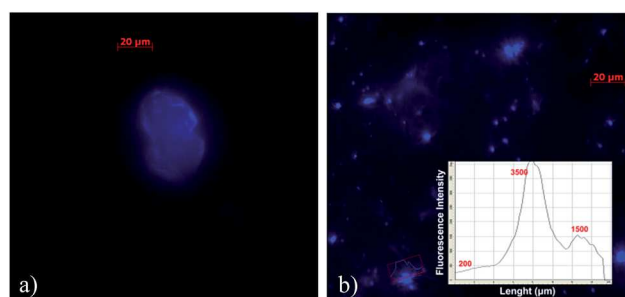

Fig. 9 Fluorescence microscopy images of labeled-HRP after CL using 5% glutaraldehyde on HOPG, imaged with the exposure time of 100 ms (a) and on spectroscopic graphite surface with 200 ms exposure time (b).
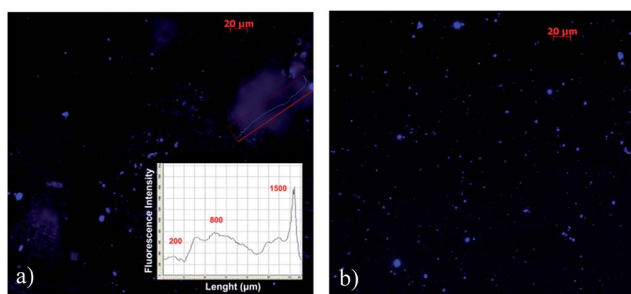

Fig. 8 Fluorescence microscopy images of labeled-HRP on the SPG before rotation, 200 ms exposure time (a) and after 2 h rotation in RDE, 400 rpm, 100 ms exposure time (b).
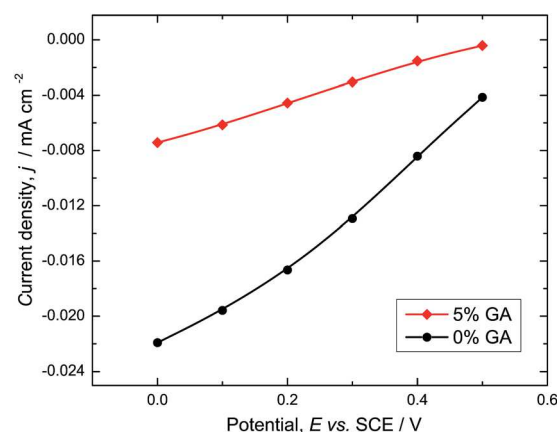

Fig. 10 Steady state polarization curves of hydrogen peroxide reduction on the HRP-modified graphite electrodes without and with cross linking. Conditions: 160 μM hydrogen peroxide concentration, 400 rpm, N_2 atmosphere, pH 6.00.

in contact with the electrode surface, which reduces further bio-electrode activity. This has been confirmed in experiment where the activities of non and cross-linked electrodes have been compared (Fig. 10). On the other hand CL increases the stability of the electrode, probably by decreasing the level of leaching. The calculated loss of activity after 2 hours at constant potential of 0.0 V *vs.* SCE was *ca.* 13% for CL electrode and *ca.* 28% for the non-cross-linked electrode (data not shown).

4.   Conclusions

In this study porous enzymatic electrodes have been prepared by following immobilization protocols with and without cross-linking. It was demonstrated that the electrodes without hydrogels and further stabilization through cross-linking show significantly higher activities for the same nominal enzyme loading. Optimized HRP-enzymatic electrodes exhibit high activity towards hydrogen peroxide reduction reaching current density of *ca.* 1.2 mA cm^{-2}, which according to our knowledge has not been reported in literature so far.

The electrochemical characterization in the absence of reactant hydrogen peroxide has shown that both electrodes have almost the same electrochemically active surface area. SEM cross sections demonstrate that the thicknesses of two electrodes were similar, but porosity of Vulcan-Gelatin electrode was reduced in comparison to Vulcan-PVDF electrode. It was shown that addition of gelatin leads to stronger agglomeration of Vulcan nanomaterial. In addition gelatin forms a film on top, which can cause mass transfer limitations. The fluorescence microscopy studies on model surfaces have demonstrated that level of enzyme agglomeration depends on surface roughness and it increases upon cross-linking. This has a negative effect on electrode activity in both onset potential values and overall activity. Physical adsorption leads to uniform enzyme distribution only in the case of ideally flat surfaces. On macroscopically flat surfaces, enzyme agglomerates are also formed but in less extent compared to cross-linked conditions. The surface utilization for enzyme adsorption is very small.

Although the presence of gelatin matrix and the reduced porosity in Vulcan-Gelatin electrodes might slow down significantly mass transfer of the substrate through these electrodes, Vulcan-Gelatin electrodes are less affected by mass transfer conditions than Vulcan-PVDF electrodes. This implies higher reaction resistance in the case of Vulcan-Gelatin. According to our results, higher reaction resistance is caused by smaller number of active enzymes or by lowering of the kinetic constants of cross-linked enzymes. These two effects can not be separated, without being able to quantify the number of active enzymes.

Acknowledgements

Notes and references

1 I. Ivanov, T. Vidakovic-Koch and K. Sundmacher, *Energies*, 2010, **3**, 803–846.
2 T. Tamaki, *Top. Catal.*, 2012, **55**, 1162–1180.
3 M. H. Osman, A. A. Shah and F. C. Walsh, *Biosens. Bioelectron.*, 2011, **26**, 3087–3102.
4 J. A. Cracknell, K. A. Vincent and F. A. Armstrong, *Chem. Rev.*, 2008, **108**, 2439–2461.
5 X. J. Wang, M. Falk, R. Ortiz, H. Matsumura, J. Bobacka, R. Ludwig, M. Bergelin, L. Gorton and S. Shleev, *Biosens. Bioelectron.*, 2012, **31**, 219–225.
6 T. Kihara, X. Y. Liu, C. Nakamura, K. M. Park, S. W. Han, D. J. Qian, K. Kawasaki, N. A. Zorin, S. Yasuda, K. Hata, T. Wakayama and J. Miyake, *Int. J. Hydrogen Energy*, 2011, **36**, 7523–7529.
7 S. Tsujimura, Y. Kamitaka and K. Kano, *Fuel Cells*, 2007, **7**, 463–469.
8 D. Svedruzic, J. L. Blackburn, R. C. Tenent, J. D. R. Rocha, T. B. Vinzant, M. J. Heben and P. W. King, *J. Am. Chem. Soc.*, 2011, **133**, 4299–4306.
9 E. H. Yu and K. Scott, *Energies*, 2010, **3**, 23–42.
10 J. Kim, H. F. Jia and P. Wang, *Biotechnol. Adv.*, 2006, **24**, 296–308.
11 E. T. Hwang and M. B. Gu, *Eng. Life Sci.*, 2013, **13**, 49–61.
12 C. F. Meunier, X. Y. Yang, J. C. Rooke and B. L. Su, *ChemCatChem*, 2011, **3**, 476–488.
13 M. J. Cooney, V. Svoboda, C. Lau, G. Martin and S. D. Minteer, *Energy Environ. Sci.*, 2008, **1**, 320–337.
14 O. Rudiger, C. Gutierrez-Sanchez, D. Olea, I. A. C. Pereira, M. Velez, V. M. Fernandez and A. L. De Lacey, *Electroanalysis*, 2010, **22**, 776–783.
15 R. Andreu, E. E. Ferapontova, L. Gorton and J. J. Calvente, *J. Phys. Chem. B*, 2007, **111**, 469–477.
16 T. Vidakovic-Koch, V. K. Mittal, T. Q. N. Do, M. Varnicic and K. Sundmacher, *Electrochim. Acta*, 2013, **110**, 94–104.
17 I. Ivanov, T. Vidakovic-Koch and K. Sundmacher, *J. Power Sources*, 2011, **196**, 9260–9269.
18 I. Ivanov, T. Vidakovic-Koch and K. Sundmacher, *J. Electroanal. Chem.*, 2013, **690**, 68–73.
19 W. Jia, C. Jin, W. Xia, M. Muhler, W. Schuhmann and L. Stoica, *Chem.–Eur. J.*, 2012, **18**, 2783–2786.
20 C. Gomez, S. Shipovskov and E. E. Ferapontova, *J. Renewable Sustainable Energy*, 2010, **2**, 013103-1–013103-12.
21 W. Z. Jia, S. Schwamborn, C. Jin, W. Xia, M. Muhler, W. Schuhmann and L. Stoica, *Phys. Chem. Chem. Phys.*, 2010, **12**, 10088–10092.
22 T. Ruzgas, E. Csoregi, J. Emneus, L. Gorton and G. MarkoVarga, *Anal. Chim. Acta*, 1996, **330**, 123–138.
23 T. Q. N. Do, M. Varnicic, R. Hanke-Rauschenbach, T. Vidakovic-Koch and K. Sundmacher, *Electrochim. Acta*, 2014, **137**, 616–626.
24 B. Limoges, J. M. Saveant and D. Yazidi, *J. Am. Chem. Soc.*, 2003, **125**, 9192–9203.
25 J. Filip, J. Sefcovicova, P. Gemeiner and J. Tkac, *Electrochim. Acta*, 2013, **87**, 366–374.

26 T. Tamaki and T. Yamaguchi, *Ind. Eng. Chem. Res.*, 2006, **45**, 3050–3058.

27 P. Gode, F. Jaouen, G. Lindbergh, A. Lundblad and G. Sundholm, *Electrochim. Acta*, 2003, **48**, 4175–4187.

28 H. P. Erickson, *Biol. Proced. Online*, 2009, **11**, 32–51.

29 M. ElKaoutit, A. H. Naggar, I. Naranjo-Rodriguez, M. Dominguez and J. de Cisneros, *Synth. Met.*, 2009, **159**, 541–545.

30 Y. H. Song, L. Wang, C. B. Ren, G. Y. Zhu and Z. Li, *Sens. Actuators, B*, 2006, **114**, 1001–1006.

31 J. L. Zhang, F. Zhang, H. J. Yang, X. L. Huang, H. Liu, J. Y. Zhang and S. W. Guo, *Langmuir*, 2010, **26**, 6083–6085.

32 K. Besteman, J. O. Lee, F. G. M. Wiertz, H. A. Heering and C. Dekker, *Nano Lett.*, 2003, **3**, 727–730.

33 K. De Wael, S. Van Vlierberghe, H. Buschop, P. Dubruel, B. Vekemans, E. Schacht, L. Vincze and A. Adriaens, *Surf. Interface Anal.*, 2009, **41**, 389–393.

34 J. D. Zhang, Q. J. Chi, S. J. Dong and E. K. Wang, *Bioelectrochem. Bioenerg.*, 1996, **39**, 267–274.

35 J. H. Wang, L. W. Ruddock and A. E. G. Cass, *Biosens. Bioelectron.*, 1994, **9**, 647–655.

36 H. P. Lu, L. Y. Xun and X. S. Xie, *Science*, 1998, **282**, 1877–1882.

37 M. Xiong, B. Gu, J.-D. Zhang, J.-J. Xu, H.-Y. Chen and H. Zhong, *Biosens. Bioelectron.*, 2013, **50**, 229–234.

38 D. Olea, P. Moreau and C. Faure, *J. Electroanal. Chem.*, 2007, **605**, 125–135.

39 A. Uygun, L. Oksuz, S. Chowdhury and V. Bhethanabotla, *Mater. Sci. Eng., C*, 2010, **30**, 868–872.

40 A. P. Hsiao and M. J. Heller, *J. Biomed. Biotechnol.*, 2012, **2012**, 178487.

41 S. E. Rosenwald, W. B. Nowall, N. Dontha and W. G. Kuhr, *Anal. Chem.*, 2000, **72**, 4914–4920.

42 B. Wetzl, M. Gruber, B. Oswald, A. Durkop, B. Weidgans, M. Probst and O. S. Wolfbeis, *J. Chromatogr. B: Anal. Technol. Biomed. Life Sci.*, 2003, **793**, 83–92.

43 T. Ruzgas, L. Gorton, J. Emneus and G. Markovarga, *J. Electroanal. Chem.*, 1995, **391**, 41–49.

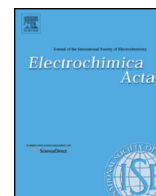44 R. A. Sheldon, *Org. Process Res. Dev.*, 2011, **15**, 213–223.

[TVK9]

M. Varničić, T. Vidaković-Koch, K. Sundmacher

Gluconic acid synthesis in an electroenzymatic reactor

Gluconic Acid Synthesis in an Electroenzymatic Reactor

M. Varničić[a], T. Vidaković-Koch[a,*], K. Sundmacher[a,b]

[a] Max Planck Institute for Dynamics of Complex Technical Systems, Sandtorstraße 1, D-39106 Magdeburg, Germany
[b] Otto-von-Guericke University Magdeburg, Process Systems Engineering, Universitätsplatz 2, D-39106 Magdeburg, Germany

A B S T R A C T

Glucose was selectively oxidized to gluconic acid in a membraneless, flow-through electroenzymatic reactor operated in the mode of co-generating chemicals and electrical energy. At the anode the enzyme glucose oxidase (GOx) in combination with the redox mediator tetrathiafulvalene (TTF) was used as catalyst, while the cathode was equipped with an enzyme cascade consisting of GOx and horseradish peroxidase (HRP). The influence of the electrode preparation procedure, the structural and the operating parameters on the reactor performance was investigated in detail. Under optimized conditions, an open circuit potential of 0.75 V, a current density of 0.6 mA cm^{-2} and a power density of 100 µA cm^{-2} were measured. The space time yield of gluconic acid achieved at a glucose conversion of 47% was 18.2 g h^{-1} cm^{-2}.

1. Introduction

Electroenzymatic processes combine the high selectivity of enzymatic catalysts with the electrochemical regeneration of their co-factors. This conceptual approach seems to be very promising for development of new biotechnological production processes [1–3]. In the present work the potential of a novel electroenzymatic reactor for the production of gluconic acid has been evaluated. Gluconic acid is a mild organic acid with applications in different industrial branches. It belongs to the commodities with an annual production of 100.000 t [4–6]. It can be obtained by partial oxidation of glucose. Glucose itself can be considered as one a renewable platform chemical [7].

Up to now, several electroenzymatic processes for gluconic acid production have been described. One of the first works in this direction was reported by Bourdillon et al. in the late 1980s [8]. Further developments of this route are listed in Table 1. Most of the described processes operate at pH 7 and a temperature of T = 30 °C or room temperature, since under these conditions enzymatic catalysts (glucose oxidase and glucose dehydrogenase) show the highest activity. Although the applied reactor configurations are quite different, there is a clear trend towards membrane reactors. Two types of membrane reactors were used. The first type implements dialysis membranes [9], while the second type uses ion-exchange (e.g. Nafion) membranes [10,11]. The mechanisms of enzyme regeneration in these two reactor types are essentially different. Reactors employing a dialysis membrane rely upon biochemical enzyme regeneration with oxygen as electron acceptor. The role of electrochemistry is the removal of hydrogen peroxide formed as a by-product of biochemical enzyme regeneration. It was shown that such an electroenzymatic process is 50% more efficient than a comparable non-electrochemical enzymatic process performed with the same quantity of enzymes [12]. Opposite to this, reactors with Nafion membrane rely upon electrochemical regeneration of co-factor, avoiding oxygen as natural electron acceptor. In these reactors, it is more common to use enzyme glucose-dehydrogenase than glucose oxidase, since the first one depends on soluble co-factor nicotinamide adenine dinucleotide (NAD), while the second one on tightly bounded flavin adenine dinucleotide (FAD) as the co-factor. The electrochemical regeneration of the co-factor was achieved with the help of different mediators (e.g. 3,4–dihydroxybenzaldehyde or phenazine methosulfate [11,13–15]. Most systems were operated in a semi-batch mode with total volumes in the range between 10 and 200 ml and electrode surface areas between 3 and 30 cm^2. The glucose concentrations ranged from 10 to 248 mM, where the majority of authors used lower concentration levels (Table 1). In most of the published works, as counter electrode materials platinum [9,12] or a carbon felt [10,11] were used. The glucose conversions in these reactors varied from 30 to 85 % at electrolysis times between 3 and 12 h.

So far, all proposed electroenzymatic processes are running non-spontaneously, i.e. they require external input of electrical energy for continuous operation. In the present work, the proposed process configuration operates in the co-generation mode, thus the process is running spontaneously like a fuel cell. Additionally, this

---

Table 1
An overview of electroenzymatic processes for gluconic acid production.

System	Enzyme	Enzyme Immobiliza-tion	Electron transfer	Electrode surface area / cm^2	Volume / cm^3	Glucose concentra-tion / mM	Time / h	Glucose Conver-sion / %	STY / $g\,h^{-1}\,cm^{-2}$	Ref.
Membrane (Nafion)	GDH	In solution	direct	24	28	10	12	85	0.16	[10]
Membrane (Nafion)	GDH	Covalent attachment	Mediated (3,4–DHB)	24	28	100	4	60	3.43	[11]
Membrane (Dialysis)	GOx	Entrapment in dialysis membrane	Mediated (O_2)	30	44	248	3	30	7.13	[9]
Batch	GOx	In polypyrrole film	Mediated (O_2)	3.14	10	20	8	62	0.97	[12]
RDE system	G6PDH	Covalent attachment	Mediated (PMS)	19.6	200	9.3	6	43	1.33	[13]
Membrane-less	GOx	3-D electrode	Mediated (TTF, O_2)	1	70	20	7	47	18.2	This Work

Abbreviations: GDH– glucose dehydrogenase; G6PDH– glucose-6-phosphat-dehydrogenase; GOx – glucose oxidase; NAD– nicotinamide adenine dinucleotide; NADP– nicotinamide adenine dinucleotide phosphate; TTF – Tetrathiafulvalene; 3, 4–DHB- 3, 4-dihydroxybenzaldehyde; PMS– phenazine methosulfate

variant is completely based on enzymatic catalysts (both anode and cathode), all catalysts and the mediator are immobilized and the reactor employs no membrane (Fig. 1). Tetrathiafulvalene (TTF) has been applied as mediator for GOx regeneration on the anode side, while on the cathode side a GOx - horseradish peroxidase (HRP) cascade has been implemented. By this enzyme cascade, glucose is first oxidized giving hydrogen peroxide, which is then further reduced to water, while HRP is regenerated electrochemically. In this way electrons are released on the cathode side, and the by-product hydrogen peroxide is locally removed, which should increase the stability of the enzyme GOx. The presence of GOx on both electrodes increases the space time yield of the gluconic acid. This is major advantage of enzymatic cascade on the cathode side, compared to the utilization of a single enzyme like Bilirubin oxidase (BOD). In the present contribution, feasibility of proposed electroenzymatic reactor for glucose oxidation to gluconic acid has
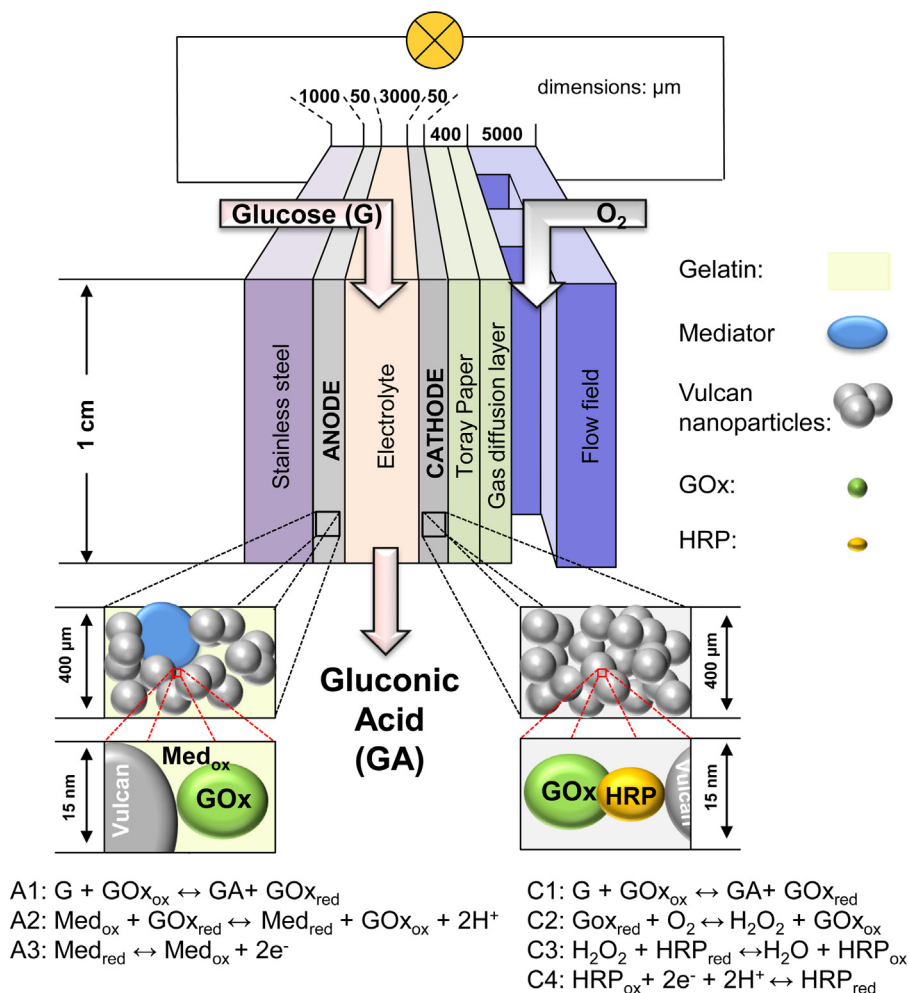

A1: G + GOx$_{ox}$ ↔ GA+ GOx$_{red}$
A2: Med$_{ox}$ + GOx$_{red}$ ↔ Med$_{red}$ + GOx$_{ox}$ + 2H$^+$
A3: Med$_{red}$ ↔ Med$_{ox}$ + 2e$^-$

C1: G + GOx$_{ox}$ ↔ GA+ GOx$_{red}$
C2: Gox$_{red}$ + O$_2$ ↔ H$_2$O$_2$ + GOx$_{ox}$
C3: H$_2$O$_2$ + HRP$_{red}$ ↔ H$_2$O + HRP$_{ox}$
C4: HRP$_{ox}$ + 2e$^-$ + 2H$^+$ ↔ HRP$_{red}$

Fig. 1. Schematic representation of electroenzymatic reactor, with anode and cathode reactions mechanisms.

been investigated. The influence of the structural and operational parameters on glucose conversion has been studied.

2. Experimental part

2.1. Chemicals and materials

Glucose oxidase (EC 1.1.3.4, GOx) from *Aspergillus niger* and Horseradish peroxidase (EC 1.11.1.7, HRP) from *Amorica rusticana* were supplied from Fluka and Serva Electrophoresis GmbH, respectively.

Gelatin for microbiology was purchased from Merck. All other chemicals including poly(vinylidene fluoride) (PVDF), glutaraldehyde (GA), 1-methyle-2-pyrrolidone, glucose and tetrathiafulvalene (TTF) were from Sigma-Aldrich. For preparation of all solutions, Millipore water was used.

Vulcan nanomaterial was supplied by Cabot Corporation. Spectroscopically pure carbon rods supplied by Ted Pella, 330 INC, USA were cut in 11 mm diameter discs. Non-treated (in text hydrophilic) Toray paper (type: TGP-H-060) was purchased from Toray Deutschland GmbH. To obtain hydrophobic Toray paper, non-treated Toray paper was immersed in 25.1% of polytetrafluuoroethylene (PTFE) emulsion for 60 min and after that dried in the oven at 90 °C.

2.2. Preparation of enzymatic electrodes

Enzymatic anodes were prepared by using the Vulcan-Gelatin procedure described previously by Ivanov et al. [16]. At first, 2% of gelatin solution in distillated water was prepared by heating the solution up to 37 °C in order that gelatin powder dissolves. After that, 20 mg of carbon nanoparticles, 10 mg of enzyme (GOx) and 10 mg of TTF mediator were suspended in 1 ml of gelatin solution (2%, 37 °C) and cast on the stainless steel supports with the geometrical surface areas of 0.28 cm^2 (for applications in the half-cell) or 1 cm^2 (for use in the reactor). The electrodes were then cross linked by dipping for 60 s in the solution of 5 % glutaraldehyde. Finally, cross-linked electrodes were rinsed with plenty of distilled water, left to dry at room temperature and stored in the fridge at -18 °C before further use. Enzymatic cathodes were prepared following two different procedures. One procedure was similar to the already described Vulcan-Gelatin procedure, with the exception that instead of pure GOx, a mixture of GOx and HRP with the optimized ratio of 1:3 was applied. The second procedure was similar to the Vulcan-PVDF procedure reported by Varnicic et al. [17]. According to this procedure, Vulcan nanomaterial was suspended in 0.25% solution of PVDF in 1-methyle-2-pyrrolidone. The ink was then cast on the spectroscopically pure graphite support (SPG) with 0.28 cm^2 geometrical surface area (for half-cell experiments) or Toray paper with 1 cm^2 (for reactor experiments). The prepared electrodes were dried at 60 °C. After drying and cooling down the electrodes to room temperature, the enzyme solution of GOx and HRP in 0.1 M phosphate buffer (1:3) was put and left to adsorb with different adsorption time (2 h or 18 h at 4 °C). Subsequently, the prepared electrodes were rinsed with buffer and were ready for electrochemical measurements.

2.3. Electroenzymatic reactor

The used electrochemical reactor was a membrane-less, flow-through device. Enzymatic anode and cathode were separated by a single channel of 3 mm width. The reactor was mounted vertically in an appropriate holder and glucose solution was recirculated from well-mixed reservoir (V_r = 70 ml) with a flow rate of 10 ml min^{-1}. Oxygen was supplied to the cathode side from the gas phase (flow rate ca. 500 ml min^{-1}). On the cathode side, a double layer of Toray paper was implemented. One layer was hydrophilic and it was serving as a support for the catalyst layer. The second layer was hydrophobic. It served as a gas diffusion layer and was directly contacted with the graphite flow field. The scheme of the electroenzymatic reactor is shown in Fig. 1. The glucose concentration was 20 mM. All reactor experiments were performed at pH 6.0 in 0.1 M phosphate buffer at room temperature.
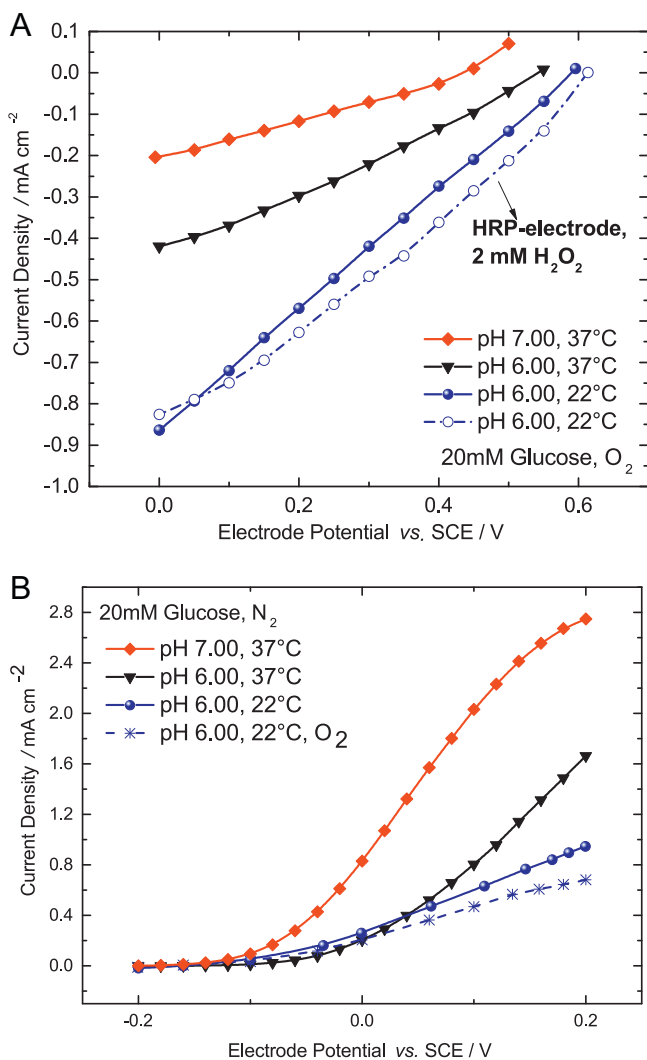

Fig. 2. Steady state performances of a) enzymatic cathode (GOx-HRP or HRP) and b) enzymatic anode (GOx/TTF) at two different pH and temperatures. Conditions: half-cell measurements, enzyme immobilization: cathode, Vulcan-PVDF; anode, Vulcan-Gelatin, rotation rate: 400 rpm.
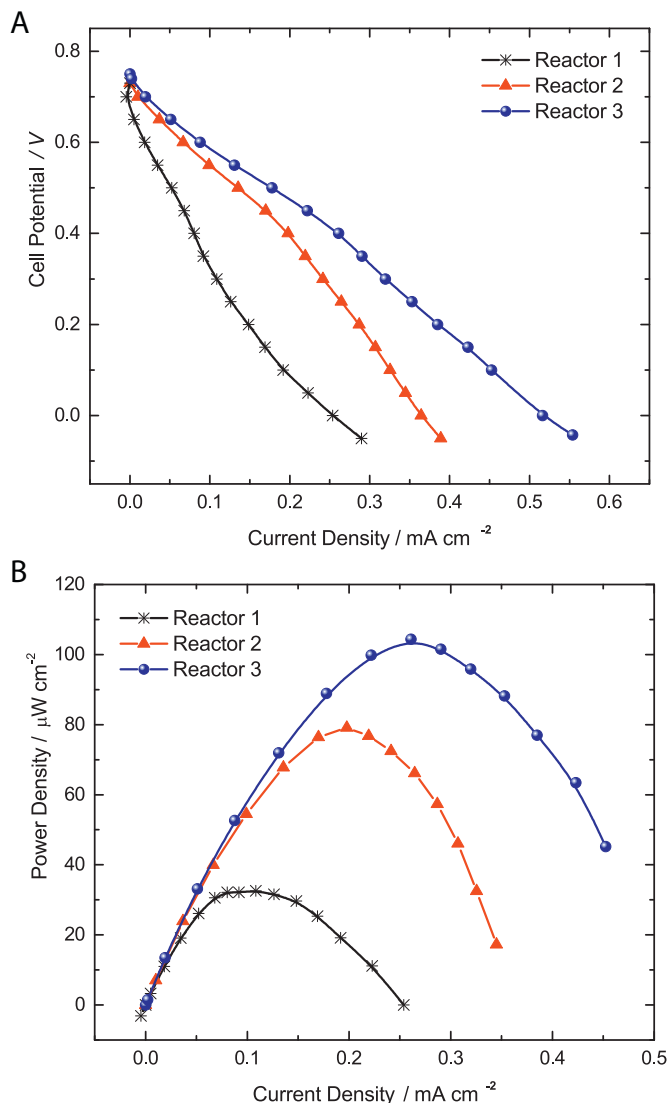
Table 2
Vulcan and enzyme loadings of enzymatic cathodes.

System	Vulcan Loading/mg cm^{-2}	Enzyme Loading (adsorption time) / h
Reactor 1	2	2
Reactor 2	4	2
Reactor 3	4	18

Fig. 3. a) Polarization and b) power curves of electroenzymatic reactors employing GOx/TTF anode and GOx-HRP cathodes; Conditions: enzyme immobilization: cathode, Vulcan-PVDF; anode, Vulcan-Gelatin, 20 mM glucose in 0.1 M phosphate buffer, 10 ml min^{-1} flow rate, O$_2$ supply from the gas phase, pH 6.00, 22 °C, volume of the glucose reservoir: 70 ml.

2.4. Measurements

Electrochemical half-cell and reactor tests were performed using the Autolab potentiostat PGSTAT302 (Eco Chemie). The reactor was connected as a 2-electrode system to the potentiostat. The anode and cathode potentials were monitored under operating conditions with the help of external voltmeters connected to the RE. Half-cell experiments were carried out in the 3-electrode configuration with a rotating disc electrode (RDE, Radiometer Analytical, model ED101). Enzymatic electrodes were used as working, Pt as counter and saturated calomel electrode (SCE) as reference electrode. All experiments were performed in 20 mM glucose in 0.1 M phosphate buffer prepared at least one day before starting the measurements. The experiments were performed at pH 6 or 7 and room temperature or T = 37 °C. Steady state polarization data were extracted from chronopotentiostatic measurements by taking the current value after 120 s at each constant potential value.

The glucose concentration was measured spectrophotometrically (UV/Vis spectrophotometer, SPECORD S600, Analytikjena,

Jena, Germany) using glucose assay kits (UV-test, R-Biopharm, Darmstadt, Germany). Every hour a small aliquot was taken from the glucose reservoir in order to control the glucose concentration.

3. Results and Discussion

3.1. Electrode preparation procedure and operating conditions

In our previous publication [17] two procedures for the preparation of enzymatic electrodes were described. In one of these, gelatin was used as a binder and electrodes were cross-linked, while in the other procedure PVDF was the binder and enzymes were only adsorbed on the surface without cross-linking. In case of HRP, the PVDF procedure without cross-linking resulted in electrodes of better performances than the gelatin procedure. It was observed that cross-linking forms enzyme agglomerates, decreasing the number of enzymes in contact with electron conductive surface, leading finally to a decrease of the activity [17]. It can be expected that this problem will always occur for Direct Electron Transfer (DET) enzymes. Since the cathode (GOx-HRP) in the present set-up relies upon DET, one can expect that the Vulcan-PVDF procedure will be more advantageous than the Vulcan-Gelatin procedure. Indeed, this has been confirmed (please see Supporting information, Fig. S1), which motivated the use of the Vulcan-PVDF procedure for the preparation of the enzymatic cathode in the present work. Up to now, the GOx-HRP combination has been mainly studied for biosensor applications where emphasis was on the electrode sensitivity and not on the utilization of high glucose concentrations and electrode performance in terms of current densities [18–20]. In the present case, optimized GOx-HRP electrode at 20 mM glucose can reach current densities of up to 0.9 mA cm^{-2}, which is comparable with performances reported for laccase or bilirubin oxidase enzymatic electrodes used in enzymatic fuel cell application (taking into account that 2 instead of 4 electrons are exchanged in the fuel cell case) [21–25]. The enzymatic cathode comprising the GOx-HRP cascade has similar performance as the HRP cathode prepared with the same procedure in the presence of 2 mM hydrogen peroxide (Fig. 2a). For the enzymatic anode, it was shown that in both procedures similar limiting currents can be reached, while the Vulcan-Gelatin procedure shows more negative onset potentials compared to the Vulcan-PVDF procedure (please see Fig. S2 in
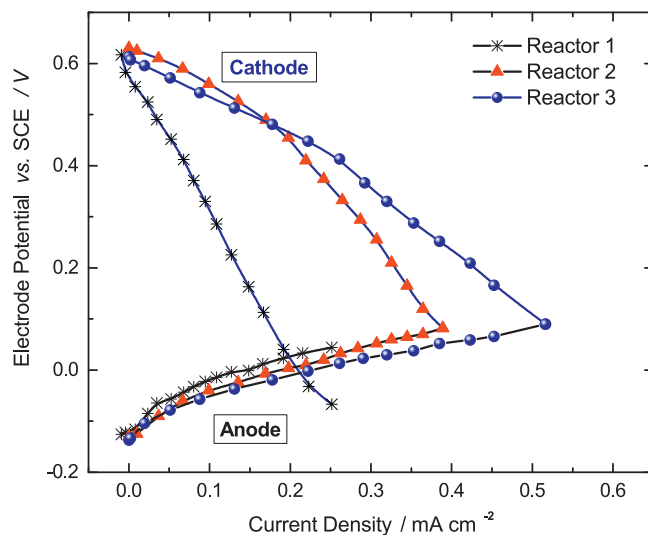

Fig. 4. Steady state performances of enzymatic cathode (GOx-HRP) and enzymatic anode (GOx/TTF) under operations conditions in enzymatic reactor. Conditions as in Fig. 3.

Supporting information). Based on this experience, the Vulcan-Gelatin procedure has been chosen for preparation of the enzymatic anode in the reactor.

After the electrode preparation procedures was establihsed, operating conditions (pH and temperature) in the reactor were investigated. These conditions largely depend on the optimal pH level and temperature at which enzymatic catalysts show their optimal activity. According to the literature, optimal conditions for GOx are pH 5.0 to 8.0 and a temperature of T = 37 °C [26–29], while for HRP pH 6.0 to 7.0 and T = 22 °C were found to be optimal [30–32]. The dependency of these conditions on the enzyme immobilization procedure can be seen in Fig. 2. The results show different optima for anode and cathode sides (pH 7 and T = 37 °C on the anode side; pH 6 and T = 22 °C on the cathode side). As seen in Fig. 2, changing of pH and temperature can also influence the onset electrode potential. For optimal cathode conditions, peroxide reduction starts at 0.6 V vs. SCE which corresponds well to the literature value for peroxide reduction on HRP-loaded graphite electrodes [33]. The onset potential of enzymatic electrode with the mediator TTF is around -0.15 V vs. SCE which is slightly more negative than the onset potential of other electrodes using TTF as mediator (around -0.1 V vs. SCE) [34,35]. The membrane-less reactor configuration in the present work requires a compromise regarding pH, temperature and composition of the electrolyte. In the present case, lower pH and temperature were chosen since the whole system is limited electrochemically by the cathode. Regarding the composition of the electrolyte, the main issue is the presence of oxygen which, as natural electron acceptor for GOx, competes with TTF as electron acceptor on the anode side (Fig. 2b). This reduces the achievable current level in the system, since part of the electronic current is lost. But this phenomenon does not influence the conversion of glucose. Still some hydrogen peroxide evolves on the anode side, which possibly decreases the anode stability. There are several approaches to tackle this issue. First, the impact of oxygen is more pronounced at more positive over-potentials (Fig. 2b), which means that careful selection of the operating potential of the anode can reduce this problem. Second, in the present reactor configuration oxygen can be supplied a) only from the gas phase, b) from the gas phase and from the solution, or c) only from the solution (Fig. 1). In the following experiments oxygen supply only from the gas phase through gas diffusion layer was applied. In this way, merely non-reacted oxygen on the cathode side might reach the anode side and react there.

3.2. Investigation of electroenzymatic reactor performance

Electroenzymatic reactor in the present work has similarities with the previously reported fuel cell device reported by Ivanov et al. [17]. Moreover, the new electroenzymatic reactor was equipped with a reference electrode in order to monitor (and control) electrode potentials under operating conditions. This enabled both the voltastatic and the potentiostatic mode of operation. The influence of the structural parameters on the electrochemical performance of the enzymatic reactor and glucose conversion was investigated in detail. As structural parameters the enzyme and Vulcan nanoparticle loadings on the cathode side were varied, while the parameters of the enzymatic anode were kept constant.

3.2.1. Electrochemical performance

Two cathode structural parameters were changed: a) Vulcan loading, and b) enzyme loading (Table 2). The Vulcan loading determines the available surface area for catalyst adsorption, electrochemical surface reactions and charge transfer. Loadings of 2 and 4 mg cm^{-2} were tested. The further increase of the loading was not possible due to mechanical instability of the electrode. The
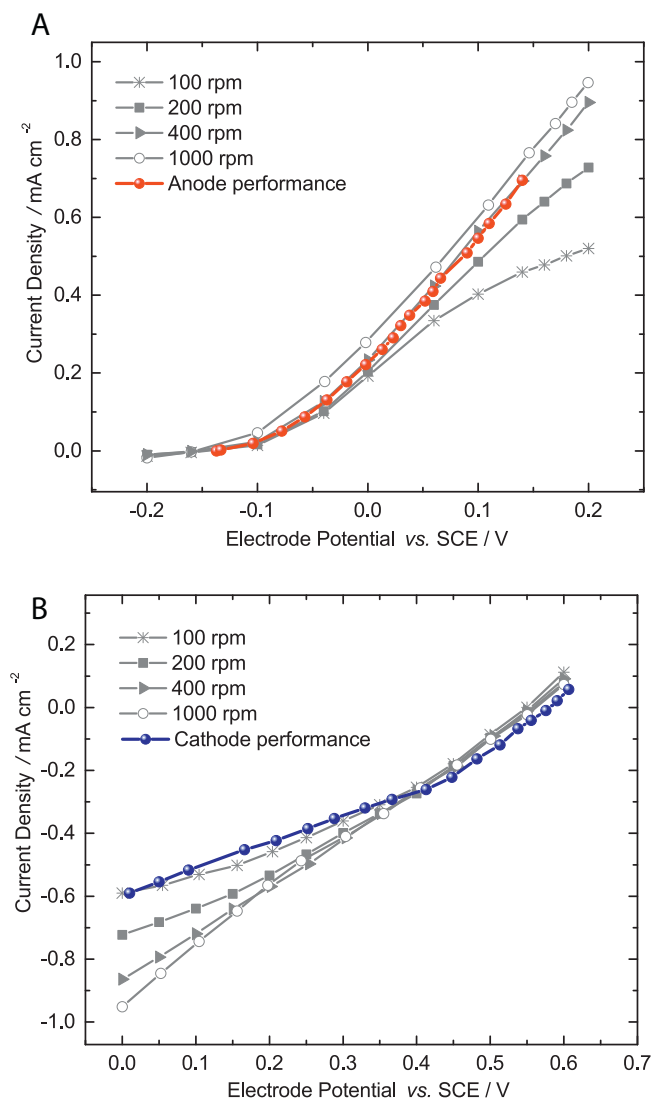

Fig. 5. Comparison between steady state performances of a) enzymatic anode (GOx/TTF) and b) enzymatic cathode (GOx/HRP) tested in half-cell and electroenzymatic reactor. Conditions: enzyme immobilization: cathode, Vulcan-PVDF; anode, Vulcan-Gelatin, 20 mM glucose in 0.1 M phosphate buffer, pH 6.00, 22 °C. Flow rates: 10 ml min^{-1} for glucose solution, O$_2$ supply from the gas phase in the reactor; rotation rates between 100 and 1000 rpm in the half-cell.

enzyme loading was varied by changing the adsorption time between 2 and 18 h. After 18 h, saturation conditions were reached and the electrode activity was not further changing. The obtained polarization and power density curves of the electroenzymatic reactors employing different cathodes are presented in Fig. 3. As can be seen, the open circuit cell potential was around 0.75 V. This value was found to be independent on Vulcan and enzyme loadings, and this is in good correlation to the value obtained at open circuit potentials of single electrodes (-0.15 V and 0.6 V vs. SCE, for anode and cathode, respectively). Different open-circuit cell potentials were reported in the literature for other glucose/oxygen biofuel cells. This depends mainly on the choice of enzymes used for the cathode side (typically BOD or laccase), and on the choice of the mediator used for GOx regeneration on the anode. The reported values in literature range from 0.45 V for the fuel cell following similar idea as in the present paper but, with phenanthroline as GOx mediator [36] to 0.9 V for the Osmium redox hydrogels as GOx mediator [37,38]. In general, the investigated electrochemical cell shows a high open circuit cell
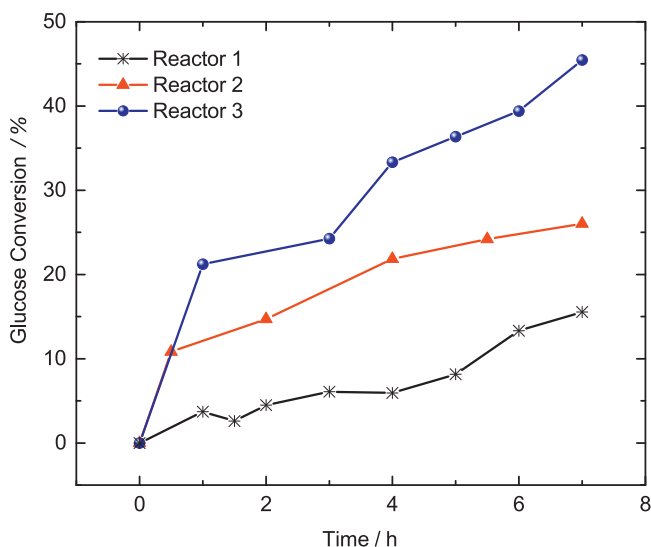
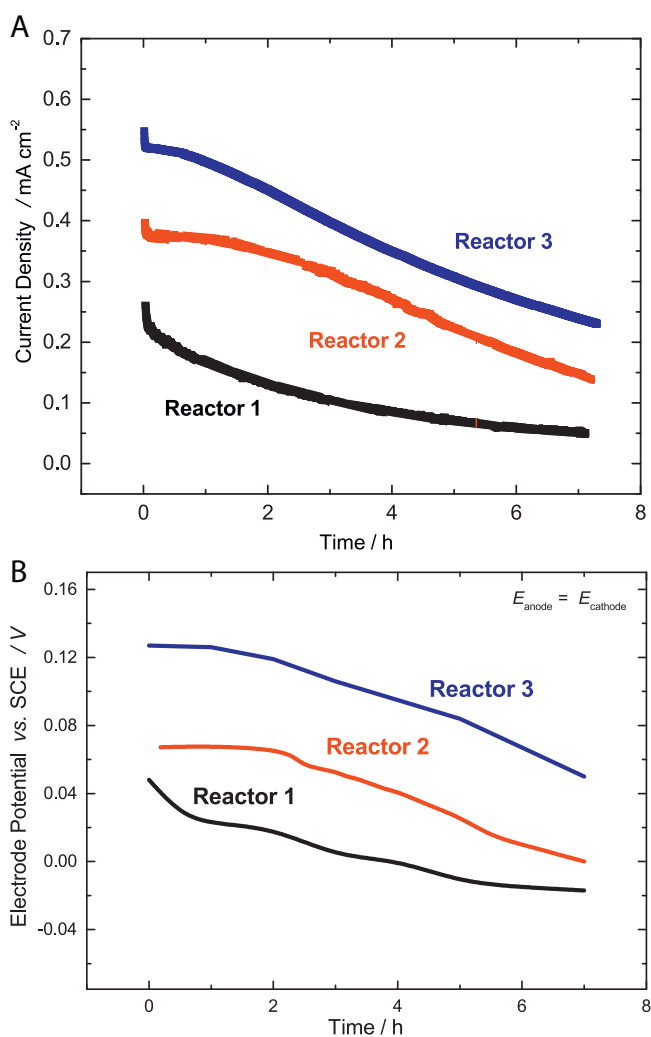**Fig. 6.** Glucose conversion during 7 h in electroenzymatic reactors.

Fig. 7. a) Current density change during 7 h of reactor operation under voltastatic conditions (U_{cell} = 0.0 V) and b) change of anode and cathode electrode potentials during reactors operation (for further explanations please see the text).

potential. As can be seen in Fig. 3, the increase of Vulcan and enzyme loadings improves the performance of the fuel cell

significantly, both in terms of current density and power output (from ca. $300\,\mu A\,cm^{-2}$ to ca. $600\,\mu A\,cm^{-2}$ and ca. 30 to $100\,\mu W\,cm^{-2}$, respectively). The power density of the here presented Reactor 3 can be compared to other glucose/oxygen fuel cells based on GOx and BOD or laccase as cathode [39–44]. The performance of our reactor is superior compared to the enzymatic fuel cell with the same combination of enzymes and a maximum power density of around $5\,\mu W\,cm^{-2}$ for 20 mM glucose solution [36]. But this power level is clearly below the performance of the so far reported best performance of enzymatic fuel cells [45].

The presence of the reference electrode in the present set-up enables to distinguish between losses on cathode and anode sides separately. As can be seen in Fig. 4 the overpotential on the cathode side is more significant than on the anode side, with the cathode limiting the performance of the whole fuel cell. The increase of the Vulcan loading (from 2 to $4\,mg\,cm^{-2}$) between Reactors 1 and 2 causes a significant decrease of the cathodic overpotential at the same current density. This allows much higher current densities to be reached. In these experiments the enzyme adsorption time was kept constant, but one can expect a higher enzyme loading in Reactor 2 than in the Reactor 1, due to higher available surface area for the adsorption. The difference between Reactor 2 and 3 is in enzyme adsorption time on the cathode side, which reflects the higher enzyme loading. It can be seen that at lower overpotential, the cathode in Reactor 2 performs a bit better than in Reactor 3, while at higher overpotential, the cathode with higher enzyme loading performs better. This can be as an indication for HRP inhibition in Reactor 3 at low overpotentials due to mismatch between the production and consumption rates of hydrogen peroxide (reaction C2 in Fig. 1; reaction C3 in Fig. 1). While the former reaction is influenced only by the enzyme loading, species concentration and flow conditions, the latter one can be accelerated electrochemically via higher currents in Reactor 3 at more negative overpotentials than in Reactor 2 [9].

At the same time, the enzymatic anode shows a moderate decrease of the overpotential between Reactors 1, 2 and 3 (Fig. 4). Although these differences can be due to deviations between single experiments, this change appears to be not a random effect, but a clear trend. A possible reason for this increase of the anode overpotential can be the presence of oxygen in the solution. Oxygen is a natural electron acceptor for GOx and thus it competes with TTF for electrons, causing a decrease of the anode current in the presence of oxygen i.e. an increase of anode overpotential at the same current density. As already discussed, in all experiments oxygen was supplied from the gas phase and it was initially not present in the liquid phase. The amount of oxygen in the liquid phase is governed by the interplay of oxygen supply to the cathode catalyst layer, oxygen consumption by the enzymatic reaction and diffusion of non-reacted oxygen away from the catalyst layer. Due to concentration gradients, one can expect that non-reacted oxygen will diffuse out to the liquid phase. If convection-diffusion conditions in the liquid phase allow it, oxygen can finally reach the anode and react there enzymatically. The amount of oxygen reaching the anode for the same flow conditions in the gas and liquid phase is mainly influenced by the properties of the cathode catalyst layer, i.e. basically by oxygen consumption in the catalyst layer. The results in Fig. 4 indicate higher oxygen consumption in Reactor 3 compared to Reactor 1, suggesting a lower influence of oxygen cross-over in Reactor 3 than in the Reactor 1.

While it was reported that the performance of enzymatic electrodes tested in the 3- and 2-electrode set-ups can differ significantly (e.g. BOD-cathode reached $5\,mA\,cm^{-2}$ in the 3-electrode set-up, but only $200\,\mu W\,cm^{-2}$ in the 2-electrode set up in presence of 50 mM glucose and at 37 °C and pH 7.2 [39]), no significant difference was observed in the present study. To assure direct comparison, the performance of anode and cathode in the 2-
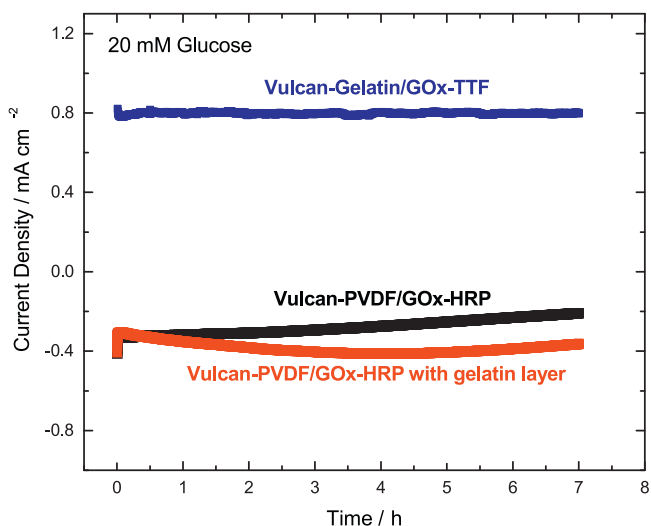
Fig. 8. Performances of enzymatic electrodes during 7 h of testing. Conditions: half-cell measurements, enzyme immobilization: cathode, Vulcan-PVDF; anode, Vulcan-Gelatin, 20 mM glucose in 0.1 M phosphate buffer, pH 6.00, 22 °C, rotation rates 400 rpm, potential of the electrodes: 0.15 V vs. SCE.

Table 3
Glucose conversion after 7 h in different reactors.

System	Total Conversion / %	Electrochemical part of conversion / %	Enzymatic part of conversion / %
Reactor 1	16	14	86
Reactor 2	30	19	81
Reactor 3	47	17	83

electrode set-up (Reactor 3) was plotted against the anode and cathode being characterized separately in the 3-electrode set-up (Fig. 5). The electrodes were always prepared via the same procedure. The experimental data indicate no significant scaling issues (0.28 and 1 cm² for 3- and 2-electrode set-up, respectively). Some differences can be explained by different flow conditions applied in the two different set-ups (rotating disc electrode in 3-electrode set-up, compared to flow-through reactor in the 2-electrode set-up).

3.2.2. Glucose conversion

The glucose concentration over time of electrolysis has been followed by taking a sample every hour and by determining glucose concentration with a help of assay kits. The conversion has been calculated as the ration of the converted amount of glucose to amount of glucose at the beginning of electrolysis. The glucose conversions during 7 h of operation in the electroenzymatic reactor under voltastatic conditions ($U_{cell} = 0.0\,V$) are shown in Fig. 6. The cumulative conversion increases from 16% (Reactor 1) to 47% (Reactor 3). One obvious reason for this finding is an improved enzymatic cathode which allows the reactor to operate at higher current density. The change of cell currents during voltastatic operation is shown in Fig 7a, while the change of electrode potentials is given in Fig. 7b. As can be seen, Reactor 3 operates at higher current densities than Reactors 1 and 2, which is also reflected by higher glucose conversion. The enzymatic anode in the Reactor 3 exerts higher overpotentials than the anodes in Reactors 1 and 2. Since the operating cell potential in all cases was $U_{cell} = 0$, the cathode and anode potentials are identical (Fig. 7b). The progress of anode and cathode overpotentials goes into different directions with the anode overpotential decreasing over time and the cathode overpotential increasing. This might be an indication

that the cathode performance deteriorates over time. To check this, anode and cathode were investigated in a differential reactor (to avoid the effect of glucose concentration variation in the batch reactor). The results in Fig. 8 show that the enzymatic anode is indeed very stable, while the enzymatic cathode shows a decrease of activity of ca. 25% over time. This loss can be attributed to the above mentioned enzyme inhibition effect or the leaching out of enzymes. In the present case, it seems that the leaching out effect dominates since the formation of gelatin film on the top of enzymatic cathode resulted in almost no loss of activity during the same time (Fig. 8).

In electrochemical systems the reactant conversion can be calculated from the electric charge passed into the reactor during a certain time, by use of Faraday's law. For this calculation a certain current efficiency for a single reaction has to be assumed. Presuming 100% current efficiency for glucose conversion, electrochemical glucose conversion has been calculated from electrical charge passed during 7 h of operation (obtained by integration of curves in Fig. 7a) and by knowing the number of exchanged electrons (2). This number has been further multiplied by 2, accounting for an glucose conversion caused by cathodic reaction. The results are shown in Table 3 in terms of the percentage of glucose converted electrochemically. Obviously, only a small part of the cumulative conversion is purely electrochemical; the larger part is probably enzymatic. It can be expected that the pure enzymatic conversion mainly takes place on the cathode side and that only a small part of this conversion takes place on the anode side. Such large enzymatic conversion on the cathode side indicates the formation of a large amount of hydrogen peroxide at the cathode side which is not further utilized by the HRP enzyme. Having the distractive nature of this by-product in mind, this issue should be studied in more detail in future. The first tests (Fig. 8) indicate no significant degradation during 7 h of operation.

3.2.3. Comparison with literature data

As already discussed, all electroenzymatic reactors proposed so far for gluconic acid production need external energy input. It can also be seen in Table 1 that the operating conditions in these reactors were very different, having different total reaction volumes, concentrations, time of electrolysis, geometry of electrodes and conversions. It is clear that the glucose conversion is dependent on the surface area of electrodes, the total volume of the reaction solution and the operation time. In order to compare data from different experimental set-ups, these parameters are to be combined to calculate the space time yield of the reactor, i.e the mass of gluconic acid produced per unit time and per unit geometric area of the electrode ($g_{gluconicacid}\,h^{-1}\,cm^{-2}$) (Table 1). Since all listed processes are batch or semi-batch systems, the mass of product was calculated based on the total volume in the system, cumulative conversion and initial concentration of glucose. The surface area is based on the geometrical surface area and the time corresponds to the total time of electrolysis. The calculated space time yield values are listed in Table 1. As can be seen, the best process based on this analysis is not related to the highest conversion achieved. Compared to other processes, the performance of Reactor 3 (Table 3) is excellent. It indicates a high potential of this reactor concept for the future development of a new biotechnological process for the electroenzymatic production of gluconic acid from glucose.

4. Conclusions

In the present work, the feasibility of the proposed electro-enzymatic reactor for gluconic acid synthesis, operated in chemical-energy co-generation mode, is demonstrated. The membrane-less reactor design enables utilization of a single

electrolyte, thereby simplifying the design and reducing the costs of the reactor. On the other hand, optimal reactor operation requires a compromise regarding pH and temperature level, which are chosen such that the conditions are optimized for the less active enzyme (HRP in the present case). It has been shown that the immobilization technique of enzymes plays an important role for optimal reactor performance. In case of DET enzymes physical adsorption of enzymes without cross-linking should be preferred. The resulting electrodes are more active, but they suffer from lower long-term stability. It has been shown that the formation of a gelatin film on top of such electrodes improves their stability without decreasing the electrode activity. The Vulcan-Gelatin procedure used for the preparation of enzymatic anodes resulted in enzymatic electrodes of excellent activity and stability over the tested time period. A glucose conversion of 47% during 7 h batch runtime has been achieved after optimizing the cathode structural parameters. The level of conversion depends on system parameters such as electrode surface area, total reaction volume and glucose concentration, as well as operation parameters like time of electrolysis and mode of operation (potentiostatic, voltastatic or galvanostatic). Careful adjustment of these parameters can result in higher conversion values, which will be reported in our next publication. It has been shown that the major part of this conversion can be attributed to the enzymatic pathway, while the smaller part is electroenzymatic. In comparison to literature data, the proposed reactor shows high potential for the development of an industrial electroenzymatic process for gluconic acid production.

Acknowledgements

Appendix A. Supplementary data

Supplementary data associated with this article can be found, in the online version, at http://dx.doi.org/10.1016/j.electacta.2015.05.151.

References

[1] T. Krieg, A. Sydow, U. Schroeder, J. Schrader, D. Holtmann, Trends in Biotechnology 32 (2014) 645–655.
[2] C. Kohlmann, W. Märkle, S. Lütz, Journal of Molecular Catalysis B: Enzymatic 51 (2008) 57–72.
[3] R. Devaux-Basséguy, P. Gros, A. Bergel, Journal of Chemical Technology & Biotechnology 68 (1997) 389–396.
[4] I. Dencic, J. Meuldijk, D.M. Croon, V. Hessel, Journal of Flow Chemistry 1 (2011) 13–23.
[5] S. Anastassiadis, I.G. Morgunov, Recent Patents on Biotechnology 1 (2007) 167–180.
[6] S. Ramachandran, P. Fontanille, A. Pandey, C. Larroche, Food Technology and Biotechnology 44 (2006) 185–195.
[7] D.Y. Murzin, R. Leino, Chemical Engineering Research & Design 86 (2008) 1002–1010.
[8] C. Bourdillon, R. Lortie, J.M. Laval, Biotechnology and Bioengineering 31 (1988) 553–558.
[9] R. Basséguy, K. Délécouls-Servat, A. Bergel, Bioprocess and Biosystems Engineering 26 (2004) 165–168.
[10] J.M. Obón, P. Casanova, A. Manjón, V.M. Fernández, J.L. Iborra, Biotechnology Progress 13 (1997) 557–561.
[11] A. Manjón, J.M. Obón, P. Casanova, V.M. Fernández, J.L. Ilborra, Biotechnology Letters 24 (2002) 1227–1232.
[12] P. Gros, A. Bergel, AIChE Journal 51 (2005) 989–997.
[13] O. Miyawaki, T. Yano, Enzyme and Microbial Technology 15 (1993) 525–529.
[14] R. Wichmann, D. Vasic-Racki, Cofactor regeneration at the lab scale, in: Technology Transfer in Biotechnology: From Lab to Industry to Production, 2005, pp. 225-260.
[15] W. Liu, P. Wang, Biotechnology Advances 25 (2007) 369–384.
[16] I. Ivanov, T. Vidakovic-Koch, K. Sundmacher, Journal of Electroanalytical Chemistry 690 (2013) 68–73.
[17] M. Varnicic, K. Bettenbrock, D. Hermsdorf, T. Vidakovic-Koch, K. Sundmacher, RSC Advances 4 (2014) 36471–36479.
[18] Y.L. Yao, K.K. Shiu, Electroanalysis 20 (2008) 2090–2095.
[19] L. Zhu, R. Yang, J. Zhai, C. Tian, Biosensors and Bioelectronics 23 (2007) 528–535.
[20] E. Csoregi, L. Gorton, G. Markovarga, Electroanalysis 6 (1994) 925–933.
[21] J. Filip, J. Sefcovicova, P. Gemeiner, J. Tkac, Electrochimica Acta 87 (2013) 366–374.
[22] C.F. Blanford, R.S. Heath, F.A. Armstrong, Chem. Commun. (2007) 1710.
[23] S. Tsujimura, Y. Kamitaka, K. Kano, Fuel Cells 7 (2007) 463–469.
[24] A. Habrioux, T. Napporn, K. Servat, S. Tingry, K.B. Kokoh, Electrochimica Acta 55 (2010) 7701–7705.
[25] L. Hussein, S. Rubenwolf, F. von Stetten, G. Urban, R. Zengerle, M. Krueger, S. Kerzenmacher, Biosensors & Bioelectronics 26 (2011) 4133–4138.
[26] M. Snejdarkova, M. Rehak, M. Otto, Analytical Chemistry 65 (1993) 665–668.
[27] W.J. Sung, Y.H. Bae, Analytical Chemistry 72 (2000) 2177–2181.
[28] W. Zhao, J.J. Xu, C.G. Shi, H.Y. Chen, Langmuir 21 (2005) 9630–9634.
[29] B.F.Y. Yonhin, M. Smolander, T. Crompton, C.R. Lowe, Analytical Chemistry 65 (1993) 2067–2071.
[30] S. Yang, W.-Z. Jia, Q.-Y. Qian, Y.-G. Zhou, X.-H. Xia, Analytical Chemistry 81 (2009) 3478–3484.
[31] R. Andreu, E.E. Ferapontova, L. Gorton, J.J. Calvente, Journal of Physical Chemistry B 111 (2007) 469–477.
[32] T. Ruzgas, E. Csoregi, J. Emneus, L. Gorton, G. MarkoVarga, Analytica Chimica Acta 330 (1996) 123–138.
[33] E.E. Ferapontova, Electroanalysis 16 (2004) 1101–1112.
[34] E. Nazaruk, K. Sadowska, J.F. Biernat, J. Rogalski, G. Ginalska, R. Bilewicz, Analytical and Bioanalytical Chemistry 398 (2010) 1651–1660.
[35] B. Kowalewska, P.J. Kulesza, Electroanalysis 21 (2009) 351–359.
[36] V. Krikstolaityte, Y. Oztekin, J. Kuliesius, A. Ramanaviciene, Z. Yazicigil, M. Ersoz, A. Okumus, A. Kausaite-Minkstimiene, Z. Kilic, A.O. Solak, A. Makaraviciute, A. Ramanavicius, Electroanalysis 25 (2013) 2677–2683.
[37] V. Soukharev, N. Mano, A. Heller, Journal of the American Chemical Society 126 (2004) 8368–8369.
[38] N. Mano, F. Mao, W. Shin, T. Chen, A. Heller, Chemical Communications (2003) 518–519.
[39] V. Flexer, N. Brun, M. Destribats, R. Backov, N. Mano, Physical Chemistry Chemical Physics 15 (2013) 6437–6445.
[40] I. Ivanov, T. Vidakovic-Koch, K. Sundmacher, Journal of Power Sources 196 (2011) 9260–9269.
[41] R.C. Reid, F. Giroud, S.D. Minteer, B.K. Gale, Journal of the Electrochemical Society 160 (2013) H612–H619.
[42] K. MacVittie, J. Halamek, L. Halamkova, M. Southcott, W.D. Jemison, R. Lobel, E. Katz, Energy & Environmental Science 6 (2013) 81–86.
[43] A. Zebda, L. Renaud, M. Cretin, F. Pichot, C. Innocent, R. Ferrigno, S. Tingry, Electrochemistry Communications 11 (2009) 592–595.
[44] M. Southcott, K. MacVittie, J. Halamek, L. Halamek, W.D. Jemison, R. Lobel, E. Katz, Physical Chemistry Chemical Physics 15 (2013) 6278–6283.
[45] A. Zebda, C. Gondran, A. Le Goff, M. Holzinger, P. Cinquin, S. Cosnier, Nature Communications 2 (2011) .
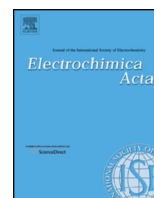
Corrigendum to "Gluconic Acid Synthesis in an Electroenzymatic Reactor" [Electrochimica Acta 174 (2015) 480-487]

M. Varničić [a], T. Vidaković-Koch [a,*], K. Sundmacher [a,b]

[a] Max Planck Institute for Dynamics of Complex Technical Systems, Sandtorstraße 1, D-39106 Magdeburg, Germany
[b] Otto-von-Guericke University Magdeburg, Process Systems Engineering, Universitätsplatz 2, D-39106 Magdeburg, Germany

Table 1

System	Enzyme	Enzyme Immobilization	Electron transfer	Electrode surface area /cm^2	Volume /cm^3	Glucose concentration/mM	Time/h	Glucose Conversion/%	STY /mg h^{-1} cm^{-2}	Ref.
Membrane (Nafion)	GDH	In solution	direct	24	28	10	12	85	0.16	[10]
Membrane (Nafion)	GDH	Covalent attachment	Mediated (3,4 – DHB)	24	28	100	4	60	3.43	[11]
Membrane (Dialysis)	GOx	Entrapment in dialysis membrane	Mediated (O$_2$)	30	44	248	3	30	7.13	[9]
Batch	GOx	In polypyrrole film	Mediated (O$_2$)	3.14	10	20	8	62	0.97	[12]
RDE system	G6PDH	Covalent attachment	Mediated (PMS)	19.6	200	9.3	6	43	1.33	[13]
Membrane-less	GOx	3-D electrode	Mediated (TTF, O$_2$)	1	70	20	7	47	18.2	This Work

Abbreviations: GDH - glucose dehydrogenase, G6PDH - glucose-6-phosphat-dehydrogenase, GOx – glucose oxidase, NAD - nicotinamide adenine dinucleotide, NADP - nicotinamide adenine dinucleotide phosphate, TTF – Tetrathiafulvalene, 3,4 – DHB- 3,4-dihydroxybenzaldehyde, PMS- phenazine methosulfate

The authors regret that the space time yield of the gluconic acid throughout the paper appeared in units of **g h^{-1} cm^{-2}** instead of in the units of **mg h^{-1} cm^{-2}**. This error is present inResearch Highlights, Abstract, Table 1 and on page 486 (Section 3.2.3). The correct way is as follows:

In the Research Highlights:
The space time yield of reactor at glucose conversion of 47% was 18.2 **mg h^{-1} cm^{-2}**.

In the Abstract:
The space time yield of gluconic acid achieved at a glucose conversion of 47% was 18.2 **mg h^{-1} cm^{-2}**.

And on Page 486 (Section 3.2.3):
In order to compare data from different experimental set-ups, these parameters are to be combined to calculate the space time yield of the reactor, i.e the mass of gluconic acid produced per unit time and per unit geometric area of the electrode (**mg$_{gluconic\ acid}$ h^{-1} cm^{-2}**) (Table 1).

The authors would like to apologise for any inconvenience caused.

[TVK10]

T. Q. N. Do, M. Varničić, R. Flassig, T. T. Vidaković-Koch, K. Sundmacher

Dynamic and steady state 1-D model of mediated electron transfer in a porous enzymatic electrode

Dynamic and steady state 1-D model of mediated electron transfer in a porous enzymatic electrode

T.Q.N. Do [a], M. Varničić [a], R.J. Flassig [a], T. Vidaković-Koch [a,*], K. Sundmacher [a,b]

[a] Max Planck Institute for Dynamics of Complex Technical Systems, Sandtorstraße 1, D-39106 Magdeburg, Germany
[b] Otto-von-Guericke University Magdeburg, Process Systems Engineering, Universitätsplatz 2, D-39106 Magdeburg, Germany

A B S T R A C T

A 1-D mathematical model of a porous enzymatic electrode exhibiting the mediated electron transfer (MET) mechanism has been developed. As a model system, glucose oxidation catalyzed by immobilized glucose oxidase (GOx) in the presence of a co-immobilized tetrathiafulvalene (TTF) mediator in the porous electrode matrix has been selected. The balance equations for potential fields in the electron- and ion-conducting phases as well as concentration field have been formulated, solved numerically and validated experimentally under steady state conditions. The relevant kinetic parameters of the lumped reaction kinetics have been obtained by global optimization. The confidence intervals (CIs) of each parameter have been extracted from the respective likelihood. The parameter study has shown that the parameters related to mediator consumption/regeneration steps can be responsible for the shift of the reaction onset potential. Additionally, the model has shown that diffusion of the oxidized mediator out of the catalyst layer (CL) plays a significant role only at more positive potentials and low glucose concentrations. Only concentration profiles in different layers influence the electrode performance while other state fields like potential distributions in different phases have no impact on the performance. The concentration profiles reveal that all electrodes work through; the observed limiting currents are diffusion–reaction limiting. The normalized electrode activity decreases with an increase of enzyme loading. According to the model, the reason for this observation is glucose depletion along the CL at higher enzyme loadings. Comparison with experiments advices a decrease of enzyme utilization at higher enzyme loadings.

© 2015 Elsevier B.V. All rights reserved.

1. Introduction

In the last decade the interest in electroenzymatic processes increased significantly due to their applications in biosensors and in enzymatic fuel cells [1–2]. Apart from sensing and energy, further emerging application of electroenzymatic processes is in the field of chemical production [3–4]. This becomes of paramount importance having in mind a steady decrease in fossil resources and the necessity to develop new processes for production of commodities and fine chemicals. In this respect new biotechnological routes based on biomass are sought after, where electroenzymatic processes have great potential especially in the field of selective oxidation and reduction reactions [3–4].

Besides enzyme stability, one of major drawbacks on the way of broader utilization of electroenzymatic systems is the low activity of enzymatic electrodes. To increase current output per geometrical surface area, 3-D structuring is commonly considered [2,5]. This strategy in addition to enzymes, introduces also high-surface area electro-conductive materials, and often binders and mediators in the electrode structure, increasing the complexity of the whole system. Consequently, the

activity of such electrodes depends greatly on the interplay between different phenomena where mass transport of reactants, products and mediators, enzymatic and electrochemical reactions as well as ion and electron transports are the most important ones. To optimize such structures, in addition to experimental efforts, mathematical modeling can bring new significant insights pointing out major limitations in the system performance [6].

Although mathematical models are extensively used in modeling and optimization of traditional fuel cell electrodes [7–8], their applications in the field of enzymatic electrodes have not been broadly considered [6,8–11]. As we discussed in our previous publication [6], among different types of models, mascroscopic models are still more practical for comparison with typical experimental data in terms of current potential curves, than microscopic models. The macroscopic models can be roughly categorized in interface and distributed models [7]. While the interface models neglect the thickness of and the morphology of the electrode, the distributed models take into account the electrode structure [6–7]. In literature, the interface models prevail in analysis of enzymatic systems [12]. Typical examples are models of amperometric biosensors where enzymes are usually entrapped behind the dialysis membrane and the mediator is regenerated at an electrode surface [12–13]. This corresponds to a physical situation where either the

soluble mediator is regenerated on the flat electrode or the current collector is covered by a thin layer of a low soluble mediator [12–13]. If the thickness of the electrode itself cannot be disregarded, typically in the case of porous enzymatic electrodes, distributed electrode models are necessary in order to study the interplay between enzyme-electrode kinetics, mass and charge transfer limitations inside of the porous electrode on its performance. Some examples of distributed macroscopic models applied on enzymatic electrodes are the studies of Lyons [8], Baronas et al. [9], Barton [10], Chan et al. [11], and Do et al. [6]. A one dimensional (1-D) macroscopic porous electrode model considering additional microscale along cylindrical fibers where the enzymatic reaction takes place was developed by Barton [10] for a mediated enzyme-catalyzed oxygen cathode. Chan et al. [11] employed transient material balances along with steady-state charge balances for the electron- and ion-conducting phases, to study the dynamic behavior of a biofuel cell anode at high mediator concentrations. In their study the mediator was dissolved in the solution. The rate limiting process in different potential ranges was determined and the control of the potential range was recommended for the optimal electrode operation. In our previous publication [6], the full porous theory was developed to describe the porous enzymatic electrode with direct electron transfer (DET), using Horseradish Peroxidase (HRP) as a model enzyme. It was shown, that realistic description of the electrode performance at different concentrations and for the different electrode structures can be obtained only with a help of distributed model formulation. The mass transfer limitations and the low enzyme utilization, especially in electrode preparation procedures using cross-linking have been identified as main limiting processes.

In the present work the porous electrode model described in our previous publication [6], has been extended to the case of an enzymatic electrode with mediated electron transfer (MET). In the model, it was considered that both enzymes and mediators are immobilized. This case has high significance for practical applications in e.g. enzymatic reactors, since the efforts for product separation are significantly reduced compared to a situation, where enzymes and/or mediators are freely diffusive [4]. As a model system glucose oxidation catalyzed by glucose oxidase (GOx) has been chosen due to high practical relevance of this system for different bioelectrochemical applications (biosensors, enzymatic fuel cells, electroenzymatic reactors). GOx usually requires the use of a mediator for efficient enzyme regeneration [14]. Among different possibilities [19], tetrathiafulvalene (TTF) has been chosen as a mediator in the present work. TTF is normally combined with tetracyanoquinodimethane (TCNQ) forming a charge transfer complex (CTC) with near-metal conductivity at room temperature [15]. The unique properties of CTC have led to its utilization as electrode material in different applications. The electrochemical properties of CTC in different aqueous solutions have been for the first time studied by Jaeger and Bard [16]. This groundwork opened up the use of CTC in more specific applications, like bioelectrocatalytic ones. Pioneering works in this direction were done by Kulys and co-workers who studied the behavior of different enzymes in the presence of TCNQ and TCNQ organic salt complexes [17–18]. These works were followed by a number of publications focusing mainly on CTC properties as a mediator [2,12,19–20, 24–25]. Since the mechanism of CTC enzyme regeneration is still a bit controversial [19], TTF has been selected as a more appropriate mediator with respect to model purposes.

The balance equations for potential fields in the electron- and ion-conducting phases as well as the concentration field have been developed and solved numerically. The lumped kinetics has been selected to study the system under steady state conditions. The additional step of the 1-D model simplification to a reduced 1-D model has been performed to justify the necessity of distributed model formulation. The main goal of the present study is to get more insight into the interplay between enzymatic and mediator kinetics and mass-transfer processes inside of the porous electrode structure and to point out major limitations under different operating conditions. Due to influence of the interplay between kinetic and structural parameters on system response significant effort has been put into reliable parameter determination.

In the following, the mathematical model equations have been formulated for two modeling domains (catalyst layer (CL) and Nernstian diffusion layer (DL)) and presented in Section 2. The experimental details are addressed in Section 3. Parameterization at steady state conditions is shown in Section 4. In the same section, the optimized set of parameters has been used to study parameter influences on the model response under steady state conditions. Furthermore, some typical experimental observations, like dependence of electrode activity on enzyme loading have been rationalized based on model predictions.

2. Mathematical modeling

2.1. Modeling assumptions

The following main assumptions have been made in this work:

a) A quasi-steady state approximation of charge balance equations has been made. This is justified due to an assumption of the local electroneutrality in the ion-conducting phase, and due to a very small time constant (compared to time constants of other processes (diffusion, enzymatic and electrochemical reactions)) of the potential field relaxation in the electron-conducting phase [6–7].

b) The enzyme and mediator are assumed to be uniformly distributed throughout the porous matrix. The amount of the total active mediator and enzyme is constant. The enzyme and mediator are in fully active or inactive form. This allows us to discuss the utilization factor of species. Enzyme activity is not a function of its position. No enzyme leaching out of the CL occurs during the experiment. The enzyme is not inhibited by the substrate or other chemicals under the experimental conditions.

c) The reaction kinetics of GOx using TTF as a mediator in the presence of glucose on conductive material follows the so-called two-substrate ping-pong mechanism [2,17–18,21–22]. All reactions are taking place only in the CL. The simplified reaction kinetics was considered instead of full Michaelis Menten kinetics. This assumption reduces the number of required kinetic parameters and it is well justified in case of steady state operation.

d) The oxidized form of the TTF^+ mediator can move freely in CL and diffuse out of CL. This is well justified with experimental evidences from literature (e.g. quartz crystal microbalance experiments in reference [23]). The increase in concentration of TTF^+ in bulk solution during the duration of the experiment can be neglected. This corresponds well with experimental observations, where no TTF compounds have been detected by nuclear magnetic resonance (NMR) spectroscopy analysis of the solution after 7 h of operation at 0.3844 vs. SHE/V (data not shown here). TTF^+ is formed only at the interface of the electron conducting phase and TTF phase.

2.2. Mathematical equations

As it was mentioned, the modeling approach described in our previous publication [6] has been extended to the porous meditated electroenzymatic system. In short, two modeling domains, CL and DL, are considered (Fig. 1). The first modeling domain relates to heterogeneous CL (from $z = 0$ to $z = L$) including non-electron- (TTF), electron- (Vulcan nanoparticles) and ion-conducting (liquid) phases. The ion-conducting-phase is characterized by the void fraction "ε". The electrochemical reaction takes place at the interface between the non-electron- and electron-conducting phases defined further as the internal active surface area "a". The second modeling domain is DL (from $z = L$ to $z = L + \delta_{DL}$) which takes into account the diffusion resistance at the interface between the liquid phase and the CL.
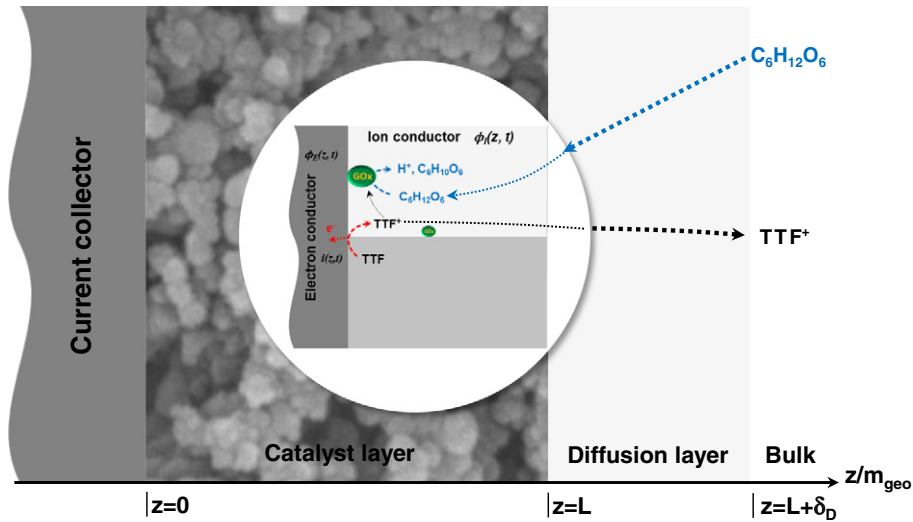
Fig. 1. Schematic representation of modeling domains.

The key model equations in the CL include charge balances at the interface, ion- and electron-conducting phases (Table 1), mass balances and reaction kinetics (Table 2). The charge balance equation for the ion-conducting phase and mass balance equations for dissolved species i.e. oxidized mediator and glucose are developed in DL.

The conductivities (κ_E, κ_I) of electron- and ion-conducting phases in Table 1 are defined as effective conductivities related to conductivities of pure phases in accordance with Bruggeman's correlation:

$$\kappa_E^{CL} = \kappa_E (1 - \varepsilon)^{1.5} \tag{1}$$

$$\kappa_I^{CL} = \kappa_I \varepsilon^{1.5}. \tag{2}$$

The conductivity of the pure ion-conducting phase is calculated from:

$$\kappa_I = F^2 \sum_f \zeta_f^2 \frac{D_f}{RT} C_f \tag{3}$$

where "f" refers to dissociated ions from buffer solution e.g.: H^+, Na^+, K^+, $H_2PO_4^-$, and HPO_4^{2-}.

The thicknesses of diffusion layers of the substrate and mediator in Table 2, in the case of a rotating disc electrode can be calculated according to:

$$\delta_i = 1.61 D_i^{1/3} \nu^{1/6} \omega_r^{-1/2} \tag{4}$$

where $i = S, M_{ox}$ stands for substrate and oxidized form of the mediator respectively and ω_r is the electrode rotation rate in the solution of kinematic viscosity ν.

The diffusion coefficient (D) in the CL is an effective one expressed in accordance to Bruggeman's correlation:

$$D_i^{CL} = D_i \varepsilon^{1.5}. \tag{5}$$

The total cell current density is obtained by spatial integration of local current densities (ι) along the CL:

$$j(t) = \int_0^L \iota(z,t) a dz. \tag{6}$$

2.2.1. Reaction kinetics

In some studies, TTF was combined with tetracyano-quinodimethanide (TCNQ) forming a charge transfer complex (CTC) which was then acting as a mediator [19–20,24–25]. TTF itself can act as a mediator as it was shown in [23,19,26]. Unlike CTC, TTF has negligible electron conductivity, which is the reason why it is usually integrated into the electron conductive matrix. While the mechanism of electron transfer in enzymatic electrodes employing CTC was somewhat controversial [19,23–29], in the TTF case most literature studies assume that TTF^+ species is a mediator for GOx regeneration [19,23]. This is supported by experimental evidences of TTF^+ freely moving and interacting with the active center of the enzyme [19,23,27]. This assumption has been also adopted in the present study.

The kinetic description follows assumption (c) in Section 2.1. The first step in the reaction mechanism is substrate diffusion from the bulk to the CL (Eq. (7)). In the CL enzymes react with substrate. This

Table 1
Charge balance equations.

| Charge balance	Mathematical equation	Boundary condition (BC)
Electron-conducting phase: $\phi_E(z,t)$	$0 = \frac{\partial}{\partial z}\left(\kappa_E^{CL}\frac{\partial \phi_E^{CL}(z,t)}{\partial z}\right) + a\,\iota(z,t)$	$\kappa_E^{CL}\frac{\partial \phi_E^{CL}(z,t)}{\partial z}\big|_{z=L} = 0$ $\phi_E^{CL}(0,t) = \phi_E^{LB}(t)$
Ion-conducting phase: $\phi_I(z,t)$	In CL $0 = \frac{\partial}{\partial z}\left(\kappa_I^{CL}\frac{\partial \phi_I^{CL}(z,t)}{\partial z}\right) - a\,\iota(z,t)$ In DL $0 = \frac{\partial}{\partial z}\left(\kappa_I^{DL}\frac{\partial \phi_I^{DL}(z,t)}{\partial z}\right)$	$\kappa_I^{CL}\frac{\partial \phi_I^{CL}(z,t)}{\partial z}\big|_{z=0} = 0$ $\phi_I^{CL}(L^-,t) = \phi_I^{DL}(L^-,t)$ $\kappa_I^{CL}\frac{\partial \phi_I^{CL}(z,t)}{\partial z}\big|_{z=L^-} = \kappa_I^{DL}\frac{\partial \phi_I^{DL}(z,t)}{\partial z}\big|_{z=L^+}$ $\phi_I^{DL}(L,t) = \phi_I^{RB}(t)$
At the interface: $E(z,t) = \phi_E^{CL}(z,t) - \phi_I^{CL}(z,t)$	$0 = \iota(z,t) - Fr_e(z,t)$	

Table 2
Mass balances.

Mass balance	Mathematical equation	Boundary condition (BC)
Substrate S	In CL $\varepsilon \frac{\partial C_S^{CL}(z,t)}{\partial t} = \frac{\partial}{\partial z}(D_S^{CL} \frac{\partial C_S^{CL}(z,t)}{\partial z}) - r_1(z,t)$ In DL $\frac{\partial C_S^{DL}(z,t)}{\partial t} = \frac{\partial}{\partial z}(D_S^{DL} \frac{\partial C_S^{DL}(z,t)}{\partial z})$	$D_S^{CL} \frac{\partial C_S^{CL}(z,t)}{\partial z}\big|_{z=0} = 0$ $C_S^{DL}(z = L + \delta_S, t) = C_S^{RB}(t)$ $-D_S^{CL} \frac{\partial C_S^{CL}(z,t)}{\partial z}\big|_{z=L^-} = -D_S^{DL} \frac{\partial C_S^{DL}(z,t)}{\partial z}\big|_{z=L^+}$ $C_S^{CL}(L^-,t) = C_S^{DL}(L^+,t)$
Oxidized mediator M_{ox}	In CL $\varepsilon \frac{\partial C_{M_{ox}}^{CL}}{\partial t} = \frac{\partial}{\partial z}(D_{M_{ox}}^{CL} \frac{\partial C_{M_{ox}}^{CL}(z,t)}{\partial z}) + ar_e(z,t) - 2r_2(z,t)$ In DL $\frac{\partial C_{M_{ox}}^{DL}(z,t)}{\partial t} = \frac{\partial}{\partial z}(D_{M_{ox}}^{DL} \frac{\partial C_{M_{ox}}^{DL}(z,t)}{\partial z})$	$D_{M_{ox}}^{CL} \frac{\partial C_{M_{ox}}^{CL}(z,t)}{\partial z}\big|_{z=0} = 0$ $C_{M_{ox}}^{DL}(z = L + \delta_{M_{ox}}, t) = 0$ $-D_{M_{ox}}^{CL} \frac{\partial C_{M_{ox}}^{CL}(z,t)}{\partial z}\big|_{z=L^-} = -D_{M_{ox}}^{DL} \frac{\partial C_{M_{ox}}^{DL}(z,t)}{\partial z}\big|_{z=L^+}$ $C_{M_{ox}}^{CL}(L^-,t) = C_{M_{ox}}^{DL}(L^+,t)$
The reduced form of enzyme E_{red}	$\frac{\partial C_{E_{red}}(z,t)}{\partial t} = r_1(z,t) - r_2(z,t)$	
Conservation of total mediator and enzyme concentration	$C_{Mt}(z,t) = C_{M_{red}}(z,t) + C_{M_{ox}}(z,t)$ $C_{Et}(z) = C_{E_{red}}(z) + C_{E_{ox}}(z)$	

step in accordance with assumption (c) was described as a single step with effective kinetic constant K_1 (Eq. (8)).

$$S^{bulk} \overset{D_S}{\Rightarrow} S^{CL} \overset{D_{CL}}{\Rightarrow} S \tag{7}$$

$$E_{ox} + S \overset{K_1}{\Rightarrow} P + E_{red} \tag{8}$$

where E_{red} represents the reduced form of the enzyme, E_{ox} the oxidized form of the enzyme and P the product.

In the next step the reduced form of the enzyme is regenerated by the mediator. The kinetics of this step has been also simplified in accordance with Eq. (9).

$$E_{red} + 2M_{ox} \overset{K_2}{\Rightarrow} E_{ox} + 2M_{red} + 2H^+ \tag{9}$$
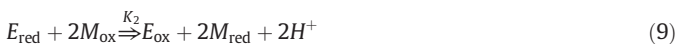
The reduced form of the mediator is finally regenerated in the electrochemical reaction on the electron conductive surface:

$$M_{red} \overset{k_{e0}}{\Rightarrow} M_{ox} + e^- \tag{10}$$

where M_{red} stands for TTF and M_{ox} for TTF$^+$.

The oxidized form of the mediator (M_{ox}) can be utilized again for enzyme regeneration (Eq. (9)). Alternatively in accordance with literature findings [19,23] it might diffuse to bulk solution (Eq. (11)) or even oxidize further [19,29]. The second oxidation step of the mediator has not been considered in the model assuming that the rate of this reaction is negligible in the studied potential range.

$$M_{ox} \overset{D_{M_{ox}}^{CL}}{\Rightarrow} (M_{ox})^{CL} \overset{D_{M_{ox}}}{\Rightarrow} (M_{ox})^{bulk}. \tag{11}$$

The reaction rate of the enzymatic step following the lumped kinetics (Eq. (8)) is expressed as follows:

$$r_1(z,t) = \underbrace{K_1 C_{Et}}_{P_1} C_S^{CL}(z,t) x_{E_{ox}}(z,t) \tag{12}$$

where C_{Et} and $x_{E_{ox}}$ are the total active enzyme concentration and mole fraction of the oxidized form of the enzyme respectively.

The reaction rate of the mediator/enzyme step follows the second order kinetics with effective kinetic constant K_2 in accordance with other reports in literature [22,30]:

$$r_2(z,t) = \underbrace{K_2 C_{Et}}_{P_2} C_{Mt} x_{M_{ox}}(z,t) x_{E_{red}}(z,t) \tag{13}$$

where C_{Mt}, $x_{M_{ox}}$, and $x_{E_{red}}$ are the total active mediator concentration and mole fraction of the oxidized form of the mediator and reduced form of the enzyme respectively.

The rate of the electrochemical step for mediator regeneration can be related to overpotential by the Butler–Volmer equation:

$$r_e(z,t) = k_{e0} C_{Mt} \left[x_{M_{red}}(z,t) e^{\alpha F(E(z,t)-E_r)/(RT)} - x_{M_{ox}}(z,t) e^{-(1-\alpha)(E(z,t)-E_r)F/(RT)} \right] \tag{14}$$

$$E(z,t) = E_{applied}(z,t) - j(t) A_{geo} R_{ohm} \tag{15}$$

where α stands for transfer coefficient, E_r for the formal potentials of the M_{red}/M_{ox} couple, A_{geo} for geometrical surface area, R_{ohm} for Ohmic loss resistance and F, R and T for Faradays and universal gas constants and temperature, respectively.

3. Experiment

3.1. Materials

Glucose oxidase (EC 1.1.3.4, GOx) from *Aspergillus niger* was supplied by Fluka. Vulcan XC72R was provided by Cabot EMEA. Tetrathiafulvalene (TTF) was supplied by Sigma Aldrich. Poly(vinylidenefluoride) (PVDF) was supplied by Merck. All chemicals were of analytical reagent grade and all solutions were prepared using ultrapure water from Millipore.

3.2. Preparation of electrodes

The procedure for porous electrode preparation incorporating GOx, TTF and Vulcan nanoparticles is similar to those reported by Varničić et al. [32]. In this procedure poly(vinylidenefluoride) (PVDF) was used as a binder and enzymes were physically absorbed into the porous electron conductive matrix. In short, 20 mg of Vulcan and 10 mg of TTF were suspended/dissolved in 1 ml of 0.25 wt.% PVDF solution prepared using 1-methyl-2-pyrrolidone. 70 μl of the prepared ink was casted on spectroscopic graphite disks (Ted Pella INC, 10 mm) and left to dry at 60 °C for 5 h. After drying, Vulcan–TTF–PVDF electrodes were modified by physical adsorption of 50 μl of solution containing GOx in different concentrations (from 0.1 mg ml^{-1} to 14 mg ml^{-1}) prepared in 0.1 M phosphate buffer, pH 7. The adsorption of enzymes on Vulcan–TTF–PVDF electrodes was performed for 2 h at room temperature. Electrodes were then left to dry at room temperature and were ready for use.

3.3. Electrochemical experiments

The prepared enzymatic electrodes were mounted into a rotating disc electrode holder (RDE, Radiometer Analytical) with the opening of 6 mm and were used as working electrodes in a 3-electrode setup. A platinum (Pt) wire and saturated calomel electrode (SCE) were used as a counter and a reference electrode, respectively. Steady state

polarization curves were obtained from current time dependences at constant potentials by extracting the current values after 2 min. Experiments were done in nitrogen atmosphere and in 0.1 M phosphate buffer solution at constant rotation rate of 400 rpm (rounds per minute) in order to ensure defined mass transport conditions. All electrochemical experiments were repeated at least 3 times using an Autolab potentiostat (PGSTAT302, Eco Chemie).

3.4. Scanning electron microscopy (SEM)

The morphology of the enzymatic electrodes without and with the TTF mediator was investigated by scanning electron microscopy (SEM) at AQura GmbH, Germany.

4. Results and discussion

The 1-D mathematical model introduced in Section 2 has been implemented in the MATLAB® software. The model has been experimentally validated under steady state conditions at pH 7 and 37 °C at different substrate concentrations. The model was also used for parameterization, parameter study and process analysis.

In the following, the parameter estimation, parameter study, concentration profiles and influence of enzyme loading have been presented.

4.1. Model parameters

Several groups of parameters appear in the model i.e. kinetic, operating, transport, structural and thermodynamic parameters as shown in Table 3. Among these parameters kinetic parameters and the diffusivity of the oxidized mediator have been obtained by fitting with experimental data while the other parameters were calculated or taken from literature or were based on experimental conditions.

The structural parameters include the electrode thickness, porosity and internal active surface area. All three parameters are interrelated, but this interrelation cannot be easily quantified and in most studies no interdependence has been considered. In our previous publication [6] the porosity of the enzymatic electrode has been estimated based on

known electrode thickness and the compact thickness of the electrode calculated according to the equation provided by Gode et al. [31]. Assuming that under present conditions, the porosity remains at 0.35 as reported in the previous work [6], the electrode thickness of 59 μm has been recalculated according to [31]. This value is bigger than the thickness of the Vulcan–PVDF electrode in [6] which appears logical due to the higher amount of material loading on the same geometrical surface area. The SEM images of the cross-section of the studied electrode without and with TTF are shown in Fig. 2a andb respectively. The SEM images of TTF–Vulcan/PVDF electrodes appear very homogenous and resemble in general the structure of Vulcan/PVDF electrodes shown in the previous publication [32]. The particle size after TTF coating (Fig. 2b, 50–125 nm) is roughly 2 times larger than the Vulcan particle size (Fig. 2a, 20–60 nm). Having in mind, that the active surface area is roughly inversely proportional to the particle diameter, an increase of the particle radius will result in a decrease of the active surface area. In the present work, the value of "a" was taken at 1×10^4 which is lower than the reported value in our previous publication (3×10^4 to 6×10^5 m$^2_{act}$ m$^3_{geo}$) [6].

The optimized parameters are obtained by global minimization of the differences between experimental data and simulated data using sum of square residues (SSR) with the following objective function:

$$X^2(P) = \min \sum_{i=1}^{m} \sum_{k=1}^{n} \left(\frac{j_{\text{sim}}(C_{\text{s,i}}, E_{\text{k}}, P) - \hat{j}_{\text{exp}}(C_{\text{s,i}}, E_{\text{k}})}{\sigma_{\text{ik}}} \right)^2 \quad (16)$$

Table 3
Overview of model parameters for simulation.

Kinetic [fitted]	
$P_1 = K_1 C_{\text{Et}}$/s^{-1}	
$P_2 = K_2 C_{\text{Et}}$/s^{-1}	
k_{e0}/m$^3_{\text{geo}}$ m$^2_{\text{act}}$ s^{-1}	
C_{Mt}/mol m^{-3}	
Operating [measured]	
T/K	310
ω/rad s^{-1}	41.87
C/mol m^{-3}	0–20
E (vs. SHE)/V	0.044–0.444
R_{ohm}/Ω	61
Transport [calculated/fitted]	
D_{S}^{CL}/m^2 s^{-1} [33]	9.56
$D_{M_{\text{ox}}}^{\text{CL}}$/m^2 s^{-1}	Table 4
κ_{E}/ S m$^{-1}_{\text{geo}}$	400
κ_{I}/ S m$^{-1}_{\text{geo}}$	0.1
Structural [measured, estimated]	
L/μm$_{\text{geo}}$	59
ε/m^3 m$^{-3}_{\text{geo}}$ [6]	0.35
a/10^4 m$^2_{\text{act}}$ m$^{-3}_{\text{geo}}$	1
Thermodynamic	
E_{r} (vs. SHE)/V [19,28]	0.394
α [34]	0.5

Fig. 2. SEM images of the studied electrodes: a) Vulcan–PVDF electrode and b) Vulcan–TTF–PVDF electrode.

where $\hat{j}_{exp}$ is the experimental output and j_{sim} is the simulated output for a set of parameters (p), σ_{ik} is the estimated measurement error, n is number of points at different applied potential values ($n = 21$), and m is the number of glucose concentrations ($m = 3$). The individual confidence interval (CI) of the parameters can be extracted from the threshold of the likelihood analysis based on Eq. (16), which is typically given by a level of significance of 95% [35].

According to model equations (Tables 1 and 2) and related kinetic expressions (Eqs. (12)–(14)), 6 individual parameters (K_1, C_{Et}, K_2, k_{e0}, C_{Mt} and $D_{M_{ox}}$) have to be obtained from the global optimization. This number of parameters can be further reduced to 5 parameters by grouping kinetic constants K_1 and K_2, with total enzyme concentration, which results in new parameters P_1 and P_2 (see Eqs. (12) and (13)). This grouping is logical, since from the model structure it is clear that these two values are interrelated and cannot be determined separately. The total concentration of the immobilized enzyme is not known, but only the nominal enzyme concentration (all enzyme loadings in the text correspond to these nominal values). It is reasonable to assume that the total enzyme concentration will be smaller than the nominal enzyme loading. The rate constants K_1 and K_2 can be discussed based on the utilization factor of the enzyme.

In the following, the influence of different glucose concentrations on steady state polarization curves and the optimized parameters will be presented.

4.2. Influence of glucose concentration

Model validation in the present paper is based on experimental data for glucose oxidation on glucose-oxidase modified Vulcan–TTF–PVDF electrodes (Fig. 3). The preparation procedure of these electrodes is somewhat different than other reported procedures using the TTF mediator [36–37]. For example in comparison to TTF–carbon nanotube (CNT) electrodes reported in [36], where CNTs were impregnated with TTF, nominal TTF concentration in the present study is much larger. Also in reference [36] Nafion was used as a binder, while we applied PVDF. In addition, their electrodes were cross-linked with glutaraldehyde and finally covered with Nafion-film on top. All these differences impact the electrode performance. Since the literature data for TTF mediator based electrodes are typically given at room temperature, for comparison with literature data experimental data at 25 °C and pH 7
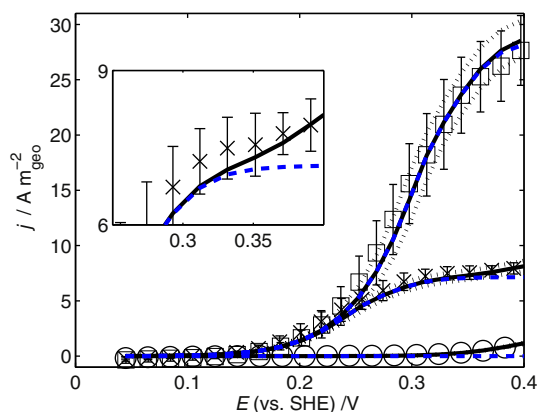

Fig. 3. Steady state polarization curves: symbols — experimental data ($\bigcirc$ 0 mM, $\times$ 5 mM and $\square$ 20 mM), full black lines — simulated curves of full model, dash blue lines — simulated curves of full model with $D_{M_{ox}} = 0$, and dash black lines: upper and lower limits of full model with 95% individual CI. Inset: magnification of steady state polarization at 5 mM glucose concentration and at more positive potentials. Conditions: fixed delay of 2 min; glucose concentrations of 0, 5 and 20 mM, temperature of 37 °C; rotation rate of 400 rpm; pH 7; and enzyme loading of 6 mg ml^{-1} with other parameters given in Table 3 and Table 4.

have been provided (please see Fig. S3, Supporting information). As can be seen, our electrodes at 25 °C achieve ca. 6 A m$_{geo}^{-2}$ at 5 mM of glucose concentration and ca. 18 A m$_{geo}^{-2}$ at 20 mM of glucose concentration. These values are higher than the reported values in literature (ca. 1 A m$_{geo}^{-2}$ at 5 mM of glucose concentration [37] and 7 A m$_{geo}^{-2}$ at 20 mM of glucose concentration [36]). At pH 7, 37 °C, the optimized electrode in the present study (Fig. 3) can reach ca. 9 A m$_{geo}^{-2}$ at 5 mM glucose concentration and ca. 30 A m$_{geo}^{-2}$ at 20 mM of glucose concentration. These performances are comparable with the performances of an Os complex based electrode incorporating multi-wall carbon nanotubes using GOx at pH 7.4, 37 °C, 5 mM of glucose and enzyme loading of 7 g m$_{geo}^{-2}$ [38]. The electrode performances in the present study are also higher than the reported values of other reported Os–GOx based electrodes at pH 7, 37 °C [39–40].

For parameter determination experiments in the absence of glucose and at two different glucose concentrations have been used. As shown in Fig. 3, the simulations using a full model (black line) agree well with experimental data at different glucose concentrations in the whole range of applied potential with $\chi^2 = 272$ (Fig. S2, Supporting information). To see the influence of the oxidized mediator diffusion, the diffusivity of the mediator in the model was set to zero and the steady state response was shown in Fig. 3 (dash-blue line) with $\chi^2 = 6292$. The influence of mediator diffusion is obvious only at more positive potentials and at lower glucose concentrations (please see inset in Fig. 3). This is logical since the mediator reaction is significantly electrochemically accelerated at more positive overpotentials. If the electrochemically generated mediator cannot be consumed in the reaction with enzymes (e.g. at lower glucose concentrations), it will diffuse out (Fig. 3).

The fitting parameters of the full model are shown in Table 4. These parameters have been determined with the help of the objective function (Eq. (16)) with 95% level of significance of individual CIs determined from Fig. S2 (Supporting information). According to Fig. S2 all determined parameters are highly sensitive. From P_1 and P_2, the explicit values of K_1 and K_2 constants can be obtained if the explicit value of total enzyme concentration would be known. For example, if the utilization of enzymes is 100%, the value of K_1 and K_2 will be 389 M^{-1} s^{-1} and 2.95×10^5 M^{-1} s^{-1} respectively. The value of K_2 constant at 100% enzyme utilization is two order of magnitude lower than the second order rate constants reported for ferrocenemethanol as a mediator (0.6–1.2×10^7 M^{-1} s^{-1}/pH 7, 25 °C) [30,36]. The calculated active mediator utilization is ca. 0.027% of its nominal concentration, which is relatively small. This indicates that the nominal mediator concentration can be significantly reduced without any loss in the performance. The electrochemical rate constant k_{e0} is 18×10^{-4} m$_{geo}^3$ m$_{act}^{-2}$ s^{-1}. If the active and the geometrical surface areas are the same (this corresponds to reaction on a smooth surface), the heterogeneous rate constant will have a value of 18×10^{-4} m s^{-1}. This is in the range of the reported values (3×10^{-4} to 2.2×10^{-2} m s^{-1}) of TTF/TTF$^+$ couple heterogeneous rate constant at a Pt micro-disc electrode in organic solvent at 293 K [27,39]. The diffusivity of the mediator is 8.61×10^{-10} m$_{geo}^2$ s^{-1} which is somewhat smaller than the reported value by Bond et al. [34] of 1.95×10^{-9} m$_{geo}^2$ s^{-1} at 25 °C for TTF$^+$ diffusion in organic solvent.

To check the influence of the charge and substrate distributions on the model response, the full model has been reduced along the spatial

Table 4
Optimized parameters.

Parameter	σ^-	P	σ^+
$P_1 = K_1 C_{Et}$/s^{-1}	0.39	0.44	0.507
$P_2 = K_2 C_{Et}/10^2$ s^{-1}	3.16	3.34	3.53
$k_{e0}/10^{-4}$ m$_{geo}^3$ m$_{act}^{-2}$ s^{-1}	15	18	21
C_{Mt}/mol m$_{geo}^{-3}$	1.03	1.05	1.07
$D_{M_{ox}}/10^{-10}$ m$_{geo}^2$ s^{-1}	8.31	8.61	8.94

coordinate. This so-called reduced 1-D model has been further used for simulations at different glucose concentrations, with parameters given in Table 4. The results have shown that the spatial distribution can be disregarded only at low overpotentials (Fig. S1, Supporting information). At more positive overpotentials the reduced 1-D model fails significantly. It should be stressed out that this model cannot describe experimental data in the whole potential range with any set of parameters.

4.3. Concentration profiles

The dynamic change of glucose concentration at one fixed position in the CL (middle of the CL) and the steady state distribution of the glucose concentration along the spatial coordinate at two glucose concentrations (5 and 20 mM) and at different potentials are shown in Fig. 4.

The dynamic profiles of glucose concentration reveal that ca. 120 s is needed to reach steady state behavior independent of the electrode
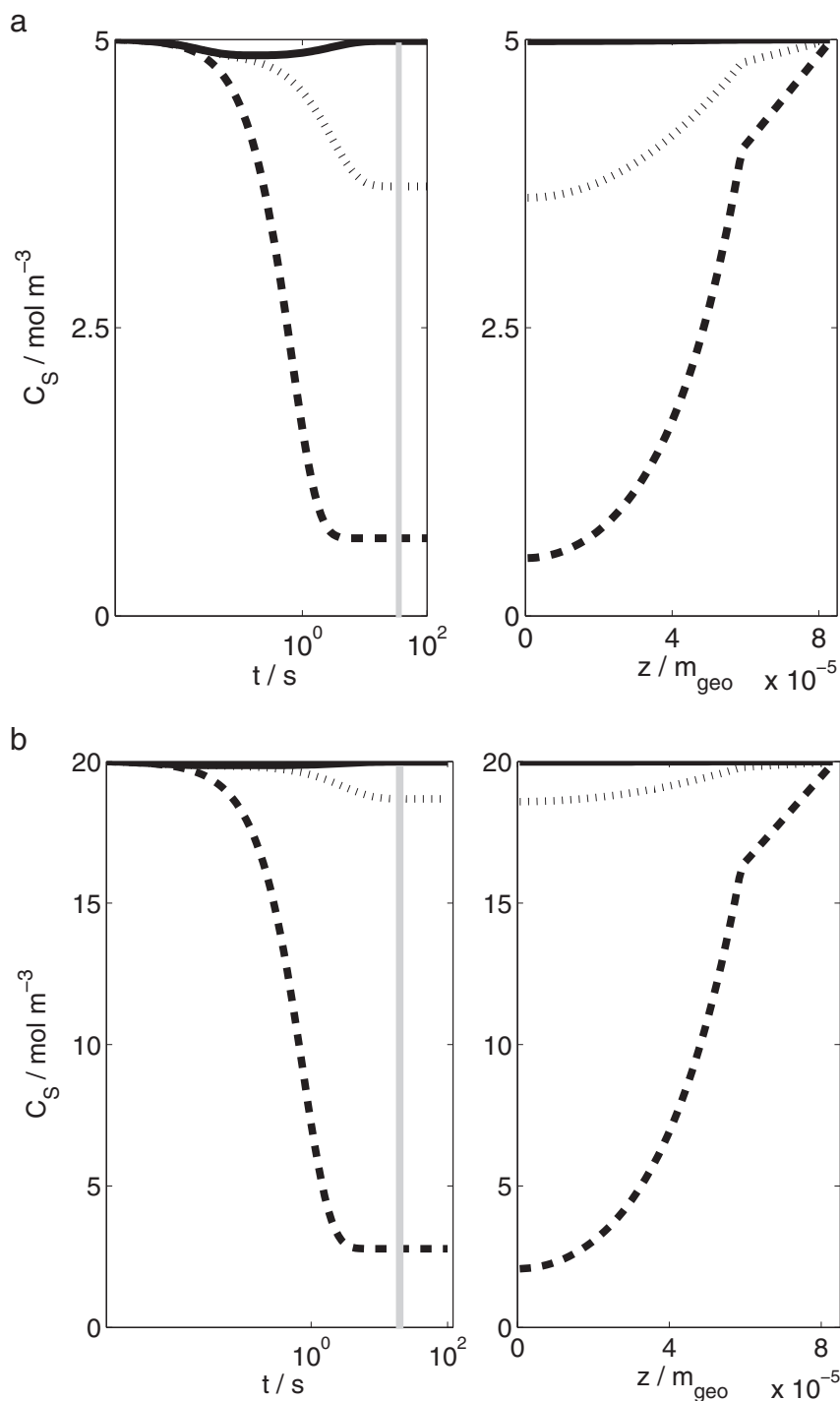

Fig. 4. Simulated transient (at fixed position in the middle of CL) and steady state (along spatial coordinate) profiles of glucose concentration at different potentials and a) at 5 mM and b) 20 mM of glucose concentration. Full line — 0.0644 V, dot line — 0.2044 V and dash line — 0.3844 V. The detail local profiles of the glucose concentration can be seen in Fig. S4 (Supporting information). Conditions: temperature of 37 °C and rotation rate of 400 rpm, with other parameters given in Table 3 and Table 4.

potential. The response time is a bit glucose concentration dependent, requiring less time at higher glucose concentrations (for example at 20 mM glucose concentration the response time is ca. 100 s, compared to 120 s at 5 mM). These correspond also to experimental observations. The transient curves reveal that at lower glucose concentrations glucose depletion can happen at shorter time scale, which will not be visible in the steady state response.

The concentration profiles along the spatial coordinate show that, independent of glucose concentration, no concentration distribution takes part at more negative potentials. This is also reflected in simulations obtained by the reduced 1-D model (please see Fig. S1, Supporting information), which showed good agreement with experiments at more negative potentials. At more positive potentials, concentration

distribution is obvious at both concentrations (for the more detailed profiles, please see Fig. S4, Supporting information). This affects not only the CL but also the DL. The results reveal that the electrode works throughout layers, which excludes pure diffusion control under studied conditions. The observed limiting currents are diffusion–reaction limited.

All other transport processes like charge transport in electron and ion-conducting phases have almost no influence on the electrode performance (not shown here). Additional simulation work has been done in order to study the influence of an electrolyte on the system response. Only in very diluted solutions (assuming 100 times smaller ionic conductivity than the nominal value) the electrode performance becomes significantly limited by the transport in the ion-conducting phase.
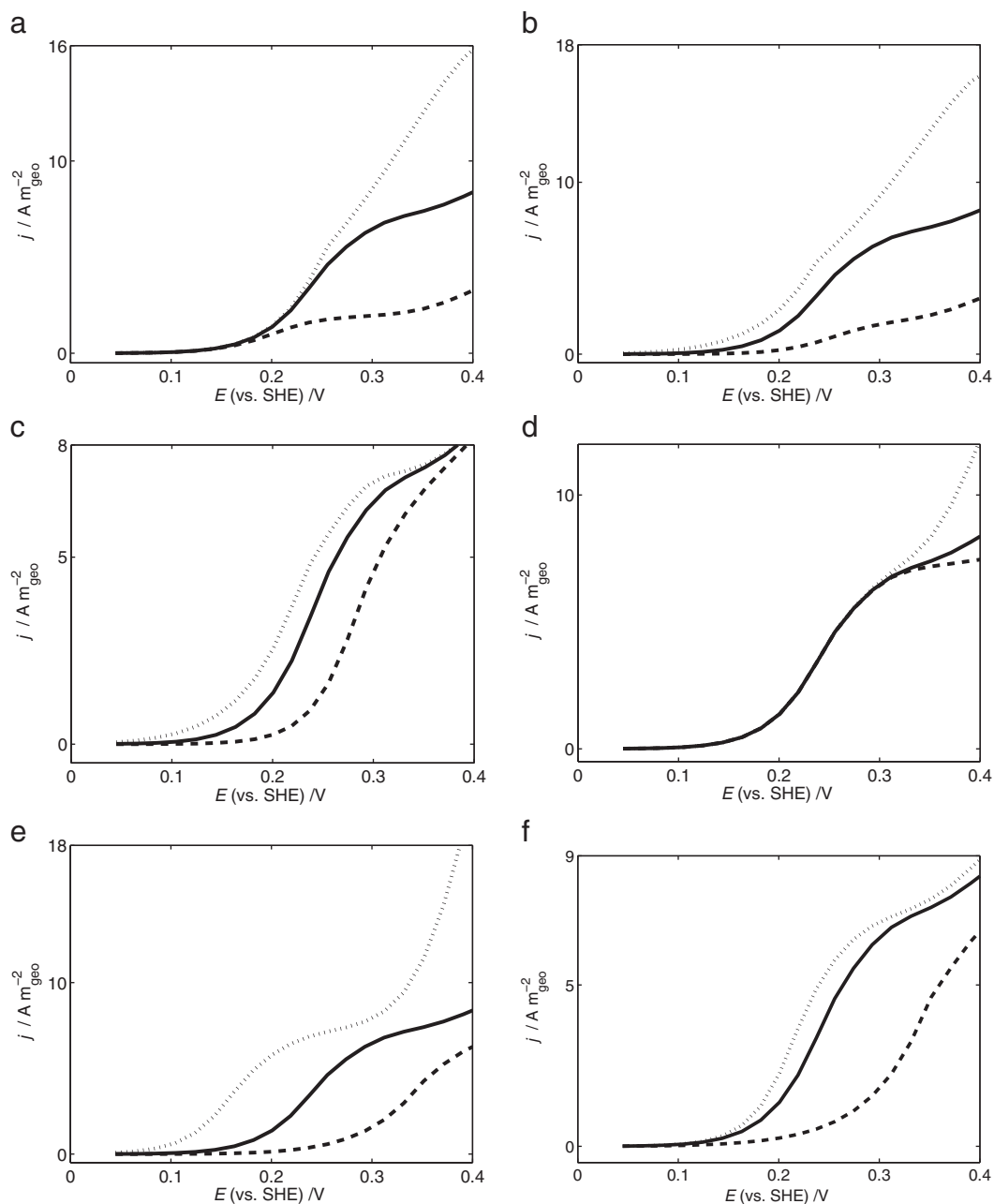

Fig. 5. Simulated steady state response of the full model showing the influence of the parameter variation with respect to their optimized values (Table 4): a) K_1, b) C_{Et}, c) K_2, d) $D_{M_{ox}}$, e) C_{Mt} and f) k_{e0}. Full line — optimized parameter value, dot line — 10 times optimized parameter value and dash line — 0.1 times optimized parameter value. Conditions: 5 mM glucose concentration, temperature of 37 °C, and rotation rate of 400 rpm with other parameters given in Table 3 and Table 4.

4.4. Parameter study

The optimized set of parameters, is now used to study the influence of parameters on the steady state response at pH 7 and at temperature of 37 °C, considering two limiting cases, a small parameter value (10 times smaller than the optimized value) and a large parameter value (10 times higher than the optimized value). To demonstrate the individual impacts of K_1, K_2 and C_{Et} parameters which were lumped into parameters P_1 and P_2, 100% enzyme utilization has been assumed for the base case.

In Fig. 5a, and b the influence of the enzymatic constant K_1 and the total number of active enzymes C_{Et} are shown. These two parameters have similar effect on the steady state response. In general, an increase of these parameters improves the electrode performance. Still, while the enzyme loading influences the performance in the whole range of potential (Fig. 5b), the K_1 constant has a strong effect at more positive potentials (≥ 0.1444 V) (Fig. 5a). This can be rationalized by the influence of the active enzyme number on two reaction steps, the enzyme substrate and enzyme mediator step, while the K_1 constant affects only the enzyme substrate step.

Increasing the K_2 constant above a certain value does not provide significant impact on the steady state response as displayed in Fig. 5c, due to the overall limitation of either enzymatic or electrochemical step. The interesting effect of the total concentration of the mediator C_{Mt} can be seen in Fig. 5e. Increasing the amount of the active mediator in the system upgrades the current in the whole range of applied potentials. Two distinguished influences in the lower and the higher range of potentials can be observed. More active TTF available in the system, for a given enzyme loading and glucose concentration, will shift the onset potential of the reaction to more negative values. At the same time at more positive potentials, the effect of TTF$^+$ diffusion will become more significant. As it was already demonstrated, the oxidized mediator diffusivity has impact only at more positive potentials (Fig. 5d). The electrochemical rate constant k_{e0} has global influence. However, the impact of the smaller k_{e0} value is more pronounced than its higher value because at a higher k_{e0} value other steps like enzymatic might become limiting.

The above simulations have shown that several parameters (C_{Et}, K_2, C_{Mt}) might influence the onset potential of the reaction. Similar findings were also demonstrated in the study of Limoges et al. [40]. From simulations above it also follows that most parameters have impact in the broad range of potential. The only parameter of local importance is mediator diffusivity which impacts only the electrode behavior in the more positive potential range. This is in some extent also true for enzymatic constant K_1 which has little influence at more negative potentials. It follows that for reliable parameter estimation global optimization including data at different concentrations and covering the whole range of potentials is necessary.

4.5. Enzyme loading

The simulations in Fig. 5b show that the electrode activity increases with an increase of enzyme loading. This increase is not linear, which can be also seen in Fig. 6 where the dependence of normalized electrode activity (current density divided by nominal enzyme loading) on the nominal enzyme loading has been shown. The simulated data are obtained assuming 100% enzyme utilization at the nominal enzyme loading of 6 mg ml^{-1} (base case), by recalculating kinetic constants K_1 and K_2 from P_1 and P_2 values (Table 4) and by using nominal enzyme loading values for simulations at different loadings. The results demonstrate that the normalized electrode activities decrease with an increase of enzyme loading, even with an assumption of 100% enzyme utilization at different loadings. This observation can be ascribed to the fact that at higher enzyme loadings due to acceleration of reaction steps with enzyme participation, some other steps become limiting i.e. mediator regeneration or substrate diffusion. Concentration profiles along the spatial coordinate, at two different enzyme loadings (low and high, for the base case please refer to Fig. 4b) show significant glucose depletion along the CL at high enzyme loading, while the concentration profile at low enzyme loading is less expressed (Fig. 6b and c). Experimentally observed dependence of normalized electrode activity on enzyme loading shows a similar trend as in simulation (Fig. 6a). However, experimental values are somewhat higher than simulated ones at low loadings while they are lower than simulated ones at higher loadings. This discrepancy
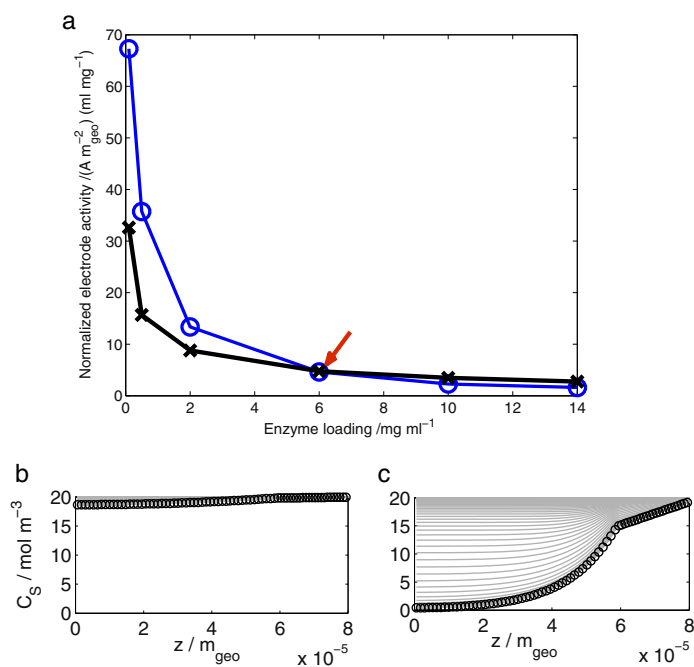

Fig. 6. a) Dependence of the normalized electrode activity on the GOx loading (-x- experiments and -o- simulation) and simulated profiles of glucose concentration along spatial coordinate at two enzyme loadings: b) 0.1 mg ml^{-1} and c) 14 mg ml^{-1}. Conditions: 20 mM of glucose concentration, $E = 0.4044$ vs. SHE/V, pH 7, 37 °C, and other parameters as in Table 3 and Table 4.

between the model and experiment suggests that the enzyme utilization for the base case (6 mg ml^{-1}) is probably lower than 100%, advising a decrease of enzyme utilization with an increase of loading. The lower enzyme utilization at higher loadings can be caused by nonidealities under experimental conditions, like a decrease of electrode porosity, decrease of electrode conductivity due to breakups of the electron conductive network caused by an increase of protein portion in the CL. These effects would contribute to the further decrease of the electrode activity at higher enzyme loadings.

5. Conclusion

The full 1-D model of porous enzymatic electrodes with MET can quantitatively describe experimental data for glucose oxidation in the concentration range from 0 to 20 mM glucose, with the optimized set of parameters obtained by global optimization. For 5 fitted model parameters, individual CIs have been extracted for each parameter from the respective likelihood. The analysis has shown high sensitivity of all parameters. It was shown that most of parameters mutually influence electrode response in the whole potential range. The only exceptions were oxidized mediator diffusivity and the enzymatic constant K_1 which had stronger influence at more positive potentials. This recommends global optimization as a most suitable tool for parameter estimation. The concentration profiles along the spatial coordinate have shown that only at more negative potentials there is no glucose distribution along different layers. This was also confirmed using a reduced 1-D model which showed agreement to experiments only at more negative potentials. It was also shown that electrodes work through under all studied conditions. This means that observed limited currents are reaction–diffusion limited.

The variation of optimized model parameters has demonstrated that three parameters (C_{Et}, K_2, C_{Mt}) can be responsible for the shift of the reaction onset potential. The normalized electrode activity decreases with an increase of enzyme loading. According to the model, the reason for this observation is glucose depletion along the CL at higher enzyme loadings. Comparison with experiments advices a decrease of enzyme utilization at higher enzyme loadings. This can be caused by nonidealities under experimental conditions, like a decrease of electrode porosity and electrode conductivity at higher enzyme loadings which were not taken into account in the model.

Acknowledgments

Appendix A. List of symbols

a	Internal active surface area	$m_{act}^2\ m_{geo}^{-3}$
A_{geo}	Geometrical surface area of electrode $= 0.28 \times 10^{-4}$	m_{geo}^2
C	Volumetric concentration	mol m^{-3}
D	Diffusion coefficient of species in bulk	m_{geo}^2 s^{-1}
E	Electrode potential	V
R_{ohm}	Electrolyte resistance	Ω
F	Faraday's constant = 96 485	C mol^{-1}
j	Total cell current density	A m_{geo}^{-2}
K_1, K_2	Reaction constants of enzyme substrate and enzyme mediator reactions	m^3 mol^{-1} s^{-1}/ m_{geo}^3 mol^{-1} s^{-1}
k_{e0}	Kinetic constant of the electrochemical reaction	$m_{geo}^3\ m_{act}^2$ s^{-1}
L	Catalyst layer thickness	m_{geo}
R	Universal gas constant = 8.314	J mol^{-1} K^{-1}

Appendix A (continued)

T	Temperature = 310	K
Greek		
α	Transfer coefficient of the electrochemical step	= 0.5
ω	Rotation rate of rotating disc electrode	rad s^{-1}
ι	Local current density	A m_{act}^{-2}
ϕ_E, ϕ_I	Potentials of electron- and ion-conducting phases respectively	V
κ_E, κ_I	Electron and ion conductivities	S m_{geo}^{-1}
δ	Diffusion layer thickness	m_{geo}
ε	Void fraction	$m^3\ m_{geo}^{-3}$
ζ	Charge number	
Super- and sub-scripts		
RB, LB	Right boundary and left boundary respectively	
I, E	Ion and electron conducting phases respectively	
sim, exp	Simulation and experiment respectively	
red, ox	Reduced and oxidized respectively	
CL, DL	Catalyst layer and diffusion layer respectively	
S	Substrate	
Et/Mt	Total enzyme and total mediator respectively	
e0	Electrochemical reaction step	
act, geo	Active and geometrical respectively	
Ohm	Ohmic	

Appendix B. Supplementary data

Supplementary data to this article can be found online at http://dx.doi.org/10.1016/j.bioelechem.2015.07.007.

References

[1] S.C. Barton, J. Gallaway, P. Atanassov, Enzymatic biofuel cells for implantable and microscale devices, Chem. Rev. 104 (2004) 4867–4886.
[2] I. Ivanov, T. Vidaković-Koch, K. Sundmacher, Recent advances in enzymatic fuel cells: experiments and modeling, Energies 3 (2010) 803–846.
[3] J.-K. Guterl, V. Sieber, Biosynthesis "debugged": novel bioproduction strategies, Eng. Life Sci. 13 (2013) 4–18.
[4] P.N.R. Vennestrøm, C.H. Christensen, S. Pedersen, J.-D. Grunwaldt, J.M. Woodley, Next-generation catalysis for renewables: combining enzymatic with inorganic heterogeneous catalysis for bulk chemical production, ChemCatChem 2 (2010) 249–258.
[5] Z. Zhou, M. Hartmann, Progress in enzyme immobilization in ordered mesoporous materials and related applications, Chem. Soc. Rev. 42 (2013) 3894–3912.
[6] T.Q.N. Do, M. Varničić, R. Hanke-Rauschenbach, T. Vidaković-Koch, K. Sundmacher, Mathematical modeling of a porous enzymatic electrode with direct electron transfer mechanism, Electrochim. Acta 137 (2014) 616–626.
[7] T. Vidakovic-Koch, R. Hanke-Rauschenbach, I. Gonzalez Martinez, K. Sundmacher, K. Swider Lyons, Catalyst layer modeling for gas diffusion-electrodes, in: C. Breitkopf (Ed.), Springer Handbook of Electrochemistry, Springer, 2014 Chapter 9.
[8] M.E.G. Lyons, Transport and kinetics at carbon nanotube–redox enzyme composite modified electrode biosensors: part 2. Redox enzyme dispersed in nanotube mesh of finite thickness, Int. J. Electrochem. Sci. 4 (2009) 1196–1236.
[9] R. Baronas, J. Kulys, K. Petrauskas, J. Razumiene, Modelling carbon nanotubes-based mediatorless biosensor, Sensors (Switzerland) 12 (2012) 9146–9160.
[10] S. Calabrese Barton, Oxygen transport in composite mediated biocathodes, Electrochim. Acta 50 (2005) 2145–2153.
[11] D.S. Chan, D.J. Dai, H.S. Wu, Dynamic modeling of anode function in enzyme-based biofuel cells using high mediator concentration, Energies 5 (2012) 2524–2544.
[12] P.N. Bartlett, C.S. Toh, E.J. Calvo, V. Flexer, Modelling biosensor responses, Bioelectrochemistry, John Wiley & Sons, Ltd 2008, pp. 267–325.
[13] R. Baronas, J. Kulys, Modelling amperometric biosensors based on chemically modified electrodes, Sensors 8 (2008) 4800–4820.
[14] P. Kavanagh, D. Leech, Mediated electron transfer in glucose oxidising enzyme electrodes for application to biofuel cells: recent progress and perspectives, Phys. Chem. Chem. Phys. 15 (2013) 4859–4869.
[15] P.W. Anderson, P.A. Lee, M. Saitoh, Remarks on giant conductivity in TTF-TCNQ, Solid State Commun. 13 (1973) 595–598.
[16] C.D. Jaeger, A.J. Bard, Electrochemical behavior of donor-tetracyanoquinodimethane electrodes in aqueous media, J. Am. Chem. Soc. 101 (1979) 1690–1699.
[17] N.K. Čenas, J.J. Kulys, Biocatalytic oxidation of glucose on the conductive charge transfer complexes, Journal of Electroanalytical Chemistry and Interfacial Electrochemistry 128 (1981) 103–113.
[18] J.J. Kulys, A.S. Samalius, G.J.S. Švirmickas, Electron exchange between the enzyme active center and organic metal, FEBS Lett. 114 (1980) 7–10.

[19] I. Ivanov, T. Vidaković-Koch, K. Sundmacher, Alternating electron transfer mechanism in the case of high-performance tetrathiafulvalene–tetracyanoquinodimethane enzymatic electrodes, J. Electroanal. Chem. 690 (2013) 68–73.

[20] R. Pauliukaite, A. Malinauskas, G. Zhylyak, U.E. Spichiger-Keller, Conductive organic complex salt TTF-TCNQ as a mediator for biosensors. An overview, Electroanalysis 19 (2007) 2491–2498.

[21] C. Bourdillon, C. Demaille, J. Moiroux, J.M. Savéant, New insights into the enzymatic catalysis of the oxidation of glucose by native and recombinant glucose oxidase mediated by electrochemically generated one-electron redox cosubstrates, J. Am. Chem. Soc. 115 (1993) 2–10.

[22] N. Anicet, C. Bourdillon, C. Demaille, J. Moiroux, J.M. Savéant, Catalysis of the electrochemical oxidation of glucose by glucose oxidase and a single electron cosubstrate: kinetics in viscous solutions, J. Electroanal. Chem. 410 (1996) 199–202.

[23] M.S. Freund, A. Brajter-Toth, M.D. Ward, Electrochemical and quartz crystal microbalance evidence for mediation and direct electrochemical reactions of small molecules at tetrathiafulvalenete, Journal of Electroanalytical Chemistry and Interfacial Electrochemistry 289 (1990) 127–141.

[24] W.J. Albery, P.N. Bartlett, A.E. Cass, Amperometric enzyme electrodes, Philos. Trans. R. Soc. Lond. Ser. B Biol. Sci. 316 (1987) 107–119.

[25] B.S. Hill, C.A. Scolari, G.S. Wilson, P.N. Bartlett, W.J. Albery, Enzyme electrocatalysis at the TTF-TCNQ electrode [and discussion], Philosophical Transactions of the Royal Society of London. Series A: Physical and Engineering Sciences 333 (1990) 63–69.

[26] P.N. Bartlett, Some studies of electrodes made from single crystals of TTF/sd TCNQ, Journal of Electroanalytical Chemistry and Interfacial Electrochemistry 300 (1991) 175–189.

[27] P.N. Bartlett, V.Q. Bradford, Modification of glucose oxidase by tetrathiafulvalene, Journal of the Chemical Society — Series Chemical Communications (1990) 1135–1136.

[28] B. Kowalewska, P.J. Kulesza, Application of tetrathiafulvalene-modified carbon nanotubes to preparation of integrated mediating system for bioelectrocatalytic oxidation of glucose, Electroanalysis 21 (2009) 351–359.

[29] L. Haiying, D. Jiaqi, Amperometric glucose sensor using tetrathiafulvalene in Nafion gel as electron shuttle, Anal. Chim. Acta 300 (1995) 65–70.

[30] A.E.G. Cass, G. Davis, G.D. Francis, H.A.O. Hill, W.J. Aston, I.J. Higgins, E.V. Plotkin, L.D.L. Scott, A.P.F. Turner, Ferrocene-mediated enzyme electrode for amperometric determination of glucose, Anal. Chem. 56 (1984) 667–671.

[31] P. Gode, F. Jaouen, G. Lindbergh, A. Lundblad, G. Sundholm, Influence of the composition on the structure and electrochemical characteristics of the PEFC cathode, Electrochim. Acta 48 (2003) 4175–4187.

[32] M. Varnicic, K. Bettenbrock, D. Hermsdorf, T. Vidakovic-Koch, K. Sundmacher, Combined electrochemical and microscopic study of porous enzymatic electrodes with direct electron transfer mechanism, RSC Advances 4 (2014) 36471–36479.

[33] A.N. Bashkatov, E.A. Genina, Y.P. Sinichkin, V.I. Kochubey, N.A. Lakodina, V.V. Tuchin, Glucose and mannitol diffusion in human dura mater, Biophys. J. 85 (2003) 3310–3318.

[34] A.M. Bond, K. Bano, S. Adeel, L.L. Martin, J. Zhang, Fourier-transformed large-amplitude AC voltammetric study of tetrathiafulvalene (TTF): electrode kinetics of the TTF^0/TTF^+ and TTF^+/TTF^{2+} processes, ChemElectroChem 1 (2014) 99–107.

[35] G. Seber, C.J. Wild, Nonlinear Regression, Wiley Series in Probability and Statistics. Wiley-Interscience, 2003.

[36] D. MacAodha, M.L. Ferrer, P.O. Conghaile, P. Kavanagh, D. Leech, Crosslinked redox polymer enzyme electrodes containing carbon nanotubes for high and stable glucose oxidation current, Physical Chemistry Chemical Physics: PCCP 14 (2012) 14667–14672.

[37] S. Rengaraj, P. Kavanagh, D. Leech, A comparison of redox polymer and enzyme co-immobilization on carbon electrodes to provide membrane-less glucose/O2 enzymatic fuel cells with improved power output and stability, Biosens. Bioelectron. 30 (2011) 294–299.

[38] N. Mano, F. Mao, A. Heller, Electro-oxidation of glucose at an increased current density at a reducing potential, Chem. Commun. (2004) 2116–2117.

[39] G. Grampp, A. Kapturkiewicz, W. Jaenicke, Homogeneous and heterogeneous electron transfer rates of the tetrathiafulvalene-system, Ber. Bunsenges. Phys. Chem. 94 (1990) 439–447.

[40] B.T. Limoges, J. Moiroux, J.-M. Savéant, Kinetic control by the substrate and the cosubstrate in electrochemically monitored redox enzymatic immobilized systems. Catalytic responses in cyclic voltammetry and steady state techniques, J. Electroanal. Chem. 521 (2002) 8–15.